# Resonant Tunnelling Diodes for THz communications

Răzvan Baba

Submitted in fulfilment of the requirements for the
Degree of Doctor of Philosophy

School of Engineering

College of Science and Engineering

University of Glasgow


June 2018

# Abstract

Resonant tunnelling diodes realised in the InGaAs/AlAs compound semiconductor system lattice-matched to InP substrates represent one of the fastest electronic solid-state devices, with demonstrated oscillation capability in excess of 2 THz. Current state-of-the-art offers a poor DC-to-RF conversion efficiency. This thesis discusses the structural issues limiting the device performance and offers structural design optimums based on quantum transport modelling. These structures are viewed in the context of epitaxial growth limitations and their extrinsic oscillator performance. An advanced non-destructive characterisation scheme based on low-temperature photoluminescence spectroscopy and high-resolution TEM is proposed to verify the epitaxial perfection of the proposed structure, followed by recommendations to improve the statistical process control, and eventually yield of these very high-current density mesoscopic devices. This work concludes with an outward look towards other compound semiconductor systems, advanced layer structures, and antenna designs.

# Table of Contents

# Acknowledgements

I thank my supervisor, Prof. Richard Hogg, for the technical, financial and pastoral support throughout this work.

*Technical*. Without Dr. Kristof J.P. Jacobs' ground work this thesis would have taken a more perilous path. Dr. Benjamin Stevens helped with the strain balancing, and detailed MOVPE & XRD training. Dr. Matthew Steer, Dr. Neil Gerrard, Brett Harrison and Timothy Roberts for advice on epitaxial growth and X-ray diffractometry. Dr. Nasser Babazadeh helped with fabrication and Dr. David Childs left a treasure trove of experimental set-ups to play with. Toshikazu Mukai, who facilitated a visit to ROHM Co., Ltd. and for keeping an interesting dialogue. All the National Epitaxy Facility and James Watt Nanoscience Centre technical staff.

*Administrative*. Mrs. Elaine McNamara and Mrs. Hilary Levesley, for their help with the sometimes incomprehensible paperwork. Ms. Eunice Lawton for nurturing a fine environment for PhD students. Supported by the EPSRC grants EP/503812/1 and EP/L505055/1 DTA studentship; the European Commission Horizon 2020 iBROW project 645369; U. of G. PGR Travel Scholarship budget.

*Personal*. To my colleagues that tolerated my endless failings, but especially Soroush Sobhani, who took upon himself to be a big brother to me, without my returning anything. Dr. Pavlo Ivanov, Dr. Negin Peyvast, Dr. Anthony Kelly, Dr. Omar Mobasher Salih, Dr. Wei Li, Avan Majeed, Guangrui Li, Danqi Lei, and all that asked for help.

Thank you, my parents, Marian and Valentina. To all that journeyed with me, Sanket Mugali, Ann Hamblen, Raluca Badea M.D., Ivan Dimov, Dimitris & Ruxandra, Susan, Frances, Joanna, Jonathan, Lămâița Antochi, Basil. To my Rev. Fr. Vasile, Edwin, George, Augustine, forefathers, and mothers, of all those who remain unnamed for their words & deeds, and those whose ever-watchful breath has followed me through the depths of optics basements and to the deceptive heights of the conference presentations, through moments of passionate insanity and the very occasional blessed clarity. For all my callousness, indifference and arrogance, I ask of you:

*O, Heavenly King, Comforter, Spirit of Truth, Who art everywhere present and fillest all things, Treasury of Good things and Giver of life: Come and abide in us, cleanse us of all impurity, and save our souls, O Good One.*

*As your bright search has enlightened the world, Fathers Dionysius Exiguus and Anthim the Iberian, ask that this trifling work endures His mercy and peace.*

## Dedication

To those who allowed this indolent beggar to pick their fruit.

To those whose spiteful fire has tempered my resolve.

To those who fell asleep before their time.

Sandra-Iris, Sabin, Adrian, Ion.

**+**

# Declaration

With the exception of the figures, where specified as being re-created after a [reference] in accordance to the license of the copyright holder, or in the case of raw TEM images obtained from Integrity Scientific Ltd., all work in this thesis was carried out by the author unless otherwise explicitly stated.

# Thesis synopsis

Chapter I walks through an up-to-date review of competing THz technologies, briefly mentioning some of their key advantages. The motivation behind generating THz is discussed, especially focused towards the case of 5G nano- and pico-cell communications, whilst also highlighting the need for wide bandwidth, secure point-to-point communication links. Other applications of THz rays are mentioned, from art preservation to industrial uses. The chapter introduces the main epitaxial growth method used in this work, *metal-organic vapour phase epitaxy* (MOVPE), and highlights the challenge to create highly ordered atomically-thin layers for the next generation of components.

Chapter II discusses the salient points of the theoretical framework upon which the thesis lays: from the nature of conductivity in mesoscopic structures, to advanced energy bands structure from a physical chemistry point of view. These concepts are then used to build-up towards explaining the assumptions made in the implementation of self-consistent non-equilibrium Green's function model, and link with the extrinsic circuit model necessary for the operation of a monolithic RTD oscillator. Parts of this chapter were featured in my paper accepted for publication in *J. Quantum Electronics*.

Chapter III discusses the results of the model in detail, including certain model sanity checks which were not deemed interesting enough to feature in my publication. Parts of this chapter were featured in my paper accepted for publication in *J. Quantum Electronics*.

Chapter IV adds a detailed non-destructive optical characterisation scheme of the challenging, single-QW RTD structures. Low-temperature photoluminescence spectroscopy (LT-PL) and high resolution X-ray diffractometry (HR-XRD) are used in combination to detect average, fractional atomic layer changes, in combination with modelling obtained from the previous chapter to detect the bound energy, and essentially verify the recommendations made. The characterisation scheme is verified with high resolution transmission electron microscopy (HR-TEM). Recommendations are provided to automate this analysis to a wafer-level automated tool.

Chapter V reviews the system-level oscillator topology and discusses possible improvements in each area: advanced structural designs employing triple barrier RTDs, different material systems, different approaches for a THz radiator/antenna, and proposes a future investigation in the physics of the epitaxial interfaces.

# List of publications

Please note the inconsistency in spelling of the word “tunnelling” (British English) & “tunneling” (American English)

## Papers

**R. Baba**, B.J. Stevens, T. Mukai, R. A. Hogg, *Epitaxial designs for maximizing efficiency in resonant tunnelling diode based terahertz emitters*, IEEE J. Q. Electron. 54 (2), 8500211 (2018), DOI: 10.1109/JQE.2018.2797960

K.J.P. Jacobs, B.J. Stevens, **R. Baba**, O. Wada, T. Mukai, R.A. Hogg, *Valley Current Characterization of High Current Density Resonant Tunnelling Diodes for Terahertz-wave Applications,* AIP Adv. 7 (10), 105316, (2017), DOI: 10.1109/JQE.2018.2797960

**R. Baba**, K.J.P. Jacobs, T. Mukai, R.A. Hogg, *Characterisation of thin AlAs Barrier Material for Resonant Tunnelling Diodes* (in preparation, targeted for J. Cryst. Growth)

## Conference proceedings

**R. Baba**, K.J.P. Jacobs, *et al. Optimisation of resonant tunnelling diodes for terahertz applications*, UK Semiconductors, June 2015, C-O-7

**R. Baba** *et al., Optimization of high current density resonant tunneling diodes for terahertz emitters* UCMMT, Sept. 2015, DOI:10.1109/UCMMT.2015.7460581

**R. Baba** *et al., Optimization of the epitaxial design of high current density resonant tunneling diodes for terahertz emitters,* Proc. SPIE 9755, Quantum Sensing and Nano Electronics and Photonics XIII, 97552W (February 2016) DOI:10.1117/12.2212346

K.J.P. Jacobs, **R.Baba**, *et al. Characterisation of high current density resonant tunneling diodes for THz emission using photoluminescence spectroscopy,* Proc. SPIE 9758, Quantum Dots and Nanostructures: Growth, Characterization, and Modeling XIII, 97580L (February 2016) DOI: 10.1117/12.2212669

**R. Baba** *et al., Strained Epitaxy Limitations to Realising High Wall Plug Efficiency Resonant Tunnelling Diode Terahertz Emitters,* UK Semiconductors, July 2016, (C-P-3)

**R. Baba**, K.J.P. Jacobs, *et al., Novel Structural Designs for Engineering Terahertz Emitting Resonant Tunnelling Diodes* UK Semiconductors, July 2016, (D-P-12)

**R. Baba** *et al., Modelling Sub-well Resonant Tunnelling Diode Terahertz Emitters to Optimise Wall-Plug Efficiency,* UK Semiconductors, July 2016,(C-O-7)

**R. Baba** *et al.* Epitaxial Design for Maximising Wall Plug Efficiency in Resonant Tunnelling Diode Terahertz Emitters IRMMW-THz, Copenhagen, September 2016 DOI:10.1109/IRMMW-THz.2016.7758959

**R. Baba** *et al., Novel Structural Designs for Engineering Terahertz Emitting Resonant Tunnelling Diodes, September 2016, JSAP 77th meeting https://confit.atlas.jp/guide/event/jsap2016a/subject/16a-B9-11/detail*

**R. Baba**, K.J.P. Jacobs, *et al., Fabrication, characterisation, and epitaxial optimisation of MOVPE-grown resonant tunnelling diode THz emitters,* Proc. SPIE 10111, Quantum Sensing and Nano Electronics and Photonics XIV, 101113A (January 2017) DOI:10.1117/12.2252377

# List of Abbreviations

RTD — Resonant Tunnelling Diode

QW — Quantum Well

MBE — Molecular Beam Epitaxy

MOVPE — Metal-Organic Vapour Phase Deposition

HR-TEM — High Resolution Transmission Electron Microscopy

HR-XRD — High Resolution X-ray Diffractometry

LT-PL — Low-Temperature Photoluminescence Spectroscopy

BZ — Brillouin Zone

IRE — Intrinsic Resonant Efficiency

$E_1$, $E_2$ — First, second, quasi-bound energy level

NDR, NDC — Negative Differential Resistance, Conductance

DoS — Density of States

QC — Quality Control

CW — continuous wave (as in: “not pulsed”)

# Chapter I : Introduction

This chapter commences with a definition of THz waves, and reviews the technological gap and challenges behind generating and receiving THz in atmospheric conditions.

An up-to-date review of competing technologies is made, briefly mentioning some of their key advantages and position in the market, where applicable.

The motivation behind the need to generate THz radiation is brought in focus, discussing past situations in recent history and how has the access to wireless data influenced them. Based on bandwidth demand trends and the direction of current standards, a warning is produced towards the imminent obsolescence of microwave sources, further stressing the case for a need of THz-based 5G communications.

A specific attention is given to 5G nano- and pico-cell communications, whilst also highlighting the need for wide bandwidth, secure communication links.

Other possible applications of THz rays is discussed, from art preservation to industrial uses to next-generation computing.

The chapter then introduces the main epitaxial growth method used in this work, Metal-organic vapour phase epitaxy (MOVPE), briefly highlighting the technical challenge to create atomically-thin layers for the next-generation of components.

A simplified explanation of the resonant tunnelling diode (RTD) as an oscillator is introduced as a semi-classical analogy to a leaky voltage-dependent capacitor.

# 1.1. Overview of THz generation

## 1.1.1. What is THz radiation?

Terahertz radiation ($10^{12}\ Hz = THz$), sub-millimetre waves, T-rays, tremendously high frequency waves are some of the most common synonyms for the currently under-serviced section [1] of the electromagnetic spectrum broadly lying between 0.1-10 THz. Strictly speaking, the <1 mm designation of the far infrared spectral region limits this region to >300 GHz, though the UN specialised body, *The International Telecommunication Union* (ITU) suggests a band allocation of decimilimetric wavelengths between 100 GHz and 3 THz[2]. These typically exhibit both photonic (typ. low divergence unless scattered) and microwave behaviour (induces surface currents in contact with metals). As an example, the spectral power density of the cosmic microwave background radiation peaks at ~160.23 GHz, corresponding to 0.66 meV, whilst the measured average temperature of the thermal black body spectrum of the measurable universe is a slightly lower 2.725 K [3]. It is therefore increasingly unlikely that photons below this energy level freely propagate in nature.

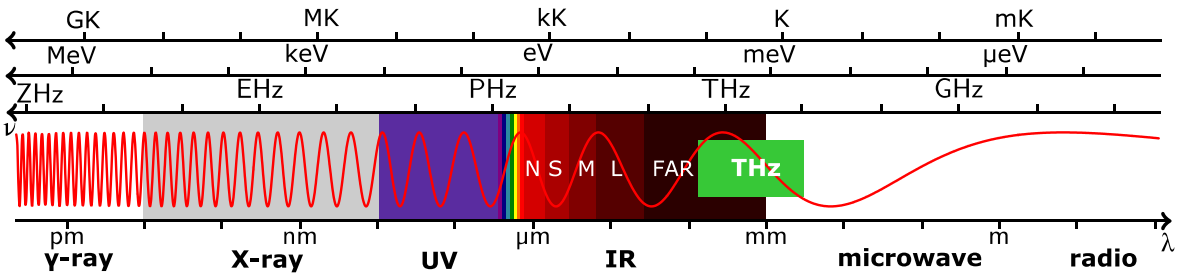


**Fig. 1.1.1. Logarithmic scale electromagnetic spectrum with the position of the THz bands (green rectangle) overlapping the upper microwave and far infrared (IR) regions. N, S, M, L stand for near, short, medium, and long IR, respectively. Relationship with particle energy in electron-Volt (eV) and black-body temperature (K) shown. Lower axis is the wavelength. Modified after *Abel* [4] (CC-SA).**

Fig. 1.1.1 presents a part of the electromagnetic spectrum in this context, focusing in the far-infrared spectral region and the overlapping THz band.

## 1.1.2. "THz gap" and emission challenges

There are multiple overlapping waveguide standards included in the current IEEE 1785.1-2012 [5] in the mm region, with varying letter designations ex: W-band (75-110GHz), 90-140 GHz, G-band (140-220GHz), H(R)-band (220-325 GHz). Sub-

millimetre bands were a recent addition[2], despite remaining unused by the general public.

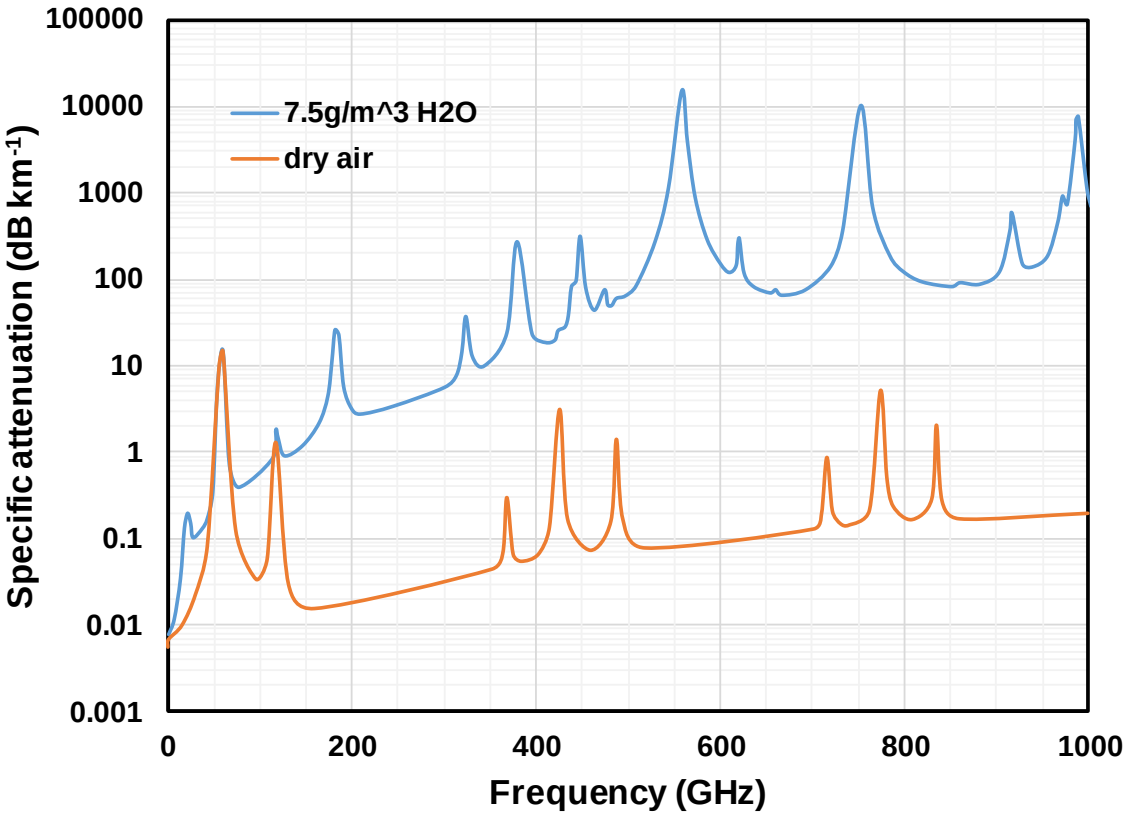


**Fig. 1.1.2a. Semilog plot of specific absorption model of atmospheric air at 288 K, sea level, generated after** [6]**. Top plot is the standard model data for air with water vapour of a** $7.5gm^{-3}$**, and lower plot is for desiccated air.**

Based on time-domain THz spectroscopy measurements[7,8], the ITU recommends a model for standard atmospheric absorption at $15°C$, sea level, and a water vapour density of $7.5gm^{-3}$ (44% relative humidity), plotted as the more absorptive line in Fig. 1.1.2a. To distinguish hydroxyl absorption peaks from other atmospheric gases such as oxygen, the 2nd plot provides a measurement of desiccated air absorption, noting an overall reduction of ~30dB in magnitude and the number of absorption peaks. Appleby and Wallace [7] also performed a measurement of humid conditions (15g$m^{-3}$, 90% relative humidity), and observed an additional average 10dB increase in absorption. As expected, micron-scale particulate matter, *i.e.* "dust", does not significantly impact the measurements.

Several windows, in GHz, are suitable for transmission: 75-110 (some bands reserved), 125-180, 200-310, 330- 415, 435-460, with increasing difficulty at band centres in 680, 800, 850, 930, 1030, 1360, 1490, 1980 GHz [8]. Several

naturally-occurring gases have absorption lines in the THz region, notably carbon monoxide [9] and ammonia[10], as well as other combustion gases[11].

In terms of their optical properties, both monocrystalline GaAs and Ge, have a relatively unchanging refractive index measured from 0.1 - 2 THz, of 3.592 $\pm$0.4%, and 3.996 $\pm$0.5%, respectively [12]. Semi-insulating silicon is even more stable, at 3.148 $\pm$0.23%. For the effect of dopant, and therefore, free carrier absorption, see Chapter V.

These properties facilitate the creation of a semiconductor-based THz emitter suited for short distance, point-to-point wireless communications that will not suffer from scattering due to particulate matter present in certain environments. This could complement and perhaps reduce the reliance on fibre optic patch cables in a server room or data centre, reduce the potential for human error, thus offering the potential for a 2-digit percentage of the fibre data rate with a fraction of the overall cost to the user.

Currently, there is a wide array of THz generation equipment available for laboratories and scientific research. Unfortunately, there is a technological challenge to realise effective sources in the 0.3 – 3THz span, referred to as the "*THz gap*", created by the relative lack of cost-effective, mass-manufacturable, efficient and compact emitters of THz. Fig. 1.1.2b non-exhaustively investigates avenues for generating THz radiation. Situated at the confluence of electronic and photonic technologies, one might expect that either would be able to service for this purpose.

The reality however, is that both sides have potential disadvantages: until recent design paradigms were introduced [13], traditional electrical waveguides were very lossy at 100GHz+ due to a requirement of surface perfection only achievable with sophisticated micro- & nano-fabrication, and temperature sensitivity. Photonic-based technologies are problematic in that carrier energy transitions in the meV levels are difficult to engineer, or require cryogenic cooling, and are sensitive to absorption from doping layers, to mention the most important challenges.

Fig. 1.12b plots this convergence of technologies estimated on the basis of the latest research, showing the dependency of radiated THz output power vs frequency, for the area of interest.

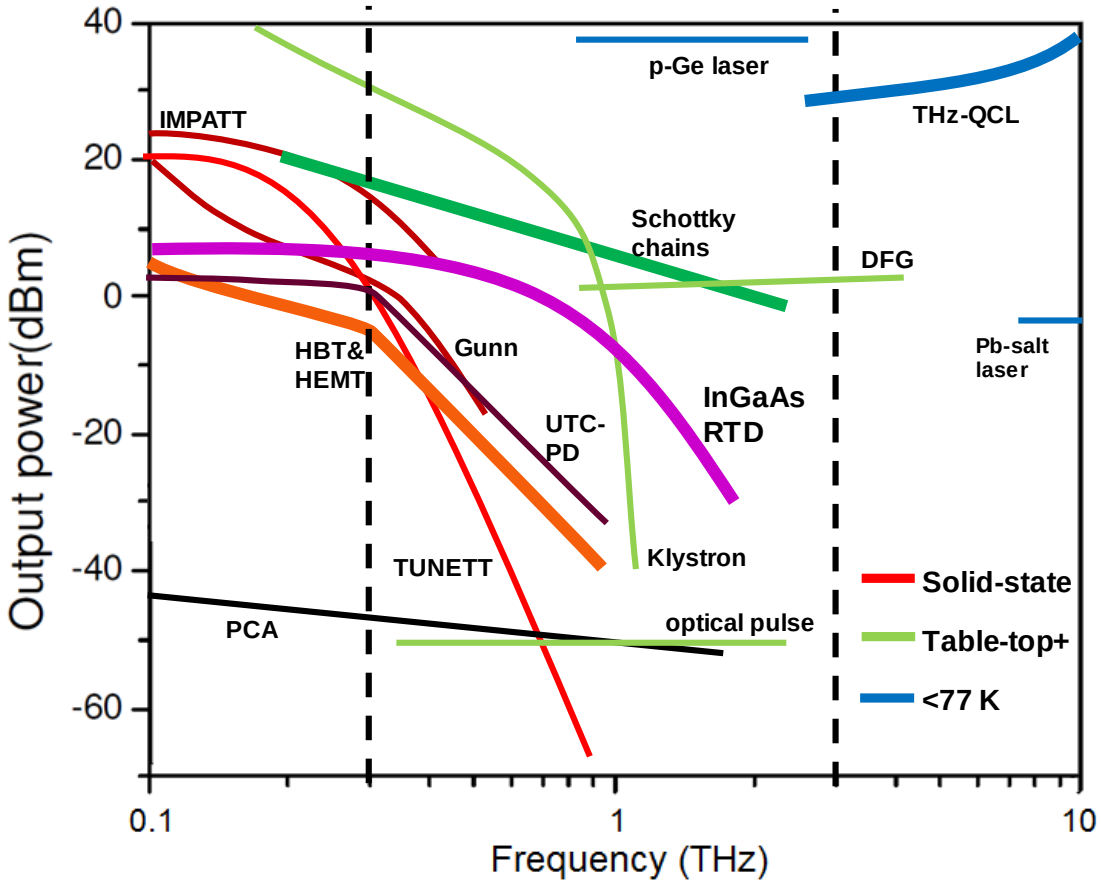


**Fig. 1.1.2b. The state of THz tech, updated after Tonouchi, Wang.** [14,15]**, plotting THz radiation power vs. frequency. The purple line is for InGaAs RTDs in this thesis. Thicker lines represent technologies that are already important for commercial & scientific endeavours. Red lines are solid-state technologies, blue lines represent those needing cryogenic cooling for maximum benefit, and green lines represent table-top and larger technologies.**

At first sight, the graphic reveals a partial overlap of several technologies. However, no current commercial state-of-the-art candidate could serve as an arbitrarily high power emitter in a small package, which is also efficient and tunable across the entire spectrum. The following paragraphs will catalogue candidates for THz sources in this domain.

*IMPATT* diodes have been demonstrated to 285GHz [16] with a DC to RF conversion efficiency ~3%. Though it is an active research area and a mature technology [17], no significant attempts to increase the maximum frequency beyond this are made. IMPATT diodes appear to be one of the technology of

choice for security scanners, therefore minimising their footprint has never been a goal.

InP *Gunn diodes* were shown to operate above 300GHz [18], based on harmonics power extraction. This is not an efficient way to generate THz, and considering that RTDs share the same doping scheme, it is not unreasonable to expect RTDs to outperform them. Single barrier tunnelling diodes such as *TUNNETT* devices, have the unfortunate problem of increasing capacitive reactance with frequency[19][20], whereas this does not appear to be the case with RTDs [21].

***HBT & HEMT & MESFETs*** certainly have the convenience factor of being able to further control the conductivity of the device with an additional electric field applied at the gate[22], but have high phase noise levels[23,24]. Used in conjunction with *monolithic microwave integrated circuits* which scale with increasing costs up to the lower THz regions, they can make interesting HF circuits; the problem is that THz MMIC require highly precise & mechanically difficult microfabrication, which greatly limits the manufacturability. A notable absence from this graph is the inclusion of the emerging plasmonic technology. Several solid-state THz emitters could, generally, directly benefit from the addition of plasmonic waveguides[25].

*Unitravelling p-i-n carrier photodiodes* are a reliable way to generate and receive THz radiation [26–31], however, it appears that they also have significant frequency response limitations. The advantage is that they are relatively cheap to manufacture, but the low raw output power (<100$\mu W$ typ. at 300GHz), and high beam divergence requiring the use of a Si collimation lens are considerable disadvantages currently.

*THz QCLs* have made impressive progress being recently demonstrated at up to 1W @3THz [32], but room temperature operation in this wavelength is perhaps not something that can be envisioned currently. There is a risk that the quantum wells become back-populated due to several thermally-assisted scattering processes[33]. The narrow linewidth paired with high power outputs make these an excellent candidate for imaging.

*Difference frequency generation* is another photonic technique that can generate arbitrary THz frequencies. In references [34][35] one such example is given by mixing 2 mid-IR QCLs to output $7\mu W$ at 80K, though such setups are difficult to configure. Whilst challenging for epitaxial crystal growth processes, better characteristics have been shown with an external cavity Fabry-Pérot photomixer, with 5-8mW across the THz gap[36].

*Lead-salt (Pb-chalcogenide)* based lasers also come from the mid-IR into the upper THz range due to their low band gaps, but it is consistently difficult to reach the lower THz region due to the lack of good reflector materials in this range[37]. Pulsed operation is possible at room temperature, though maximum continuous wave (CW) power is attained with liquid nitrogen cooling or better.

*Heavily doped p-Ge lasers* were amongst the first methods to generate far-IR, and whilst the power output figures are impressive, reaching that of >1W with the potential for tunability within a wide range[38], they require high-performance He-cooling due to the fragile meV state transitions involved.

*Schottky chain multipliers* have been famously implemented in ESA's Herschel Heterodyne Instrument for the far-IR (space observatory) [39]. They employed a RF master oscillator source, and to ensure low broadening and frequency drift, a He-cooled Gunn diode in this particular distance. The complexity of the switching and superconductive waveguide relied on immersion in nitrogen tanks to operate. Fortunately, table-top Schottky chain multipliers are available as off-the shelf extender units for vector network analysers from reputable manufacturers, with various waveguide options, but require considerable active cooling and waveguides of suitable ceramic waveguides which can conduct and dissipate heat effectively, therefore this technology is highly unlikely to be featured in mass-produced consumer goods.

*Photoconductive antennas*[40], other photonic-based[41] THz generation techniques are reliable, but produce a weak THz pulse (typically $< 1\mu W$), which is a problem as several common THz detector types reach the noise floor at this level. Transmissive antennas that employ quantum beat oscillations from pumped lasers may be a direct alternative [42], though currently, fabrication presents several challenges.

*Klystrons* are some of the most high-powered vacuum tubes created, which have seen use from previous' century VHF amplifiers and beyond. They scale up easily and are the generator of choice for microwave& mm-wave where powers in excess of 1kW are required, particularly in military applications[43]. These devices will resonate into the THz range through harmonics, albeit with the worst wall plug efficiency so far in this list. For RF powers in the kW range, research in backward-wave oscillating *gyrotrons* is undergoing at the time of writing[44].

*Free electron lasers* (FEL) are a last-resort alternative, as this is scientific apparatus requires a dedicated building section to itself and should be resigned for specialist investigations. The FEL can generate wavelengths across the entire spectrum, from THz to hard X-rays, and typically include the previously mentioned klystron as a source for a linear electron accelerator, ultimately requiring shielding, vacuum, possibly cryogenic lines (to reduce noise), and a cohort of personnel to maintain.

## 1.1.3. Communications applications

### 1.1.3.1. Humanitarian by-product

Most of my PhD programme was notably marked not by any minor personal and technical accomplishment, but by grim war and tragedy covering the world, in many cases, too close to home and friends for comfort. The "Arab Spring" revolution series of 2010-2012 sent ripples throughout the world which, for the foreseeable future appear unquenchable. According to the UN Human Rights Council, 2015 marked a record year where the number of new refugees and internally displaced persons exceeded, for the first time, the 15 million estimation attributed to the entirety of the 2$^{nd}$ World War[45]. A significant fraction of the people involved fled the multi-sided Syrian war, being absorbed by neighbouring countries, yet ~1 million are estimated to have entered Europe[46]. This sparked one of the most severe political crises in the European Union since the formation of its post-war predecessor entities.

However, the most striking aspect of this crisis, was not the political handling, the impressive lack of faith manifested through the cynical rise of the

“alternative-right” populism, or a cruel indifference to the plight of refugees, but how technology, shaped the flux of migration and tragedy surrounding the exceptional circumstances of individuals’ lives. Refugees have been often-documented[47–50] to use 3.5G+ enabled smartphones to communicate between their travelling groups, with their displaced families, and reduce their reliance on human traffickers. In one report[50], a refugee relayed the GPS coordinates to the nearby maritime authorities when the dinghy the group was travelling in stalled and started sinking. On land, cell phone operators and charities distributed battery banks and charge points[47,48]. E-payments[51] and e-learning have reduced the absolute reliance on perishable physical objects, offering alternatives to those affected[52], whilst an “artificial intelligence” in the form of a web & SMS-based interactive chatbot was reported to have helped asylum seekers with their claims[53]. One may only speculate on the benefits of increasing the reliability of high data rate coverage, or potential of the future 5G networks to deliver information quickly to both rescuer and the ever-increasing number of subscribers in large-scale disaster stricken areas.

#### 1.1.3.2. Digital merchants

Beyond the humanitarian response, e-payments, in the form of Near-Field Communications (“Contactless”) are becoming increasingly common, but so is fraud [54]. Despite this, digital wallets may well be more secure than traditional “physical wallet” payments, due to the extra tracking involved, encryption-by-design, and ease of blocking access to stolen smartphones and digital tokens [55,56]. However, the disadvantages of NFC and other similar RFID methods is their reliance on omnidirectional radio waves. Tokens and sensitive biometric data from passports can be read from a distance with the appropriate tools. By contrast, THz waves, with their highly directional beams and large bandwidth, carry the possibility of short data pulses limited in range by atmospheric absorption, which would greatly limit the window of opportunity for data packet sniffing.

#### 1.1.3.3. Data rate and 5G prospect

The ability of THz carrier waves to carry Gbit/s data channels before complex modulation schemes are considered is potentially useful in offering a particulate

matter-insensitive alternative to fibre optic communications in data centres, for board-to-board communications. Additionally, 4G microwave carriers may soon be inadequate to carry over the annual 50% increase in data transmission requirements, known as Nielsen's law in the industry [57]. Fig. 1.1.3.3 plots an estimation of the ever-increasing global bandwidth requirements for mobile devices, in part popularised by on-demand entertainment and high-resolution video streams.

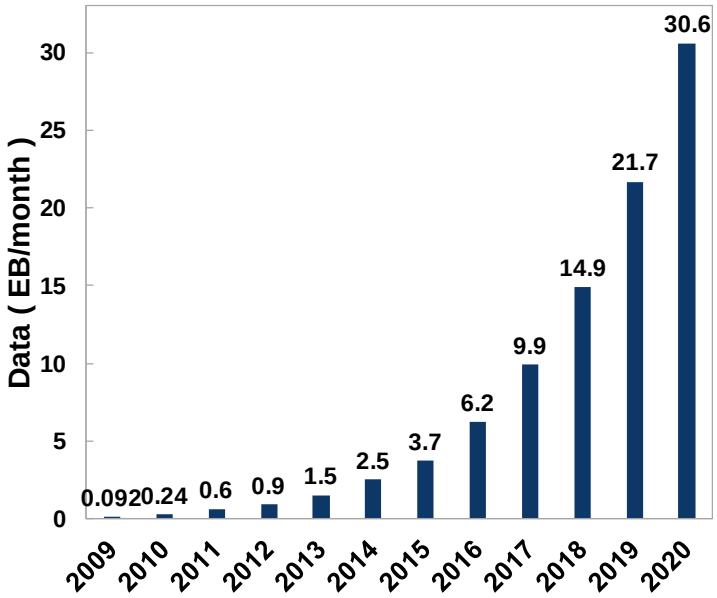


**Fig. 1.1.3.3. Cisco Visual Networking Index compilation of forecast global mobile data traffic from 2009-2020, in exabyte ($10^{18}$ B)/month, with an average compound annual growth rate of 47%, after** [57].

Worryingly, Edholm's law of bandwidth states that a convergence between wireless, nomadic, and wired networks data rates [58] is inevitable, extrapolated to the year 2030. The low efficiency of data transmission through copper has curbed growth. Unfortunately, fibre optics are not a direct replacement for backhaul applications (*i.e. the intermediate portion of a network between the regional exchange and the subscriber node sub-network*) from a business perspective. For instance, replacing a land-based fibre section due to *erroneous* copper theft (*i.e.* outdoor fibre can be confused with copper cabling) is not straightforward: fusion splicing of a fibre optic section is not desirable in the field. At a sub-network level, a need to manufacture hardware that can handle mm and sub-mm waves is imperative[59] to increase the robustness and future-proof data networks. As an alternative to high data rates, should cost-effective 300GHz+ high Q-factor filters be a possibility [60], a standard specification for a THz 5G nano/picocell could opt to decrease the

channel separation in frequency division multiplexing, such that more subscribers could benefit of simultaneous service vs. traditional UMTS/LTE in crowded areas, *i.e.* entertainment venues, busy transport hubs, or *ad-hoc*, in disaster sites.

#### 1.1.3.4. Live video streaming

Wireless streaming of 4K video is no trivial matter with today's 802.11ac Wi-Fi standard. One-antenna using 256-point quadrature amplitude modulation currently yields a theoretical 867 Mbit/s in perfect reception conditions. Ideally 4 such links are needed to transmit MPEG-2 compressed video in real time. On the other hand, TV professionals use uncompressed [61] 4K video over IP (8-bit, 3840x2160 @ 60 fps) yielding a stream of 7.6 Gbit/s, before any parity data is considered → 12G-SDI(SMPTE ST-2082) standard. ROHM Co., Ltd. and Professor Nagatsuma Group of the Osaka University have consistently shown technological demonstrations of RTDs [62,63], with a 2016 attempt reaching 9 Gbit/s virtually bit-error free using the simple OOK modulation scheme with a bowtie antenna, also quoting receiving capabilities of RTDs in excess of 17Gbit/s. There is much scope for realistic improvement in the immediate future, and this work will discuss important parts of this long journey.

### 1.1.4. Other applications

Though the design of the RTD device in this thesis is geared towards improving characteristics ideally suited for communications, once the core technology behind an emitter-receiver system is unlocked, applications outside communications may be considered.

#### 1.1.4.1. Imaging

There are many categories for imaging, and one of the early successes for THz solid state emitters were in automotive radar. Initially meant as a rangefinder for adaptive cruise control systems, the idea is to develop the application towards an advanced collision-detection driving assist [64,65], which could work in tandem with visible and invisible light camera systems.

Reconstruction of artwork and cultural objects may be made possible by such multispectral imaging without the risk of damage to metal-organic pigments posed by ionising X-ray analysis. Fig. 1.1.4.1. presents an example where the THz wave can penetrate deep behind the layers of varnish, paint, and gypsum substrate to reveal invaluable, hidden information about the state of the painting [66,67]. Though in its infancy, this can be particularly valuable for understanding and reconstructing murals and other traditional objects which use gilding and other 3D techniques in their composition.

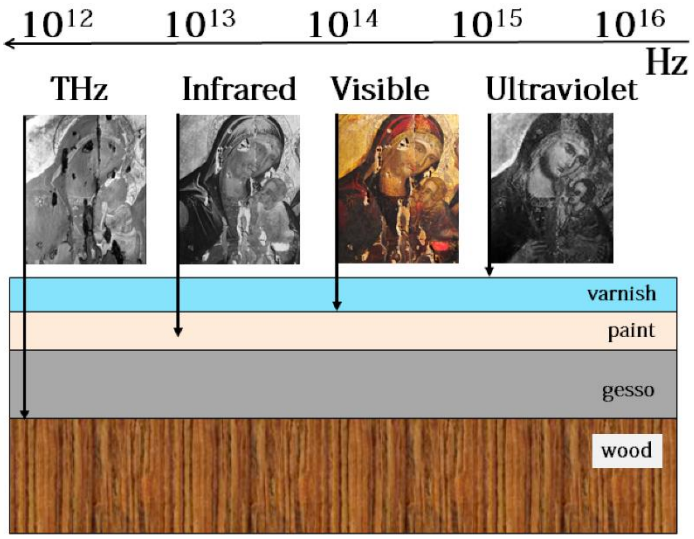


**Fig. 1.1.4.1 Multiple images of a damaged 14th c. Christian iconographic painting from Sicily, illuminated under THz, Mid-IR, visible light and ultraviolet. Reproduced from** [67] **(CC-BY)**

In industrial applications stress-induced microfractures are an important sign of impeding failure of a rigid material[68,69]. A future hand-held THz scanner could complement lower resolution ultrasonic imagers, and would be more convenient than *ex-situ* X-ray equipment to detect such fractures. Airframe components, such as power plant mounting bolts or ceramic wind turbine blade tips [70] are candidates to benefit of such analysis. Dental enamel may also be imaged by THz [71].

### 1.1.4.2. Gas spectroscopy, detection, and identification

THz spectroscopy has been successfully used to detect $CH_3Cl$ vapour at ppm concentrations using a specially engineered White cell with a known path length[72]. These cells are “off-the-shelf” components at the time of writing. The advantage of spectroscopic gas detection is that alarm thresholds could be

configured on-the-fly for specific absorption lines of various gases, increasing the palette of safety tools available for the chemical & semiconductor industry.

Generally, current demonstrations for remote THz gas sensing use complicated photonic mixing techniques resulting in bulky systems with complex parts [73,74], though several aspects of such systems could be integrated with the right business case. Whilst such THz detection instruments have been used with success by the European Space Agency Herschel THz space telescope [39,75], atmospheric absorption of THz emission peaks complicate the matter on Earth. NTT have demonstrated the possibility of remote detection of $N_2O$ [73], one of the poisonous gases generated by combustion. A demonstration of THz-spectroscopy enabled *in-situ* scanning of combustion gas was shown by Uno and Tabata[11].

#### 1.1.4.3. Organic compound identification & Security

Like gases, organic compounds present several distinct absorption lines in the THz range [76,77]. To this effect, a frequency-tuneable RTD has been demonstrated in an early spectroscopic experiment [78], though it remains to be seen whether it will be a technological winner in this area.

THz & mm-wave body scanners are not a new concept and are already featured in airports security gates [79–82]. Foreign objects attached to the body such as firearms, knives or fluids can be identified without the need to individually pat-down every passenger. Figures concerning the detection reliability of these scanners are not available.

A perhaps unexpected application of RTDs with large-scale imperfections induced by the currently poor statistical process control methods surrounding their manufacturing is to employ the physical disorder unique to each RTD as a physically unclonable hardware seed or key as a part of an encryption system [83].

#### 1.1.4.4. Memory and A/D Converters

The quality of a digital signal is limited no only by the responsivity (A/W) of the detector, but also by its impulse response characteristic, limited by its cut-off

frequency. Per Nyquist theorem, the usable bandwidth is half that of the sampling rate of the signal. But to continuously sample a signal with maximum amplitude fidelity to detect low picosecond events is one of the key ingredients at the input impedance of the next-gen analogue to digital converters, where the simplicity of RTDs make them a viable candidate [19,84–86].

The direct band gap of III-V semiconductors and possibility of operating at higher frequencies vs. silicon has always fascinated the industry, though the slow adoption (hence lower profitability) of III-Vs relegated them special applications, as miniaturisation and silicon technologies progressed in a quick pace. Whilst billion-transistor CPUs are unlikely to have master clock trees running at mm-waves , application-specific chips and microcontrollers could benefit of a mixed-mode THz input section, which would entail a cache able to store any waveform or data captured. To this extent, RTD-based memory advantaged by the inherent bistability characteristic of the device has been proposed throughout the decades [87–89].

## 1.2. Gaps in knowledge

Much fundamental work remains to be done to investigate the behaviour of matter exposed to THz radiation. Consequently, there is no advanced THz propagation model that would be suitable for either typical indoor or outdoor environments.

There are many potential applications for THz radiation, and at the time of writing, there are no emitters compatible with the form factor requirements of contemporary wearable electronics. Larger scale, table-top, high quality, tunable THz systems do exist, but often come with inaccessible price tags due to the expensive materials used in manufacturing and large proportion of non-recurring engineering costs. It is highly likely that RTDs will eventually find a position in one of these applications, therefore continuous research & development behind the device is required.

A concentrated engineering effort will be required to bring THz transceivers from the research labs and into the hands of consumers. On the other hand, small-scale alternatives do exist and founding research can be unlocked now using THz time-domain spectroscopy, uni-travelling carrier diodes, or Schottky multiplier chains. When this work started, no device simulation studies existed taken in the context of the THz oscillation. Chapters II and III assess the quantum transport models and present a figure of merit for the optimisation of the RTD as an oscillator-emitter.

To date, reliable manufacturing of RTDs with a low statistical deviation has not been reported in a commercial environment. The next chapters will highlight steps taken to improve the epitaxial growth of these devices, by discussing refinements brought to *ex-situ* wafer-level non-destructive optical characterisation schemes, and corroborating with advanced modelling of the device to predict its performance.

## 1.3. Epitaxial Growth

Metal-organic vapour phase deposition (MOVPE, OMVPE), also commonly referred to as metal-organic chemical vapour deposition (MOCVD) is a technique of growing single-crystal phases onto a substrate. One of the first reports of monocrystalline GaAs growth was made at North American Rockwell Corp. [90], though throughout the years, MOVPE became one of the most commercially successful growth technologies in use for compound semiconductors.

MOVPE employs inorganic atoms linked to organic radicals. The underlying physical chemistry is relatively simple: the metal-organic molecule strikes a heated surface (the substrate in this case), upon which the weak bond binding the metallic atom is cracked, and the nominally heavier metalloid is deposited on the surface with unsatisfied bonds, whereas the gaseous radical quickly binds with intentionally injected hydrogen, being released from the reaction chamber through an exhaust.  The activation energy upon which the cracking occurs is dependent on the strength of the bond, and thus fine temperature control is required for the process[91].

However, the details behind the realisation of this process matters. Contemporary reactor designs employ a top-flow “shower-head” towards the reactor chamber, and the gases are further distributed through a sieve-like distributor. Wafers typically sit in crevices rotating in two different directions to ensure uniformity. This system is affectionately called “planet and satellite”.

Typical precursor gases include trimethylgallium (TMGa), triethylgallium (TEGa), trimethylaluminium (TMAl), all in *liquidus* phase, whereas the commonly used trimethylindium (TMIn) is in *solidus* phase. Each of these precursors are boiled (or sublimated) inside bubblers, each generating a pressure. The amphoteric silicon acts as a n-type dopant in III-V systems between certain carrier concentration limits, therefore favouring the use of silane or disilane (the latter showing lesser thermal dependence [92]). To ensure adequate flow to the reaction chamber, a series of programmable valves are turned on and off by a closed loop system. One of the main limitations of MOVPE in the context of epitaxial growth of layers only a few atoms thick is the transient switching time [93]of these valves leading towards the manifold. In practice, the resulting pressure transients need minimising, though unfortunately the stopping of the growth process is not always an option, particularly with regards to the deposition of highly reactive atom species such as [Al].

Another disadvantage seen in MOVPE systems is the traditional lack of *in situ* characterisation of the layers grown, though advanced flow monitoring systems [94], as well as pyrometry and multiple wavelength reflectometry systems [95] can compensate this to some extent.

This is not a problem with the competing molecular beam epitaxy (MBE), a physical reactor type favoured by academic institutions. MBE uses a completely different approach; the elements of semiconductor-grade purity (vs. MO-cylinders) are heated in special crucibles (typically using a Ta or W filament) and accelerated toward the rotating substrate using the beams from special “effusion cells”. To monitor the state of the surface growth, a system called *Reflection High-Energy Electron Diffraction* (RHEED) is used. A soft X-ray beam is shot towards the substrate, generating a diffraction pattern, information which can then be shown in an amplitude-time oscillogram, where the growth of individual atomic layers can be monitored [96]. Typical growth rates from MBE

are an order of magnitude slower than MOVPE, but there is a complication: the crystal quality is dependent on the level of the vacuum, a known application where ultra-high vacuum levels are involved, and the cleanliness of the chamber. This results in low yields due to the difficulty of scaling up the chamber and prolonged downtime periods. To work around the lower availability of the system, several MBE reactors would need to run simultaneously.

On the other hand, large-scale MOVPE reactors are commonly employed by electronic & opto-electronic manufacturers, making it a uniquely profitable tool where advanced epitaxy is a requirement, despite the necessity for environmentally-aware chemical treatment & disposal of the growth chamber exhaust.

The problem lies with verifying the accuracy of the growth method to a specified structure. Chapter IV investigates this issue with an advanced non-destructive characterisation scheme. As it will turn out, the analysis can be very challenging in terms of hardware requirements (measurements close to the noise floor), interpreting, and de-convoluting the data.

## 1.4. Simplified operation of the RTD

Resonant tunnelling diodes draw from a family of 2-terminal devices with superficially similar features and characteristics. RTDs share the n+ - (i)intrinsic - n+ doping scheme of the Gunn diodes, with the layers near the contact region being heavily doped (to degeneracy) in order to facilitate high-conductance electrical contacts. With tunnelling diodes, they share the thin epitaxial layers necessary for quantum tunnelling of carriers to be possible, however, the nature of tunnelling is different. All 3 devices have another characteristic in common: the current rises and falls with increasing bias, creating a letter N-shape I-V characteristic, but the method of how this is produced is different in all cases.

Conventional tunnel diodes employ a single barrier and a p-i-n doping scheme, and the method of tunnelling is *inter-band* when voltage is applied: carriers transit the ground state(valence energy band edge) towards an excited state

(conduction energy band) [97]. One of the best brief introductions I have encountered on tunnel diodes was written by Ian Poole [98].

RTDs do not employ p-doping, and use 2 or more potential barriers, trapping carriers (and therefore charge) between them. It is not arbitrary that this effect was called "quantum capacitance" [99]. Therefore, upon the application of an electrical potential, carriers resist the escape from this potential-barrier cavity, until the stored charge reaches a critical value and penetrates the barrier. A more in-depth treatment of this effect is covered from a particle-wave point of view in Chapter II.

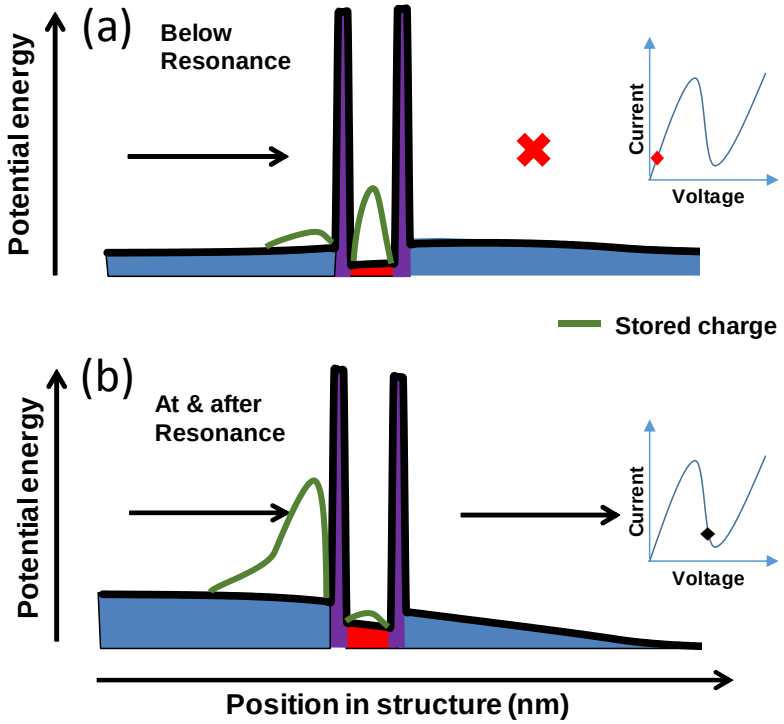


**Fig. 1.4. Semi-classical mechanics analogy to the operation of an RTD below the resonant condition (a) and after the resonant condition (b). The different potential levels are caused by different epitaxial layers. Insets show a schematic current-voltage characteristic. The amount of charge stored at a given point of the RTD structure is marked with a green line.**

Fig. 1.4 shows a simplified visual explanation of the RTD functionality: the ideal resonance condition is achieved when the charge stored towards the entry region and between the barriers is equalised, but the current continues to flow even after the stored charge is depleted. The name "*resonant*" comes from the wave-like behaviour of the carriers, in an analogy with a musical flute or pipe of an organ to produce a "standing wave". These imply a dominating phase-coherence, though the semi-classical picture, in which incoherent, successive,

“bounces” off the potential walls inside the cavity causing energy loss, do exist and are one of the mechanisms of efficiency drop.

The THz oscillation can be captured after the carriers transit the resonant barrier structure into the drift region, towards the lowest state reservoir available in the system before the electrical contact. Unlike other semiconductor structural effects, the hole current does not contribute to this resonant process.

This description will receive a more detailed treatment in Chapters II & III.

# Chapter II : Modelling background of RTDs

This chapter covers several theoretical aspects underlying the concepts that make RTDs work, and propose a methodology for the design of these mesoscopic devices.

Before one can discuss the origin of the *negative differential resistance* (curious as electrical resistance itself has no definition to allow it to become negative), it is important to think about bulk resistivity, and the structure of solid state matter that allow this property to change in the presence of excitation. The models that simplify the quantitative and qualitative understanding of atomic arrangements are discussed. This builds up a discussion of different crystalline material pairs, and the artificial exploitation of their unique properties to engineer selective traps for charge carriers, resulting in counter-intuitive charge carrier transport.

The discussion then proceeds to show how this understanding of quantum confinement can be flawed in situations where the particle-waves interact with each other, and a more advanced model is required to describe carrier transport. A high-level description of the operation of software is included.

The discussion continues with extending the mesoscopic system with a lumped electrical circuit and show how to extend quasi-DC predictions into the frequency domain.

The chapter ends with a consideration of the limits of accumulated stress in these material pairs.

# 2.1 Band Structure

This section introduces elements of solid state physics that form the basis of semiconductor devices.

## 2.1.1. Conductivity

The conductivity of materials is one of the fundamental physical properties taught in early school years, shortly after the introduction to the states of matter. This often happens through the incomplete division of matter into "insulators and conductors". This idea, though didactic, readily neglects materials which have non-ohmic conductivity changes with temperature, strain, or magnetic fields, which is why the word 'semiconductor' often elicits blank stares from non-specialist audiences.

One classical way to express conductivity is:

$$\sigma = \frac{\vec{J}}{\vec{E}} = n\mu_e q \qquad (1)$$

where:

- $\sigma$ is the conductivity $(kg^{-1}m^{-3}s^3A^2)$
- $\vec{J}$ is the electric current density vector $(A \cdot m^{-2})$
- $\vec{E}$ is the electric field vector $(kg \cdot m \cdot s^{-3}A^{-1})$
- n is the number of carriers
- $\mu_e$ is the carrier (electron) velocity $(kg^{-1} \cdot s^2 \cdot A)$
- q is the carrier (electron) elementary charge $(1.602 \cdot 10^{-19}A \cdot s)$

It is known that different materials show different conductivity/resistivity values from temperature-dependent V-I measurements, therefore this deceptively simple model has several corollaries:

1. In a metal, increasing the temperature of the system lowers the conductivity. As n and q are constant if J is constant, this means that $\mu_e$ is reduced. The explanation was found that the ordered atomic lattice vibrates (quantised by *phonons*), which statistically disrupts the path of charge carriers. To employ a classical analogy, additional "collision" centres are created.

2. The simple model cannot explain materials whose electric conductivity has been observed to increase with decreasing temperature.

The materials which do not have a monotonic *decrease of conductivity with temperature* are called *semiconductors*. Though it is incidental that most conductors have a higher conductivity than semiconductors at room temperature, this is not a *sine qua non* condition.[100]

To account for the chief cause of non-linear conduction with temperature, an additional term is included in equation (1) for semiconductors, $\mu_h$ mobility of the *hole*. The hole is a quasi-particle introduced to describe the opposing drift current to the wake of injected electrons. A favourite analogy amongst science educators and students alike is the water bottle and air bubble model: The air bubble can be clearly seen quickly rising to the top if the bottle is tilted, whilst the water has a turbulent, stochastic flow downwards which reduces its apparent velocity. Both hole and electron paths are stochastic; however, the *group velocity* of electrons is generally expected to be higher as they are travelling from a higher towards a lower energy potential, whereas holes quantify the displacement in states of the directed, averaged, electron movement.

A notable exception is represented by a certain group of solid state materials, *superconductors,* which show infinite conductivity (no opposition to current flow) below a critical temperature. Though forming the basis of important technological applications [101], such materials are beyond the scope of this thesis.

### 2.1.2 Electronic structure

The underlying idea for the existence of the band gap/forbidden band energy appears in inorganic crystalline materials as a natural consequence of the highly regular, periodic, atomic *crystal lattice*.

As a general rule, elements from group 13 (III) to group 16 (VI) of the periodic table are optimally placed as candidates to form semiconductor compounds: Their unfilled valence orbital creates an electron cloud, or shell, with state vacancies. Furthermore, when several atoms come together in a highly regular crystalline *allotrope*, the orbital states merge, forming a continuum of energy bands (method also known as *linear combination of atomic orbitals*). However, these vacancies are also shared, realising a practically unfilled energy potential trapped between two partially unfilled bands.

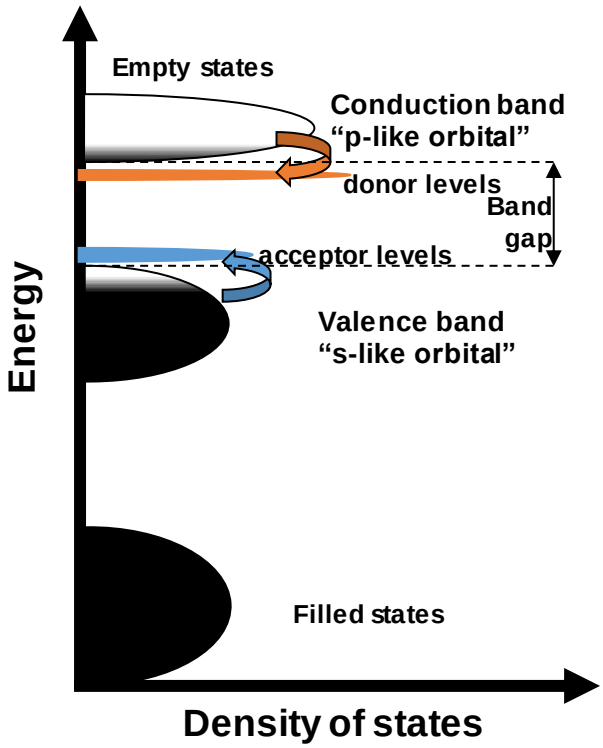


**Fig 2.1.2. Schematic diagram showing the valence, conduction and acceptor (p)/donor (n) impurity bands plotted against density of states in a typical bulk semiconductor. Partly-filled bands reflect the Dirac-Fermi distribution near room temperature. The unfilled energy region between the bands is the band gap. The contribution of impurity levels (whether intentionally engineered or not) is shown as additional states inside the band gap.**

The merging of orbitals is a natural consequence of the hybridisation of the bonds under the influence of the strong and weak nuclear forces. Generally, the width of the forbidden band depends on the overall strength of the inter-atomic separation and the distance between the s and p orbitals present in the material. To exemplify the previous, crystalline *aluminium nitride* (AlN) (either in a cubic or hexagonal allotrope), with relatively small atomic radii and thus less interaction, have a very large band gap of 6.015 eV, whereas indium antimonide (InSb), with much higher atomic numbers, is notorious for being the

III-V compound semiconductor with the lowest gap of 0.17 eV. It is perhaps interesting to note that aluminium is a good conductor whilst nitrogen is normally a biatomic gas, whereas both In and Sb have above average conductivities for this group, where Sb is a metalloid. The properties of the final material are not always intuitive simply by glancing at the periodic table.

Heavier atoms with a d-band are an analogous case, though more complex behaviour may emerge as a result due to the differing orbital symmetry configuration. III-V group metals however will have a completely filled d band, which results in more predictable conductive behaviour. Moving towards even heavier atomic numbers, due to the complexity of f-orbitals, these elements further depart in their optical and electronic behaviour from other d-block metals. Gold for instance has a poorer electrical conductivity and exhibits a characteristic reddish-yellow hue compared to its group neighbour, silver, for this reason.

#### 2.1.2.1 Tight-binding

A parallel development to the Drude-Sommerfeld nearly-free electron model is represented by the *tight-binding approximation,* widely in use today for simulation of electronic and optical devices. The nearly-free electron models do provide a qualitative description of the phenomena, however fail to describe the complicated bonds within an atomic system and relate to the formation of energy bands. The model assumes that the crystal lattice is periodically uniform in all directions, with the valence electrons of the atoms being distributed throughout the structure. The wave functions given by the interactions of ion-covalent bonds are therefore expected to be similar.

In this approximation, seen in Fig 2.1.2., the valence band states assume a behaviour similar to p-orbitals, whereas the conduction band deals with the s orbitals. This is a likely *flawed understanding* based on the behaviour of an *isolated atom* species, though it is used in the context of a highly-ordered lattice as it provides satisfactory results in most scenarios.

### 2.1.2.2. Fermi distribution and Fermi level

When the temperature is at a theoretical 0 K, electrons occupy the lowest energy states available, as possible. As fermions, by definition, up to 2 electrons may occupy a state. The level formed by the highest energy state thus occupied is defined as the *Fermi level*. As the system is excited with higher temperatures, electrons gradually depart from this *reference or sea level,* following the *Fermi distribution.* As the energy gap largely forbids occupation, the promotion of electrons from the valence band to the conduction band is what causes the conductivity of a semiconductor to rise with temperature, up to a critical point where other effects dominate.

### 2.1.2.3. Density of States

Finally, energy bands may contain states in an asymmetric fashion. The *density of states* of a material can be defined as the number of states found between an arbitrary point $E$ and $E + \delta E,\ where\ \delta E \to 0$. It follows that a material with a high density of states would allow more opportunity for carrier transport, therefore is more conductive.

In a tight-binding scheme, the carrier densities and dispersion relationships are often conveniently plotted within the periodic $-\frac{\pi}{a}, \frac{\pi}{a}$ limits, where *a* is the lattice parameter (in the context of a cubic crystal lattice). This plot of energy vs. crystal period can be found under several analogous (though not always physically equivalent) guises in the literature, such as *momentum space, k-space, reciprocal space*, and others.

### 2.1.2.4. Electronic band structure and origin of oscillation

The transformation of the face-centred cubic Wigner-Seitz unit cell in reciprocal (Fourier) space is a truncated octahedron, called the *Brillouin zone* (BZ)[102]. The BZ contains all possible Bragg reflections of a wave vector inside a crystal. In three dimensions, any wave vector that runs from the centre of the BZ, denoted with $\Gamma$ (also the point where all momentum→0), to a plane perpendicular to the bisecting point between the centre and the next reciprocal lattice point, satisfies the Bragg condition[102]. To aid understanding to the

student reader, interactive BZ construction tutorials are available in reference [103].

The edge of a BZ therefore “reflects” the particle-wave back inside. However, different directions impart differing dispersion relationships. Some critical points are represented by the X and L points, the geometrical centres of a square and hexagonal face, respectively. These points are the source of the complicated multi-band structure in a crystal. In some materials, the angle of the lowest edge of the conduction band does not align with the angle of the topmost edge of the valence band; this means that electrons need to change direction before they can transit through that level. A change of direction, in semi-classical mechanics implies a collision (phonon), thus a loss of energy. In this case, the excitation energy passes through a mixture of s-like longitudinal states and p-like transverse states. Such materials have an *indirect band gap,* and are therefore poor candidates for optical and tremendously high frequency electronic emitters. These losses of energy through phonons however, regularly occur in direct band gap materials as well, and are an important consequence for RTD design.

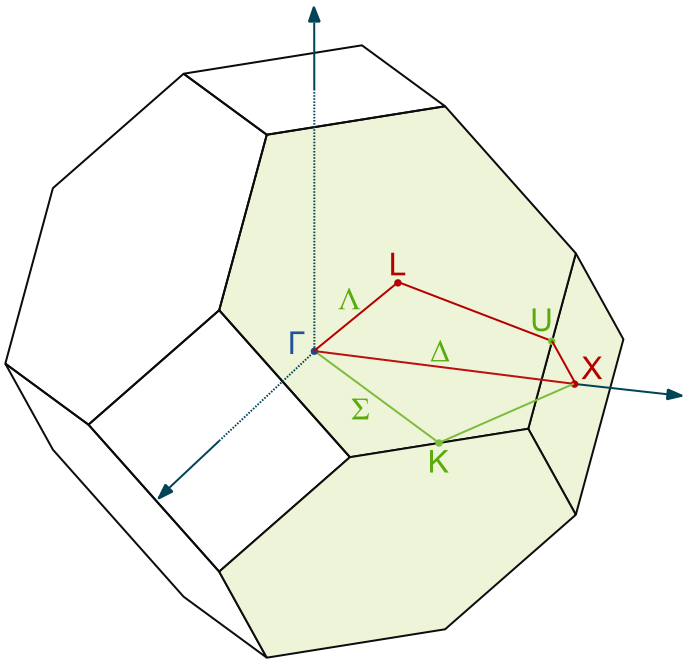


**Fig 2.1.2.4a. First Brillouin zone representation in k-space, after[104]. Γ, L, X points highlighted. Connecting lines show the route depicted on the horizontal axis of Fig. 2.1.2.4b**

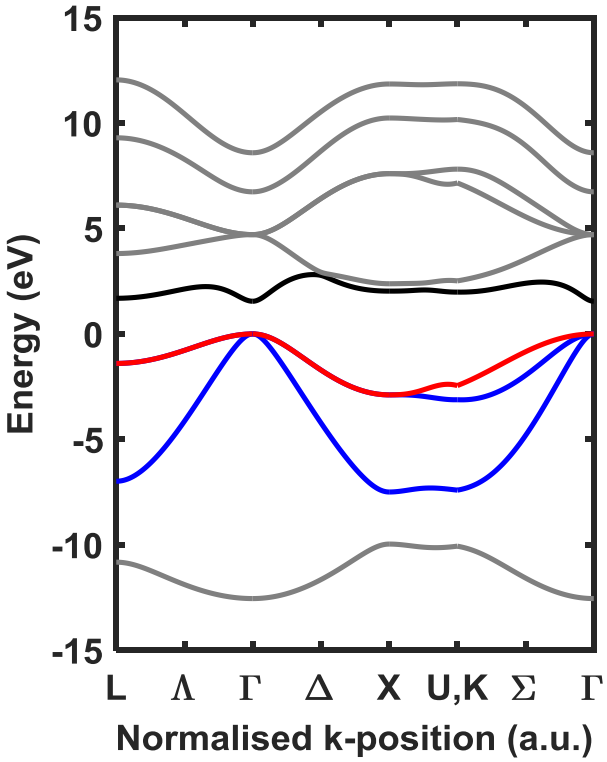


**Fig 2.1.2.4b. Theoretical calculation of a complicated energy band structure in GaAs at 0K, using the 10-band $sp^3s^*$ model after [105]. The 0 energy level is arbitrarily chosen as the valence band edge at the direct band gap point (Γ). X and L are centre points corresponding to a square, and hexagonal face, respectively. $\Lambda, \Delta, \Sigma$ represent the bisection in the distance and correspond to (111), (100), (110) real-space crystal plane groups. U is the bisection of the line dividing the X and L faces. Valence and conduction bands coloured red and black, respectively. The horizontal axis represents a linear interpolation of the movement towards the corresponding *Brillouin zone* point.**

In Figure 2.1.2.4b, a theoretical calculation of GaAs band gap is presented. The universal $sp^3s^*$ model[105] is not the most frequently used tight-binding approach to describe the shape of energy bands at various points of the BZ, but perhaps easier to understand compared to other multi-band simulations due to its practical origin in its description of the covalent bond hybridisation. It is important to note that plotting the full range of motion of the dispersion relationship $E(k)$ inside the BZ, we would need 3 dimensions spatial + amplitude, which may be rendered as colour-intensity, though it would not make for a very intuitive plot. This is one simplified way to present the changing nature of the band gap, depending on the position of the wave vector as traced by the connecting line in Fig. 2.1.2.4a. For the purpose of investigating the dominance of electronic and optical effects, transitions between the zero level and the conduction band points, particularly in the L and X indirect valleys are important. It is important to note that the origin of NDR for GaAs Gunn diodes (with a similar doping scheme to RTDs, but without the 2D confinement) is

understood to be the $\Gamma - X$ indirect transition (also referred to as *transferred electron effect*)[106,107], which is also the source of the high-order electronic oscillation. The U and K points are only shown for comparison purposes with the canon.

In this figure, it is notable that the light and heavy hole bands merge at 0K, and the split-offset band at $\Gamma$ is simply not modelled [108,109]. A more reasonable attempt using this band structure model was updated by Klimeck *et al*. [110], with coefficients obtained from fitting models to known data points using a genetic algorithm. As the authors highlight, it is important to note that even this relatively complicated model cannot take into account all conditions and usage scenarios associated with electronic band structures. The study could not be reproduced at the time of writing, however it is beyond the scope of this work.

In Figure 2.1.4.2c, a schematic of these band gap parameters is shown. Important interband transitions (VB-CB) are noted as the $E_{gap}$, $E_{x,}$ and $E_{L.}$ Inter sub-band transitions (for instance $\Gamma\ to\ X$) may occur with varying frequency in a bulk crystal chiefly depending on excitation pump, temperature, and the level of occupancy. The split-offset band appears as an effect of spin-orbit interaction. The opposing (small) magnetic fields created by the respective orbits of the s-like orbitals in electrons (see §2.1.2) create different possible energy transitions. This can also be seen in the spectra of hydrogen.

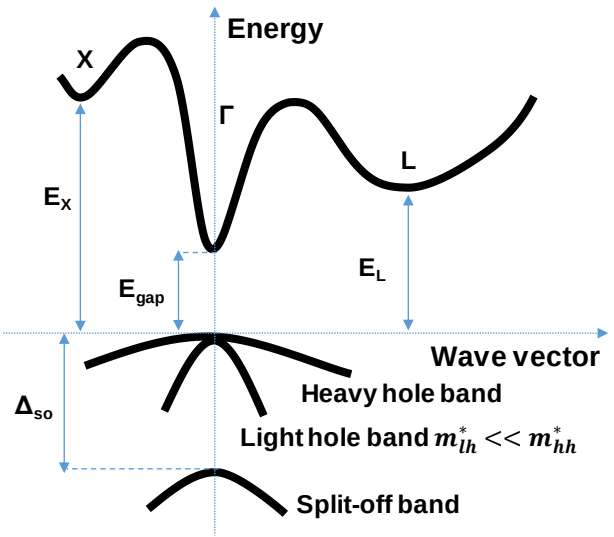


**Fig. 2.1.2.4c Schematic dispersion relation diagram in momentum space, showing key valleys which facilitate energy transitions.**

A fairly comprehensive compendium of $\Gamma, L, X$ energy band values can be found in reference [111], combining [108,112–114] for the AlInGaAs and AlGaN material systems.

### 2.1.2.5. Effective mass approximation

The presence of multiple momentum states as shown in the bands in Fig. 2.1.2.4d can be best approximated by carrier (hole) bands with differing particle masses. This is another effect of the spin-orbit coupling modifying the charge distribution.

The dispersion relationship of an electron can be locally approximated as

$$E(k) = E_0 + \frac{\hbar^2 k^2}{2m^*}$$

This Equation introduces the effective mass $m^* = m_{fraction} * m_0$ where $m_0$ is the rest mass of electron and $m_{fraction}$is an arbitrary fraction, typically between 0 and 1.5 for FCC semiconductors. The $m_{fraction}$ is simply an adimensional modifier added to explain the behavioural changes of the electric field in different materials.

In real materials however, as we have seen in §2.1.2.4, the electronic band structure is asymmetric at different points of the BZ. This confirms the expectation that $m^*$ is dependent on the wave vector position:

$$m^*(k) = \hbar^2 (\frac{\delta^2 E_N(k)}{\delta\, k^2})$$

In Fig. 2.1.2.4b & c, lower m* holes are shown to have an increasing curvature of the band, at the expense of a narrowing of the band, resulting in reduced DoS.

A corollary of the energy-dependence of m* results in a rough proportionality of m* with the band gap, as shown in Fig. 2.1.2.5.

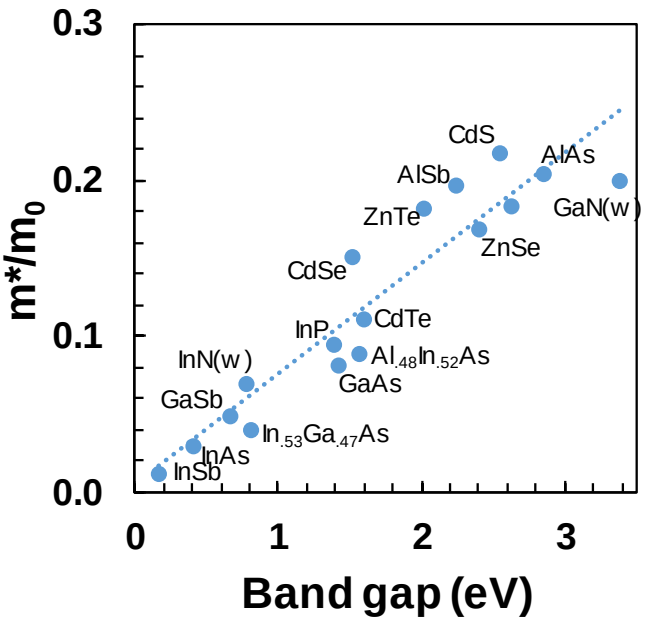


**Fig. 2.1.2.5 Effective mass fraction compared against band gap energy for various III-V and II-VI semiconductors. The InGaAs & AlInAs ternary alloys shown are lattice matched to InP. AlN (wurtzite unit cell) off the scale, with 6.015eV and $m_e$=0.3. Updated after ref.** [115].

## 2.1.3 Heterostructures

The discussion so far has revolved around the properties of single materials. However, often in the case of electronics and high frequency devices, certain optical and electronic transitions are desirable. In other cases, a high level of charge confinement is desired. The umbrella term that covers such cases is *band gap engineering*. Early attempts were made through defect engineering, *i.e.* selective adding of impurity bands to a highly purified crystal (doping, see Fig. 2.1.2.). However, this method has its limitations. The next obvious method was to adjust the lengths of the p and n layers (resulting in Esaki and Zenner diodes), and add supplementary layers (diac, triac, transistor, etc.). Adding different metallic contacts to the semiconductor junction was initially done as a matter of practicality, but it was soon observed that not all metallic combinations form ideal, Ohm-law following (*ohmic*) contacts. The departure from the linearity is attributed to a difference in work functions between the free valence band of the metal and the relative alignment with respect to the conduction band of the semiconductor. Other combinations, such as gold on silicon are known to cause reliability problems due to the tendency of Au atoms to diffuse into the structure and cause trap-defects [116].

### 2.1.3.1. Band gap alignment

However, the problem is not any less complex for semiconductor-semiconductor junctions, even in highly-compatible, well-studied material species.

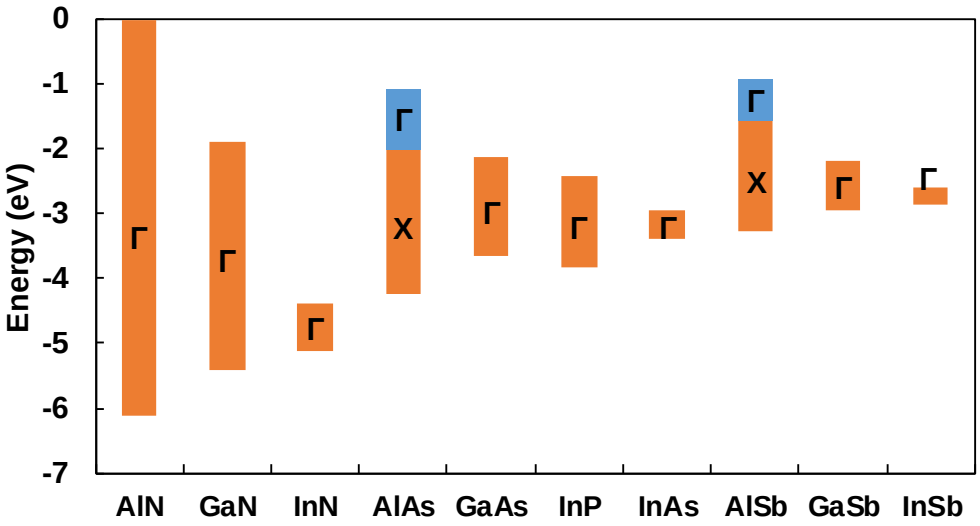


**Fig 2.1.3.1a. Band edge alignment of commonly used binary III-V semiconductors, with the minimum conduction band edge of AlN chosen as an arbitrary reference level. The bar represents the band gap at 0 K. With the exception of AlAs and AlSb, all materials are direct band gap. AlN, GaN, InN in wurtzite form.**

Figure 2.1.3.1a. plots the relative positions of valence and conduction band potentials in several III-V semiconductors of particular interest for RTD epitaxy. Generally, the forbidden zone (whether direct or indirect) can be revealed in the bulk material using both electronic (e.g. electroluminescence spectroscopy) and optical excitation techniques (e.g. photoluminescence spectroscopy), without the use of sophisticated modelling techniques or scientific equipment with limited availability and significant running expenses (e.g. synchrotrons). However, the determination of other possible energetic transitions within the atomic energy potentials (either interband or inter-sub-band) is not guaranteed with any of the above techniques. The uncertainty of the offsets is therefore particularly large for comparatively (viz. GaAs/AlAs) less-studied material pairs such as GaSb on InAs, where the valence band offset error bar is $\pm 20\%$ [108,117].

It is also worth noting that some heterojunctions thus realised, may have a straddling (Type I e.g. AlAs/GaAs), or staggered (Type II e.g. InAs/AlSb) gap alignment, as shown in Fig 2.1.3.1.b. Where the alignments of the gap do not intersect at any point, it is called a broken (Type III) gap, however, these are

more readily achieved in II-VI semiconductors, with a possible exception for $Ga_xAs_{1-x}Sb$ and InAs, when certain conditions of mole fraction and misfit strain are achieved. The contribution of the latter is discussed in the next sections.

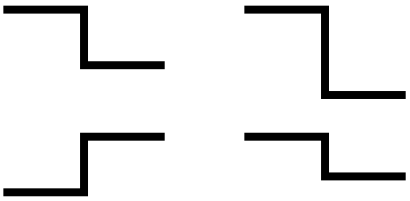


**Fig. 2.1.3.1b Type I and II heterojunctions shown with their respective valence and conduction band potentials.**

It may be worth noting that type II heterojunction resemble biased p-n junction. Depending on the applied electric field, both electrons and holes either need to overcome a barrier potential or drop towards their respective band-edge.

In the case of type I heterojunctions, depending on the direction of the bias, either the electrons, or the holes, will need to overcome a potential barrier, resulting in asymmetric I-V characteristics, assuming identical contacts to both metal types.

### 2.1.3.2. Model-solid theory

In section VI of their paper, Vurgaftman *et al.*[108] suggest that subtracting the bulk valence band positions from 2 materials is a good method to approximate the valence band offset. However, as THz-waves correspond to energies of in the orders of meV, additional precision is required in order to increase the utility of further modelling.

Fig. 2.1.3.2a. re-plots Fig. 2.1.3.1b in a form that highlights the technological difficulty of epitaxially growing different species of crystals. The grey bars of phosphide-containing compounds are occasionally avoided in commercial environments due to the explosion hazard of atomic phosphine exposed to atmospheric oxygen. This is not a problem if the material is chosen as a substrate, where InP is ideally placed between the tensile, high band gap AlAs and compressive, low band gap InAs.

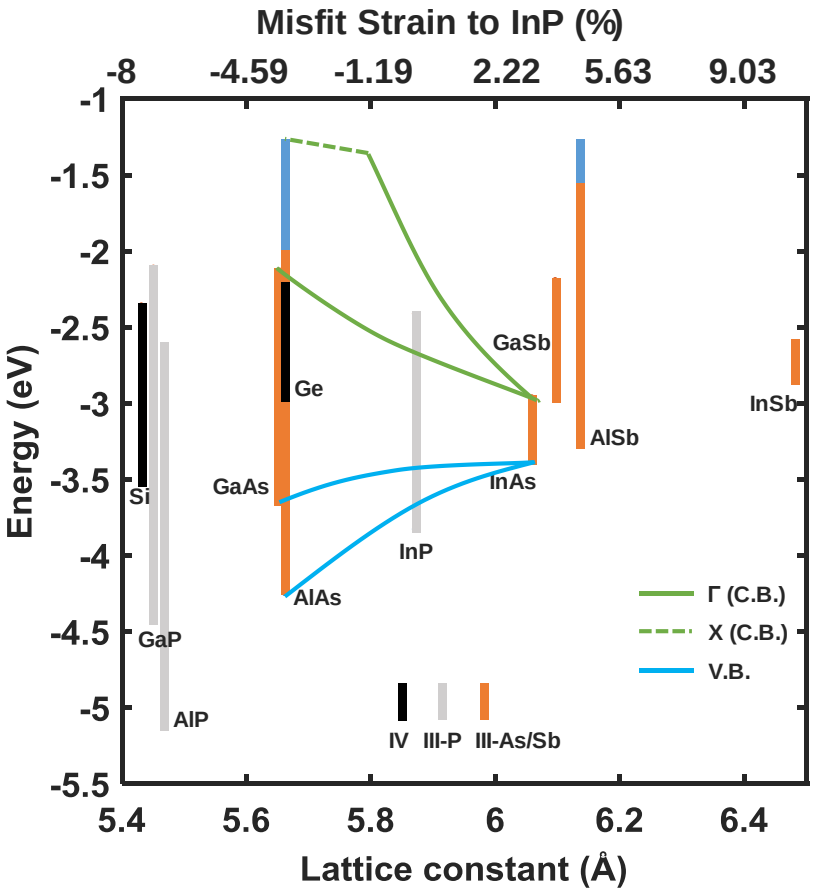


**Fig 2.1.3.2a. Band edge alignments with respect to the conduction band of AlN, as in Fig. 2.1.3.1a. Lower horizontal axis is the cubic lattice constant *a*, and upper axis is the misfit strain with respect to InP substrates. The connectors represent the approximate change in band energies with the variation in lattice constant, corresponding to $In_xGa_{1-x}As$ alloy.**

One problem that arises is that the relative valence band offset in Figs. 2.1.3.2 is only true for *pseudomorphic*ally grown crystals. Accumulated stress inside a semiconductor structure with one or more such heterojunctions lead to deformations of the band gap potential[118]. The Model-solid theory was used to take into account the deformations resulting in changes in that alignment [109]. The paper employs several important assumptions:

- The split-band offset is taken into account by creating an average value of the valence band energies.
- As a consequence, the effect of modelling the deformation of the valence band is de-emphasised.
- The model assumes absolute abruptness of the bulk band-edge at the heterojunction, seldom true due to arbitrary epitaxial growth imperfections. The model can therefore break down if the diffusion of the ionic centres is highly irregular, an effect exacerbated by ternary and quaternary alloyed III-V semiconductors in atomically thin layers.

- As the lateral dimension is assumed to be infinite for the purpose of the calculation, the stress tensor is assumed to develop in the same orientation with the crystal growth direction (thus perpendicular to the crystal plane). In this work, all cubic crystal planes are (001), excluding the $0.1 - 0.7°$ wafer miscut used to facilitate nucleation centres in MOVPE growth techniques.
- The theory still uses the bulk-calculation valence bands offsets used as a starting point, which, as highlighted before, may have a significant uncertainty associated with them.
- The contribution of impurity bands due to atomic oxygen gettering or presence of undesirable dopant species is not included, introducing a*dditional possible uncertainty* due to mis-alignment of the Fermi levels.
- The model employs an average of the light hole, heavy hole, and split-offset bands to simplify the potential calculations in software. To get a better estimation of the band-edge, a $\Delta_{SO}/3$ split offset contribution is added to the average of the valence band edge. This change is illustrated in Fig. 2.1.3.2b.
- The junction is assumed at thermal equilibrium.

Additional clarifications and notations before the calculation method is shown, are noted below:

- In this work, the atomic distance of the substrate used is chosen as the 'unstrained' point, in this case, the cubic lattice constant $a$ of InP at 0.5869 nm.
- The material with the smaller band gap will be named material "1" and the material with the larger band gap is material "3".
- Material "2" is used in the case of ternary alloys, henceforth, all parameters required for material 1 are also required for material 2. If there is no known non-linearity between parameter changes in the material pair, for instance GaAs and AlAs to form $Al_xGa_{1-x}As$ for a given x mole fraction, a linear interpolation is assumed (Vegard law).
- The following parameters are needed for materials 1 & 2: lattice constant $a$, split offset energy difference $\Delta_{SO}$, tensor vectors $c_{11}$ and $c_{12}$, valence band hydrostatic deformation potential $a_v$, the average of valence band energies $E_v, av$, any band gap bowing parameters and temperature-dependent Varshni $\alpha\&\beta$ parameters, and the value of the band gap $E_g$ at 0 K itself.

- The following parameters are needed for material 3: band gap $E_g$ at 0 K, Varshni $\alpha\&\beta$ parameters, the average of valence band energies $E_v, av$, split offset energy difference $\Delta_{SO}$

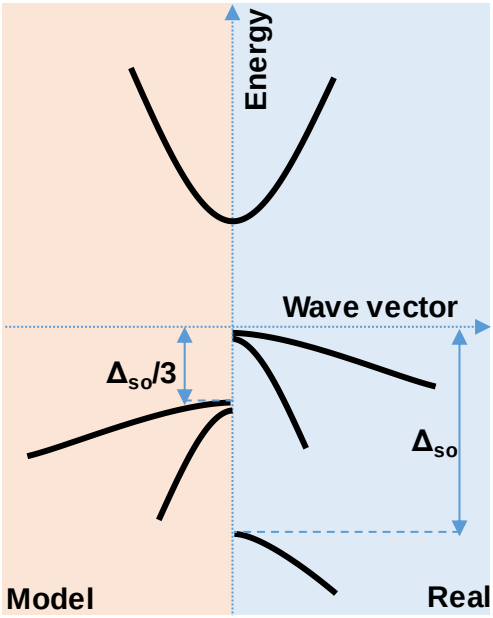


**Fig.2.1.3.2b band gap model containing the direct conduction band edge Γ (see Fig. 2.1.2.4c), and the simplified split-offset approximation.**

### 2.1.3.3. Calculation procedure

Firstly, the $E_g$ for all materials is to be calculated.

Then, the deformation coefficient for each material, defined as:

$$d_{001} = \frac{2c_{11}}{c_{12}}$$

Following that, the relative band edge of material 3 is calculated:

$$E_{v,mat3} = E_{v,av\,mat3} + \Delta_{SO}/3$$

Following that, any ternary material parameters, as required:

$$P_{ternary} = P_{mat1}x + P_{mat2}(1-x) - bow \cdot x(1-x)$$

Where x is the mole fraction, $x \in (0,1)$, and if $bow$ is the bowing factor (if known). If $bow$ is unknown (or $bow = 0$), the above becomes Vegard's law.

To calculate the pseudomorphic band edge:

First, calculate the pseudomorphic layer perpendicular lattice ct in z-direction:

$$a_{\perp} = a_{mat}[1 - d_{001,mat}\left(\frac{a_{sub}}{a} - 1\right)]$$

With the fractional volume change:

$$\epsilon_{zz} = \frac{a_{\perp}}{a_{sub}} - 1$$

Change in average valence band energy:

$$\Delta_{Ev,av} = a_{v,mat} \cdot \epsilon_{zz}$$

Therefore the strained upper valence band energy is:

$$\boldsymbol{E_{v,strained}} = E_{v,av\,mat} + \frac{\Delta_{SO,mat}}{3} + \Delta_{Ev,av}$$

**And, as such, the calculated valence band offset:**

$$\boldsymbol{\Delta_{E,v} = E_{v,strained} - E_{v,mat3}}$$

The sign of the result must be checked to ensure correctness. In the case of ternary on ternary material (e.g. $In_xGa_{1-x}\,As\ on\ In_yGa_{1-y}As$, $x \neq y$) it is strongly advisable to write a computer program to calculate the hundreds of pairs.

## 2.1.4. Accumulated stress limitations

The coherent growth of strained layers upon a substrate without the formation of dislocations is a key challenge for epitaxy. There are several models available to calculate the so-called *critical thickness* for a layer of given strain. Matthews & Blakeslee (M&B) [119] developed a model based purely on mechanical equilibrium theory, yielding a lower theoretical limit of the critical thickness. People & Bean (P&B) considered the format of misfit dislocations to be determined solely by energy balance rather than mechanical equilibrium

[120,121]. In general energy balance (P&B) considerations indicate that thicker strained layers can be grown than predicted by mechanical equilibrium (M&B). Experimental studies of InGaAs/InP epitaxy indicate that poor surface morphology occurs when M&B limits are exceeded, and poor photoluminescence emission and poor surface morphology occur as the P&B limit is exceeded [122].

The growth of strained layers, strain-balanced QWs and our partially strain balanced structures is represented schematically in Fig. 2.1.4 (not to scale). Fig. 2.1.4a shows the case for the growth of a strained layer upon unstrained layers. In this case stress accumulates in the structure until a force (M&B) or energy (P&B) limit is reached (shown by a dotted line) and misfit dislocations are formed. Fig. 2.1.4b shows the case for the strain-balanced structures where the average lattice constant of the structure is designed to be equal to that of the substrate in order to overcome limitations in growing multiple QW layers [123]. This situation balances accumulated stress within the structure. The situation used by the RTDs in this work is shown in Fig. 2.1.4c where partial strain-balancing is achieved, with an $In_{.80}Ga_{.20}As$ QW (+1.72% lattice constant) and binary AlAs barriers (-5.32% lattice constant).

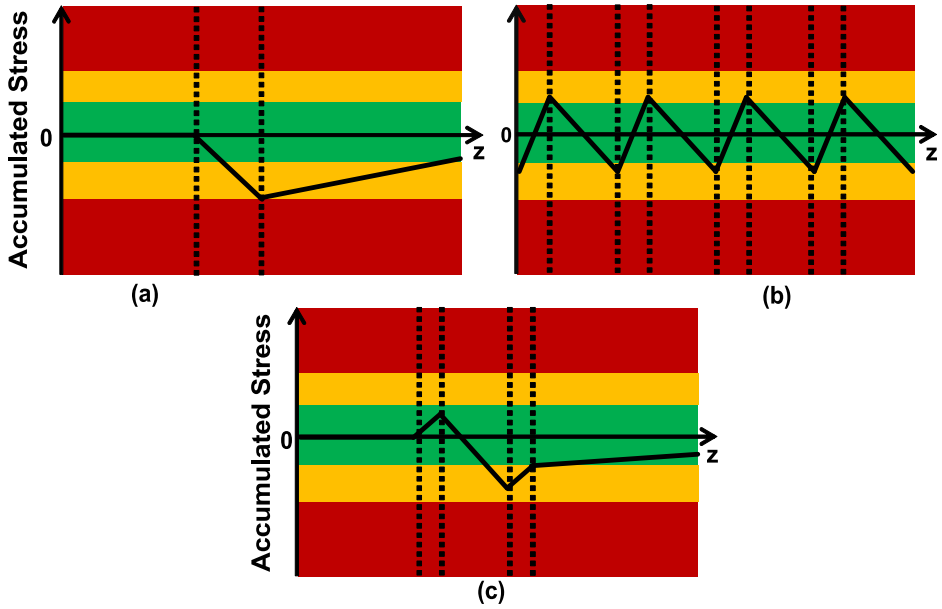


**Fig. 2.1.4. Diagram (not to scale) of (a) strained layer (central) grown within an un-strained matrix. (b) strain-balancing in a MQW stack incorporating alternating strained (thin) and lattice-matched (thicker) layers, and (c) (our structure) incorporates partial strain-balancing. Dotted lines delimit different layers.**

The recurrent equation (5) from M&B is solved, using standard material parameters [108,118], starting with an arbitrary positive guess value for $h_c$. $a_{InP}$

is taken as a strain-balanced point, & a graphic is plotted as $h_c$ vs the mole fraction *x* of InGaAs. The process is repeated for $h_c$ for AlAs, then added to InP/$In_xGa_{1-x}As$ trace, as AlAs creates opposite plane strain.

$$h_c = \frac{b}{2\pi f}\frac{(1-\nu\cos^2\alpha)}{(1+\nu)cos\lambda}(\ln\frac{h_c}{b}+1)$$

where:

- $b$ is the slip plane constant, kept at 0.4 nm due to the similarity of the cubic systems.
- $\nu$ is the Poisson constant of the material
- $\cos\alpha = 0.5,\ \cos\lambda = 0.5$
- $f$ is the misfit strain vs. $a_{InP}$

$a_{InP}$ is taken as a strain-balanced point, & graph is plotted as $h_c$ vs the mole fraction *x* of InGaAs. Repeat $h_c$ for AlAs add to InP/$In_xGa_{1-x}As$ trace, as AlAs creates opposite plane strain. M&B model was conceived with the cumulative stress of both sides of a QW in mind in a near-LM system. The difference vs. equation 5 of the paper is that the worst-case strain is assumed, with contribution from 1 barrier. Therefore an additional ½ factor is multiplied with the converged result to obtain this.

Finally, the critical thickness against the unstrained lattice constant of InP, is plotted depending on the mole fraction x of $In_xGa_{1-x}As$. According to the M&B model, 5.04 ML of InAs can be uniformly grown on an InP substrate before strain relaxation through the formation of misfit dislocations become a problem. This area is shown in green in Fig. 7. To obtain the yellow region, we add the critical thickness of the tensile AlAs barrier to this value, as InAs is compressive. We assume the worst-case scenario where only the first barrier matters in the relaxation scheme [122]. The red zone will thus exceed this limitation, where growth may be possible, with the risk of introducing increasing numbers of defects the further the distance from the strain-balanced point. Furthermore, the black zone also exceeds the P&B limit. We are not aware of any high-quality epitaxial growth attempts that breach this limit.

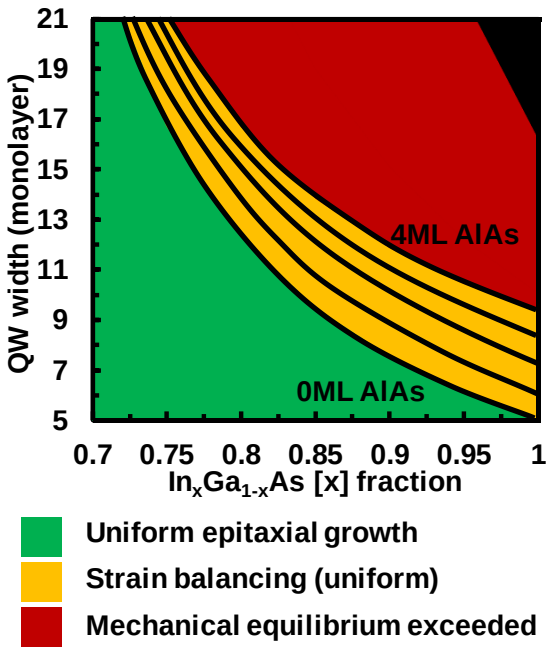


**Fig 2.1.4d Modelled schematic showing which combinations of QW width and indium composition that may be successfully realised. Green region is uniform epitaxial growth within the limit of Matthews & Blakeslee. The yellow region is also expected to be uniform, but with the contribution of the critical thickness to the tensile AlAs, in monolayer bands. The red region exceeds the M & B equilibrium region, but is within the People & Bean energy theory.**

## 2.2. Mesoscopic scale modelling

This section introduces the background theory used to simulate the electronic and optical properties of RTDs.

### 2.2.1. Quantum confinement

It is possible to create artificial trap-states by creating a band potential 'well', comparable with the wavelength of electrons. In practice, the easiest way to achieve it is to epitaxially grow thin (from monolayers to tens of nm) sheets of material, with a different material in the middle.

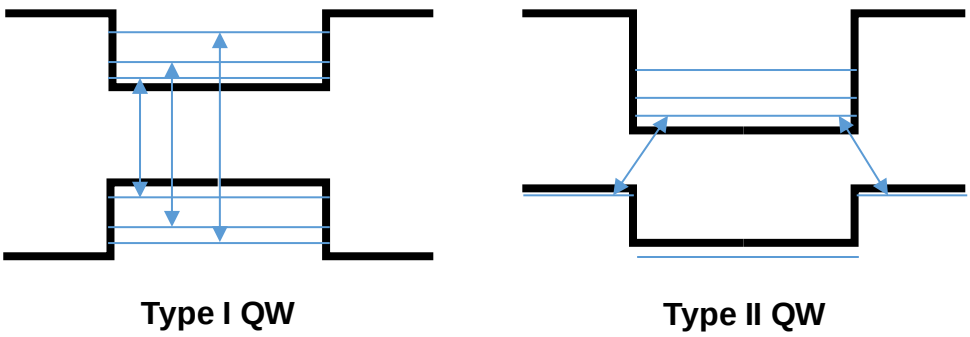


**Fig. 2.2.1a. Discrete confined energy levels in Type I and Type II quantum wells and their respective dominating transitions without bias.**

Figure 2.2.1a exemplifies 2 common band edge potential arrangements seen engineered to obtain such potential wells. In a semi-classical analogy to a pipe with air travelling inside, the confined electron-wave will resonate producing a standing wave. There can be 1 or more harmonics as a result, which, by necessity, have different numerical values from the respective band edge. The energy and spacing between those confined levels varies with the potential depth and width.

When external excitation (either electrical, optical, magnetic, tribologic) is applied to the structure, electrons and holes have a chance to form an electron-hole exciton pair, which, after a given life time, will collapse via an emission of a photon, or be re-absorbed via a phonon, whilst an electron will lose momentum and fall to a lower energetic state. The reverse absorptive process is also possible, hence the double-sided arrows.

In a Type I QW, the energy of a photon created by the transition of a particle from conduction band confined level, to a valence band confined level, has a unique energy signature that is different from either band gaps of the material pairs involved.

Uniquely, in a Type II QW under a *low density of excitation*, the hole levels do not efficiently align, therefore, the electrons of the QW recombine with the hole levels of the bulk material.

QWs provide 2D dimensionality reduction in the Fermi sphere, but are without a doubt the easiest to fabricate amongst the quantum confinement structures. Entire classes of devices, such as QW lasers[124] and MESFETs[125] benefit from this form of band gap engineering. 0D confinement is practically realised with Quantum Dots, and have opened a great niche in optoelectronic components due to their reputed reliability and stability over time[126], however, growing highly uniform dots to attain ultimate confinement remains elusive[127]. 1D confinement given by nanowires is still mostly exploratory at the time of writing, though techniques to aid manufacturability have emerged over the past few years[128].

## 2.2.2. Transmission matrix theory and RTD operation

When several well potentials are spaced apart periodically, with the periodic potential variation spaced within the *mean free path* of an electron inside the lattice, the wave functions representing the carrier confinement in these wells interact with each other.

These interactions form a series of mini-bands across the BZ, merging confined states into a continuum of energy levels across such a periodic structure[129]. Such structures are called superlattices, with an apt analogy to superstructures in civil engineering. RTDs do follow this essential criterion, but it is of note that crystal growers refer to a superlattice exclusively as a *periodic layer structure* of different material pairs.

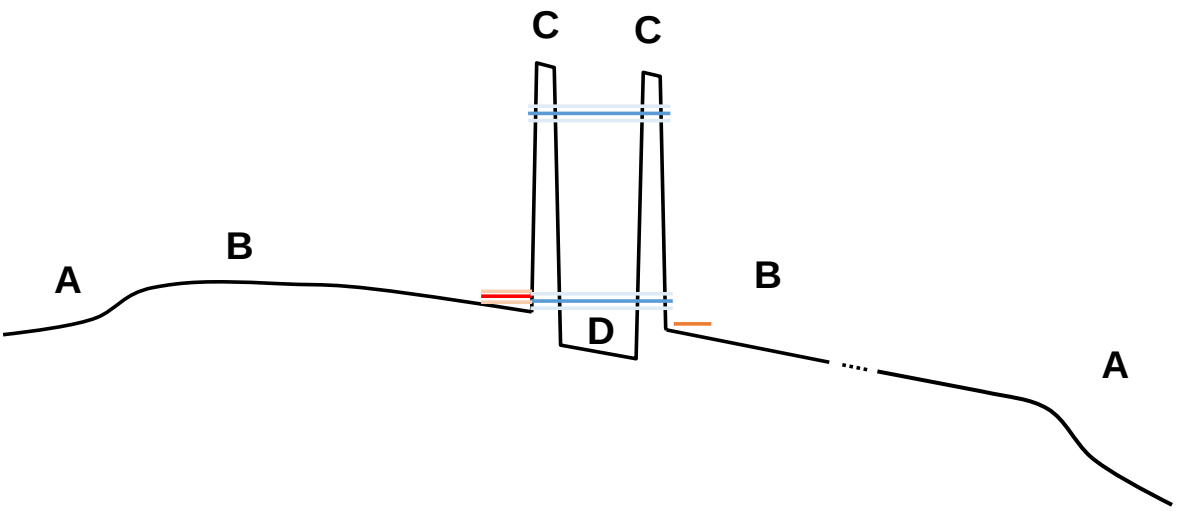


**Fig 2.2.2. Conduction band edge potential (vertical), under an applied electric field with a double barrier tunnelling structure. Material A is a degenerately n-doped version of material B, whereas material C forms a high potential barrier. Material D may be engineered to be purposefully different from B. The lines illustrate the alignment of the Fermi level and their respective linewidth broadening due to the triangular well potential.**

Fig. 2.2.2 presents the conduction band of a superlattice of different materials, a double-barrier tunnelling system shown under bias. The merged mini-bands of the QW(material D) + barrier system(material C) appear as a quantifiable quasi-bound level, with a degree of linewidth broadening due to the triangular potential wells thus formed [130]. Depending on the relative height of the barriers, as well as the relative band alignment and thickness of D, less/more quasi-bound energy levels may be present. Esentially, given a certain bias, the quasi-bound level of C+D (pushed down), aligns with the Fermi level of B,

resulting in a permeation of the entry-barrier. After a given saturation point, the QW leaks charge via tunnelling towards the device collector.

However, carrier leakage in and out of the C+D structure happens within an average dwell lifetime $\tau_{dw}$. Though previously thought so, it appears there is no immediate correlation between $\tau_{dw}$ and the maximum modulating frequency of the device[131]. Instead, tremendously high cut-off frequency devices have evidenced that the length of unintentionally doped material (and thus, transport relaxation times after the entrapment) is more important for *unity gain bandwidth* vs. $\tau_{dw}$ [132].

#### 2.2.2.1. Operation of the RTD resonator

To better illustrate the principle of band alignment in Fig 2.2.2, a model of a GaAs/AlAs RTD is presented using the method presented in §2.2.3.

Fig. 2.2.2.1 plots the density of states at the $\Gamma$ point (traced as a potential outline in the top figure), using the multi-band approximation calculated in Fig. 2.1.2.4c. This is a GaAs/AlAs RTD symmetric structure with $3 \cdot 10^{18} cm^{-3}$ n-impurity near the contact layers, with 1.2nm thin AlAs barriers and GaAs well of 5nm.

In the top figure, at 0V, the first quasi-bound level, $E_1$ is apparent near the conduction band edge, sitting at +85meV above the $E_F$ given by the emitter. A broadened state is observed between 250-300meV, caused by discontinuities in indirect band gaps (X and to a lesser extent, L valleys). Finally, a 2nd resonant state $E_2$ lies at 430meV. I would remind however, that the *DoS* plot is not an *indication of the occupation* of the states, but a mere indication of their existence.

The outline of the conduction band is traced as a darker grey zone along this level. Fig.2.1.3.1a shows that the relative position of $\Gamma$-band edge of AlAs vs. GaAs is ~800meV. It is notable that the perturbations of the DoS reaches beyond this level, merging with the continuum states. However, the X-point of AlAs is offset by only ~70meV, which leads to phonon-activated sub-band tunnelling processes, which are necessarily lossier and slower compared to $\Gamma - \Gamma$

transitions[133,134]. This process is the main reason as to why the GaAs/AlAs material system has been largely abandoned for RTD applications, as it would necessitate powerful heat extraction in order to perform within expected design parameters.

In the middle figure, a voltage has been applied and one can note the position of the injector level being slightly out of alignment. A fraction of the carrier energy will be lost tunnelling through the AlAs barrier, which is why the “on-resonance” condition before the onset of the negative differential resistance, may not necessarily correspond to the bias point. In the limit of no phonon contribution and perfect crystal quality, at this point, 100% of the electrons would transit the structure.

The lower figure shows a minima in the conduction point (current valley), where the injector level is misaligned with respect to either $E_1$ or $E_2$, but before thermal effects begin to dominate. For thin barriers, attempting to exploit $E_2$ may result in electrical fields close to the ionisation breakdown of the material.

In all cases, some peculiar striations may be observed in as alternating levels of DoS. These are a knock-on effects of simulating crystal orbitals in the tight-binding approximation (travelling Bloch wave), and are particularly visible in this multi-band case, showcasing the BZ edge. I would note that the sp3*s* model does not include a treatment of the 5 atoms found in an FCC unit cell, but in this implementation models 2 atom-like objects with 5 pairs of tight-bound orbitals, therefore the predictions brought by these waves should be interpreted with caution.

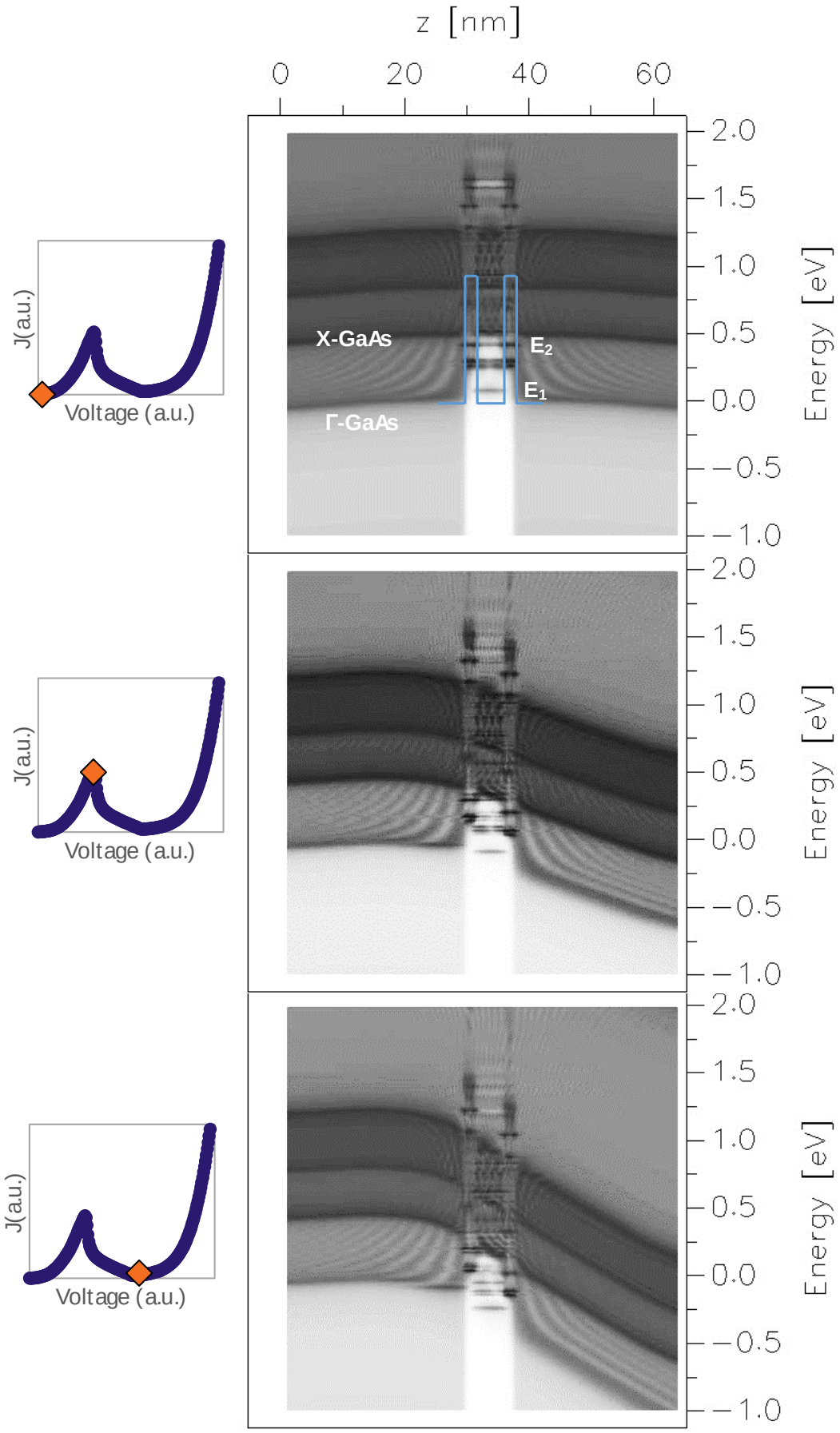


**Fig 2.2.2.1. Plots of a multi-band model of the active region of a GaAs/AlAs RTD at 300K, at 3 different bias points. Grey level represents the density of states in arbitrary units. Darker is a higher density.**

### 2.2.2.2. Extensions to the transmission matrix theory

The first attempts to describe the electrical transport properties [129,135] have had the important consequence of explaining the possibility of obtaining *negative differential resistance* decoupled from the conventional *transferred electron effect* used by n-i-n Gunn diodes.

The result is attributed to a combination of the narrow mini-band region across a slice of the Fermi sphere leading to the possibility of exciting conduction band electrons to a level beyond that of the band-edge of the bulk material. However, this effect has a critical threshold requirement for an applied electric field. When the electric field increases past a certain point, it is expected that Zener tunnelling, avalanching, impact ionisation[129], and other thermal scattering-assisted events[136] will dominate over the increased conductance, practically losing the excess energy to heat.

Later, the result was extended to apply for multiple-barrier tunnelling systems [137], leading to what is widely referred to as the Tsu-Esaki formula of the electrical current density for resonant tunnelling diodes [138]. However, one must be careful about generalising such concepts, because the definition of the electrical current, that of a group of travelling particles-waves, only applies to bulk solids. Though apparently pedantic, when mesoscopic structures and carrier confinement come into question, values for the conductivity may be obtained, which do not necessarily have a direct physical correspondence [139].

Initially, this model included the assumption that the effective mass *m* would be constant throughout the structure*, as each carrier with different m*. Later, Schulman[140,141] extended the model to allow different m* between the emitter-level and QW of a double barrier tunnelling structure. Schulman presents a case that even if the same semiconductor material is used between the emitter and well, the different dispersion relationships, exacerbated by the quantum-confined Stark effect, result in different energy separation levels, thus the integration for the parallel component of the momentum vector $k_{\parallel}$ happens between different $\Delta E$.

### 2.2.3. Self-consistent non-equilibrium Green's functions

The transfer matrix theory provides a great analytical base, however extending the model to include elastic carrier-carrier interactions and arbitrary losses through changes in $\vec{k}$ components (e.g. scattering through an optical or acoustical phonon), can prove to be very costly from a computational point of view, even on contemporary hardware, as the contribution of each carrier will require integration, summation and verification at every step. An alternative method for this multi-carrier problem was proposed in the mid-80s, using the Landauer-Büttiker [142,143] formalism as a base.

In this context, Green's functions are employed as an *integral kernel* to simplify calculation of the system's many-body Hamiltonian after the interaction with the voltage potential. Fig 2.2.3. shows this interaction for a 1-particle event, resulting in the separation of the incident wave-function into a transmitted(T) and reflected(R) wave. In the ideal case where an additional potential due to carrier scattering does not exist:

$$T^2 + R^2 = 1$$

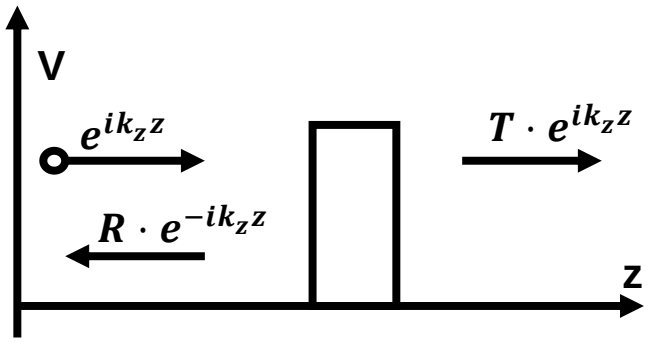


**Fig. 2.2.3. Diagram representation of an incident wavefunction of a given wavevector $k_z$ separated into a Transmitted (T) and Reflected (R) wave. The vertical and horizontal axis are the potential and crystal direction, respectively, in arbitrary units.**

Generally, with RTDs, it is assumed that the device is *identical in lateral directions*, therefore the potentials are similar, reducing transport calculations to a *1-dimensional problem*.

An important consequence of the Fermi-reservoirs represented by the 2 n-doped contacts of the device is that each transmitted wavefunction contributes to a minimum of:

$$\frac{2e^2}{h} = 77.4\mu S$$

to the conduction of the device[139], where $e$ is the electron charge and $h$ is the Planck constant. The strength of the coupling of an incident wavefunction from the emitter potential to an arbitrary intermediary level is noted $\Gamma_{\mathrm{L}}$ and the correspondent from the collector is $\Gamma_R$. The sum of the two terms can be seen as a broadening function of the transmission probability.

There are several tutorials for varying levels of understanding [139,144–147] and papers[148–151] that discuss the assumptions and equations behind the complex non-equilibrium self-consistent Green's functions model. This must be understood as a generalist mathematical method that is given physical meaning in the context of semiconductors. The non-equilibrium is meant that the system is not under equilibrium (energy & momentum is transferred from the emitter to the collector), whereas the self-consistency means that the modelling includes recurrent checks whether a condition has been satisfied, in this case if the Poisson charge distribution and the band potentials respect a convergence criterion. This is highlighted in the next sections.

#### 2.2.3.1. WinGreen software description

D. R. Hartree [152,153] is generally credited in creating the bridge between the Bohr understanding of an atom as orbital shells, and the Schrodinger's formulation of an atom with a wave-like energy behaviour. The problem with the formulation of the Schrödinger equation is that the Coulomb interaction term is based on the relative distance $r$ between 2 electrons, whereas the wavefunction $\psi(\overrightarrow{r_1}, \overrightarrow{r_2})$ is multivariate and cannot be separated due to the presence of the positional vectors. Nor could the Coulomb term be neglected, because e-e repulsion becomes significant as $r \to 0$.

The Hartree approximation assumes that the value of the e-e interaction is roughly given by a spherical symmetry of the atomic system at the position r. An important contribution here was to express the new equation in the spherical coordinate system, greatly simplifying its form. A detailed treatment of the Hartree potential from a contemporary perspective is available in Ref. [154].

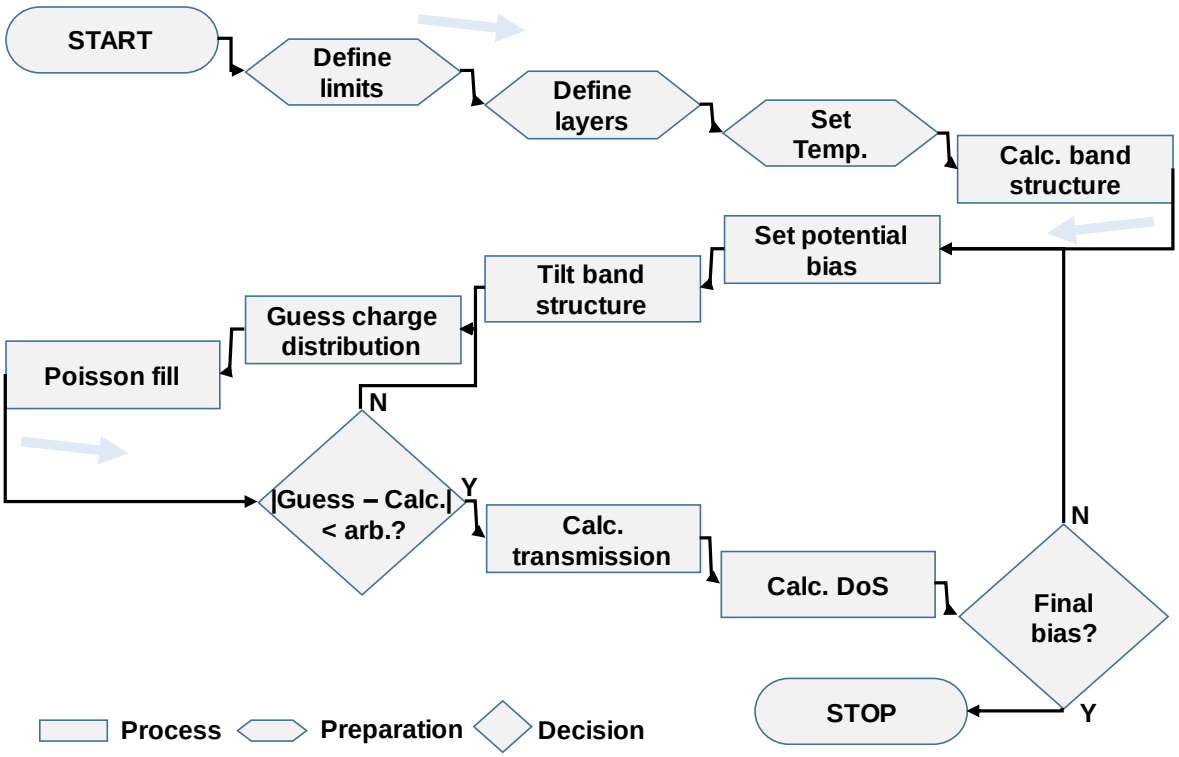


**Fig 2.2.3.1a High-level WinGreen self-consistent iteration flowchart neglecting file handles**

Fig. 2.2.3.1a. shows a schematic block chart of the operation of one such piece of software that implements the NEGF with charge self-consistency. The self-energy of a given atomic orbital is calculated recurrently, initially assigning a guess, to then iteratively converge until the difference between the sum of guesses and the calculated charges is below an arbitrary threshold number. In order to fill occupancies in the valence band, a Poisson distribution is calculated at every step. Once the charge distribution passes the self-consistency test, current, energy transmission and the density of states can be quickly calculated.

Determining the band potentials, simulation boundary conditions and applying the temperature constant is a one-time process per run.

However, filling multiple bands per run can take a significant amount of time, (particularly when a matrix of simulations are required to fit a set of parameters) and may not be necessary to explain conduction around the $\Gamma$ point of the BZ expected for higher occupancy states of the valence band. Fig. 2.2.3.1b compares a conduction-band-only density of state plot with that seen of the multiple-band case. It is of note that $E_1$ and $E_2$ can be predicted within$\pm 15meV$, without additional differences between the two. Bearing in mind the difficulty in determining the precise band alignment inside a structure with

unknown hydrostatic strain (§2.1.3.2.), it is not unreasonable to assume that these numbers can be fit quantitatively with additional correction factors.

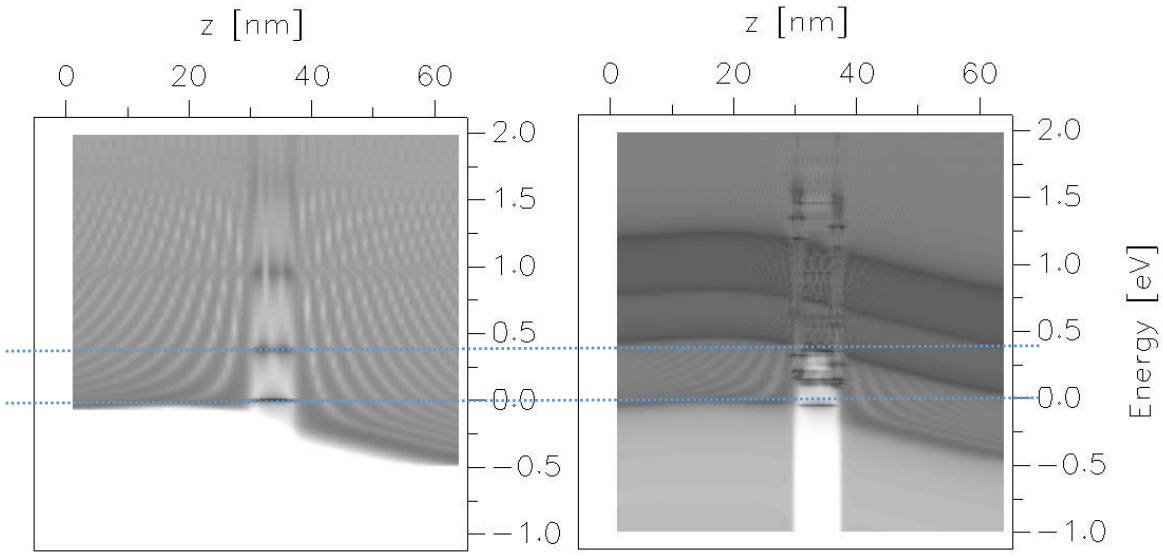


**Fig 2.2.3.1b WinGreen Density of State in a 1-band model and 10-band sp3*s* (as seen in Fig. 2.2.2.1.). The dotted lines are a guide to the eye for the relative positions of $E_1$ and $E_2$ quasi-bound states.**

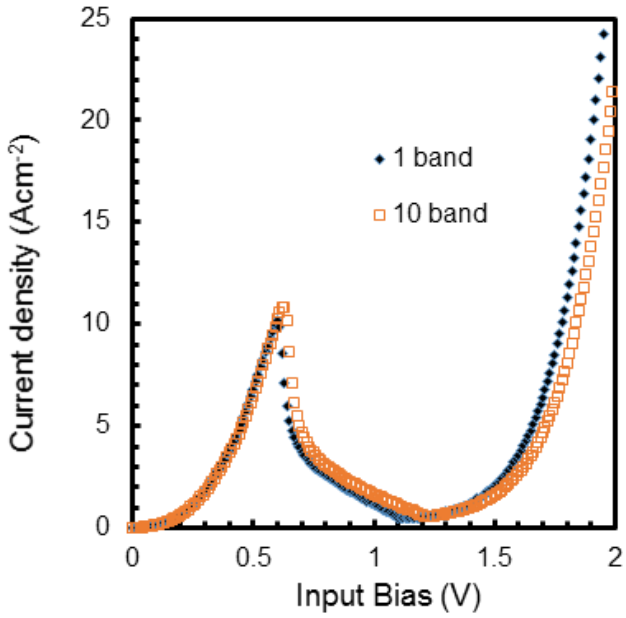


**Fig 2.2.3.1c. Uncalibrated I-V characteristic of 1-band and 10-band sp3*s* models for a GaAs/AlAs RTD.**

The relatively small differences in I-V characteristics of the 1-band and 10-band case do not warrant the additional complexity implied by the latter for Type-I QW RTDs. This case is particularly interesting for GaAs/AlAs due to the indirect band gap alignment concerns.

### 2.2.3.2. Regions of simulation

Importantly, the user can define the regions of the simulation. For instance, the large Fermi reservoirs of a RTDs reach equilibrium fairly easily compared to the active region. For these, the semi-classical Thomas-Fermi charge calculation is perfectly adequate. However, due to level quantisation complicated by the charge interaction, this is not sufficient inside the QW region, thus a full Hartree potential enabled calculation is required. This process is significantly more computing intensive compared to the semi-classical case, noticeable even on contemporary computing hardware.

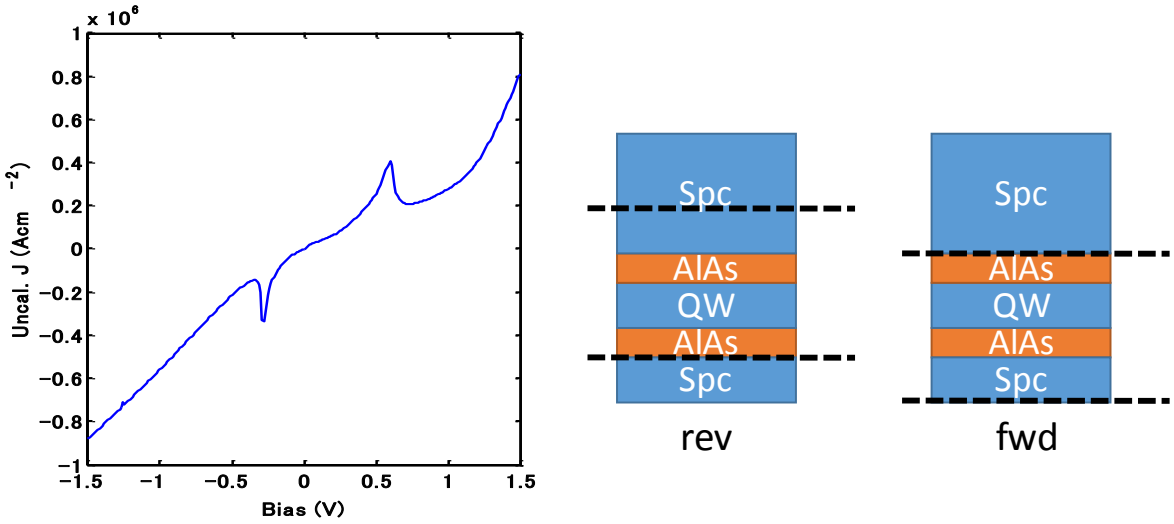


**Fig 2.2.3.2a. Uncalibrated modelled forward and reverse I-V characteristic of an RTD, with the Hartree potential calculation region as shown by the dashed line.**

In Fig 2.2.3.2a an example is shown suggesting the way to choose the boundary regions. A design necessity of RTDs is to contain an unintentionally doped spacer layer between the highly-doped reservoir and the barrier. The role is two-fold: protect the active region from incorporating dopant, and facilitate the creation of a higher "launch" level for the electrons to tunnel through the barrier (triangular potential to QW pseudo-2D → 2D tunnelling), reducing the bias requirement. It is common to utilise asymmetric spacer layers [155,156] to balance the minimal carrier transport $\tau$ at the expense of biasing increases. The origin of the I-V asymmetry in the above graphic can be traced to the intentional variation in spacer thickness, as well as the slightly asymmetric doping profile.

Ordinarily, the Hartree region is logically chosen between the double barriers as its limits. However, one way to simulate the multiple relaxation processes that may happen inside an imperfect RTD structure is to extend this region by a few

monolayers after the exit-barrier in the direction opposed to the conventional current flow.

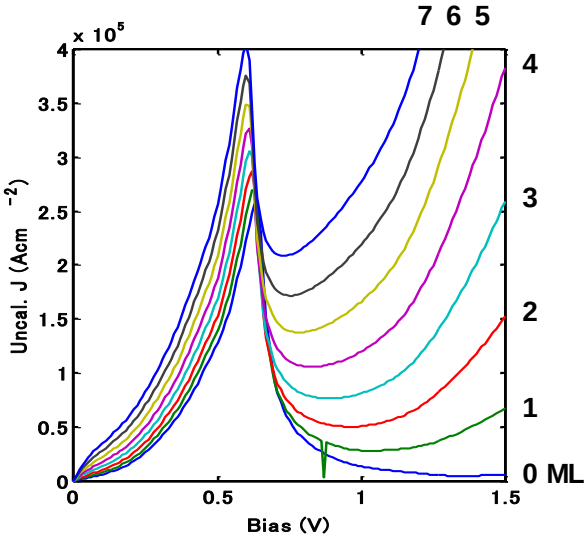


**Fig. 2.2.2.3b Forward I-V characteristic shown with Hartree region taken at the edge of the exit-barrier (0 ML), with increasing monolayer steps.**

Fig 2.2.2.3b exhibits the effect of varying this charge calculation region. It is notable that the slope of the NDR is preserved as this region is increased. Furthermore, because the total charge in the QW-continuum is integrated over a larger "device" area, the overall current peak can be fit over $\pm 30\%$, before considering additional contact effects, including imperfections and Fermi-pinning due to Schottky junctions. In this case, the 1 ML plot shows a random point of numerical convergence failure, normally removed from data sets.

WinGreen should not be seen as a "black box" simulator that applies these models of quantum electrodynamics to an arbitrary structure. The guess and Poisson iteration parameters are customisable, allowing more convergence options in the case strong non-equilibrium region, such as those posed by severe band discontinuities (modelling polar effects in GaN crystals or several monolayer-thin bands). In order to make effective use of the relatively simple software, one must have a good grasp of its limitations. For instance, whilst bulk hole charge calculation is performed, hole current is not shown. As an effect, Type-II structures, pn junctions or Schottky contacts are less likely to be simulated correctly. However, simple-electron hole interactions may be modelled, separately, by flipping the band gap upside down and changing the effective mass to that of holes, to obtain the quasi-bound hole levels. This method is adequate for Type-I QW RTDs.

### 2.2.3.3. Scattering parameter

In the limit of suitable mini-band alignment, both the transmission matrix theory and NEGF suggest that in a coherent $\Gamma - \Gamma$ tunnelling process, there is a 100% chance for electrons of a certain energy to transit the structure. However, the carrier wave vector does not always remain bound to the $\Gamma$ point of the BZ, and there may be several ionic impurities and other scattering centres that would cause the carriers to lose their evanescent coupling. Therefore, a provision to model these in-plane travelling wave vectors is a necessity to increase the accuracy of the simulation. WinGreen provides this via the means of an imaginary component added to the real part of the wave vector.

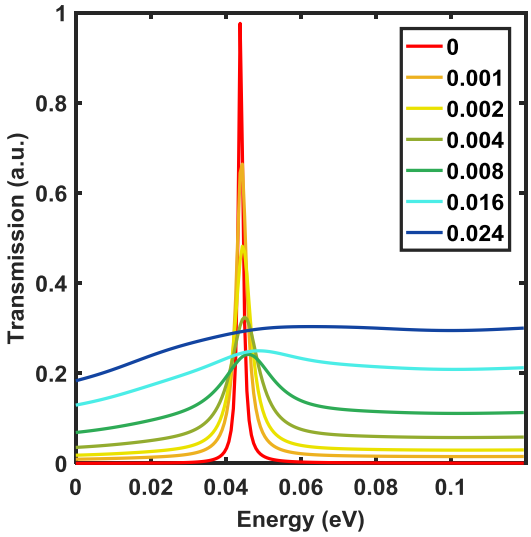


**Fig 2.2.3.3a. Transmission plot throughout the structure focusing on $E_1$, shown with several variations of the 'scattering' parameter inside the QW**

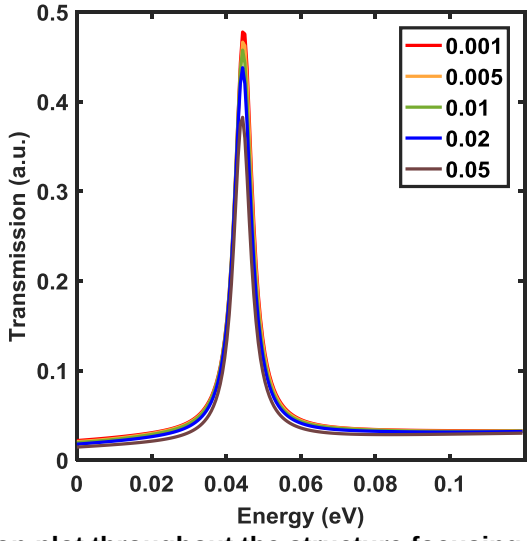


**Fig 2.2.3.3b Transmission plot throughout the structure focusing on $E_1$, shown with several variations of the 'scattering' parameter in the degenerately doped regions**

Fig 2.2.3.3 a & b plot the variation of this 'scattering' parameter for the QW and Fermi reservoirs, respectively. The scattering parameter is larger in the doped region by a factor ~5-10, as expected by the increase in ionic impurity centres. In both cases, increasing this parameter broadens the linewidth of the function, exhibiting non-resonant tunnelling behaviour. Fig. 2.2.3.3c shows the large variations in I-V characteristics achievable simply by adjusting this scattering parameter.

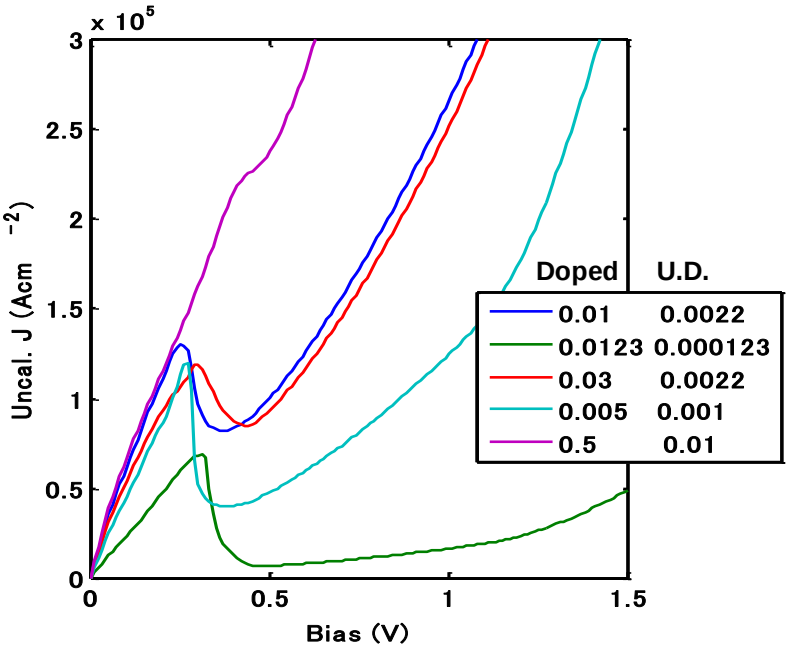


**Fig 2.2.3.3c Uncalibrated I-V plot of RTD simulations using different values for the scattering parameter.**

One of the arguments to employ the Green's function method has been due to the unphysical discontinuity calculated in the I-V characteristics with the transmission matrix theory, particularly with high-density current systems such as InGaAs/AlAs on InP or InAs/AlSb on InAs [157]. This discontinuity, manifested as an artificially high $\delta I/\delta V$ before the peak current has not been observed experimentally, however, it does occasionally appear in theoretical studies [158]. It is possible to reproduce this problem in WinGreen by setting $\Gamma \to 0$ in the active region, which results in random fluctuations of the QW charge near the on-resonance condition, due to the very narrow linewidth of the transmission levels thus computed.

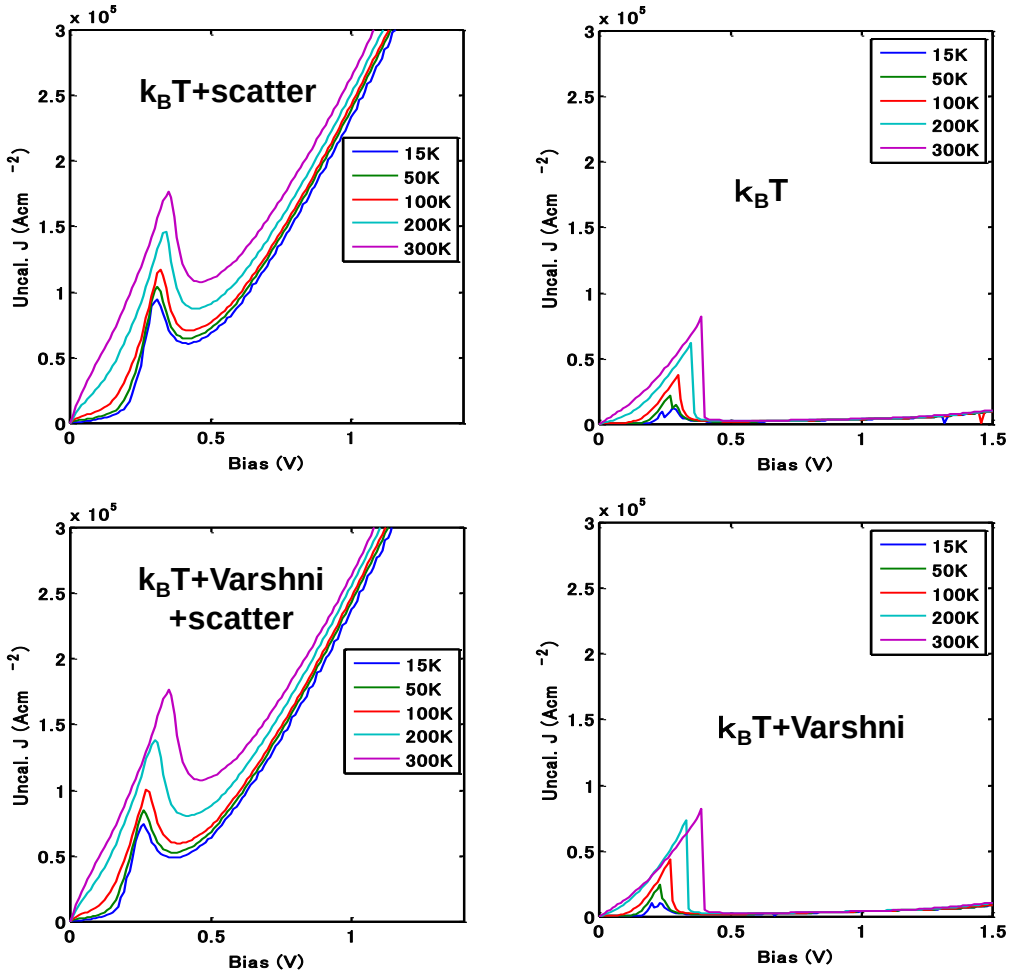


**Fig 2.2.3.3d Simulations of temperature-dependent I-V using 3 different conditions: Boltzmann factor, scattering parameter, material band gaps changed with temperature. Scatter assumed constant where $\neq 0$.**

Finally, Fig. 2.2.3.3d simulate InGaAs/InAs/AlAs on InP RTDs found in this work using different combinations of all simulation parameters in this section. There are several key points observed here:

- Tunnelling appears to be thermally activated, consistent with early observations seen in GaAs/AlAs RTDs, but inconsistent with the latest temperature-dependent I-V measurements in InGaAs on InP RTDs [159]
- Low scattering values create a very high NDR at room temperature, but appear to cause bias-dependent charge oscillation in the QW.
- Using the Varshni correct band gap for a given temperature better predicts the $E_1$ energies, with a distribution of the peak V with temperature approaching that observed experimentally.
- In the limit of no scattering, the simulator fails to replicate realistic results. This is a limitation of the method, and it is considerably difficult to decouple scattering mechanisms unlike Monte-Carlo simulations.
- The slope of the NDR varies with drastically with lower temperatures, again suggesting that individual calibrations need to be performed to

replicate temperature dependent IV-T characteristics with a high degree of accuracy.

Furthermore, the components of the extrinsic circuit also alter their values with temperature non-linearly, correspondingly skewing the results of the model which are not modelled here. Early GaAs/AlGaAs RTD attempts[138,160] which followed this distribution may have lost the advantage to impurity scattering in their thick barriers at lower temperature, as well as the lossy indirect sub-band transitions.

### 2.2.4. Software alternatives

**Nanohub.org NEMOv5**

Based on Prof. Datta's work, this Purdue University-created simulator[82] has a multitude of solvers and an ever-growing complexity. Its feature set is unique, but community support is very limited for the offline version. The compilation tree of this software is impressive and requires specific outdated versions of some packages, notably VTK 5.1, and making several alias paths in Linux distributions (attempted on Ubuntu and CentOS), which makes the installation difficult. There is a precompiled build available[83] that works on all Linux distributions tested, but will have some limitations: i.e. the version was nearly 2y old at the time of writing and some data output fails unless the specific dependencies are installed; particularly 3D data to visualise structure or atom distribution in real space.

The RTD example files no longer work with the current versions, as the 'ramper' simulator is deprecated. The other retarded Green's function solvers are not directly compatible and need a re-write of the input file[84]. Thus the conclusions drawn on the NEMO engine for RTD simulation are based on a simplified online tool provided as a virtual environment[85], limited only to the GaAs/AlGaAs system. Another quirk of this solver is that turning off the resonance finder (Lanczos iterations) will greatly improve the speed of simulation, but will yield a different shape of the IV curve. Another disadvantage in this online teaching tool is that the Hartree solver is unstable and will yield oscillations in the valley which are not seen in IV plots of real devices.

Overall, NEMO should be the main point of a simulation paper, as its capabilities are the most advanced of all the software reviewed.

**WinGreen v. 2.1.1**

WinGreen [86] was written by then RAs at the Forschunszentrum Jülich with an interest in digital signal processing, computer engineering and with a pedigree in semiconductor physics. Much of their materials database is based on Palankovski's PhD work at TU Wien[69], but fortunately it can be re-written to include newer findings such as Vurgaftman *et al*. [70].

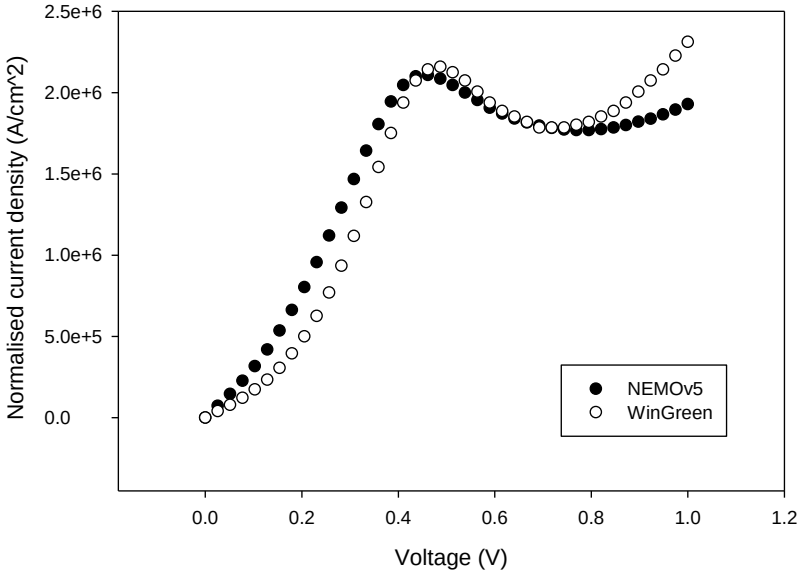


**Fig 2.2.4. I-V characteristic of an identical structure computed in NEMOv5 and WinGreen**

It is an attractive piece of software tailor-fitted for RTDs; moreover, it has a very small program size and its use is very straightforward due to an intuitive simulation software. As an added feature, it supports modelling in different growth directions if the 10-band s*p3* parameters are specified. The interface between two materials is defined with an abrupt model, and the program files does caution about the accuracy of the simulations when large band offsets are involved and/or 2-3 monolayers are implied.

Like NEMO, the Schrödinger solver works with absolute values for the z direction, whereas all other computations use a fixed 'lattice constant' parameter and samples points 1 monolayer at a time. The software can only be obtained by contacting the authors directly and is no longer maintained.

The differences in Fig. 2.2.3 between the two software could be explained by a slightly different interpretation of the scattering parameters and different assumptions on the initial conditions

**Quantum Wells, Wires and Dots (QWWAD)**

This software [87] started out of the necessity to simulate Leeds' University grown quantum cascade lasers, and the software known as QWWAD is a fraction of that program [88]. As other simulators, it is a collection of numerical and analytical solvers that can be linked together using the formally rigid Linux *awk* C-like scripting framework.

Its main goal is to be an accompaniment to Paul Harrison's eponymous book [89], but it can be a quite formidable 1D solver if used correctly, including the NEGF method. QWWAD was released to the public after the simulations had been completed.

**Sivaco ATLAS 2D**

Part of the TCAD, one of the industry-standard suites for device physics, this can simulate any device geometry. A 1D device is treated as a slice of a 2D surface, where less mesh points need be defined. It has a capable quantum solver, though without much novelty about it and a well-written manual, as well as a good tech support.

The scripting language is similar to MATLAB and the syntax is generally equally forgiving (forgotten semicolons for instance).

The simulation software needs to be acquired as a bundle, annual licensing.

**Synopsis TCAD**

A competitor to the Sivaco offering, it tends to be better when batch processing jobs are required due to its powerful queuing system, hence very suitable for a computer cluster scenario. The programming language is more strict and closer

to C in terms of syntax. The manual is much shorter and support for academic versions is placed as a low priority.

**COMSOL Multiphysics**

It has been suggested [90] that this generalist software is also useful for simulating short period superlattices and other nanostructure systems.

**NextNano 3 and nextnanomat**

The base versions of nextnano offer more complex models for acoustic and optic phonon interactions [91] where the authors claim to make an important difference in this class of devices [92]. A tutorial for RTDs is available [93], but it is not particularly helpful for novel device simulation, as the barriers are 3nm thick with $Al_{0.3}Ga_{0.7}As$ on GaAs, and no source code is present for duplication of the results. Nextnano features few example files and is not the most user-friendly software, but does work under Windows.

There is an additional solver version that has a novel NEGF algorithm claimed to be more efficient at a minimal expense of accuracy [94], though the latest version is dated 2013, and no updated licensing file was released to test it.

## 2.3 Electronic modelling

The RTD device, with its very thin active region and generally shallow contacts is one of the fastest solid state devices. The previous section have highlighted the theory behind the origin of the resonance. As the conduction band potential diagrams suggested, the role of the metallic contacts cannot be understated, particularly for high speed, high current density applications, where minute changes in the complex impedance of the device, could result in vastly different optical power extraction. In this section the circuit topology of a typical extrinsic RTD quasi-optical emitter-oscillator is presented, and explained why it matters.

### 2.3.1. Circuit model

The DC-to-RF conversion efficiency has always been a concern for RF and optical components, and the trend is particularly important with personal mobile devices and large data centres alike. Battery life is limited, and the aggregated energy usage of IT infrastructure is significant (See Chapter I).

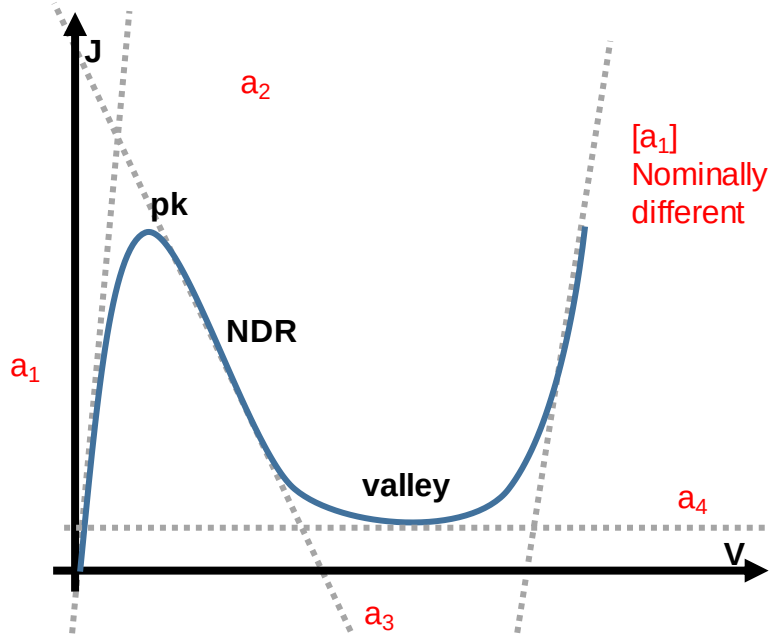


**Fig. 2.3.1a Idealised RTD I-V characteristic separated in asymptotic components corresponding to the 3rd order polynomial approximation to the Van der Pol oscillator. Adapted after** [161].

So far, the mesoscopic modelling has been shown capable of highlighting key predictions about the shape of the I-V curve of a device, including the peak voltage, the NDR, and the positive differential resistance curves given by the off-resonance conditions. Early theoretical attempts based on the understanding of vacuum tube oscillators [162] were made to describe the extrinsic NDR behaviour of a tunnelling diode. The model is still valid for RTDs. Essentially RTDs have been described as a Van der Pol oscillator, a special case of the Liénard equation[163], in its canonic form:

$$C\frac{\partial^2 v}{\partial t^2} - \{(g_d - G_L) - 3hv^2\}\frac{\partial v}{\partial t} + \frac{v}{L} = 0$$

This equation is used to characterise a lossy tank circuit with a pure capacitance C, transconductance $g_d$, negative differential conductance $G_L$, and a pure inductance L, all in parallel.

Transferred into the current domain, and approximated to the 3rd order polynomial, the equation can be approximated [164] to:

$$i(v) \approx a_1 v^3 + a_2 v^2 + a_3 v + a_4$$

In Fig. 2.3.1a. the contributions of the parameters $a_1..a_4$ are highlighted. A limitation of the 3rd order polyniomial is quickly apparent when one notes that real RTD devices may have different PDR slopes, whereas here $a_1$ is the slope for both (given by the 3rd power parabola). Also with a direct physical equivalent is $a_3$, which equates to the NDC. Instead, $a_2$ provides the $\Delta V$ swing voltage between the peak and the valley, and $a_4$ is a constant dependent on structural imperfection [159]. Therefore, when $a_2, a_4 = 0$, we are dealling with the ideal, adiabatic RTD. The polynomial itself is an imperfect fit, as when $v \to 0$, $i = a_4$ which cannot occur in practice.

If the power over the NDR region is integrated, one obtains:

$$P_{NDR} \approx \frac{3}{16} \cdot \Delta V \Delta I$$

where $\Delta V, \Delta I$ are defined by the difference in peak vs. valley voltage and current, respectively, for the static DC signal. This important approximation has been linked to the maximum extractable oscillation power achievable[164] at DC levels.

However, for an accurate picture, one must consider the role of the small-signal oscillation and how it might be influenced by the reality of the circuit extrinsic to the device. In Fig. 2.3.1b an equivalent circuit for the RTD THz emitter is shown and note several device parameters that impact conversion efficiency. To achieve this, several components are of note: the DC power supply and the electrical leads or traces, seen as extrinsic impedance elements, the fabricated RTD device, consisting of the intrinsic I-V characteristic of the RTD, and its

associated waveguide and antenna. The summary diagram represents the various elements as complex impedances, all which need to be matched to satisfy the maximal power transfer conditions. $Z_s$ is the input impedance of the power supply unit. $Z_{tr1,2}$ represent the impedance due to the traces, module and packaging found in a typical system. $Z_{ce}$ and $Z_{cc}$ represent the emitter and collector contact impedance due to the metallization. $Z_{sheet}$ represents the impedance that can appear due to various mesa fabrication configurations, including the contribution of sidewall leakage current. The intrinsic characteristics of the RTD are included as a single element (a non-linear voltage controlled oscillator). $Z_{cpl}$ is given by the λ\4 coupler and $Z_L$ represents the load, or antenna, impedance. In order to produce a tunable system, several elements require controllability [7].

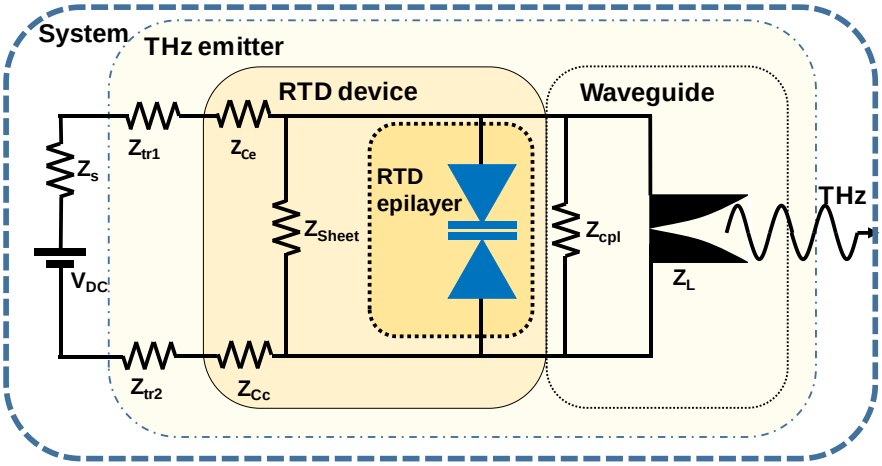


**Fig 2.3.1b A system diagram showing equivalent circuit model using complex impedances. The RTD THz emitter neglects the power source, and is compartmented in the semiconductor resonator device, and its radiating elements. The former includes the RTD epitaxial layers, modelled as a single element.**

Several elements are apparent in this extrinsic circuit which govern the overall oscillator performance, and at a system level, losses (via both real and imaginary conductance components) through the power distribution network cannot be understated. Most attempts to realise THz emitters using RTDs have employed monolithic circuits with the shortest possible electrical lengths. Keeping with the trend of other parametric resonators, the RTD element is usually sat directly into a cavity, slot, or connected to a patch antenna via a microwhisker.

$$a_3 = \frac{3}{2} \cdot \frac{\Delta I}{\Delta V}$$

$$a_1 = 2\frac{\Delta I}{\Delta V^3} = \frac{4}{3}\cdot\frac{a_3}{\Delta V^2}$$

Therefore, in this ideal approximation, the small signal conductance given by the oscillation could be written as

$$g_d = a_3 - \frac{3}{4}a_1 V_{ac}^2$$

This is an important theoretical result that is the first step in estimating the maximum frequency[164,165], however, precisely determining the maximum amplitude of the oscillation, $V_{ac}$, can be difficult in practice due to the DC instability of the device skewing the measurements.

## 2.3.2. Maximum Operation Frequency

In practice, to optimise the RTD resonator topology, inductive components are reduced to a minimum through careful placement of metal-insulator-metal elements. In the limit of frequency independence of the component values, Sollner *et al.*[166,167] obtained a simplified equation for the maximum frequency attainable:

$$f_{resonant} = \frac{1}{2\pi C}\sqrt{-\frac{G}{Rseries} - G^2}$$

where C and Rseries are also assumed nearly-independent of bias voltage, and Rseries represents the cumulative resistance added by the series components. Whilst this might be true for bulk approximations of the contacts and epi-layer capacitance, in practical measurements, one may observe a variation in G (NDC) with bias[159].

The impedance matching between the RTD and antenna is thus achieved when $G_{max} < \frac{1}{-2R_{series}}$, where:

$$f_{max} \approx (4\pi C R_{series})^{-1}$$

### 2.3.3. Dynamic capacitance

As mentioned in §2.2.2, the operating frequency of the RTDs also depends on the carrier transit times. Previously, the model of the circuit also assumed that the capacitance of the device is unchanging. However, the capacitance-voltage characteristic deduced from electrical measurements, also follows areas of negative differential capacitance[21]. In electrical terms:

$$C_{dyn} = \left(\Delta Q_{depl} + \Delta Q_{QW}/2\right)/\Delta V$$

Where Q is the 1-D case charge stored in the depletion area and QW, respectively. To adapt this for the case of WinGreen 1-D simulation:

$$C_{dyn} = \left( \left(Q_{depl\,Pk} - Q_{depl\,Val}\right) + \frac{\left(Q_{QW\,Pk} - Q_{QW\,Val}\right)}{2} \right) \cdot step_{size} \cdot q_{electron} \cdot area \,/\, (V_{val} - V_{pk})$$

Where the $step_{size}$ is always the lattice-matched constant half-distance a/2, for InP~0.293nm, $q_{electron}$ is the elementary charge of the electron, and area is scaled for the mesa area of the diode to verify dimensionality, as the charge at a given point is at the cube root.

A key problem however is given by the choice of the depletion area in simulation results, which will also be, to some extent influenced by the Hartree region choice in §2.2.3.2.

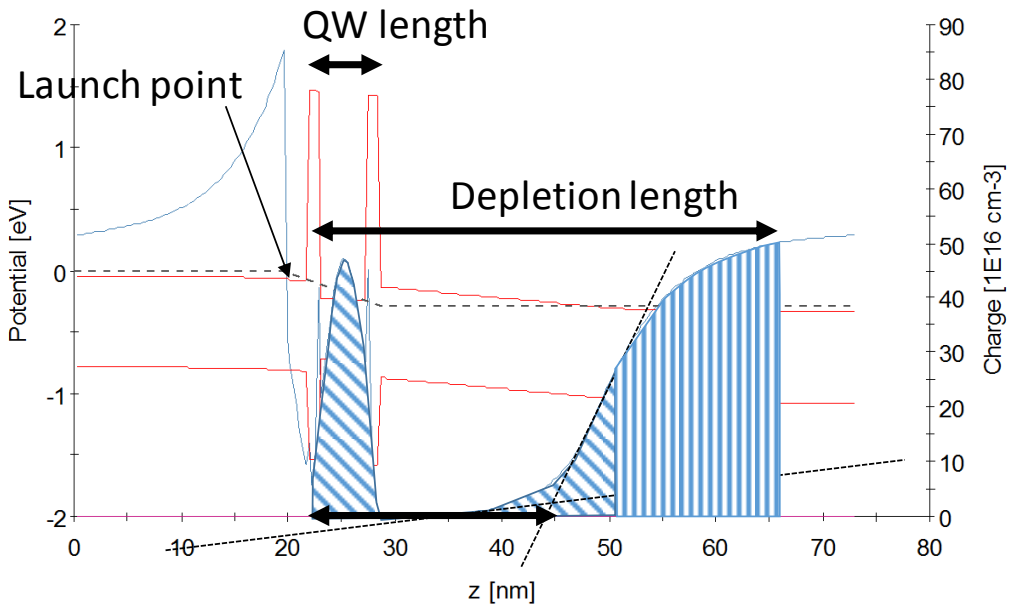


**Fig 2.3.4. Band potential (red) with the top band representing the conduction band, biased at on-resonance condition. The blue plot is the stored charge at the given point. Different choices of the depletion length are shown.**

Fig. 2.3.4. shows several possible choices for a depletion area, which will ultimately depend on the doping profile of the RTD structure. As the carriers travel after the unintentionally doped spacer layers, they reach an equilibrium state, to increase to even greater concentrations in the degenerately doped contact regions. The best estimations so far could be achieved by taking the limit of the near-equilibrium state in the sub-collector doped step region, yielding an estimation of $C_{dyn\_peak} = 4.88\, fF \cdot \mu m^{-2}$, within the higher range quoted in Shimizu *et al.* [21].

This has not been confirmed with measurements. The static DC capacitance due to the epi-layer themselves is ~150fF.

## 2.4 Further work

Whilst the RTD can be understood qualitatively at a high level, with models of varying complexity having been attempted in the past, details pertaining to the fine operation of this mesoscopic devices are still obscured.

Notably, the theoretical framework behind the understanding of solid-state physics is a work in progress. Sophisticated models that may benefit RTD modelling are not be widely in use by the general scientific community, and could easily constitute the topic of a doctoral thesis on its own. From electronic

band structure, band alignment, to the theory of stress and strain deformation potentials, the expectation is that in the upcoming decades, the theoretical toolbox used in this work will be considered obsolete and superseded by quantitatively accurate methods.

At the time of writing, the non-ohmic low temperature behaviour [168,169] of the RTD contact layers could not be correctly accounted for. Top contact metal layer surface roughness has also been quoted as a source of conduction loss [170]. Therefore a more advanced investigation is needed to accurately simulate a full RTD system at an arbitrary temperature.

The semi-physical scattering parameter added in the self-consistent calculations cannot deconvolute sources of elastic scattering (phonon, impurity, interface roughness). More sophisticated work has been carried [171] to extend the NEGF method to improve the utility of its output without the computational expense of Monte Carlo-based simulators.

# Chapter III : Modelling Results

This chapter elaborates on the concepts introduced in Chapter II and discusses practical factors that influence the RTD performance of a given layer structure.

Firstly, several candidates for a figure of merit are presented from the canon, followed by a discussion on the assessment criteria and their possible shortcomings.

Before the modelling parameter space is explored, impactful modifications due to structural imperfections are presented. An explanation of possible departures from measurements is given for the negative differential resistance region of the RTD due to DC instability, re-visiting the role of the scattering parameter, introducing the series resistance loss to compensate for the role of the extrinsic circuit. The role of variations in fabrication is discussed, including local variations of doping density and AlAs barrier thickness. The role of the effective mass is considered in isolation. Each energy band of a given material has an associated effective mass of its carriers, therefore, a decoupling is pursued to differentiate from differences in the band energies that appear as a result of changes in the .

Then the parameter space analysis proceeds to evaluate the barrier and QW thickness, as well as mole fraction of the $In_xGa_{1-x}As$ crystalline alloy inside the QW. This is carried out for a proposed efficiency figure. The analysis concludes by highlighting the manufacturable structures based on accumulated stress limitations, to then turn the attention towards the specific requirements of >1 THz devices.

Finally, the rationale for the manufacture of InGaAs / InAs / InGaAs “sub-well” devices is explored in a parameter space similar to the previous.

## 3.1. Figure of merit candidates

In the previous chapter a modelling methodology was discussed, without suggesting a figure of merit. In line with optimising other sophisticated engineering products, certain performance trade-offs may be required to reach a design specification given by the application. A semiconductor laser for instance may increase production costs and sacrifice overall peak emission energy output to attain tunability and the lowest possible divergence angle in the far-field.

Likewise, a resonant tunnelling diode may have different requirements with realisable applications given the power budget (see Chapter 1): board-to-board communications, mobile phone transceivers, local oscillators, THz receivers, *etc*. Several key performance indicators for RTDs are presented below and discussed.

| Symbol | Meaning | Typical Unit |
|---|---|---|
| $J_{pk}$ | Peak current (density) | $MAcm^{-2} = 10\ mA\mu m^{-2}$ |
| $J_{val}$ | Valley current (density) | $MAcm^{-2} = 10\ mA\mu m^{-2}$ |
| $V_{pk}$ | Peak voltage | $V$ |
| $V_{val}$ | Valley voltage | $V$ |
| $V_{pk} - V_{val} = \Delta V$ | NDR region voltage | V |
| $E_1$ | 1st quasi-bound state level | $eV$ |
| $\Gamma_n$ | 1st Bound state (“resonance”) linewidth [172] | $eV$ |
| $J_{pk}/\Gamma_n$ | Peak current to resonant state linewidth[173] | $mA\mu m^{-2}/eV$ |
| $P_{NDR}$ | Extractable Pwr. $3/16(V_{pk} - V_{val})(J_{pk} - J_{val})$ | $\mu W\mu m^{-2}$ |
| $\frac{J_{pk}}{J_{val}} = PVCR$ | Peak to valley current ratio | — |
| $-G$ | Negative differential conductance | $mS$ |
| $f_{max}$ | Unity gain bandwidth | $Hz$ |
| $\frac{\Delta J}{C\Delta V} = G/C$ | Speed gradient- Schottky, TD… [19] | $mS/fF$ |
| $\sqrt{G}/C$ | Speed gradient – RTD [165] | $\sqrt{mS}/fF$ |
| $\frac{\delta^2 I}{\delta V^2}/2G^2 = \beta_0$ | Short circuit responsivity(Schottky)[22,174] | A/W |

**Table 3.1. List of RTD performance indicators and their corresponding measurement unit**

This is not an exhaustive list, and is likely to be updated with more specific metrics as the technology approaches maturity. The table is chiefly focused on the relative merits of an RTD device with respect to another, not at the system level where additional elements intervene, as shown in §2.3.1.

The analysis of the 3rd order polynomial of the idealised I-V response in Fig. 2.3.1a has shown the key contributors that influence the peak and valley points. But independently, these points do not paint the complete picture of the NDR/NDC $(G)$, the *raison d'être of* an RTD. In order to obtain a high absolute value of the NDC, it follows that $\Delta I$ requires maximisation, with a simultaneous minimisation of $\Delta V$, where the difference is given between the points of the peak and valley, where NDC exists. However, the role of $\Delta V$ is more complex than it may be apparent, as it is important for impedance matching to realise high quasi-optical power outputs (see §5.3, §5.4 for an example).

However, whilst $P_{NDR}$ contains the $\Delta I \Delta V$ product, individual parameters remain important. A high bias requirement given by a higher $V_{pk}$ is a main contributor to phase noise in receiver systems [22]. In emitters with thin barriers, the charge density may be sufficiently high to cause dielectric or avalanche breakdown, especially as this is a doping-dependent phenomenon.

The valley current $J_{val}$ is ideally 0 ($a_0 \to 0$ in §2.3.1), but the ideal blocking characteristic cannot be realised due to sources of quasi-bound resonance broadening: interface and alloy scattering [175], point and line defects in the crystal, as well as losses through indirect sub-band states [159].

The peak current $J_{pk}$ is an interesting, multi-faceted variable. On one hand, in Fig 2.3.1a one may notice how the 3rd order parabola influences both PDR and NDR regions. One the other hand, the NDR is also modified by the 2nd order term. Therefore, if one assumes that $a_0$ is a constant structural parameter, improvement of the peak-to-valley-current-ratio (PVCR) $J_{pk}/J_{val}$, is expected from a monotonic increase in $J_{pk}$. However, the PVCR has been attributed as an indirect measure of the transmission efficiency of the electrons throughout the structure [130,172]. Analogous to the internal quantum efficiency of a laser

diode and photodetector, this metric has different levels of importance in the case of an emitter or resonator vs. that of a receiver.

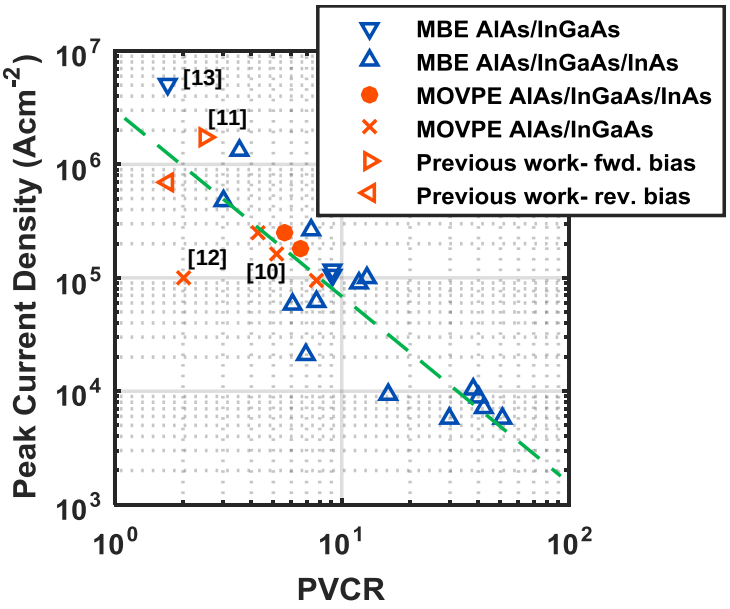


**Fig. 3.1a. Assessment criteria from Ref.** [176] **of fabricated RTDs, comparing epitaxial growth methods , updated after Sugiyama *et al.*** [93]**. Horizontal: measured peak to valley current ratio. An observed trend is marked with a dotted line.**

In Fig. 3, reproduced with updates after Sugiyama *et al.*[93], a visualization of data from the canon(over a span covering ~30 years of development) is achieved by plotting measured peak currents against the PVCR. Since the $J_{pk}$ has a roughly exponential dependence on the barrier thickness, the data is presented in log-log scale. An inverse linear trend over 3 decades of $J_{pk}$ is observed, with deviation being attributed to design variations and different layer/interface quality [93]. Previous assessment criteria [93] compare the PVCR against the $J_{pk}$ , with an increase in either PVCR and/or J (with no ill-effect to either) being highlighted as advantageous.

This figure plots *high current density* MOVPE-grown RTD devices [177,178] with 1.1 nm AlAs barriers. In contrast, the previous THz frequency emission record holder [179] contains a highly-strained QW with 0.9 nm AlAs barriers. Presented here are a variety of designs including MBE, MOVPE-grown devices accompanied by an intermediary QW containing an InAs region (sub-well) bounded by lattice-matched InGaAs to avoid the effects of alloy scattering [175] as much as possible. The accumulated stress in sub-well structures can be engineered to resemble the case of a purely ternary, high indium composition alloy. The data

points from from previous work [177] reflects the forward (intended) bias and reverse bias.

It is apparent that reaching a high $J_{pk}$ necessary to maximise the $\Delta J$ factor in the maximum extractable Power over the NDR region of the I-V ($P_{NDR}$) comes with the trade-off in reduction of the PVCR. If heat dissipation can be effectively managed, this may present itself as a turning point in the wall plug efficiency (DC-to-RF conversion efficiency) of an emitter. In the case of a receiver operating in conditions where the signal to noise ratio may be poor, is an important factor. Therefore the internal conversion process (field oscillation or photon to electron) gains significant importantance in achieving the resonance condition. Qualitatively, enhancing PVCR without a reduction in $J_{pk}$ and viceversa, has been highlighted as advantageous for an improvement in THz emission power [93]. In this regard, RTD DC-to-RF conversion efficiencies are reportedly poor, with a relatively recent case declaring 0.33% [180].

The author previously reported on a figure of merit that provides a measure of this conversion efficiency [176]:

$$IRE = \frac{3}{16}\frac{\Delta I \Delta V}{V \cdot I} = \frac{P_{NDR}}{P_{chip}}$$

This figure of merit, named *intrinsic resonant efficiency* (IRE) contains the ratio of two parameters: the time-averaged electrical chip power, $P_{chip}$, and the small signal power, $P_{NDR}$. The bias point is chosen as the mid-point of the NDR, where $\delta I^2/\delta V^2 \to 0$, as measurements have shown this to correspond to a peak THz emission [177,181] vs. bias. The extractable NDR power, a predictor of the THz power, was discussed in §2.3.1.

Figure 3.1b highlights the two power regions as rectangular areas toward the origin of a V-I characteristic of an RTD. The inset shows the conduction band edge potential (at the $\Gamma$ point) of the RTD active region. I remind the reader about the 'on-resonance' biasing condition where the injector energy level $E_F$ aligns with the QW quasi-bound $E_1$ level, allowing free flow of carriers. Three compositional parameters are highlighted, used extensively in the sensitivity and optimisation analysis in §3.3.

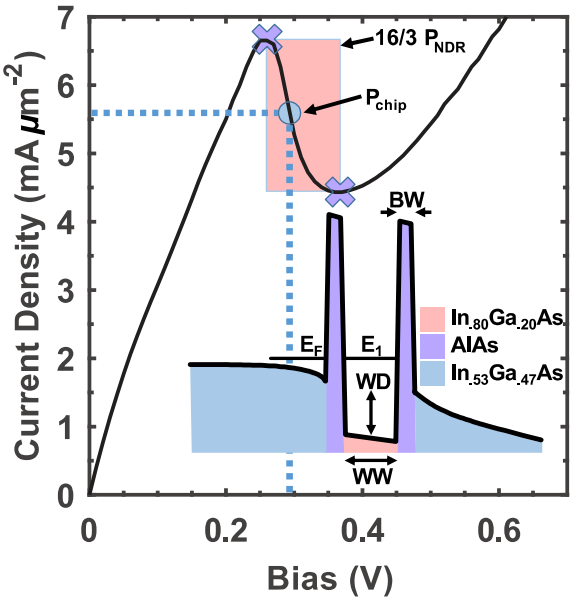


**Fig. 3.1b. Sample modelled RTD I-V characteristic shown with electrical chip power ($P_{chip}$ , mid-point of negative differential resistance) and extractable power ($P_{NDR}$). (inset) Approximation of the active-region conduction band potential under bias in the near-resonance condition, shown with the 1st quasi-bound state $E_1$. Highlighting parameters: well width (WW), well depth (WD), and barrier width (BW), used later in this work.**

Another suggested way to evaluate the performance of an RTD includes the speed gradient, inherited from related devices, such as IMPATT, and single-barrier tunnelling diodes [19]. However, Asada *et al.* [182] suggested that an approximate proportionality to $\sqrt{G}/C_0$, where $C_0$ is the static DC (geometric) capacitance of the epitaxial layer, is closer to representing the speed limitation of an RTD.

Finally, the 2nd order derivative of the current with respect to the applied voltage can be seen as an indication of the heterodyning performance of a receiver. The derivative is a part of the 2nd term of the Taylor expansion [174] of the quadratic approximation of the I-V of a conventional diode (*i.e.* Schottky or p-i-n). Therefore, the figure of merit for the efficacy in the positive differential region is [22,174]:

$$\psi = \frac{1}{2} \cdot \frac{\delta^2 I}{\delta V^2} \cdot \frac{\delta V}{\delta I} = \frac{1}{2G} \frac{\delta^2 I}{\delta V^2}$$

This is used as the short-circuit responsivity of a receiver in A/W. However, since $G$ is negative in the desired RTD region of operation, and the corresponding 2nd derivative may not necessarily be negative as well, this figure requires further consideration.

## 3.2. Model fit to a measured device

This section presents the steps taken to realise an adequate model of the RTD device.

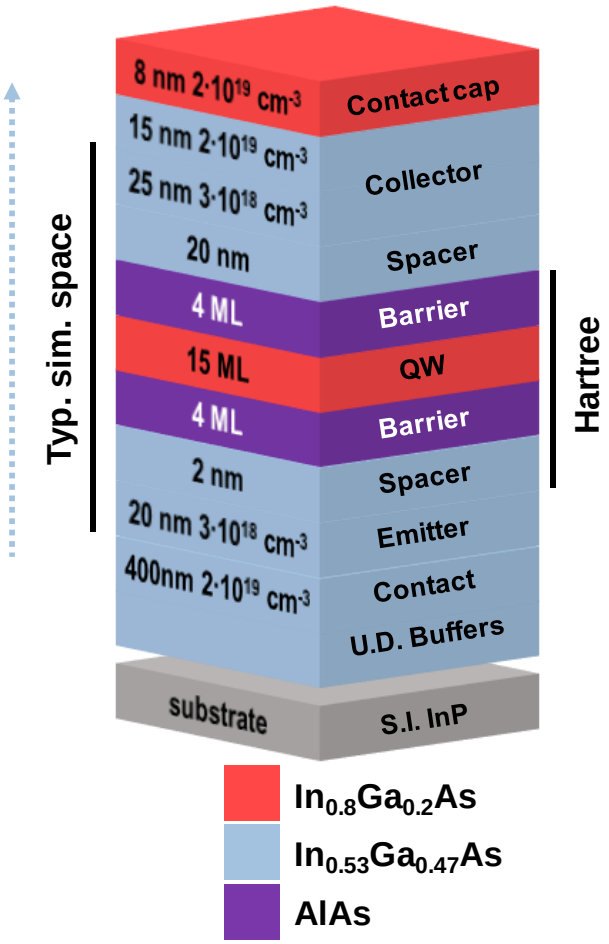


**Fig. 3.2. Reference RTD structure with Hartree potential-enabled region, and the typical simulation region shown. The dotted arrow represents the direction of the electron travel.**

Fig. 3.2. shows the RTD structure modelled after the smallest mesa area of $3.3\mu m^2$ from [177]. The Hartree modelling region, as indicated, is intentionally asymmetric (See §2.2.3.3). To save computational time, the simulation region is limited to include the sub-collector regions, doped to $3 \cdot 10^{18}$ carriers/cm$^3$. This comes at a minimal expense of accuracy (added series resistance neglected), otherwise the injector and collector regions are sufficiently wide to reach their respective charge distribution equilibrium states.

Unless explicitly indicated, the structure in the simulation space is modelled in §3.2 and §3.3.1, pending a sensitivity analysis to fit factors.

### 3.2.1. DC instability of an RTD

It is worth noting that practical devices, particularly those with a small cross-section, may oscillate in this region due to DC instability. This manifests itself as a current-average 'plateau' region under DC measurements [183]. Liénard oscillators are a type of chaotic oscillators, and are considerably difficult to stabilise in practice for accurate quasi-static measurements. Partial DC bias stabilisation methods were proposed [184–186], but the most common solutions for AC operation involve a parallel resistor [181,187] to achieve the optimum power transfer condition.

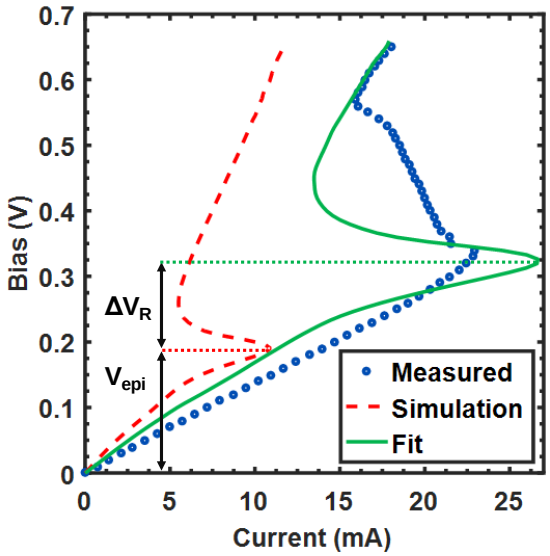


**Fig 3.2.1. Modelled and measured** [177] **V-I characteristics of the RTD. Fit achieved using mesa resistance determined from consecutive wet etch measurements.**

Fig. 3.2.1 plots the simulated I-V characteristic of the RTD active region. Since the simulator output is unidimensional, raw values are expressed in terms of current density, which is extrapolated to the mesa size (3.3 μm$^2$). A fit is produced that takes into account the $\Delta V_R$ added by the extrinsic circuit, which is compared with the fabricated device by Jacobs *et al.* [177]. A good fit to the NDR could be achieved only by modifying $\Gamma$ to a suitable value. The accuracy of the $E_1$ level prediction, and thus $V_{pk}$, was later verified using low temperature photoluminescence spectroscopy [188]. In order to transform the simulated curve to include the extrinsic circuit, a series (emitter & collector contacts) and parallel (contribution of sheet resistance, defect & oxidation-driven side leakage) resistor are added, resulting in an adequate fit. These values were deduced from sucessive wet etch and electrical measurement steps [177] (see

Chapter V). It is worth noting that the non-linear positive differential region is an artefact of the Hartree region selection (see Fig. 2.2.3.3b). However, an accurate fit to the NDR is more important in terms of predictions to device design, therefore some model instability can be traded-off in this case. Fig. 3.1b. has shown a model curve where the Positive DR does not depart from linearity.

There are two possible mechanisms that lead towards an observed hysteretic behaviour of fabricated RTDs: a) the split of the $E_1$ level into two distinct levels due to scattering and triangular potential present into the pre-barrier emitter region ($2D \rightarrow 2D$ tunnelling, 'fast')[150,189], b) bulk charge transfer at a given bias point due to an electrostatic feedback effect given by the charge depletion in the collector region immediately following the exit barrier ($3D \rightarrow 2D$, 'slow') [190,191]. A model of tristability was also proposed for an AlGaAs/GaAs double barrier system [192].

These effects may contribute to create current instability in the NDR region without an advanced stabilisation network. Consequently, the "true" valley current point may be hidden by this current oscillation, therefore, it is very important to take into account the highest slope of the NDR observed in a model when applying the IRE figure to a real device. The middle bias point for the IRE should be ideally taken on this slope, rather than the geometric centre of the $\Delta I \Delta V$ region, as it will form a more representative indication of the device performance.

## 3.2.2. Scattering

One of the factors that influence the outcome of the RTD modelling is the scattering parameter $\Gamma$. Chapter II highlighted the necessity and significance of this value, resulting in a (non-dominant) presence of incoherent tunnelling.

Fig 3.2.2a and b show the effect of this parameter upon the I-V characteristics and IRE, respectively. As expected of an increase in the frequency of incoherent tunnelling processes, a larger value reduces the PVCR drastically with a moderate increase in peak current. The relationship against IRE is exponential, a clear indication that in order to improve overall device performance, reducing

the causes that lead to carrier scattering is of prime importance. This may be realised practically by striving for epitaxial perfection, carefully managing the doping profile, and avoiding fabrication techniques which may introduce unwanted states into the crystal lattice [193]. The +1dB peak seen in Fig.3.2.2a around 0.28 V is an after-effect of charge interaction due to the asymmetric Hartree region selection (see Fig. 2.2.3.3b), and is not likely to be an observable effect in a real device. For the same reason, the positive differential resistance (<0.1 V) departs from a straight line and appears bowed.

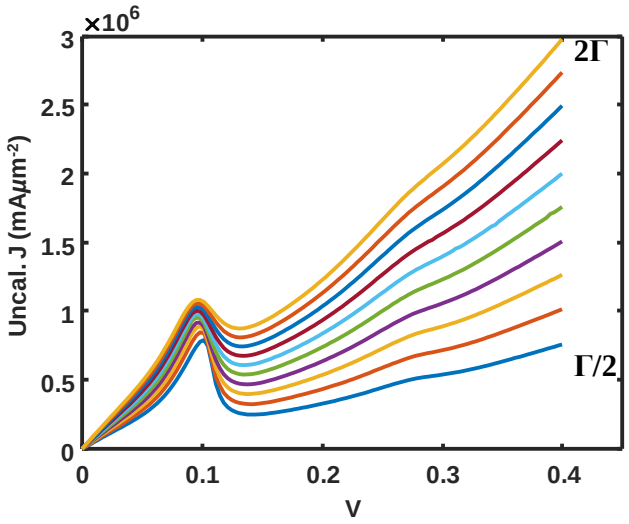


**Fig. 3.2.2a. The variation of modelled I-V characteristics using different values for an empirically chosen scattering parameter Γ, shown between $\frac{\Gamma}{2}$ and 2Γ**

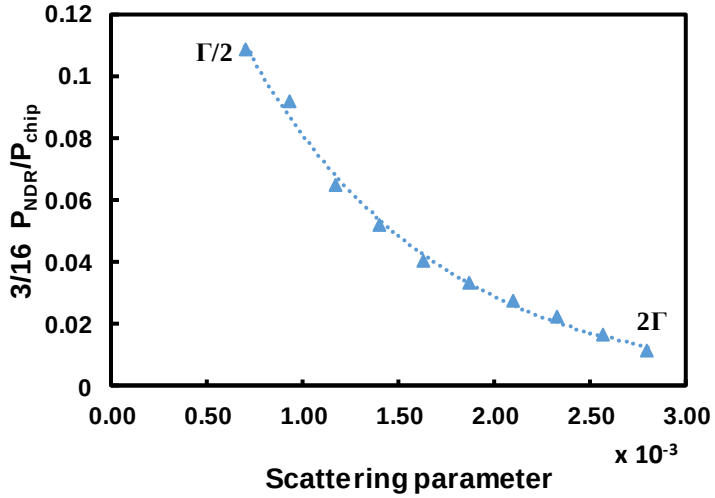


**Fig. 3.2.2b. The variation of the IRE obtained from Fig. 3.2.2a, with different values of Γ**

### 3.2.3. Contact doping

Increasing the donor concentration reduces the resistance of the contact. As the number of electrons that can participate in conduction is increased, $J_{pk}$ is expected to increase.

Fig. 3.2.3 models this change between 25% and 200% of the reference structure. For this simulation, the full structure was modelled. It appears that there may be a point of diminishing return in the increases of $J_{pk}$ and reduction of $V_{pk}$ with increasing doping density. A caveat of the quantitative agreement is represented by the lack of changing the scattering parameter. Increased doping alters the distribution of the ionic centres throughout the crystal structure. Therefore, the reduction of PVCR may be worse than simulated. However, this effect was not observed.

The *conventional* wisdom for fabricating TD & RTDs is to push the degenerated doping to the maximum level the system tolerates, the limit given by efficiency of the solid diffusivity of the species of the dopant used, growth temperature, and activation energy of the doping process, as well as free carrier absorption (see Chapter V).

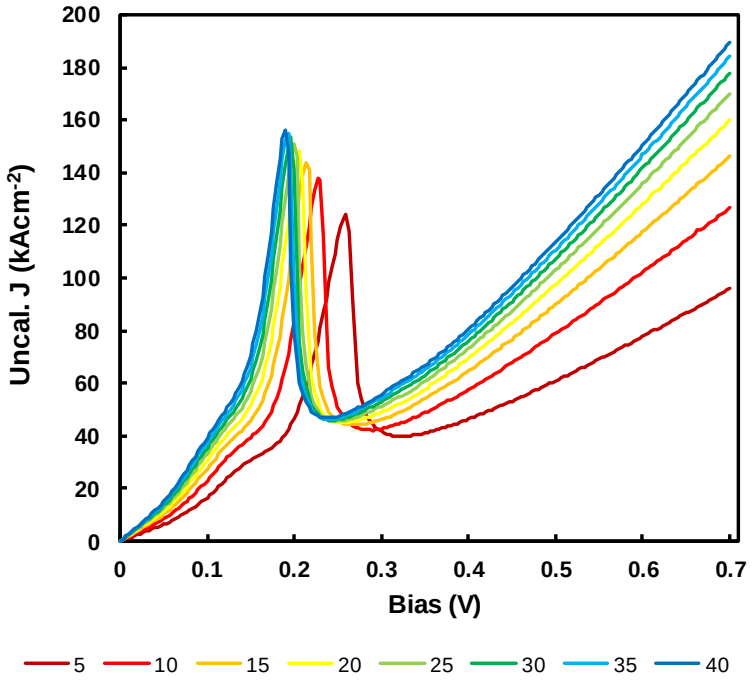


**Fig. 3.2.3. Uncalibrated modelled I-V characteristics varying the doping density in the collector and emitter layers simultaneously.**

Specifically, in an MOVPE two common dopant gas options include *silane* ($SiH_4$) and *disilane* ($Si_2H_6$). Sciana *et al.* [194] achieved $2.8 \times 10^{20}$ carriers/cm$^3$ in QCL structures (also a unipolar device) using 200ppm silane at 645°$C$, which may not be possible to do with disilane under the same conditions due to premature Si-Si bond cracking. However, this came at the expense of noticeably worse crystal quality. Another report by Singh *et al.* [30] details growth conditions similar to our own, on an Aixtron 200 reactor with disilane at 630°$C$ achieving $1 \times 10^{19}$ carriers/cm^3 with good crystal quality.

A more unorthodox way to achieve high doping is to employ Group 16 atom species, such as Te, in "sheets" yielding an excess of $5 \times 10^{19}$ carriers/cm$^3$ [195].

### 3.2.4. Effective mass

A lower effective mass $m^*$ translates into a decrease in the available density of states within the QW, resulting in a lower $J_{pk}$. This is a necessary investigative step before more complex band gap engineering is attempted.

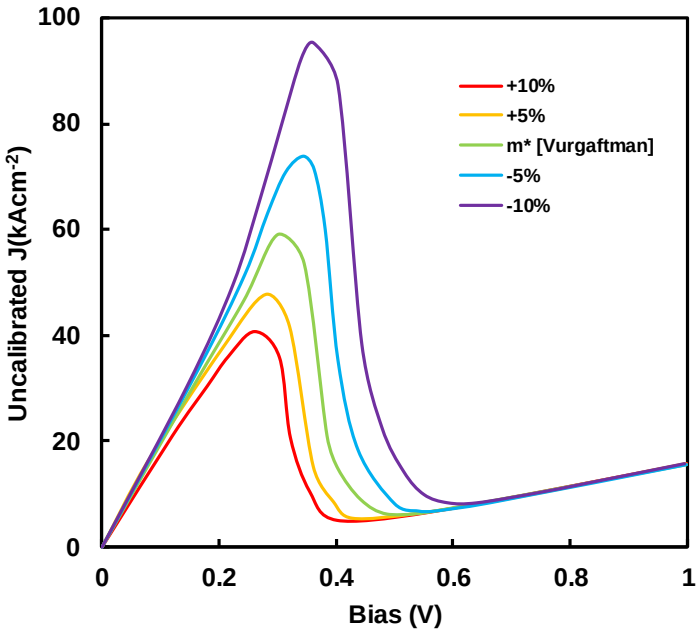


| material | $m_e^*$ |
|---|---|
| InAs | 0.026 |
| GaAs | 0.067 |
| InP | 0.075 |
| AlAs | 0.15 |
| GaSb | 0.039 |
| InSb | 0.0135 |
| AlSb | 0.14 |
| GaN(zb) | 0.15 |
| AlN(zb) | 0.25 |
| InN(zb) | 0.12 |

**Fig 3.2.4 Uncalibrated modelled I-V characteristics varying the electron effective mass ($m_e^*$) material parameter *vs.* Vurgaftman *et al.* [108]. Presented with a reference table.**

In Fig. 3.2.4 it is observed that a modest variation of -5% of $m^*$ alters $J_{pk}$ by +18% and shifts $V_{pk}$ by 50mV. This effect is important in correctly interpreting the changes brought by the ternary $In_xGa_{1-x}As$ alloy inside the QW. This suggests

that a move towards the antimonide-based system could be an advantage if epitaxial perfection is realised. Indeed, the record frequency for such an RTD [196] was held for over a decade until integrated microfabricated resonators in the current system were realised [197].

### 3.2.5. Barrier asymmetry

Realising perfectly symmetrical barriers may not be easily achievable in the context of highly-strained epitaxy, particularly as the barriers in questions are 4 ML (1.172 nm lattice-matched to InP) thin. Therefore it is important to consider the sensitivity of the structure to these fluctuations.

Broekaert & Fonstad [198] have shown that there is a trade-off between $J_{pk}$ and PVCR when modifying the barrier width, verified experimentally at Manchester University with MBE-grown RTDs [199]. Capasso *et al.* [200] also show a strong non-linear influence of the exit-barrier thickness (collector) on the $J_{pk}$, hence optimisation is possible. This has been physically attempted in the past with comparatively thick barriers (2nm+). [158]

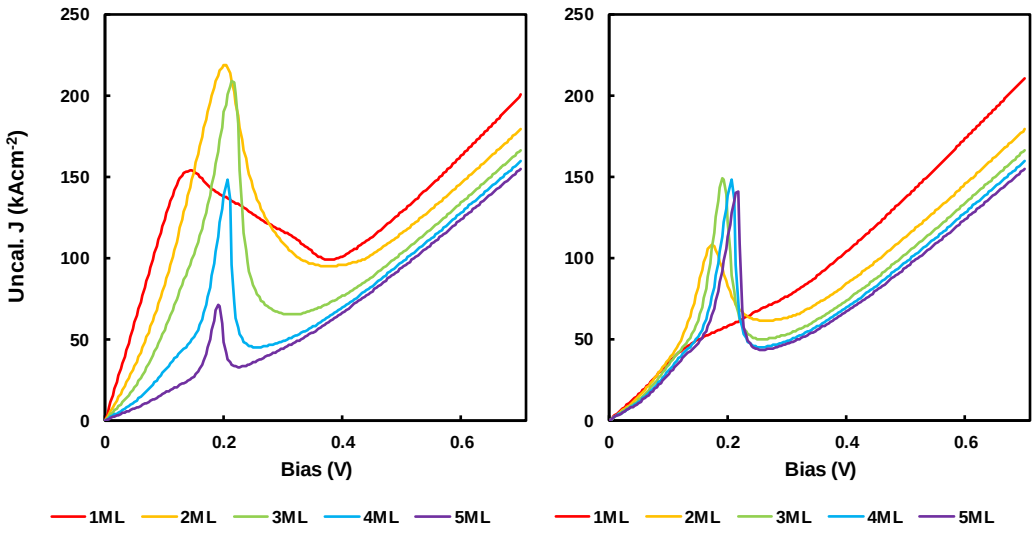


**Fig. 3.2.4. Uncalibrated modelled I-V characteristics varying the thickness of the entry (left) and exit (right) barriers, with sizes quoted in monolayers**

Fig. 3.2.4 presents a comparison between an alteration of the entry barrier, and that of the exit barrier, with alterations as marked. In both cases, the shape of the I-V characteristic is vastly different for the 1 ML barrier compared to other sizes. There are several reasons for this, but it can mostly be attributed to the discontinuity in the charge distribution caused by the presence of a single point

with the barrier potential. An expected effect however is correctly predicted, with the loss of confinement lowering the energy level (hence, biasing requirement). In practice, it may be difficult to reliably create a 1 ML barrier with any known growth method. Carriers may pinhole through lower potential regions cause by local absence of Al atoms, causing early device failure.

The change is disproportionate comparing the entry with the exit barrier. From TEM characterisation of the device in Ref. [177], we have seen that the unusually high forward (for the given structure) current of 17 $\mu A \cdot mm^2$ in the intended forward bias is attributable to a 2ML thin entry barrier. Fluctuations in the exit barrier therefore lead to less statistical variance of the $J_{pk}$ and $V_{pk}$ than the comparative entry barrier case.

However, in either cases, creating an asymmetric barrier profile is analogous to reducing the finesse factor in a Fabry-Pérot (optical) interferometer, and it is recommended to avoid this practice for maximum resonator stability, if possible.

## 3.3. Intrinsic Resonant Efficiency optimisation

### 3.3.1. InGaAs QW

The investigation proceeds with a design sensitivity analysis, by varying 3 key parameters of the RTD: the barrier width, QW width, and QW depth. Firstly, this data is presented without the concern of lattice misfit strain.

The strain is then modelled and the IRE is plotted against the $J_{pk}$—PVCR canon trend, and I comment on how this may provide an alternative optimisation strategy to the current practice. These steps are repeated in §3.3.2, albeit with a different QW structure.

Then we will look at the individual contribution of the unintentionally doped spacer layers next to the AlAs/QW/AlAs structure. Finally, the modelling results of further improvements are discussed.

### 3.3.1.1. Optimization of barrier, QW, Indium

Starting with the sensitivity analysis, Fig. 3.3.1.1. plots the IRE for the reference structure (Fig. 3.2.) varying a single parameter at one time, and its associated transmission probability for: (a & d) the AlAs barrier width, (b & e) the QW width in ML, and (c & f) the QW indium composition [201,202]. The $E_1$ quasi-bound energy level (the first transmission peak of the lower graphs) is overlaid in green to show the relative change with a variation in these structural parameters. The same vertical scales are used for ease of comparison.

Reducing the barrier width (Fig. 3.3.1.1a) from the initial value of 4ML is observed to result in an exponential increase in $J_{peak}$. This also comes at the expense of PVCR, attributed to the reduced dwell time [203], in line with previous work [93]. The increase in IRE may also in part be due to a decrease in NDR which results in a reduced $P_{chip}$ with essentially identical $P_{NDR}$. However, one may note that a maximum IRE figure is obtained with 2ML barriers. A strong increase in non-resonant tunnelling current occurs for 1ML barriers which reduces IRE and renders the NDR region non-observable for well widths below 13ML. The broadening of the resonance linewidth is also notable (Fig. 3.3.1.1d), accentuated by thinner barriers.

Initially, increasing the QW width (WW = 9 .. 13 ML) (Fig. 3.3.1.1b) results in a monotonic increase in IRE, attributed to bringing the 1$^{st}$ quasi-bound resonant level closer to the conduction band potential, at the expense of an increased carrier dwell time [203]. The reduction in IRE by further increasing the QW width (>13ML) occurs as the broadened resonance linewidth begins to fall below the Fermi energy level where the optimal bias point would lie, therefore the resonance energy becomes misaligned with respect to the emitter states. The modified reference structure with 4MLs barrier and $In_{0.8}Ga_{0.2}As$ QW has a maximal IRE with a 13ML QW. A cause of concern with wider QW is shown in Fig. 3.3.1.1e, is brought by the drop in the 2$^{nd}$ resonance level. It is conceivable this may align with indirect bandgap states to result in an increase in phonon-activated non-resonant tunnelling, however, the dominating mode of tunnelling remains through the $\Gamma$ point of the gap [143].

Increasing the well depth is achieved by altering the indium composition in the InGaAs alloy (Fig. 3.3.1.1c). This has a two-fold effect: a higher indium composition decreases the band gap, but the lowered effective mass translates into a decrease in the available density of states within the QW, resulting in a lower $J_{peak}$. It may appear as a trade-off between $J_{peak}$ and PVCR, however, the simulations predict that a higher indium fraction will reduce the linewidth of the resonant state, resulting in a higher Q-factor of the resonance. Additionally, the resulting reduction of the operational bias, a probable source of phase noise in voltage controlled-oscillators, makes a desirable emitter. Fig. 3.3.1.1f shows an opposing trend of the 2nd linewidth resonance compared to the QW shift; at first sight, increasing the mole fraction towards binary InAs appears to have no downsides. To summarize thus far, the ideal RTD would have a combination of 2 ML barrier pairs between an InAs QW, with possible local optima for the WW.

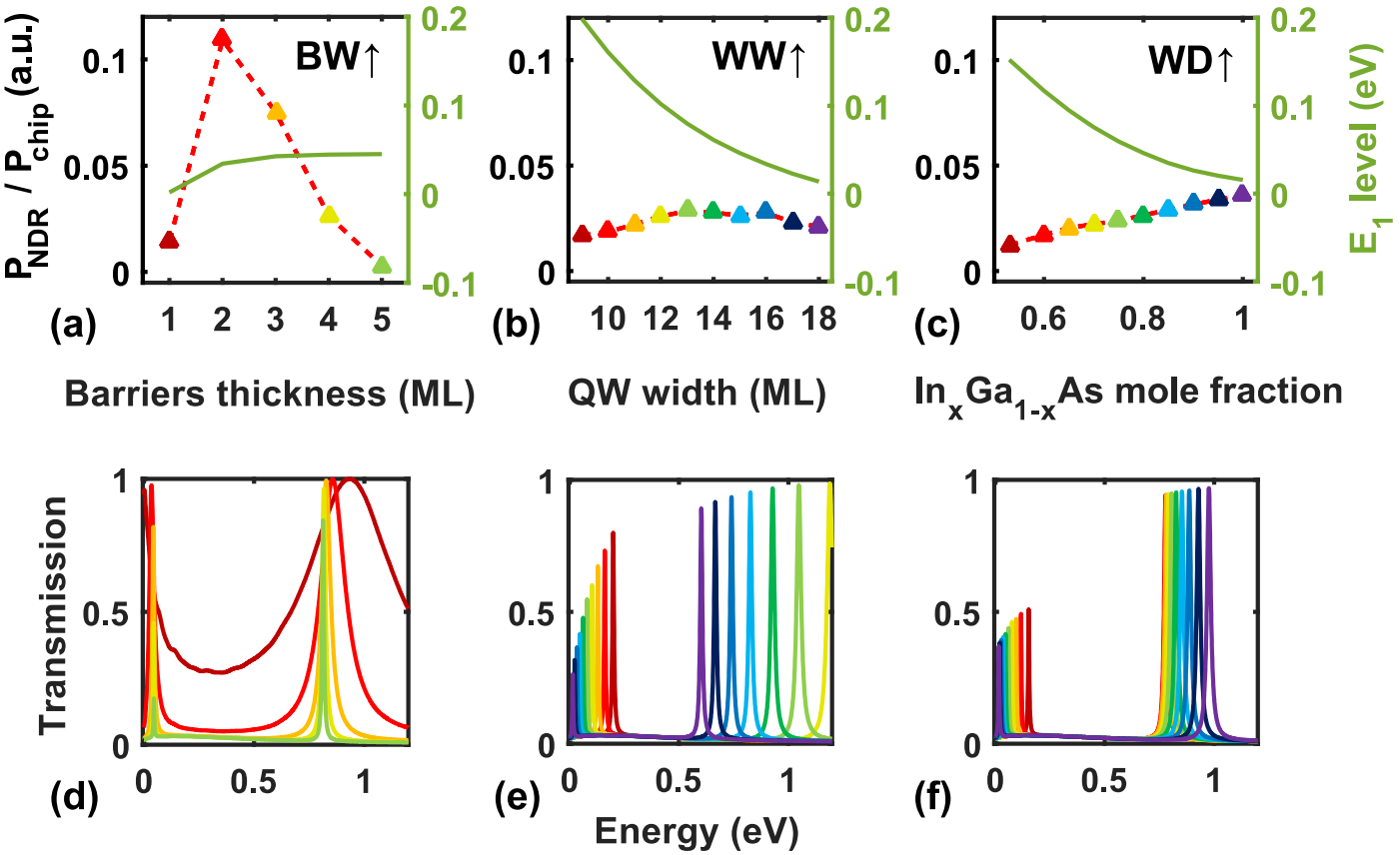


**Fig. 3.3.1.1. Modelled intrinsic resonator efficiency figure of merit for individual changes to the reference structure, (a) the width of the barriers in monolayers, (b) the QW width in monolayers (c) varying the depth of the QW through the composition of the ternary. (d), (e), (f) are their corresponding energy transmission results (at 0V bias), with peaks representing the quasi-bound levels. The overlaid line in (a), (b), (c) shows the shift in the 1st quasi-bound state. The dotted line is a guide for the eye.**

Fig. 3.3.1.1g. plots the IRE as a function of well width and indium composition for an RTD design (a) 1ML AlAs barriers, (b) 2ML AlAs barriers, (c) 3ML AlAs

barriers, and (d) 4ML AlAs barriers. The colour coding of the stress balancing regions in §3.2.4 is preserved for structures which satisfy the requirements for lattice misfit dislocation formation. Once more, the variation of barrier thickness is shown to have the main effect upon IRE. From the analysis of this graph, an optimal device structure is suggested (*point B*, IRE = 0.158) with 2MLs barriers, 17ML QW and a QW alloy of $In_{0.75}Ga_{0.25}As$, a perhaps counter-intuitive result based on current literature where barrier thickness tends to be kept constant, and the push is for deeper and narrower QWs [93,204,205]. The reduction in IRE seen with certain combinations of well width & depth is attributed to the drop of the resonant state below the injection energy level. Further improvement of this figure may be achieved by reducing the carrier scattering within the structure, either by improving epitaxial processes or designs (discussed in the following section), or by reducing the operating device temperature [159]. An alternative material system with greater conduction band energy offsets may also enhance this figure.

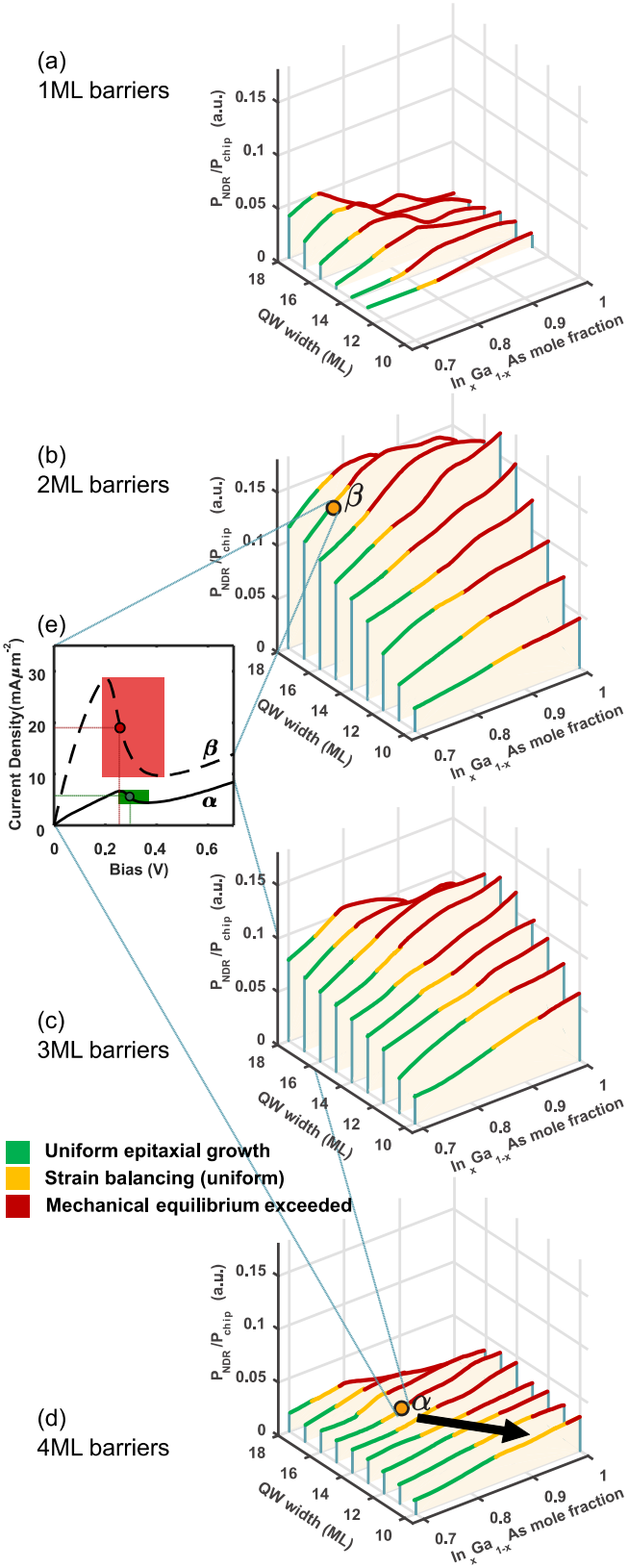


**Fig. 3.3.1.1g. Isometric graphic of the intrinsic resonator efficiency for the uncalibrated (a) 1ML (b) 2ML (c) 3ML (d) 4ML barrier structures as a function of QW width and indium composition (in plane). Colour coding to match the stress scheme in Fig. 7. The arrow in graph (d) shows present growth trends of employing narrower, higher indium mole fraction QW. (e) The proposed optimum I-V characteristic is shown side-by-side with the reference device. Updated after** [201,202]**.**

The simulated I-V of the optimized structure is plotted in Fig. 3.3.1.1g-(e), along with the reference structure[177]. Not only is the PVCR and $J_{peak}$ higher, but it

also exhibits lower biasing requirements compared to the reference design (identified by *point a*). Noting again that this structure is not strain balanced, but designed to be compressively strained to the maximum acceptable limit based on the adjusted projection of the M&B model, in order to avoid the onset of the generation of misfit dislocations. These findings must acknowledge the new demand imposed on the epitaxial process in realizing high performance THz emitters. Not only are highly uniform thin layers required (e.g. 2ML AlAs barriers), but the limits of strain relaxation must be pushed in order to maximize efficiency of these THz light sources.

In Fig. 3.3.1.1h $J_{pk}$ is plotted as a function of PVCR for the 3ML and 2 ML barrier devices from Fig. 8 (c) and (d), respectively. These are the previous metrics established by Sugiyama *et al.*[93]. The coloured lines denote identical mole fractions, whereas the markers denote identical WW. It is noted that the scatter from the line of best-fit in Fig 3 is ~factor 10 in J and ~factor 4 in PVCR, and the axis limits are significantly smaller in Fig. 3.3.1.1f than in Fig. 3.1a. Furthermore, the data in Fig. 3.1a contains a sub-set of designs, with varying epitaxial processes, of which a subset will be reported due to self-selection by the authors and the selectivity of the peer review process. Therefore, the data in Fig. 3.3.1.1h is not considered in disagreement with the canon.

The dotted line is the trend line as seen in Fig. 3.1a. The difference in the distribution of 4ML and 2 ML devices is worth noting. In the sensitivity analysis it is predicted that a higher indium mole fraction would improve the device performance, whereas this statement is not true for deep QW with long WW. The point of inflection seen in the 2 ML case illustrates the combinations of QW widths and depths that result in $E_1$ levels which fall under the $E_F$ when the required bias is applied, resulting in sub-optimal performance. This does not occur for the parameters discussed in the 4ML case. Unfortunately, this visualization (Fig. 3.3.1.1h –(b)) does not necessarily highlight the difficulties associated with uniform growth of thin barriers. For instance, the placement of the starting and optimized devices (*α* and *β*, respectively), suggest that there may be significant room for improvement in both cases, even if both are approaching the limits of pseudomorphic growth. Furthermore, *these criteria fail to account for changes in the slope of the NDR*, an otherwise critical

parameter for optimum power transfer of the resonator to the rest of the system. This unique combination of parameters, as well as the uncertainty in $\Gamma$, leads to the difference in my recommendation of having the widest, deepest QW possible within the limit of the accumulated stress and desired resonator frequency, given the current parameter set.

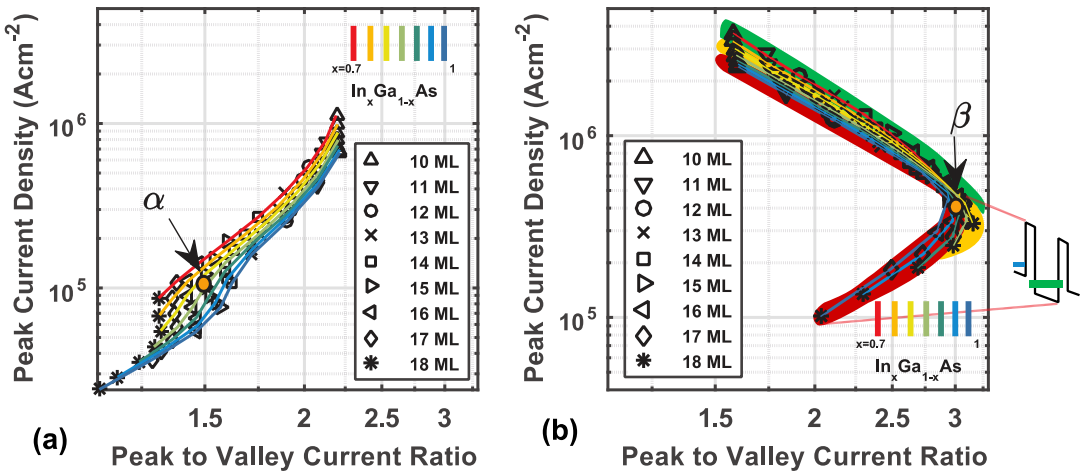


**Fig. 3.3.1.1h. Modelled device properties as a function of the assessment criteria from Fig. 3 using (a) 4 ML (b) 2 ML AlAs barriers. In plot (a), point α is the reference device ($In_{0.8}Ga_{0.2}As$, 15 ML QW) with 4 ML symmetric barriers. In plot (b), point β is the proposed growth optimization for 2 ML symmetric barriers, $In_{0.75}Ga_{0.25}As$, 17 ML QW. Colour regions follow the stress scheme from Fig. 7. In both cases, the dotted green line is the same trend from Fig. 3. The turning point in plot (b) is represented by combinations of well widths and depths where the resonance level falls below the injector layer under optimal bias conditions.**

### 3.3.1.2. Optimization of spacers

The previous section has so far discussed the impact of the 3 geometric parameters on the device conversion efficiency. I have shown how the conventional assessment criteria are insufficient to predict application performance.

The frequency response of an RTD is important for al THz applications, whether oscillators, amplifiers, detectors, or bistable elements. In §2.3.2 a first-order approximation of $f_{max}$ was given. However, the maximum oscillation of the RTD device excluding the in-series impedance is shown to be significantly higher [206]. In further attempts, it was shown [22,205,207] that both the real part of the conductance and $f_{max}$ are dependent on a leverage factor $\frac{d}{d+l}$, where d is the emitter-to-QW and l is the emitter-to-collector distance. It would appear therefore that the longest collector to emitter ratio would be advantageous, though a particularly long collector will increase the responsivity time, which

dominates in the NDR region [207]. Notably, in §2.3.3, an explanation for the non-linear C-V characteristics was offered, based on Shimizu *et al.* [21].

The existence of the undoped (UD) spacer regions may be seen as a necessary evil: the carrier depleted regions have naturally decreased conductivity, which would act as a series resistance to the device, therefore lowering the $J_{pk}$. However, a thicker region may prevent the (comparatively) high-energy ion implants from reaching the sensitive active region, where the creation of a trap level may result in loss of resonance efficiency. In the reference structure, this thicker region is at the top, and intended to act as the collector.

The bottom UD spacer, is intended to act as the entry, or emitter-side spacer, which is why it is only 2 nm (~6 ML) thin. Ideally, there should be no need for an entry spacer, as this will create a higher local potential region w.r.t. the Fermi sea. However, for the reasons of epitaxial optimisation and stability of the AlAs/InGaAs interface, this small UD region was opted. These findings were performed in our group through epitaxial optimisation in 2011 at the University of Sheffield (unpublished). The model below will corroborate these as suitable values for an RTD in the intended application.

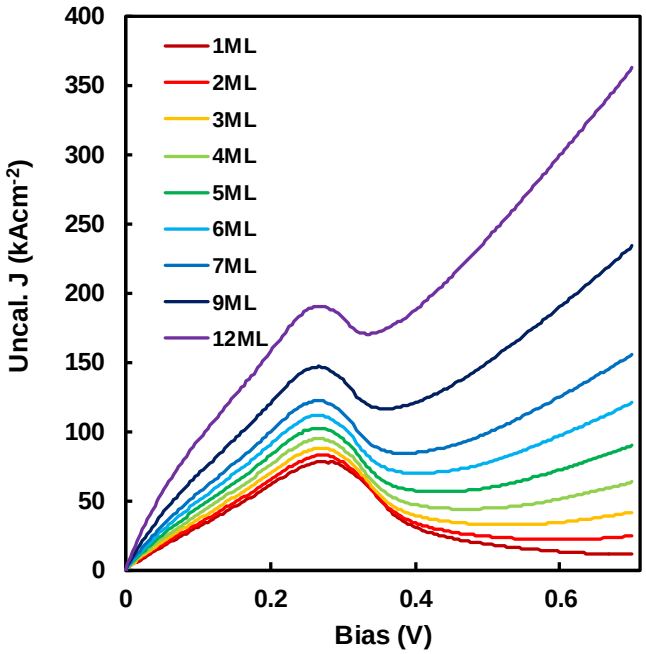


**Fig. 3.3.1.2a Modelled, uncalibrated I-V characteristics presented against the change of UD entry spacer thickness, in monolayers.**

In Fig. 3.3.1.2a, the effect of the changes to the thin entry spacer is shown. It is immediately apparent that the $V_{pk}$ does not shift, however, the $J_{pk}$ (seen in Fig

3.3.1.2b) counterintuitively increases with a longer emitter region. Every monolayer of undoped material here adds to the length of the triangular-well potential under bias, therefore allowing the opportunity for more carriers to couple into the leaky $E_1$ confined states.

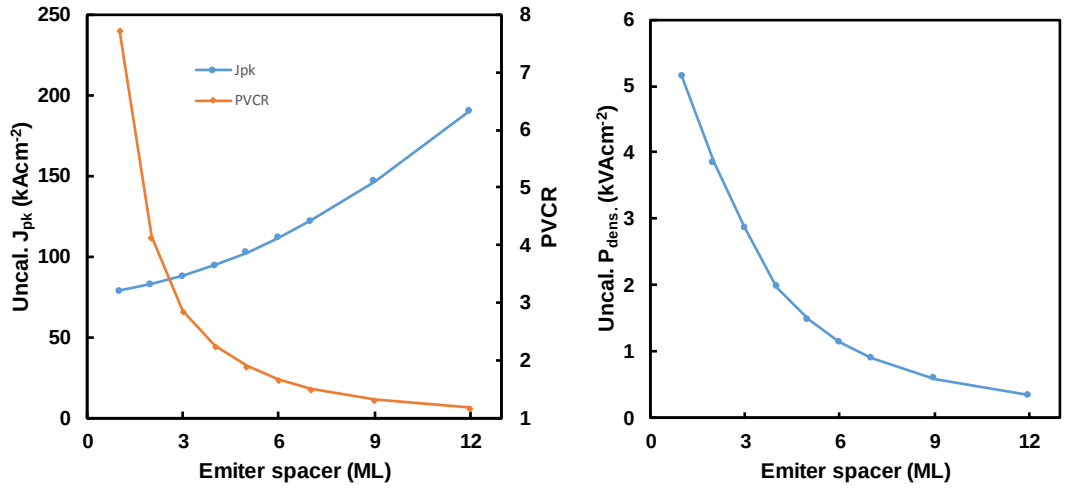


**Fig. 3.3.1.2b Graphics showing the change of the uncalibrated PVCR, $J_{pk}$ (left), and extractable $P_{NDR}$ (right) with varying UD entry spacer thickness, from the plots in Fig. 3.3.1.2.a.**

This comes at the expense of an overall reduction in $PVCR$ and the maximum extractable $P_{NDR}$. In turn, the expectation that the entry region must be kept as thin as possible is confirmed, limited by the stability of the growth conditions rather than carrier transport.

The width of the collector region is perhaps more directly relevant to the $f_{max}$ as it will have a direct bearing on the dynamic capacitance. A wider collector spacer creates a lengthier depletion region as well. Not only does this limit the maximum possible current, as there are less states available to donate towards the conduction band edge, but it may also give a chance for the escaped carriers to reach the equilibrium region without interacting with the double barrier tunnelling system, possibly causing additional parasitic oscillation.

Fig. 3.3.1.2.c plots the changes in I-V characteristics with suitable alterations to the collector spacer. It is immediately apparent that the changes do not influence $J_{pk}$ or the PVCR considerably, although the slope of the NDR is progressively wider with increased sizes.

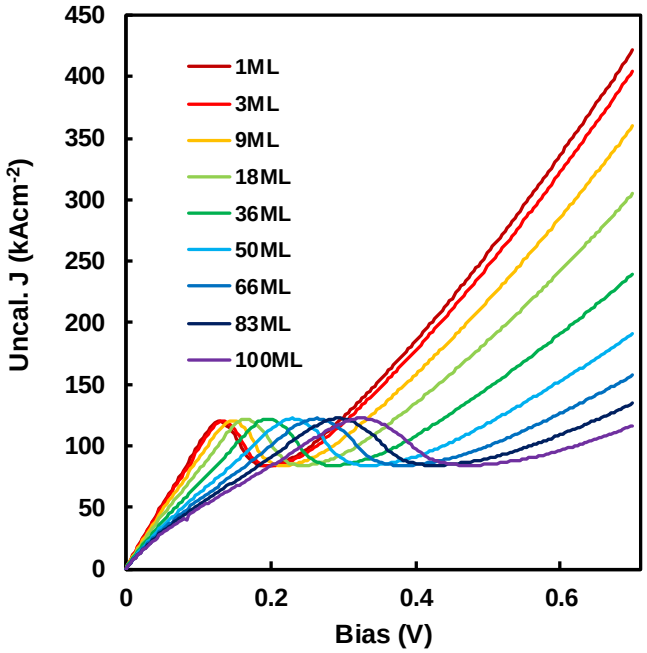


**Fig. 3.3.1.2c Modelled, uncalibrated I-V characteristics presented against the change of UD exit spacer thickness, in monolayers.**

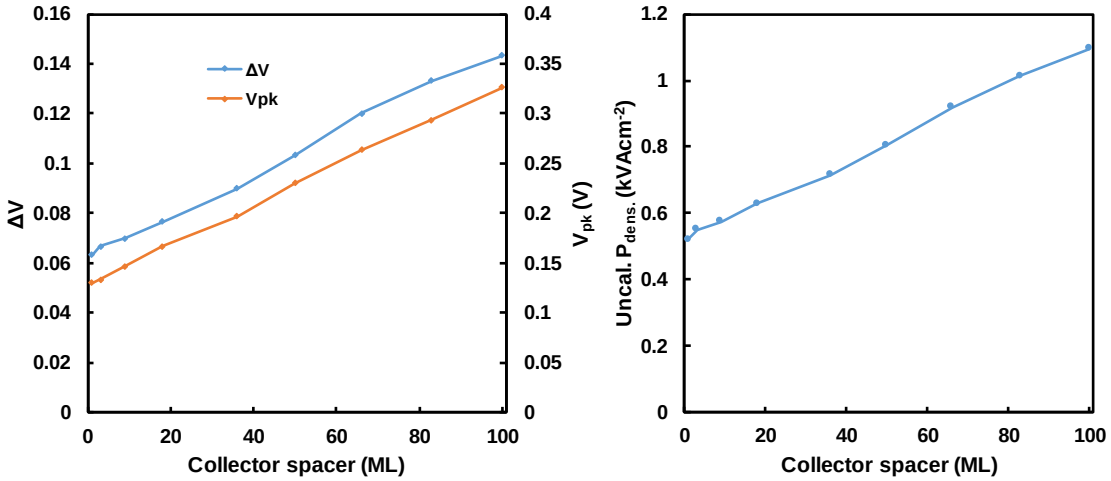


**Fig. 3.3.1.2d Graphics showing the change of the uncalibrated $V_{pk}$, $\Delta V$(left), and extractable $P_{NDR}$ (right) with varying UD exit spacer thickness, from the plots in Fig. 3.3.1.2.a.**

Fig 3.3.1.2d shows a remarkable linear dependency on $V_{pk}$ with the spacer width. We have previously established that a higher biasing requirement is generally best avoided for high-J devices. The reason that the extractable $P_{NDR}$ also increases can be traced to the respective increase in $\Delta V$. However, these findings have not been confirmed experimentally. It is important to note that devices with a collector region of 25 nm (~83 ML) has been grown to demonstrate 550 GHz emission [204]. The thinner, previous-record-breaker at 1.92THz was held at 12 nm (~41 ML) [208], whereas a first attempt to reach 353 GHz [181] in the first window of transmission used the reference structure (~68 ML).

### 3.3.1.3. Graded emitter

In the attempt to create InGaAs/AlAs on InP RTD resonators above the 1THz, Asada *et al.* found that such RTD structures would suffer from diminished power output due to the non-linearity of the NDR resulting in reduced electron velocity in the collector depletion region vs. expectation. This has been attributed to transition loss through $\Gamma - L$ states [195,209], a phonon interaction that may happen in the presence of the higher electric field RTDs are subjected to.

In order to mediate the low electron velocity in the depletion region, 2 strategies exist: the direct approach of $\delta$ —doping [210](*i.e.* degenerate doping in a "sheet", typically using a group 16 ion such as tellurium —Te) in the depletion area, or the indirect approach to increase the energy of the launched electrons into the active region, by raising the conduction band potential through the means of adjusting the ternary material [209]. The $\delta$ —doping method proved to store too much charge for the operational requirements at 1 THz, effectively behaving as a series capacitance with the RTD active region [195].

Though counterintuitive in its possible undermining of the efficacy of the $2D \rightarrow 2D$ tunnelling process, employing a stepped emitter was the first successful attempt to create a RTD resonator with a primary oscillation at 1.04 THz, and this approach has been carried forward to attain the current frequency record of 1.98 THz [211] at the time of writing. The difference however, was that steps of $In_xGa_{1-x}As$ with a total 4% grading of the mole fraction x were altered to the $Al_xIn_{1-x}As$ material system due to the more suitable $\Gamma - L$ band offsets.

Modelling of this InGaAs grading is presented in Fig. 3.3.1.3a. The difference to the "step" approach suggested by the paper is that I suggest performing a linear grading of the $In_xGa_{1-x}As$ alloy, an approach which would simply involve linearly adjusting the gas flows (trimethylindium & triethylgallium for instance) of the corresponding atom species. Overshooting or undershooting the start and stop targets would have an effect of changing the overall indium content by mass, though the suggested changes may be sufficiently small as to not necessitate a supplementary calibration step before the epitaxial growth run.

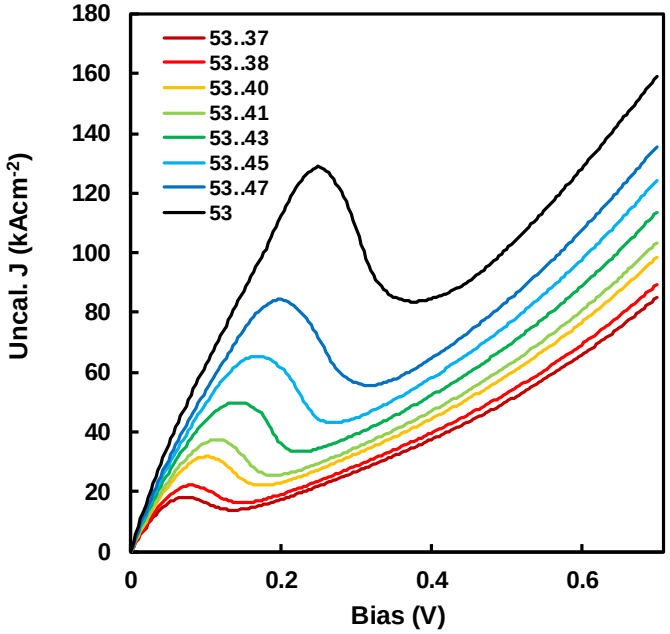


**Fig. 3.3.1.3a Modelled, uncalibrated I-V characteristics presented for devices with a linear-graded ternary $In_xGa_{1-x}As$ lower emitter & spacer region of Fig.3.2. The legend shows the start point of mole fraction x (%) to the end point, before the entry AlAs barrier. Black line (x=53%) is the reference structure.**

The gradient is always sloped such that the region incorporating less indium is affixed to the entry AlAs barrier, to achieve the desired effect of raising the conduction band potential under bias. An example conduction band profile is later shown in Fig 3.3.1.4d.

The figure successfully predicts a reduction of the peak voltage with an increase in the mole fraction gradient compared to the literature[210] . However, if the collector loss is indeed related to the $\Gamma - L$ transition, in this case, a multiple sub-band model is required to accurately describe the problem, and with expectedly different values of the scattering parameter for each case.

In this case, the model could not predict the increase in PVCR with a graded emitter. The local increase in the 6% gradient could not be decoupled from a convenient coincidence of numerical errors. However, it does appear that a point of diminishing returns exists.

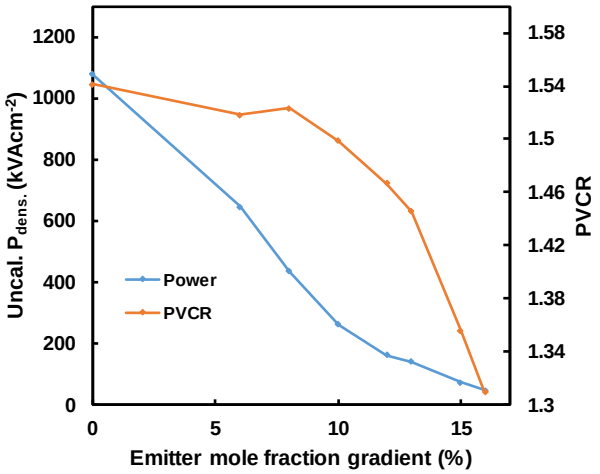


**Fig. 3.3.1.3b Uncalibrated extractable power density ($P_{NDR}$) and PVCR with respect to the change in the InGaAs mole fraction linear of the emitter and spacer region, from Fig. 3.3.1.3a.**

The extractable $P_{NDR}$ seen in Fig. 3.3.1.3b also appears to drop with an increase in gradient due to a decrease in $\Delta V$. Whether this is a sensible trade-off of $f_{max}$ with $P_{NDR}$ or a result of the limitations of the model is a matter subject to further practical investigation. In any case, for RTDs intended for atmospheric transmission windows up to ~500GHz should be able to attain the $f_{max}$ requirement simply by altering the thickness of the collector region.

Advantages of InGaAs graded emitter:

- Less additional epitaxial calibration
- No Al atom species to affect local barrier thickness
- Less cumulative epitaxial stress in the region near the barrier

Advantages of AlInAs step emitter:

- No complication in optical structural characterisation methods. Due to different band profile alignment, it can be engineered to not interfere with other optical transitions.
- Potentially simpler growth recipe, allowing the use of a wider variety of epitaxial fabrication equipment.
- May be the technology of choice to reach ~2 THz primary oscillation due to the larger $\Gamma - L$ separation of AlAs & InAs vs. GaAs and AlAs.

### 3.3.1.4. Graded QW

Under applied bias, a typical QW will have the conduction band edge potential tilted, to form a more triangular than a rectangular well. This would mean that the cavity would have different resonance modes across its length, or in other words, it will result in a broadening of the confinement levels [130].

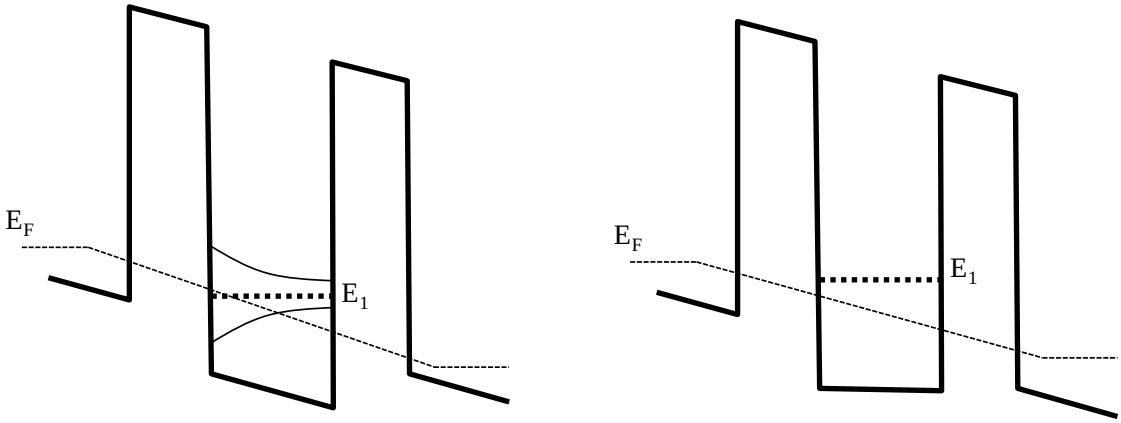


**Fig. 3.3.1.4a. Schematic representation of states in a triangular well(left) and graded well (right)**

Echoing the changes to the emitter in the previous section, it is possible to correct this triangular potential by intentionally grading the $In_xGa_{1-x}As$ mole fraction inside the well, such that the conduction band edge rate of change across the structure is zero at a specified bias.

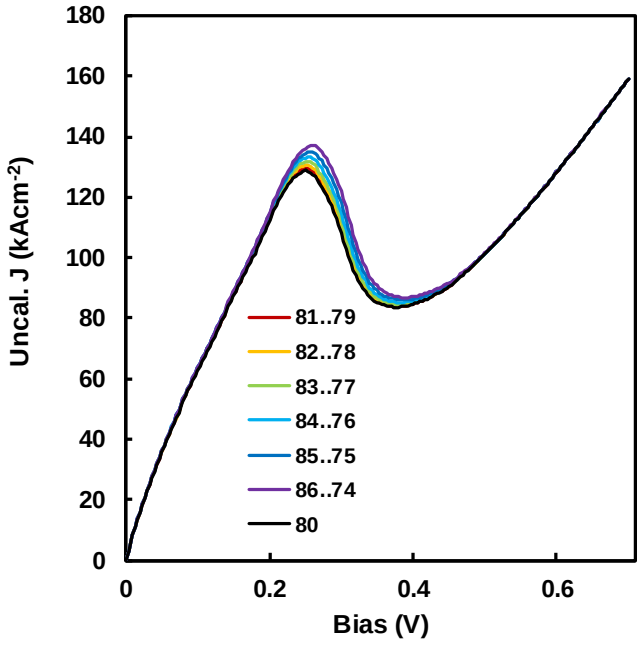


**Fig. 3.3.1.4b Modelled, uncalibrated I-V characteristics presented for devices with a linear-graded ternary $In_xGa_{1-x}As$ QW. The legend shows the start point (towards the entry AlAs barrier) of mole fraction x (%) to the end point (towards the exit AlAs barrier).**

Several mole fraction gradient changes, from 0% (reference structure) to 12% are plotted in Fig. 3.3.1.4b, showing their respective I-V characteristics. A trend of a modest increase in $V_{pk}$ is apparent. However, this also comes with minor gains in PVCR and $P_{NDR}$.

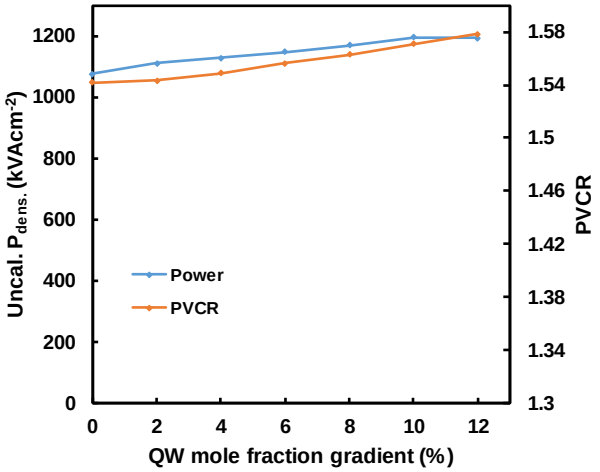


**Fig. 3.3.1.4c Uncalibrated extractable power density ($P_{NDR}$) and PVCR with respect to the change in the InGaAs mole fraction linear of the QW, from Fig. 3.3.1.4a, plotted on the same vertical axes as Fig. 3.3.1.3b.**

As the grading affects the slope of the conduction band edge, there is an optimum bias where the QW will be flat. This dependency is shown in Fig. 3.3.1.4d. The departures from linearity are attributable to numerical error. For an optimum case with the structures simulated above, an additional 5% increase in the $E_1$ transmission peak is observed compared to the non-graded case. However, no discernible difference could be verified with regard to the full-width to half maximum. The difference is expected to be higher with material systems that necessitate higher bias (GaAs/AlAs, GaN/AlN etc.).

It is worth reminding the reader that this prediction does not take into account the series resistance added by the contact mesa and other parasitics present during an I-V measurement.

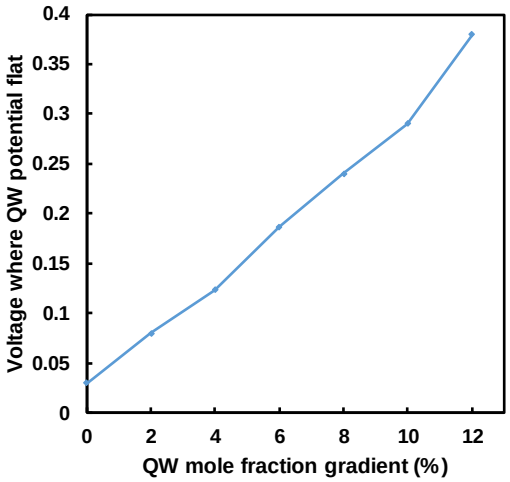


**Fig. 3.3.1.4d Bias where the conduction band edge inside the QW is constant, with respect to the change in the InGaAs mole fraction linear of the QW, from Fig. 3.3.1.4a**

Pairing the best 8% graded emitter from the previous section with the suitable 6% QW grading does not yield a significant improvement over the graded emitter alone. The valence & conduction band potentials under bias are shown in Fig 3.3.1.4e, without Fermi-level pinning on the metallic contact side.

In the interest of keeping the fabrication of the RTD as simple as possible, thus less prone to equipment calibration errors or even user error, it is therefore recommended that a graded QW is not used for Type-I InGaAs/AlAs RTDs. An additional inconvenience of this method is that an RTD device thus created will have a further asymmetric potential, which would discourage its use in the reverse bias. This limitation may cut into the yield, and hence, profits, of a semiconductor fab.

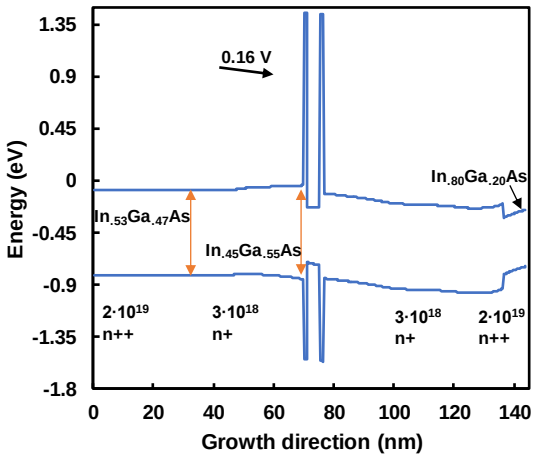


**Fig. 3.3.1.4e Conduction and valence band potential under bias, depicting an altered reference structure including both a graded emitter and a graded QW.**

To the best of my knowledge, this graded QW has not been practically realised for double barrier RTDs, though it has been suggested for similar reasons in a model of a triple barrier RTD by Datta *et al.* [212].

### 3.3.2. InGaAs/ InAs / InGaAs QW

The devices with a constant mole fraction of InGaAs QW shown previously are one of the conventional methods of growing RTDs. However, as evidenced by Fig. 3.1a, there are many more examples of growing a deeper InAs sub-well sandwiched between lattice-matched InGaAs QW layers. There are two main reasons for this approach: i) minimize local barrier thickness extension due to the pseudomorphic AlAs lattice [175] ii) results in a reduction of calibration steps in the initial wafer epitaxial process.

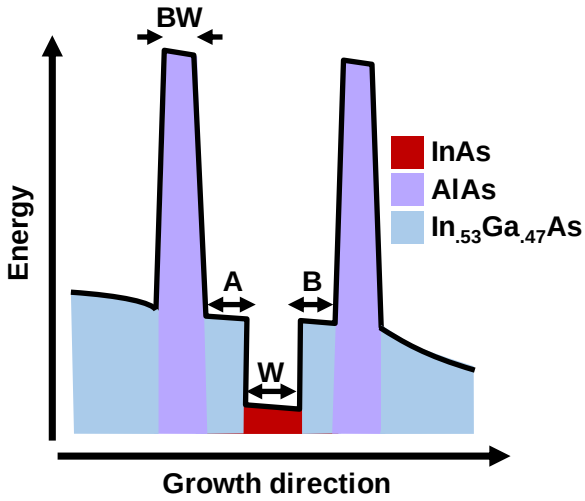


**Fig. 10. Schematic modelled conduction band diagram of the Ternary/ InAs / Ternary epitaxial alloy device. The letters denote dimensions of the barrier width (BW), sub-well width (W), and emitter- (A) and collector-sided (B)**

Fig. 10 shows the schematic representation of the conduction band potential of the sub-well device. The InAs layer creates an additional Type-I QW, the sub-well. We initially investigate the merits of this structure using the previously established methodology. All parameters are related to the width of the epitaxial layers: A is the distance in ML from the entry barrier, whereas B is the distance from the exit. W is the width of the InAs sub-well. We note that the ratio between W and overall QW width (A+W+B) is analogous to changing the mole fraction of the equivalent $In_xGa_{1-x}As$ layer in the ternary QW case. One such example is given in the simulation of the device described in Table II of Sugiyama *et al.* [93]. For the equivalent structure of 5ML/5ML/5ML of

ternary/InAs/ternary alloy, the equivalent indium mole fraction if the QW were a constant composition is x=0.686.

Fig. 11 compares the active region of this ternary and sub-well devices, with similar barrier widths and identical $\Gamma$ parameters. The dotted line represents a 15 ML sub-well device, divided as 5 ML $In_{.532}Ga_{.468}As$/ 5 ML InAs / 5 ML $In_{.532}Ga_{.468}As$, whereas the dashed line is a ternary device with $In_{0.8}Ga_{0.2}As$. Their corresponding conduction band potentials with the computed positions of $E_1$ and $E_2$ is shown. In the sub-well device, a computed +4.9 meV shift of the $E_1$ is noted, resulting in a +10mV bias point requirement compared to the ternary device. The PVCR also worsens (1.79 vs. 1.57), and so does the IRE (1.87% vs. 1.72%). Based on these minor differences, departure from the measurements in Ref. [93] may be attributed to statistical fabrication variations and/or the changes in the scattering parameter $\Gamma$ between the 2 different nanostructures, as well as the varying [001] distances with pseudomorphic growth.

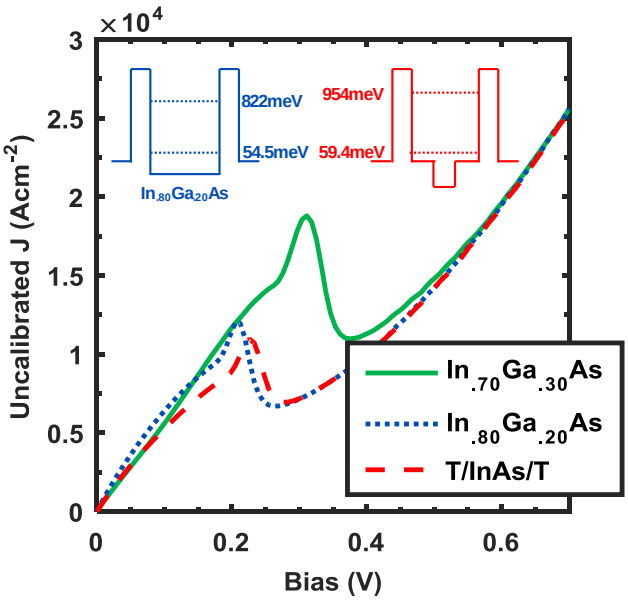


**Fig. 11. Comparison of simulated uncalibrated I-V characteristics against 2 ternary alloy devices with mole fraction x=0.7 and 0.8, respectively, and a lattice-matched ternary alloy InGaAs\InAs\InGaAs sub-well device. For comparison purposes, same modelling fit parameters are used as the devices in Fig.8-9.**

I would draw attention to the 2nd quasi-bound level 954 meV being shifted +142 meV compared to the InGaAs QW structure, which further reduces the already low chance of phonon-assisted tunnelling through this state. Therefore, an investigation on whether the trend of achieving an improved IRE with a slightly

better compressive stress budget is consistent throughout sub-well devices is carried out.

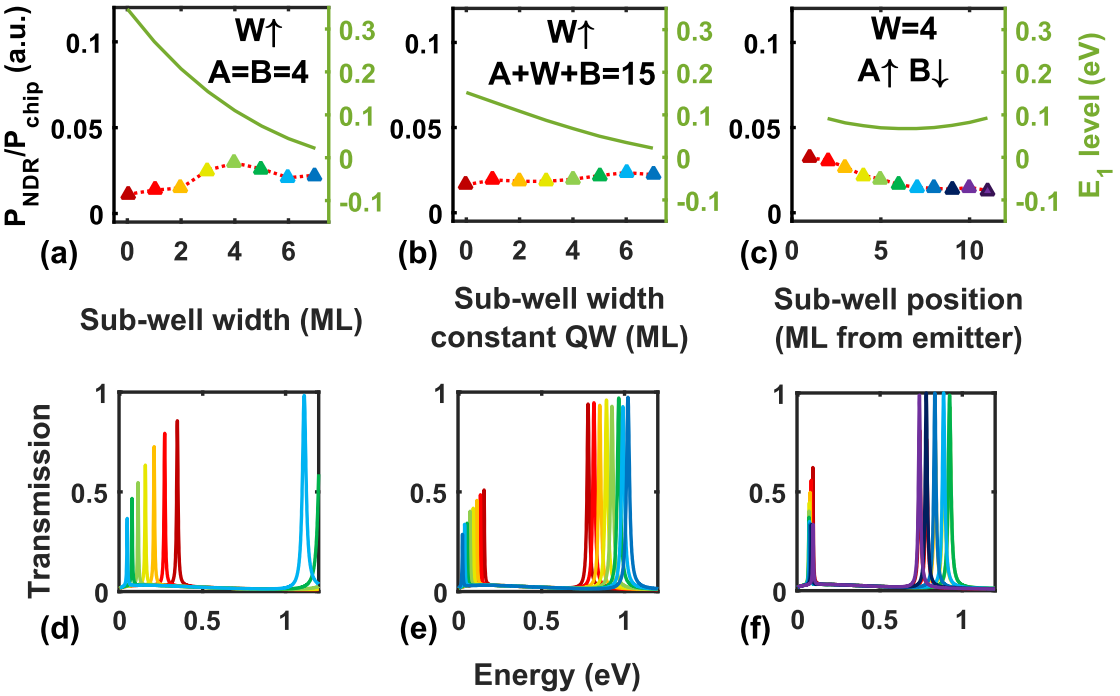


**Fig. 12. Modelled intrinsic resonator efficiency figure of merit for individual changes to a structure of 4 ML InGaAs/ 4ML InAs/ 4ML InGaAs (a) adjusting QW width with a constant sub-well width(b) keeping QW width constant (c) varying the position of the sub-well inside the QW (d), (e), (f) are their corresponding energy transmission results. The overlaid line in (a), (b), (c) shows the shift in the 1st quasi-bound state. The dotted line is a guide for the eye.**

Fig. 12 repeats the representation for chosen for Fig. 5, with the different set of geometric parameters previously mentioned. The modified reference structure has W, A, B are all 4 ML. but varying a single parameter (a) varying the sub-well width (W), whilst A, B are constant (b) keeping the overall well width fixed whilst W increases (c) the relative offset position in ML from the emitters.

Increasing the sub-well width (Fig. 12(a)) from the initial value of 4ML results in moderate gains with a clear optimum. Shorter sub-wells, therefore reducing the relative concentration of indium, increases the 1st quasi-bound energy level with respect to the Fermi level, resulting in higher device bias requirements. With several combinations, the 2nd resonance merges with continuum states above the AlAs *Γ*-point of 1.16eV. However, greatly increasing the well width may have a deleterious effect upon the cut-off frequency of the device, due to an increase in carrier transit times.

If the overall well width is to be kept constant (Fig. 12(b)), there is a monotonic improvement with the sub-well width. In line with increasing the indium mole

fraction of the ternary device, this results in apparently direct improvements without penalty, as the 2nd quasi-bound state is pushed into a higher level.

Altering the position of the sub-well whilst keeping its width constant (Fig. 12(c)) is another important factor to investigate, as the precise position inside the well cannot be guaranteed. A surprising result was the increase in the IRE as the sub-well is placed closer to the entry-side barrier. This effect may be due to the average of well potential appearing to be flatter under the bias compared to the formation of a triangular well in the ternary device, resulting in less linewidth degeneracy. An analogous case has been suggested with a ternary device, by ramping up the indium mole fraction [130]. Parabolic conduction band potential QWs have also been created in the GaAs/AlGaAs system[213], however, this is not a direct comparison due to the closer band offsets of the material pair, likely favouring tunnelling through indirect band gap states.

In Fig. 13, we expand upon the previous parameter sensitivity analysis and present the result for (a, b) 4 ML barriers and (c,d) 3 ML barriers, with the sub-well placed in the centre, and immediately attached to the emitter-side barrier, respectively. The simulation predicts a best-case IRE of ~5% (+30% improvement vs. ternary device) for the 4ML devices. At a +29% improvement, from 11% to 15.1% IRE, the trend is preserved for a 3ML device, rivalling the previously suggested 2 ML barrier which may decrease the yield of highly-similar diodes. I remind the reader that ~3 ML devices have been successfully grown to obtain 1.92THz [179] primary oscillation.

The accumulated stress limitations in these devices may manifest themselves as Stranski-Krastanov (3D) growth modes, particularly with wider sub-wells. In Fig. 7, a prediction dependent on suitable flow and temperature conditions, 5 ML of InAs may be successfully grown on lattice matched InGaAs. However, the question that arises is whether a high-quality interface between the AlAs barrier and InAs sub-well placed towards the emitter side is possible, taking into account the lattice constant misfit of -6.06%. This provides a new challenge to the epitaxial process.

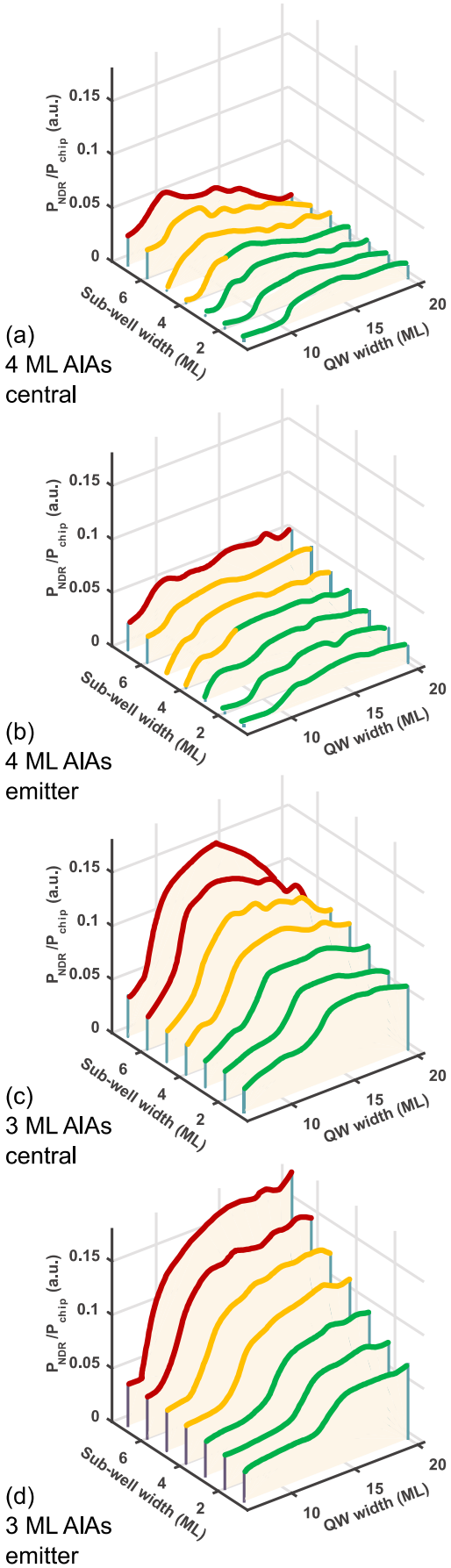


**Fig. 13. Result of simulating 4 ML (a,b) and 3 ML (c, d) barrier RTDs with an InAs sub-well located in the centre (a,c) and attached to the entry-barrier (b,d). Colours reflect the stress diagram in Fig. 7.**

## 3.4. Summary and further work

This chapter has evaluated the conventional peak current ($J_{pk}$) vs. the peak to valley current ratio (PVCR) performance assessment scheme, suggesting that the application will ultimately drive the parameters to optimise. A universal intrinsic resonant efficiency figure is proposed which rolls several quasi-static (DC) performance figure in one number.

The reasons for the DC instability are discussed and several points are mentioned that may impact on obtaining an adequate fit of an RTD to a measured device.

An optimal device is proposed by varying 3 essential geometrical parameters. The requirements for strain balancing indicate that a wider QW with lower [In] mole fractions, but much narrower AlAs barriers provides a route to higher efficiency sub-millimetre sources. In the same time, the role of the emitter and collector spacer layers in realizing a high cut-off frequency device is discussed, and discuss the role of emitter spacer mole fraction grading to aid in this function. A possible trade-off between PVCR and THz power is suggested.

I then discussed the advantage with respect to the accumulated stress and intrinsic resonant efficiency of moving to a sub-well structure, and have shown such structures benefit from careful design of QW width and position. Additional advantages in reduced alloy scattering and barrier perfection may lead to even greater intrinsic resonance efficiency enhancements for sub-well structures.

The emerging complexity from a relatively simple layer structure leaves several open questions. For one, if an ideal frequency-dependent figure of merit may be developed, and if so, whether this item would be valid for optimising an RTD resonator as a THz receiver element. One approach to realise this would be to multiply IRE with a compensation factor obtained from the decline in amplitude with increasing frequency.

Then, there are several gaps in the literature about the nature of the valley current, and whether it would be possible to provide immutable evidence about the proposed $\Gamma - L$ transition as a conduction loss mechanism.

Last, but not least, the behavioural bistability of a double-barrier RTD is still a source of uncertainty that may result in new design paradigms and potential applications in the foreseeable future.

# Chapter IV : Epitaxy Characterisation

This chapter opens a case study in characterising the thin active region of the RTD consisting of a few atomic sheets of III-V material. As a consequence, most analysis techniques are expected to give poor results. A review of common techniques is outlined, and after a separation into destructive and non-destructive methods, the latter are put under scrutiny.

High Resolution X-ray diffractometry (HR-XRD) and LT-PL (low temperature photoluminescence spectroscopy) are complementary techniques used here in combination to increase the confidence in the results of the analysis.

Based on modelling data, a map of the geometrical structural parameters provides an anchor point to compare and describe departures of the sample from the designed structure.

Several PL & HR-XRD good practices are discussed, as well as conditions that could conceivably invalidate a believable result or fit.

This work culminates with the description of a variation of 2, 3, and 4 atomic sheets of AlAs (0.6 ~ 1.17 nm). Barriers with this thickness were not previously reported in the literature. It is shown that using this optical characterisation scheme, the uniformity and thickness of the barriers can be tracked.

Finally, the discussion is rounded off with a TEM analysis.

## 4.1 Characterisation methods

There are several methods available to characterise the quality of the epitaxial semiconductor growth. Depending on the method, they may be classified depending on their destructiveness to the sample under test, pricing and availability, the difficulty in processing a sample, whether they require an electronic contact, whether they reveal the required information directly.

The ideal characterisation method would be non-destructive, sufficiently widespread in the industry as to be cost-effective, fully automated, optical in origin such that it will have no need for electronic contacts, necessitating essentially zero sample preparation and offering the capability to be integrated on a wafer-line tool.

If a given characterisation tool may be employed to be part of the epitaxial fabrication process, it becomes a form of profit-maximising Quality Assurance. As we had seen in Chapter I though, *in-situ* monitoring of the growth conditions is particularly challenging; by the time the data may be properly recorded and interpreted by the operator, it may be too late to correct the issue causing a drift from the designed structure.

- In an MBE system, even as the growth rate may be suitably slow (~0.03 nm/s), the intensity oscillation peaks from the RHEED system may not be sufficiently defined in certain layer combinations as to describe the material interface, due to loss of resolution due to diffraction scattering and other less well-understood processes [96]. RHEED systems are not typically used outside of calibration runs, with notable exceptions for more exotic growth modes [214]. Additionally, whilst layer steps may be identified, precise mole fractions are not readily extractable parameter.
- In an MOVPE system, the most common *in situ* growth monitoring technique is *emissivity-corrected pyrometry* designed to infer the surface temperature of the wafer [215]. More usefully, such a system presents a graph of the sample reflectivity depending on time (therefore, as the growth progresses) [95], which may later be fit with the simulated optical properties of the material. However, even if a system is developed to provide real-time closed loop control for the susceptor plate temperature (attainable with a mixed-mode system-on-a-chip), in the case of gas intermixing, a skilled operator may decide not to act upon automatic

recommendations, due to various reasons related to the operation and design of the reactor. The information could therefore be considered more difficult to interpret than RHEED oscillograms, providing reliable information mainly regarding the growth conditions.

Therefore, baring significant, cost-effective advancements in reactor design, academic environments and small & medium enterprises will need to work around the lack of high-confidence *in-situ* characterisation with *ex-situ* methodologies. This is particularly true in environments where a high variation of grown layer structures is required.

### 4.1.1. Destructive

The choice for ultimate layer thickness measurement is given by ***H**igh **R**esolution **T**ransmission **E**lectron **M**icroscopy* (HR-TEM) [216]. By filtering the interference of multiple sample-diffracted electron beam in Fourier space, one may obtain an image of the interaction of the wave fronts with the crystal lattice[217]. Several conditions need to be fulfilled before this happens: the beam is expected to tunnel through the sample, therefore a combination of high-energy (~400kV acceleration voltage), fast-electrons (little interaction with the sample) and the thinnest sample achievable possible to maximise signal to noise ratio. Specimens tend to be thinner than 100nm, typically achieved by precise ion milling. Due to the fragility of the specimen thus produced, this process tends to have a failure ratio associated with it. Specimens thus prepared are also exposed to atmospheric oxygen. Finally, in order to obtain a clear image, a multi-step process is required to align the sensitive optics of the instrument, requiring a mechanical vibration-free environment. Thus sample preparation, beside the availability of the equipment itself, is the main downside of this technique. However, not only could a good quality image reveal the nature of the hetero-interfaces in the active region of an RTD, the chemically-sensitive [002] plane may also reveal compositional information, based on contrast differences [93].

***S**econdary Ion **M**ass **S**pectroscopy* (SIMS) is a characterisation technique which detects ejected surface ions upon bombardment with a foreign ion species, a procedure developed from the sputtering tool family [218]. It is therefore

destructive, and highly recommended to cleave the wafer before attempting this to prevent contamination. SIMS systems may be configured to detect the linewidths of certain ejected ions, therefore displaying the information as counts of a given atom at a given etch depth, which can later infer InGaAs alloy mole fractions. However, the accuracy in detecting the spread of different ion species is traded off with the thickness at each measurement point. As multiple ions (typ. Ar+ or Ga+) plastically collide with the specimen surface in different points, the ejected clump may not follow a deterministic pattern, therefore thickness/etch depth measurements have a considerably higher error bar compared to HR-TEM. In this work I am not presenting the data obtained from SIMS, due to finding the result quality directly inferior to TEM images, particularly with respect to the thickness resolution of ~0.9nm/data point, and due to their proprietary nature of the data involved. Different ions may yield better results in detecting the dopant species (in this case, Si) Furthermore, the nature of the characterisation scheme described in this chapter made SIMS data redundant, but it remains a worthy technique should this equipment be available. The main sample preparation requirement is cleaving, cleaning, and mounting.

***E**lectrochemical **C**apacitance-**V**oltage* (E-CV) profiling is another locally destructive technique. The instrument etches a crater area using a weak acid (in this case used a light-sensitive 1 molar concentration (1 M) Tiron solution [219]) and applies a known current, to measure subtle conductivity changes and deduce carrier density. UV light acts as a catalyst, and can further moderate the reaction rate. We have previously used E-CV profiling to confirm doping densities in different InGaAs material test stacks and full RTD structures [220]. E-CV may not be effective if the semiconductor is not doped, due to the lower conductance bringing the voltage measurements closer to the noise floor. E-CV profiling has also been used to determine InGaAs/GaAs conduction band offsets [221].

### 4.1.2. Non-destructive

X-rays have been used to study the properties of crystals shortly after their discovery. A standard piece of equipment found alongside growth facilities, *high resolution X-ray Diffractometry (HR-XRD)* rocks a highly collimated X-ray beam

of a precise wavelength near the Bragg angle of the substrate of a sample. The diffracted beams follow specific laws, and a good fit of a model to measured data may be achieved if the crystal growth is pseudomorphic (as opposed to having relaxation regions)[222]. Generally, however, short period superlattices and/or thin layers produce very low intensity and weakly angle-separated Pendellösung fringes and satellite peaks, which may require a high resolution goniometer and the a good X-ray spectroscopy system, components which are examined later. Many purpose-build new HR-XRD machines should be capable of reaching this standard at the time of writing. The technique is generally considered non-destructive, and runs at room temperature However, the confidence of the data obtained may be lower in the case of complex growth structures, and as such it is used in tandem with other optical techniques.

Photoluminescence (PL)[223] spectroscopy, together with photocurrent [224], photoluminescence excitation (PL-E) [223,225], and Raman spectroscopy [226] are a closely-related group of optically pumped spectroscopy methods employing visible and near-visible pump wavelengths. All of these may be employed to excite valence band electrons into superior conduction band states, resulting in various radiative optical transitions. The efficiency of this process depends on the doping scheme of and layer thickness of the structure, as well as temperature and the optical properties of each material. Photocurrent only provides a limited measure of absorption rather than emissivity, whereas PL-E can measure both absorption and emissivity, typically scanned around a desired peak. The PL spectroscopy kit (or in this work, micro-PL) provides a base template for the others: PL-E involves measuring the response of the sample against a tunable laser. Raman spectroscopy is also excellent in showing the simultaneous emissive and absorptive characteristics of the sample, by measuring the Stokes, and anti-Stokes shifts, respectively [227]. Unfortunately, the confocal Raman spectrometer available at the time of test was equipped with a manufacturer-installed long-pass filter and could not display the anti-Stokes shift.

### 4.1.3. Semiconductor surface & electrical measurements

The semiconductor surface is also a revealing indicator of epitaxial quality. Whilst the previous techniques could be used to detect imperfections in the

buried structure, it is often useful to check the top surface in order to obtain ideal conditions for the adherence of the metallic contact. In this regard, conventional profilometry techniques such as mechanical stylus profiling or even the non-contact optical version do not offer a sufficient resolution to observe sub-micron features clearly [228]. Atomic force/ scanning probe microscopy may be the ultimate tool in determining such fine features, when needed [229]. However, for most purposes, typical threading dislocations may be spotted using ***d**ifferential **i**nterference **c**ontrast*(DIC)/Nomarski microscopy, comparing defect count per area (or given field of view if area cannot be calibrated). DIC is by far the most affordable, rapid, and easy to interpret technique, and as such, has been featured in National Epitaxy Facility quality control documents.

Electrical measurements complete the last piece of the puzzle, though they come with the evident disadvantage of requiring electrical contacts to be fabricated first. In this class, one finds: temperature dependent I-V probing (either 2-wire or Kelvin probing), Van der Pauw (Hall) measurements, and electroluminescence spectroscopy, all which may be done against temperature dependence, as required. The latter uses an electrical pump to obtain an emission spectra from a sample.

## 4.2 Low Temperature Photoluminescence Spectroscopy

### 4.2.1. Setup description

A brief description of the apparatus used to produce the measurements in this section follows. This is shown schematically in Fig. 4.2.1.

A 532 nm 1W (output optical power) diode pumped solid state laser (DPSS) is produced from a 808 nm source diode crossing through a neodymium-yttrium vanadate medium ($Nd{:}YVO_4$) resonating at 1064 nm, which is then frequency doubled through a $KTiOPO_4$ nonlinear optical crystal. The laser operates in CW mode and power output stability is achieved by an active controlled heat pump, and starting the laser early in the experiment to allow reaching thermal equilibrium with the ambient. The room itself is ideally air-conditioned to ensure that fine optics do not go out of alignment with variations in temperature.

The beam path goes through 2 silver mirrors for convenience (not shown), losing an average of 6dB of laser power measured with a power meter in the process. The beam passes through a dichroic mirror with a long-pass cut-off at 650 nm, losing another 3dB, and a collimating lens to focus onto the sample. This last addition marks the distinction between regular PL, and micro-PL, where the spot size is smaller, and therefore the emission from a spot of fewer excitons is captured. The convergence can be coarsely adjusted with a CCD monochrome camera, and further adjusted with a power meter.

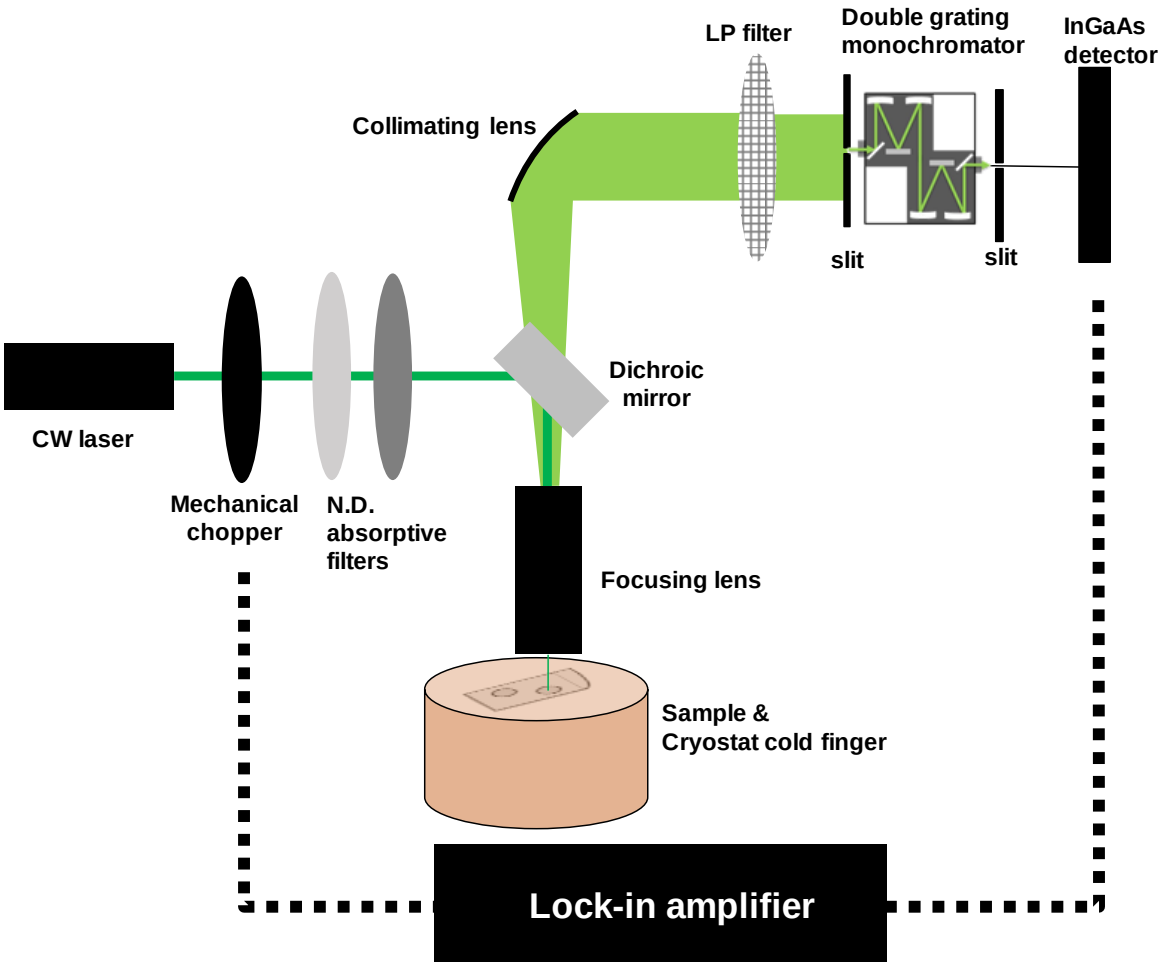


**Fig. 4.2.1.Schematic description of the Low temperature microPL kit used in this work.**

The sample absorbs the pump light (deep green line) and scatters the excited light in a cone (light green cone, arbitrary colour designation due to IR wavelengths), which is then collected through a Au-plated parabolic mirror to collimate the beam. Before entering the spectrometer, another pump long pass filter at 650 nm is applied.

The monochromator uses a double-grating Czerny-Turner configuration, of Bentham DMc150 make, of which 150 signifies the 150mm focal length. The

gratings are synchronously tuned by a computer controlled screw-rod. There is no compelling reason to use this particular monochromator model. The slits are variable for finer bandwidth control. Series dual gratings tend to obtain a better wavelength selectivity at the expense of further attenuation of the PL signal. The gratings installed have a blaze centred on 1250 nm (0.99 eV), with ~5% responsivity each at 700 nm (1.77 eV), which together with the constant-step screw rod deviate $\pm 2\ nm$ at the extreme ends of the tuning range from the ideal centre frequency, in a *Railsback* distribution (*i.e.* standard musical piano tuning). The rod limits the maximum travel (angle) of the grating, which could measure up to 1700 nm (0.729 eV) reliably in a previous version of the setup, and may now move at 1780nm (0.696 eV).

To work around the potential low signal problem when scanning weak emission features from the sample is required, in the right conditions ~1 order of magnitude of signal may be recovered from using a lock-in amplifier synchronised to a chopping disk place in front of the beam. Some pump lasers accept electrical chopping as well. This setup may be called quasi-CW, as the quality of the light is not affected by transients. The lock-in amplifier may then discriminate between the signal and detector dark current, using a series of electrical integrators, counters, narrow-bandwidth filters and differential amplifiers to obtain the final waveform (in this case, a DC-level signal).

The detector itself is an InGaAs PIN diode with active bias and a fixed electrical gain factor, yielding a reliable sensitivity range of ~2.5 orders of magnitude of signal in most conditions. A typical useful responsivity values for an InGaAs detector lies within 800 nm (~1.55 eV) to 1800 nm (0.688 eV). Additional absorptive filters before the monochromator may be installed.

### 4.2.2. Measurement challenges

At room temperature, the PL light emitted by the sample is broadened due to phonon scattering and of weak intensity[181]. In Fig 4.2.2 one may see such an example of temperature-dependent spectroscopy, using the same pump power of 1 mW and spectrometer settings throughout the measurement.

The peak emission has a redshift of ~0.09 nm eV/K. Most of this emission would be attributable to InGaAs radiating photons throughout carrier transition over its band gap. The redshift is attributable to the *Varshni* band gap change. However, even at near room-temperature it is possible to observe that the peak follows the shape expected of a binomial distribution (instead of a Gaussian or Voigt-like shape), suggesting the contribution of another set of wavelengths. Moreover, outside of this distribution, a trail spread out across the blue part of the spectrum may be observed at temperatures below 110 K (within the reach of Nitrogen cooling). We have previously shown that the -20 dB point in this trail is caused by the Moss-Burstein effect [230,231], and has been used to successfully estimate and map doping levels present on 2 & 3 inch wafers [181,220].

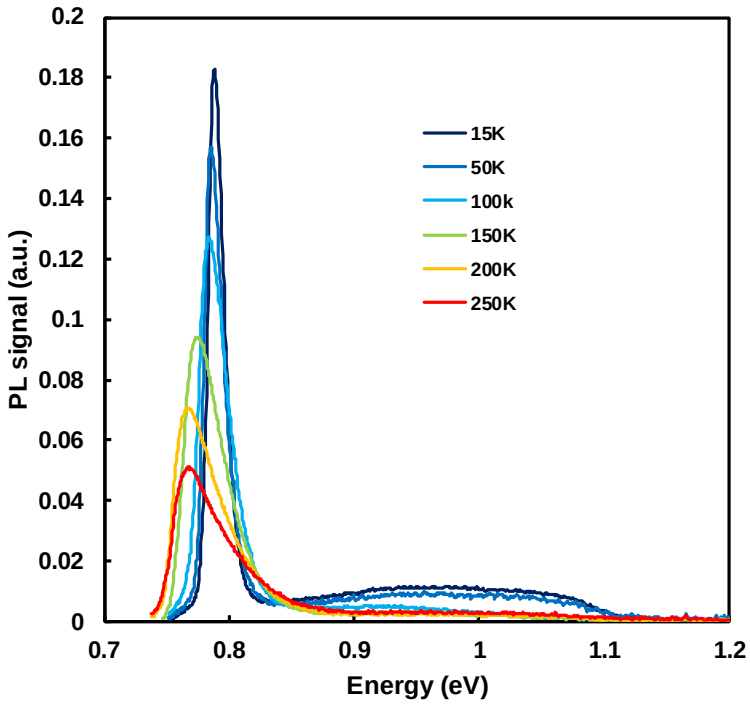


**Fig 4.2.2a. Temperature dependent photoluminescence spectra, varying no additional experimental conditions. Receiving amplitude uncalibrated and expressed without units.**

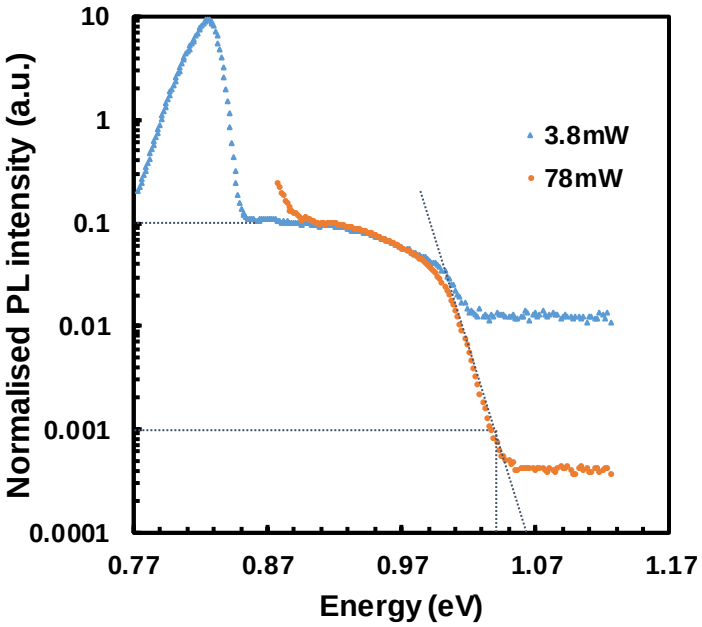


**Fig 4.2.2b Estimation of doping using the -20dB level Moss-Burstein shift from the "plateau"**

Fig. 4.2.2b Shows such a PL scan on TS1902, a sample nominally identical to the reference structure. In this example, the estimated doping density at 1.03 eV is ~$1.5 \cdot 10^{19}$ carriers/cm$^{-3}$, derived from Ref. [220].

As it stands, these spectra provide limited information about the layer structure. The band gap of $In_{.532}Ga_{.468}As$ at 15K is 815 meV, whereas the peak is seen at a wavelength of 788.7 meV, corresponding to a slightly compressive $In_{55}Ga_{45}As$ alloy. As described in Chapter II, the presence of strain may locally affect the shape of the valence band orbitals, and thus band gap [118]. The TS2470 nominally identical wafer tested in Fig. 4.2.2c, known to have a good emission characteristic, sees the InGaAs peak at 806 meV.

The difference from expectation may be further explained by poor thermal mounting. The samples are attached to the cold finger using vacuum grease. Conventional electronics thermal compounds are often unsuitable for the cryostat environment due to their tendency to flake under high vacuum. Unfortunately, there are few vacuum grease products simultaneously rated for both medium vacuum ($2 \cdot 10^{-9}\ bar$) and helium temperatures, though a suitable product was found. User error cannot be ruled out: mounting the fragile $350\ \mu m$ InP substrate requires a fairly precise amount of grease, and pressure in the wrong spot may contaminate the sample. Though the protocol was improved over the years for samples <1cm$^2$, highly strained epitaxy will tend to bow the

wafer, with effects exacerbated due to temperature. It is therefore difficult to obtain uniform surface measurements with a flat disk as the cold finger base.

Fig. 4.2.2c illustrates the difference in peak wavelength distributions at different scan points across a wafer between a known strain-balanced wafer(top) (similar to the reference structure of Chapter III: 4ML $AlAs$/ 15 ML $In_{.8}Ga_{.2}As$ /4ML $AlAs$ active region), and an intentionally tensile triple barrier RTD (4ML $AlAs$ / 12 ML $In_{.85}Ga_{.15}As$ / 3 ML $AlAs$ / 16 ML $In_{.532}Ga_{.468}As$ / 3 ML $AlAs$). Both wafers have a centre of $1539.92 \pm 2.05\,nm$ (805 eV) and $1541.15 \pm 11.53\,nm$ (804 eV), respectively. However, the tensile wafer visibly bows in the cryostat to an extent where portions of the wafer lift off from the cold finger. In this scenario, pinning the wafer down may cause it to fracture.

No deviation for the calibrated LM-InGaAs was expected in the given context. The large deviation of $\lambda_{peak}$ in the case of the strained wafer, as well as the pattern seen in the left-hand side of the figure corroborate to the visual observation of the wafer lifting off the cold finger at 15K. This can be noted thanks to a 2mm copper lip surrounding the wafer edge. Therefore, it is likely that the redshift is attributable to variation in temperature.

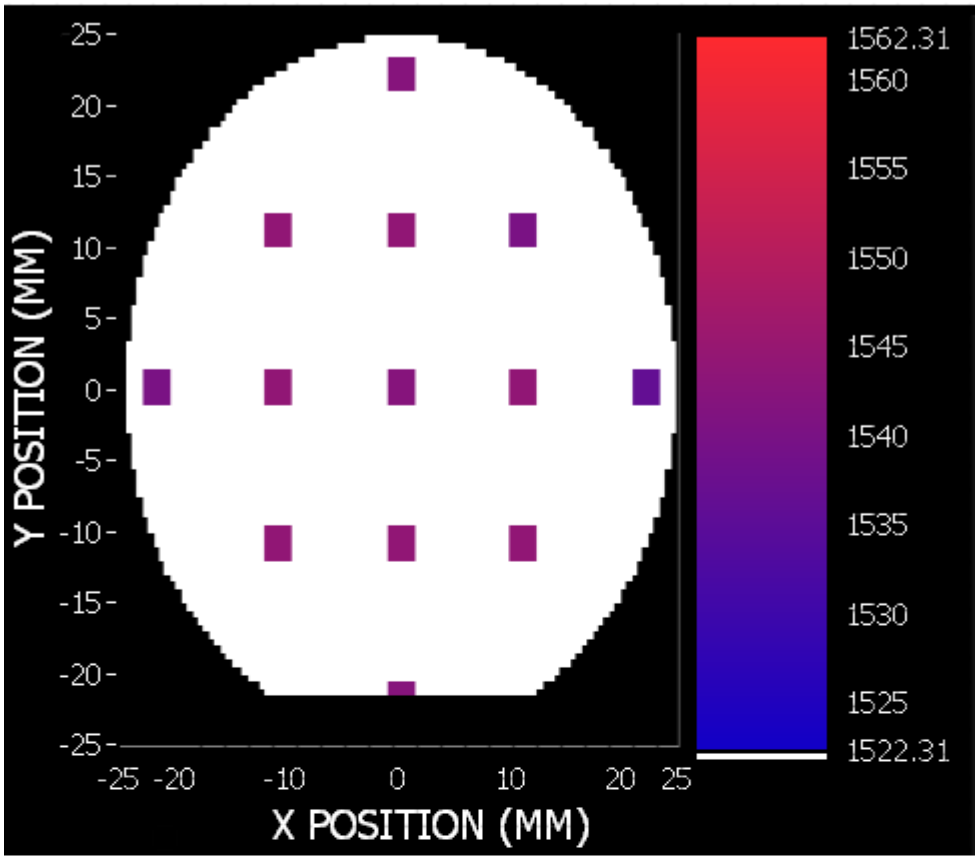


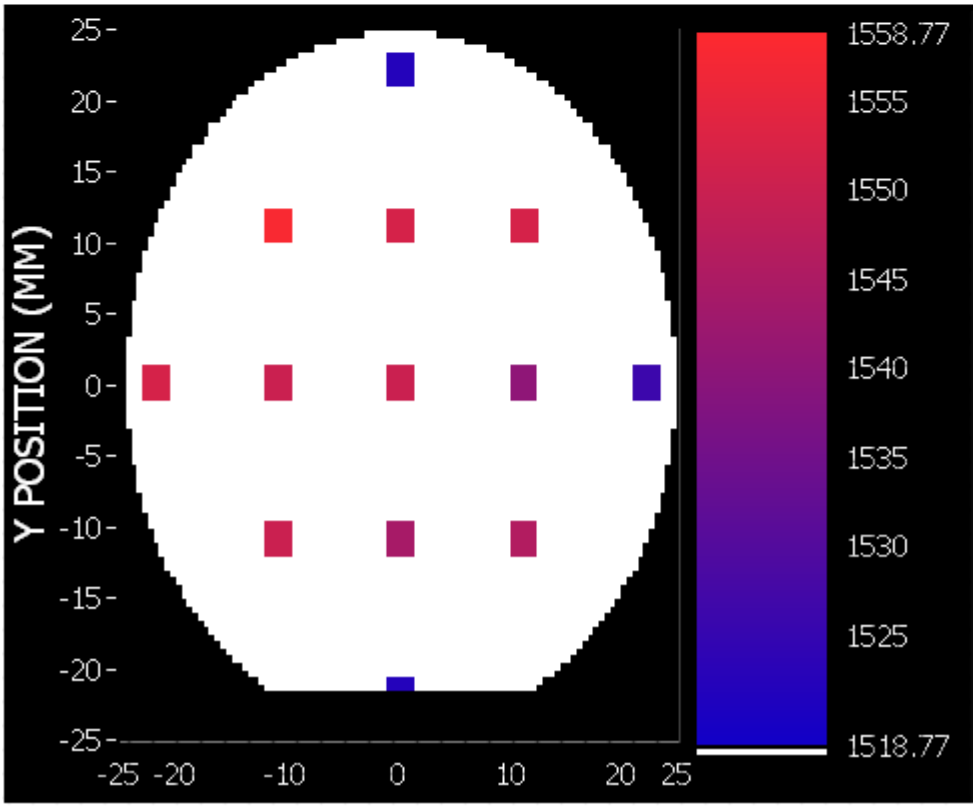


**Fig. 4.2.2c X-Y map of the peak wavelength in a partially strain-balanced wafer (top) and tensile wafer (bottom)**

### 4.2.3 Optical transition modelling

In §2.2.1, several optical transitions were revealed for the case of a QW. The results in Chapter III so far have only presented the confinement energy with respect to the Fermi level. This alone cannot address the skewed spectral distribution seen in Fig 4.2.2. Furthermore, PL only reveals relevant energy peaks, whereas the confined $E_1$ level essential for the operation of the RTD is effectively a difference of levels.

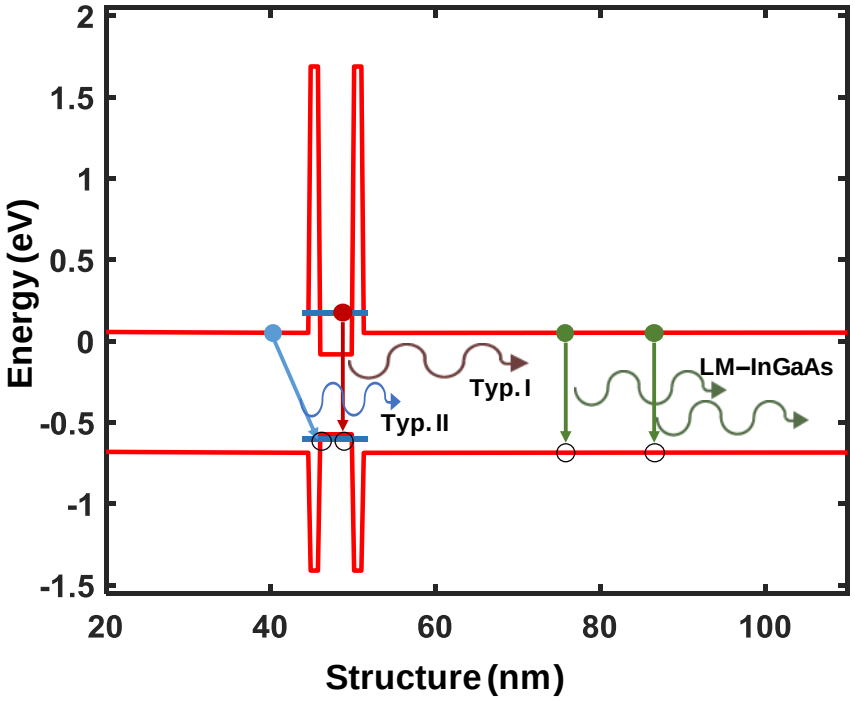


**Fig. 4.2.3a. Simulated conduction (Γ) and valence band potentials, after reference structure in Chapter III, but without any (intentional) doping. Excited carriers are shown with 3 main radiative transitions.**

In Fig. 4.2.3a the reader is reminded about 3 main types of optical transitions. The reference structure in Chapter II is nominally doped. The overall raising of the level of the structure compared to the "Fermi sea" in the contact-levels (not shown in this schematic) facilitates the transfer of the carriers to the first quasi-bound $E_1$ level, and as such, the step-like Type-I transition becomes the dominant of the two linewidths responsible for characterising the QW. The estimated lifetime of the $E_1$ state with 4 ML barriers is 184,153 and 45.1 fs for 15, 14 and 12 ML respectively. Additionally, the tunnelling time was estimated at 58fs at 4 ML AlAs. However, in the nominally doped structure, the conduction band-edge does not correspond to the Fermi level, which would mean the *difference in Type I and Type II emissions* is different compared to the undoped

case. Both transitions terminate in the valence band QW confined level, meaning that in the ideal case, $Type\ I - Type\ II\ = E_1$. However, in this case Type-II transitions are only possible for the short UD spacers of the RTD, resulting in very weak spectral features.

Unfortunately, degenerate doping is a mandatory requirement for the operation of high current density RTDs. In order to fulfil the requirement for characterisation (and implicitly, provide a form of quality control for the epitaxy), a buried device active region-copy was proposed in our previous work [232]. Though a top layer may be preferable for PL and X-Ray characterisation, also potentially opening the door for X-ray reflectometry, it was found that the top dummy well has a tendency to relax. There are also concerns regarding the loss of profitability due to the extra etch step involved in fabrication.

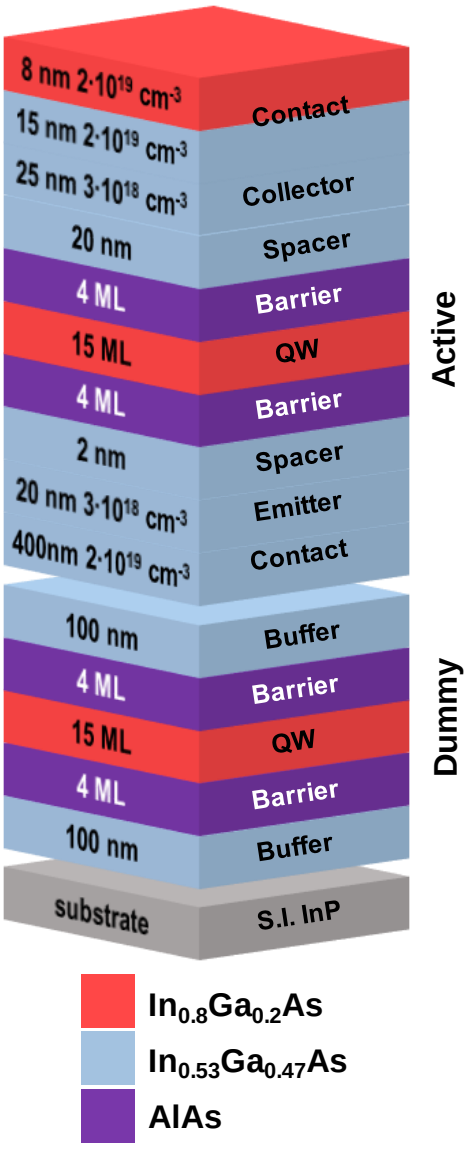


**Fig. 4.2.3b Modified reference structure including a buried duplicate of the active region.**

In order to predict the optical transitions, it is necessary to look at the modelling of the device. Based on Fig. 4.2.3a:

$$E_1 = E_{confined\_e} - E_F$$
$$E_{hole} = E_{confinedh} - E_F{}'$$
$$E_{Type\ I} = E_{confined} + E_{gap} + E_{confinedh}$$

Holes can be computed in any single band simulator capable of dealing with thin layers where wave functions interact (see Chapter II for a non-exhaustive list), by mirroring the band structure upside down to reflect to valence band potential, and specifying the correct heavy/light hole effective mass m*. Hence, the presence of an artificial $E_F{}'$ in $E_{hole}$. It is worth noting that with the previous reference settings for the scattering parameter, the hole levels are degenerate and may be considered identical to the valence band edge. If elastic scattering is not considered ($i.e. \rightarrow 0$), there are several energy levels starting 10-50 meV from the band edge, with separations <70meV. This occurs due to the $\Delta E_v$ of AlAs vs. InGaAs being smaller compared to the conduction band case.

Fig. 4.2.3d plots various combinations of Type I and Type II transitions for different well widths and well depths (achieved by varying $In_xGa_{1-x}As$ mole fractions). Between InAs and GaAs,$m_e^*$ varies by a factor of ~x3, therefore the relative changes in mole fraction produce a more pronounced increase of photon energy with lower mole fractions, also in line with forbidden band changes. Between 2 adjacent QW from a compositional perspective ($\pm 1\ ML\ WW, \pm 3\%\ x$), the difference in energy in Type I states varies between 10 to 30 meV.

A +8.5% fit factor was added to the alignment of the averages of the valence band potentials to better match the PL measurements seen in trial structures. Unfortunately, the band offsets of AlAs/InGaAs lattice-matched to InP were not studied to my best knowledge, however, similar studies also shifted the energies “by a few percent” [233,234] between photoexcitation spectroscopy results to obtain the best line of fit. These results are explored in §4.3.

A similar modification is explored with the variation of AlAs barriers. Fig. 4.2.3e plots the changes in Type I and Type II optical transitions with different symmetrical barrier width. It is noted the energy scale bar in this plot is

different from the previous figure. We note that with the exception of no AlAs presence, the model predicts that Type-II transitions are largely invariant with barrier thickness. This may aid overall in the verification of barrier thickness when referring to Type I transitions, as on average, fractional ML variations could mean that the Type I line shifts by $\pm 10\ meV\ per\ 0.5\ ML$. This suggests that it is very difficult to decouple well width, depth and barrier thickness using LT-PL alone, with the linewidth offering a *space map of >10 plausible combinations* of all parameters. A genetic algorithm employed for automatic curve fitting could be a subject worth of closer attention. This is of particular value should there be several similar wafers ready for characterisation.

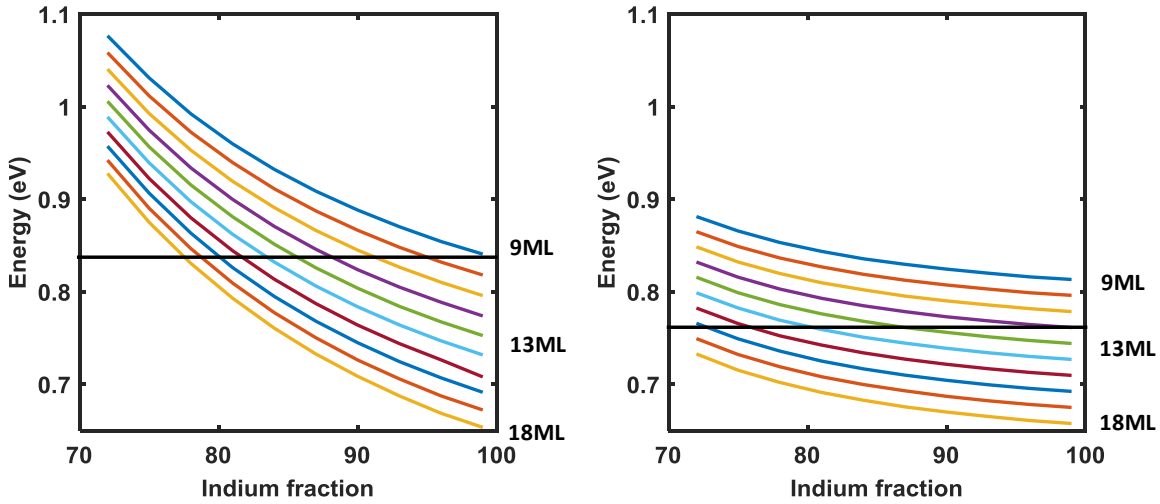


**Fig. 4.2.3c. PL Type I & Type II transitions diagram. QW well depth [In] and well width (expressed in monolayers) influencing Type I (left) Type II (right) transitions. Horizontal line represents lines obtained from LT-PL alone. The horizontal axis represents the mole fraction in percentages, where 100% is InAs, and the curves represent the well width, in 1 ML steps.**

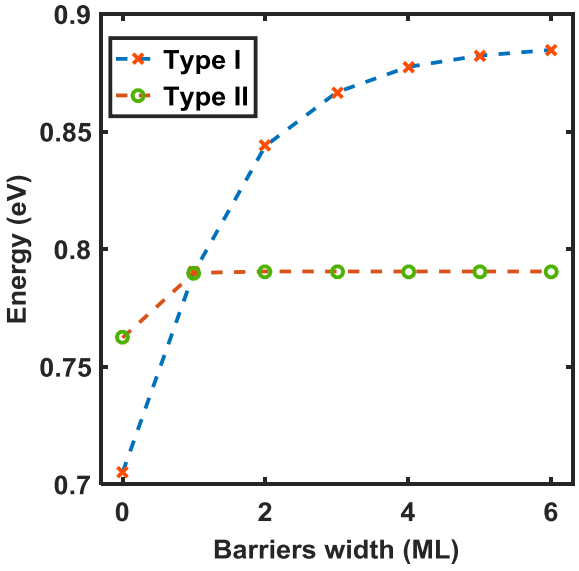


**Fig. 4.2.3d. Change in Type I and Type II PL transitions by varying symmetrical AlAs barrier widths**

Indeed, our previously published attempt [220] had a significant splitting between the InGaAs and QW emission, due to a unintentionally asymmetric AlAs barriers of 2 and 4 ML respectively. These findings were later confirmed by HR-TEM, and HR-XRD.

### 4.2.4. Power dependency PL

The cooling power of the cryostat is approximately 1W across the surface of the copper cold finger 12.56 $cm^2$. Whilst the thermal mass of the copper block may account for minor temperature fluctuations due to the instability of the optical pump power, in a typical measurement the micro-PL measurement is performed with optical power densities in excess of 20W/$cm^2$. In order to account for any heating effects, pumping power dependent spectra are nominally taken.

Power-dependent PL at 15K within 4 orders of magnitude of pumping power was performed to confirm our previous findings in [232]. For the higher power measurements seen in Fig. 4.2.4a, adding neutral density filters was necessary to prevent saturation of the detector, such that the monochromator slit settings remain unaltered for linewidth comparison purposes. As such, the amplitude of the data is presented in units normalised to percentages, then offset for better presentation. The normalisation process has a tendency to improve small peaks and worsen the apparent signal to noise ratio. The anomaly on the 2$^{nd}$ power from the top (i.e. noisy signal) in the virgin surface series of scans was caused by experimental error —an absorptive-type neutral density filter in place to avoid saturating the detector was not removed, causing a worsening of the signal–to-noise ratio. This does not affect the results otherwise.

In Fig. 4.2.4a a comparison between the virgin surface (laser pointing towards active region) and etched surface (laser pointing towards dummy copy) is presented, noting the lack of Type- I transitions in the latter, and the relative increase in amplitude of the Type- II with respect to the remaining InGaAs material peak. It is also confirmed that the Type –II transition does not shift due to having the active region on top, however, repeated practice has revealed that the heavy doping concentration may easily quench this emission, which often finds itself at the limit of the DC detectivity in this particular system. This means that if appropriate signal recovery techniques/ wide slits are employed, it

may be possible to avoid etching a small spot on the wafer, reducing contamination and mishandling risks.

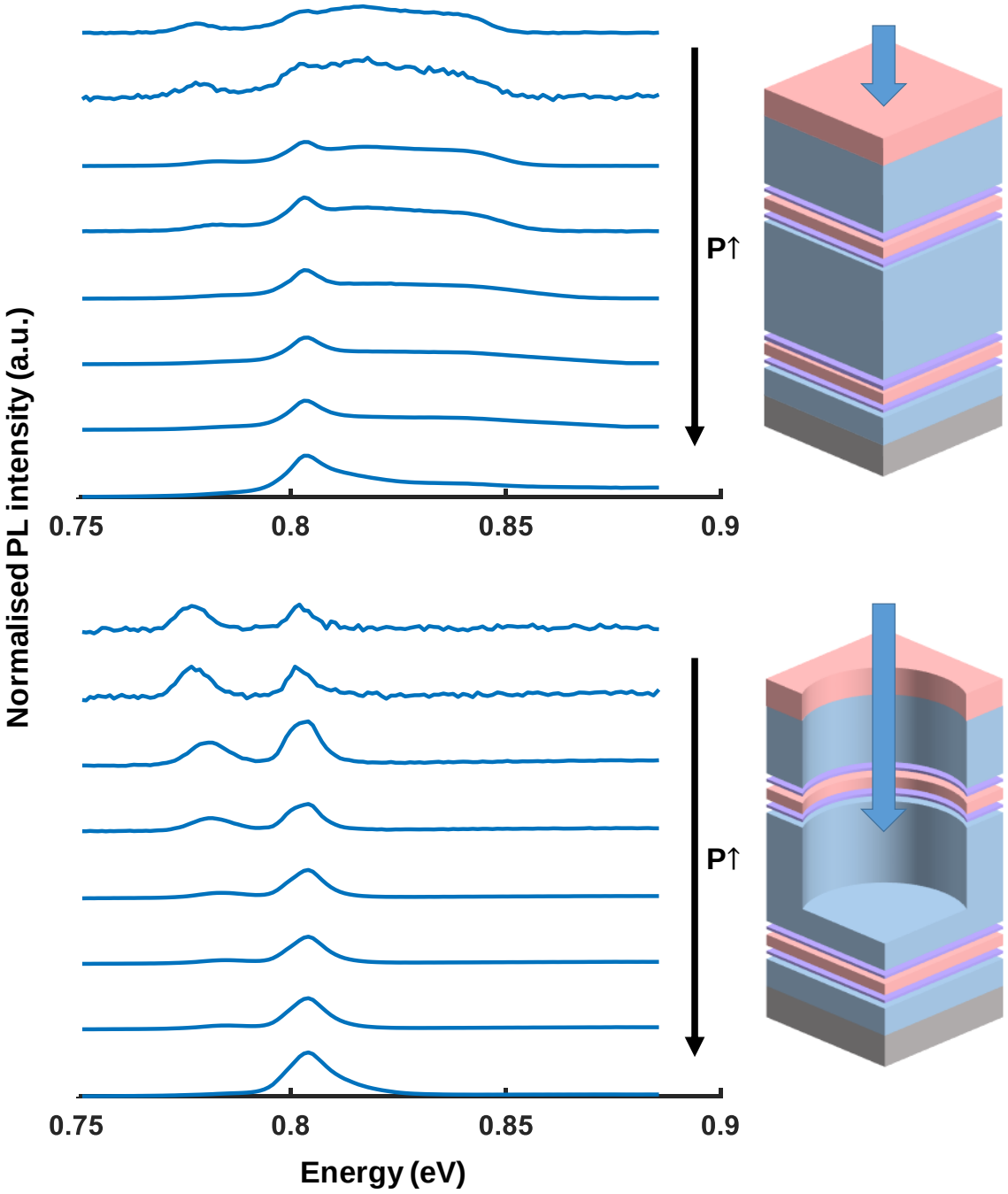


**Fig. 4.2.4a. Normalised power dependent PL @15K, scanned on a single point on the virgin surface (top), after the active region was wet etched (bottom), spot focused on crater edge. The 2nd spectrum from the top in the virgin sample noisy due to a misplaced filter.**

One way to discern features from the obtained PL spectra is to fit Gaussian and Lorentzian functions, as appropriate, to obtain a fit to the Voigt profile. In the case of RTDs, as the confinement is always 2-dimensional, we will refer to Gaussian probability distributions.

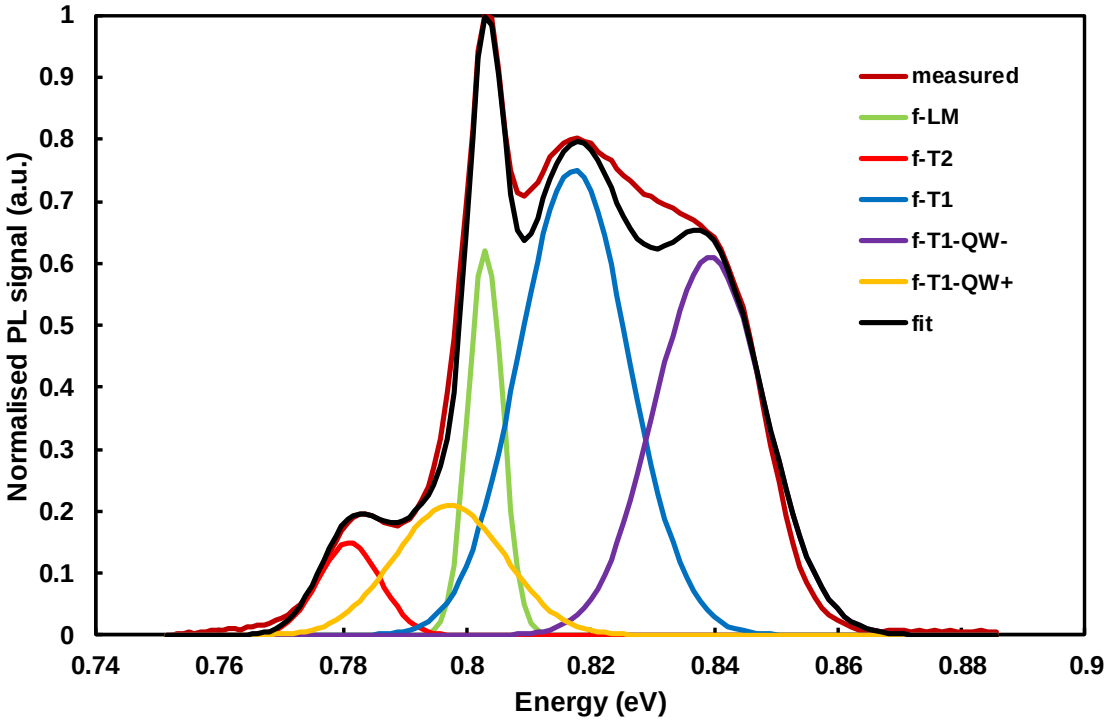


**Fig 4.2.4b. Example of a Gaussian fit to 0.29mW pump power (3rd spectra from top, virgin surface in Fig 4.2.4a.). Dark red is the measured spectrum and the fit line is solid black. Type- I emission separated in 3 components (see text).**

In Fig. 4.2.4b, variations of $\pm 1\ ML$ of the Type-1 well width are accounted for by fitting 3 different Gaussians with an identical full-width to half-maximum ratio. In line with the model from Fig. 4.2.3c, these peaks are separated, on average by $\pm 20\ meV$ each, an average value of the changes of the Type-I transitions. The reader is reminded that the shifts account for changes of $m_{hh}^*, m_e^*, E_g$, in addition to the confined levels *w.r.t.* the band-edge.

Even if the trailing spectral edges are not perfectly accurate with this first-order approximation, the resulting fit is remarkably accurate. The Type-I emission from what would be a 16ML is comparatively weak to the target 15ML and 14ML, but could be detected in lieu of the shape of the asymmetric spectral edge near the narrow LM-InGaAs peak [220]. This is attributable to the average QW thickness being between 15-16 ML around the radiated spot. In practice, the arbitrary growth of the AlAs/InGaAs interface (see §4.4) cause the linewidth to broaden more than would be expected for a SQW emission.

By adding the contributions of the deviation from a target QW width, it is noted that the Type-I emission components overlap with the InGaAs peak to varying extents, at lower pumping powers dominating the spectral features.

In Fig. 4.2.4c the peak emission from Fig 4.2.4b are plotted against 8 different pump powers, following a cubic dependency. In a 2010 paper on quantum dots [235], it was proposed to separate this into a quadratic dependency for lower powers and biquadratic dependency for higher powers. The InGaAs peak does not significantly shift with pumping power, suggesting that the thermal bonding of the sample is adequate.
In the limit of zero optical power, the difference between the highest energy Type I transition (QW minus 1 ML) and the Type II transition yields a maximum $E_1$ unbroadened peak level is 57 $\pm$2 meV . This is in good agreement with previously presented data [232].

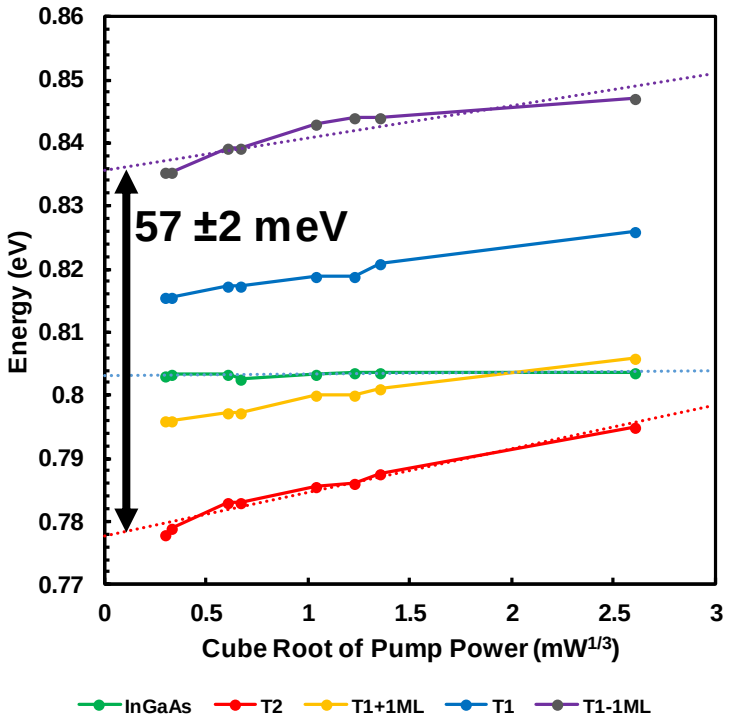


**Fig 4.2.4c Shift of PL emission peaks @15 K with the cube of the 532nm pump. Bulk InGaAs emission in green parallel to the horizontal, Type II in red (lower part of the graphic). The other lines correspond to Type I emissions**

To summarise thus far, LT-PL is an excellent method to characterise Type-I InGaAs/AlAs on InP RTDs, revealing indication of the average thickness of the QW through 3 distinct, broadened components corresponding to $\pm 1\ ML$ variation in QW thickness observed at lower pump power densities. One of the main causes which might invalidate the spectroscopy results is the thermal bonding. Whilst

not a problem for small samples, highly strained wafers may visibly bow, losing thermal contact with the cold finger at the point being scanned. This, however, can be easily tracked with power-dependent pump spectra at the LM-InGaAs peak (expected between 803- 823 eV), which should not considerably shift with an increase in the cube root of the laser pump power.

The correct identification of Type-I and Type-II transitions from doped and unintentionally doped structures can give the value of the $E_1$ quasi-bound energy level *w.r.t.* Fermi injector level, greatly reducing the need to take into account the absolute valence band offsets, which appear to have strain-associated uncertainty. For this particular study, comparing LT-PL with LT-photoexcitation spectroscopy (LT-PLE) may reveal more detail. An additional benefit of LT-PL is that the doping level can be mapped on the wafer, something we studied extensively in our previous work [220].

### 4.2.5. LT-PL and barrier thickness

In §4.2.3, it was suggested that the AlAs barrier may have a convoluted spectroscopic contribution with the various possible combinations of well widths and well depths. However, one advantage of micro-PL is given by the relative size of the exciton to the diameter of the irradiated spot. In Ref. [236] InGaAs/GaAs QD structures at 16 nm have been intentionally grown to confine excitons of 10-15 nm diameter. The $e^{-2}$ beam diameter (beam diameter falling between 13.5% radial points from maximum intensity) for a focused laser at typically low powers is $< 50\mu m$, yielding ~33 averages per sample. This is one of the  By comparison, the $CuK_\alpha$ emission of 0.1506 nm used in HR-XRD, fits ~664000 times in a beam with a 0.1 mm diameter.

Wafers were grown at the National Epitaxy Facility at The University of Sheffield. In this particular epitaxial growth run, the QW was cautiously modified to 12 ML of $In_{.85}Ga_{.15}As$, with the mention that in Fig. 2.1.4d stress diagram, it is shown that the stress-equilibrium point for 4 ML AlAs is predicted to allow 14 ML of $In_{.85}Ga_{.15}As$. Three wafers, namely TS 2474, TS2478 and TS 2483 have 4, 3, and 2 ML symmetric AlAs barriers, respectively.

The 15K PL spectra at the same pumping power of 0.81 mW is presented in Fig. 4.2.5a. The spectra are plotted at a similar pump power level to those in Fig. 4.2.4b, however, Nomarski microscopy revealed surface defects at higher magnifications (without a consistently countable large-scale defect per field of view) that was not apparent in the previous wafer, attributable to the lesser strain-balancing effect in these samples, whereas the previous sample was designed with this intent.

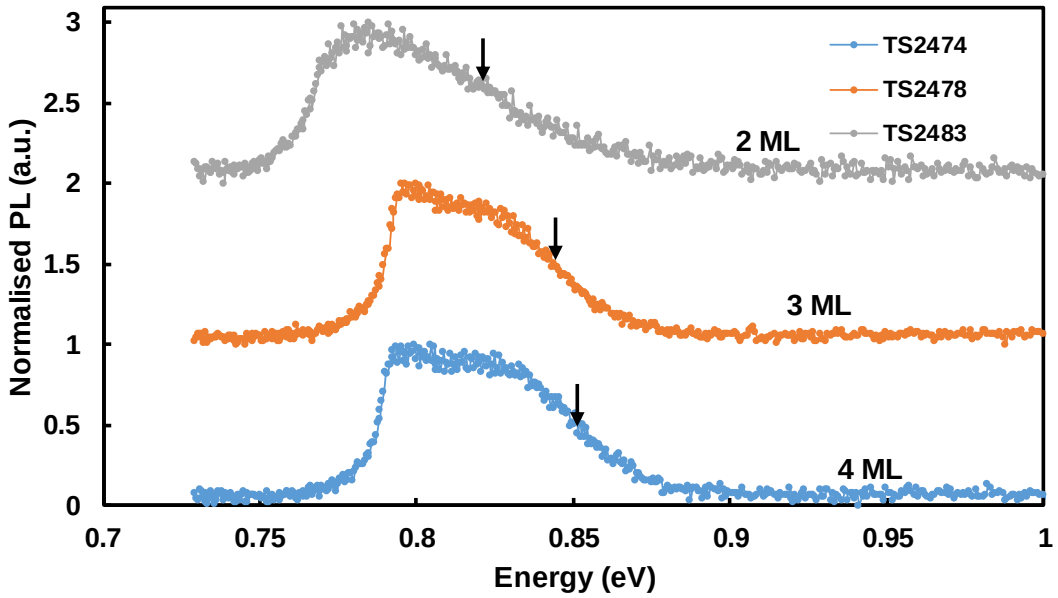


**Fig. 4.2.5a Normalised LT-PL spectra of 3 wafers with a nominally identical QW and varying symmetrical barrier widths of 4, 3, 2 ML for TS2474, TS2478, TS2483, respectively. See Table 4.2.5 for effective numerical comparisons.**

It is immediately apparent that 2 ML barriers have a different spectral shape compared to the 3 & 4 ML. The difference between the latter is more subtle. As a contribution of several wavelengths is expected, in this diagram I have proposed to look at the half-maximum (-3dB) point of the PL signal, where QW Type-I transition would be expected.

From Fig. 4.2.3c, it is expected that for this QW and at 4 ML barriers, the modelled Type I transition is at 864 meV and the Type II at 787 meV. Assuming that the InGaAs emission remains within 803-808 meV (with different pump powers), a fit to the 15K data of the 4 ML AlAs wafer is produced in Fig. 4.2.5b.

An adequate fit is only resolved with a centre layer at 840 meV, being dominated by the emission from a +1ML wider QW vs. design. In terms of epitaxial optimisation, it is perhaps safer to slightly overshoot an epi-layer

thickness than to undershoot. In this case, a slightly longer QW average may reduce bias requirements by lowering the position of the $E_1$ weakly bound level. The Type-II emission was found at 793 eV, within expectation. What is not expected however, is the strong contribution of the Type-II, which may suggest the presence of an additional linewidth, possibly caused by the formation of nearly lattice matched AlInGaAs alloy. This partial fit is the subject of further consideration for publication.

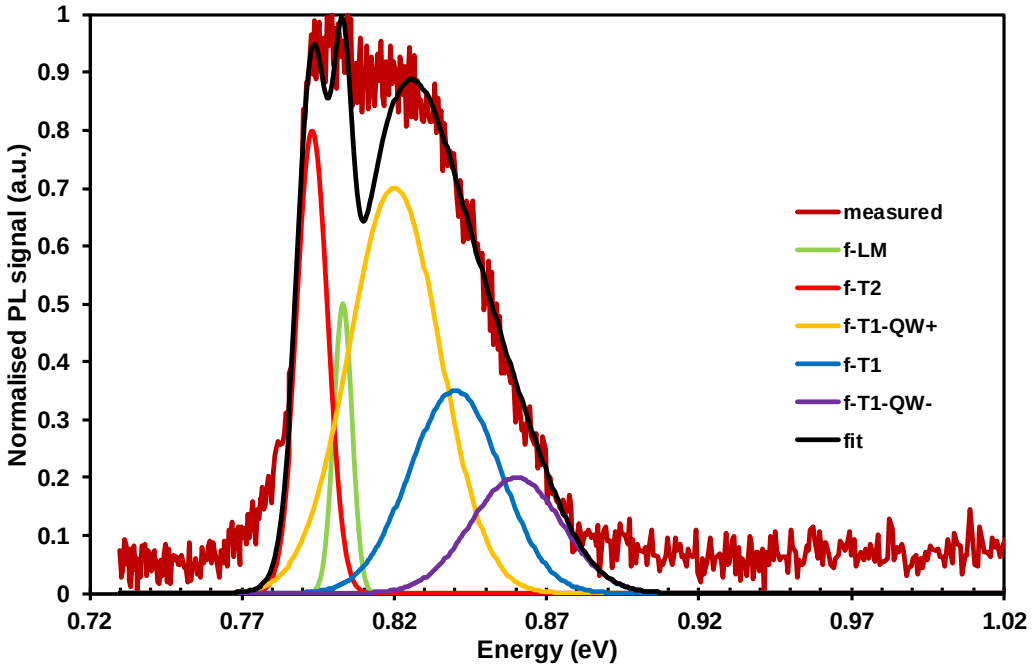


**Fig. 4.2.5b PL spectrum at 15K of TS2474, fit with Gaussian distributions corresponding to different emission lines, as seen in Fig 4.2.4b.**

The summary from the data of Fig. 4.2.5a and the wafer maps is presented in Table 4.2.5. The strongest PL median peak was recorded with the 3 ML wafer, but the larger spread in absolute values seem to put that advantage in question. Interestingly, though Fig. 2.1.4d predicted that 2 ML barriers may push the limit of uniform epitaxy, which may concur in the corresponding lowering of the median peak, the overall emission characteristic deviates notably less.

The -3dB point slightly undershoots, but follows the trend of Fig. 4.2.3d, with a -6.9 meV shift from 4 to 3 ML , and a -18.1 meV from 3 to 2 ML, whereas the computation suggests a -40 meV shift from 4 to 2 ML. The 14 meV discrepancy can be explained by the misaligning of the band levels under stress, which could not be fully considered without empirical evidence.

This suggests that the stress calculations of Fig 2.1.4d hold appreciably well in these circumstances, predicting that the partially strain-balanced TS2478 would perform better compared to the tensile TS2474 or the slightly compressive TS2483. This analysis does not fully describe the RTD active region, however, the obtained linewidth greatly limits the number of border cases.

| Wafer no. (NEF Sheffield) | Barrier Width (ML) | Peak intensity (a.u.) | Standard deviation (%) | Half-Max. cut-off (eV) |
|---|---|---|---|---|
| **TS2474** | 4 | 0.045 | ±31.19 | 0.852 |
| **TS2478** | 3 | 0.056 | ±38.36 | 0.8451 |
| **TS2483** | 2 | 0.019 | ±23.20 | 0.827 |

**Table 4.2.5. PL data summary from 3 wafers with nominally symmetrical AlAs barriers.**

## 4.2.6. LT-PL and InAlAs buffer layer

An intentional omission in Fig. 4.2.3b was a 200 nm $In_{.52}Al_{.48}As$ gettering layer added the InP substrate prevent possible barrier asymmetry. Whilst analysis in 3 different rows of test structures consisting of stacks of doped and their respective undoped barrier/QW layers, did not confirm beyond any doubt that there is an improvement, the InAlAs layer was kept. This is an important point for the XRD analysis as it will be seen in the next section.

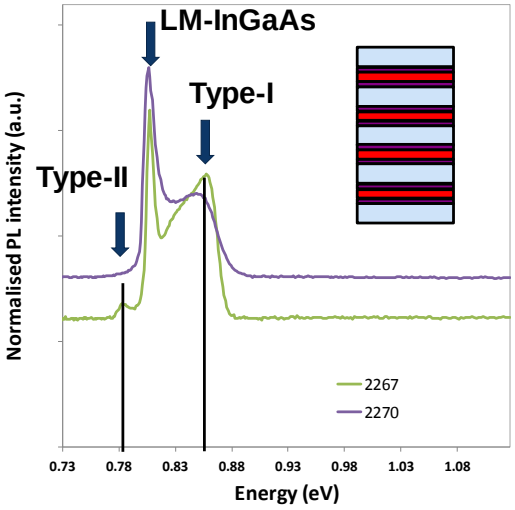


| AlInAs | Type I | | Type II (U/D) | |
|---|---|---|---|---|
| | Expect | Fit | Expect | Fit |
| 12 ML | **861** | **860** | X | 778 |
| 15 ML | X | | X | |

| InGaAs | Type I | | Type II (U/D) | |
|---|---|---|---|---|
| | Expect | Fit | Expect | Fit |
| 12 ML | **861** | **854** | X | 782 |
| 15 ML | X | | X | |

**Fig. 4.2.6 Virgin surface LT-PL spectra of looking towards a doped 12 ML QW with $In_{.85}Ga_{.15}As$. Sample TS 2267 is a stack with an AlInAs buffer, sample TS 2270 has InGaAs only. Type I and II emissions come from this top, and a bottom identical, UD QW, respectively.**

Fig 4.2.6 compares 2 such stacks. Upon normalising the peaks, the relative intensity of the peaks of the sample with the AlInAs gettering layer is understandably lower. Moreover, due to this scaling, the Type –II emission appears invisible in this context. It was however, noted that Type-II emission is more thermally and spot-sensitive on average, and thus, do not consider these spectra statistically significant. In effect, the swap of AlInAs from InGaAs material may help LT-PL characterisation by preventing the “blinding” of nearby spectral features, without necessitating reducing the slit size, which could render low-signal features (doping, Type-II emission) undiscoverable.

## 4.3 High Resolution X-Ray diffractometry

### 4.3.1. Setup Description

Though X-ray diffractometry (XRD) systems are available from various vendors, and are presented in the form of a stand-alone laboratory cabinet with leaded glass, it is important to acknowledge that these are highly modular, precise, and rather delicate systems that must not be treated as a black-box.

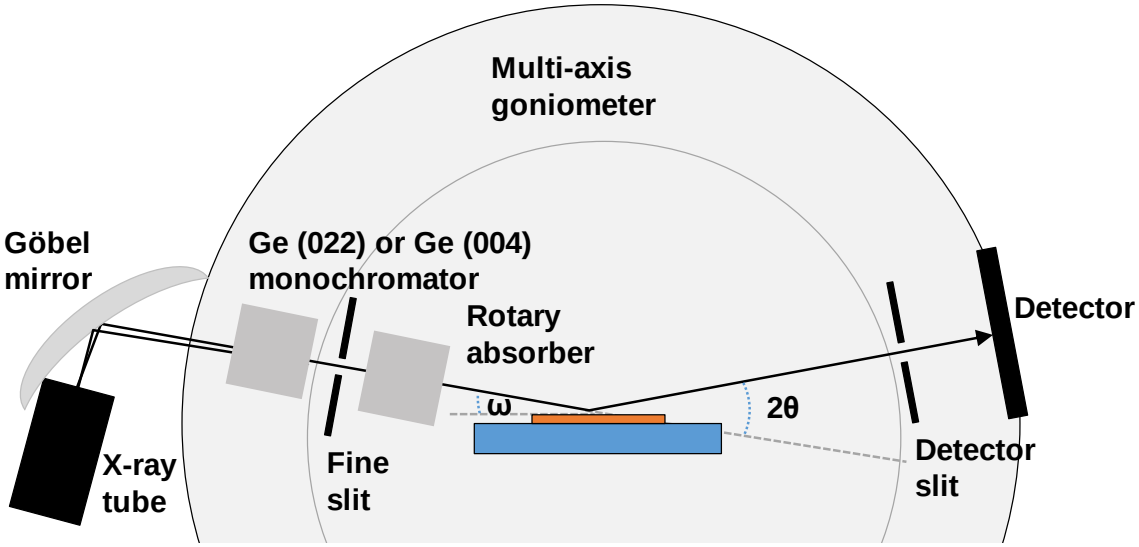


**Fig. 4.3.1. Schematic of a possible configuration of a XRD system. Specimen in the centre of a goniometer with 3 axes of rotation.**

At the centre of every XRD system capable of regular crystal analysis is a finely actuated goniometer, which can rotate, tilt and rock the specimen with respect to the incident beam in most required orientations.

X-rays are generated from a vacuum tube source, an omnidirectional emitter of *Bremsstrahlung* from a copper target bombardment, is shielded with the exception of a circular exit aperture. In order to produce a usable beam, the aperture is set close to a Göbel mirror. Because of their small wavelength, X-rays cannot be typically reflected in the sense comparable to a visible and near-visible light, but highly pure, regular crystals of certain orientations can cause the beam to selectively diffract, absorbing high angle scattered X-ray photons.

After the exit from the Göbel mirror, the beam is collimated but contains several wavelengths in the vicinity of the desired emission peak. A copper target produces 2 high intensity peaks at slightly different wavelengths, labelled $CuK_{\alpha 1}$ & $CuK_{\alpha 2}$ at ~0.1506 nm. Monochromators in this case are an additional crystal which bounce the beam 2 or more times, trading off linewidth with intensity at each hop. One of the systems used in this work had interchangeable monochromators, a 2-bounce and 3-bounce Ge crystal of different orientations, which could be used to reduce the $CuK_{\alpha 2}$ emission to reduce fringe interference effects.

Slits, both entry and exit, may be used to limit the number of high-angle scattered electrons entering the detector. An absorber material may be placed in front of the source when grazing angle scans are performed (X-ray reflectometry XRR). Both the absorber disk and slits may be either user-operated or motorised and computer-controlled, or may be completely hidden to the user and integrated in a source & detector monolithic blocks.

For a typical symmetrical $\omega - 2\theta$ rocking curve measurement, the incident $\omega$ is equivalent to $\theta$. Asymmetrical curves are useful for mapping reciprocal spaces, and may employ a 1D detector array instead of a “single pixel”/ 0D detector.

The specimen is mounted on the centre of the goniometer, and when a rocking curve is performed, most systems actuate the rocking angle continuously, albeit slowly, and acquire data at the frequency specified by the user. The $\omega - 2\theta$ scans taken in this work take between 30 minutes and 2 hours each, to gain as much signal as possible from the very thin layers of the RTD.

Each system has its own software and describing the operation is beyond the scope of the work, as it will be subject to training and approval in the laboratory where the equipment is seated. A typical pre-scan checklist follows:

- Mount sample, ensure safeties are latched.
- Set X-ray generator acceleration voltage and current
- Tilt sample $\chi = 90°$, perform Bragg-peak $\omega$ scan and optimise
- Optimise FWHM of $2\theta$ scan
- Correct any wafer miscut, $\psi$ angle
- Repeat $\omega$ and optimise peak intensity until intensity deviation is low
- Perform quick $\omega - 2\theta$ scan to ensure corectness and obtain useful scan angle limits

### 4.3.2. HR-XRD model

A corollary of the $CuK_{\alpha 1}$ emission being $\approx 1/2$ of the atomic radii, is that invariably, the tube will produce a beam with a wide diameter $\lambda$, despite the beam itself having negligible divergence. The previous section discussed how this beam may be conditioned to an extent, yet this is insufficient to produce a lower statistical averaging of the spot size. And because some defects such as point-defects and dopant species tend to be spread throughout the lattice, XRD cannot be expected to reliably detect such conditions. One notable exception can be mentioned in the case of solid-diffusivity limit cases that realistically impact upon the overall strain and stress of the epitaxy [194]. Should such effects be invisible with other surface scanning equipment, it may be difficult to de-convolute from the complex factors that impact the structure using XRD alone.

Hence, Fig. 4.3.2. presents a simplified layer structure of the RTD, noting the merging of the “staircase” [220] doping regions into a large layer for this purpose. The colour-coding on the left is used to suggest that for a first approximation of obtaining a fit, the growth-related parameters of layers of identical colours (mainly mole InGaAs mole fraction and thickness in all cases) may be “linked” together. The role of the thick lattice-matched InAlAs buffer layer can be expected to be analysed with greater accuracy vs. an InGaAs-detector enabled PL, but will be later confirmed in §4.4.

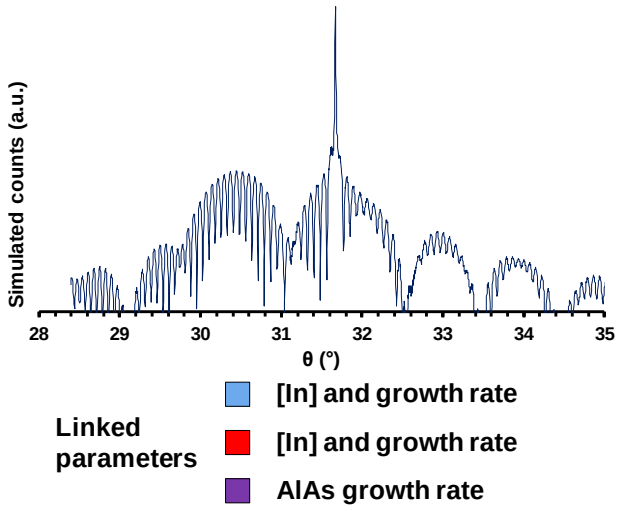


| | Design | | XRD approximation | |
|---|---|---|---|---|
| | $In_{0.8}GaAs$ | 8nm | $In_{0.8}GaAs$ | 8nm |
| | $In_{0.532}GaAs$ | 15nm | $In_{0.532}GaAs$ | 60nm |
| | $In_{0.532}GaAs$ | 25nm | | |
| | $In_{0.532}GaAs$ | 20nm | | |
| | AlAs | 4ML | AlAs | 1.172nm |
| | $In_{0.8}GaAs$ | 15ML | $In_{0.8}GaAs$ | 4.395nm |
| | AlAs | 4ML | AlAs | 1.172nm |
| | $In_{0.532}GaAs$ | 2nm | $In_{0.532}GaAs$ | 422nm |
| | $In_{0.532}GaAs$ | 20nm | | |
| | $In_{0.532}GaAs$ | 400nm | | |
| | $In_{0.52}AlAs$ | 200nm | $In_{0.521}AlAs$ | 200nm |
| | InP sub | | InP | |

**Fig. 4.3.2. Sample $\theta - 2\theta$ rocking curve scan (left) and designed layer structure with used HR-XRD model neglecting doping. The colour-coding uses the schema of Fig. 4.2.3b to reveal intermixing fractions and thickness measures relating to the growth rate of a calibrated epitaxial process.**

The left-hand side of Fig. 4.3.2 is the semilog plot of the $\omega - 2\theta$ symmetrical rocking curve along the (004) direction of the reciprocal space. The horizontal axis shows the angle, which may be expressed in absolute terms (here), or relative to the highest intensity peak, given by the Bragg condition. In this case, this is the InP substrate diffraction. The angle is expressed either in degrees of an arc *or* arc seconds ($1° = 3600\ arcs$), though rarely in radians.

The vertical axis is a measure of arbitrary intensity, in this particular case, expressed as particle counts at a given measurement of $\theta$. To show that the experiment depends on the time-integration, many systems display the counts/second by default. However, the information in the low-magnitude region is important, and decided that the detector particle counts are a more effective way to present the information in this case. Regardless, as the previous description tells, this is a qualitative measure, rather than quantitative, and is mostly interesting with respect to the relative order of magnitude changes, which is why it is always presented in the log scale in this work.

It is of note that the data presented in Fig. 4.3.2 cover $\sim 7$ orders of magnitude, whereas the noise floor of the detector may be reached sooner should the beam be conditioned. In addition, the model assigns arbitrary real numbers to the magnitudes, whereas the detector cannot count a fraction of a particle, devoid of physical meaning. This results in a discretised “low-resolution” window of the

data in low counts regions, and is thus a quantisation/visualisation problem rather separate from the technical capability of the detector.

### 4.3.3. XRD sensitivity analysis

Several steps need undertaking before the complicated rocking curves can be understood and analysed with a minimum of error. A manual sensitivity analysis is performed in this chapter. Several XRD modelling software were used throughout the duration of the work, depending on the physical kit available at the time. As X-ray propagation is highly deterministic [237,238], minimal differences exist between software, with the more advanced types being able to account for X-ray optics, substrate curvature or feature advanced fitting algorithms and industrial/lab-customisable user interface. One of the best royalty-free simulators is available online from the Argonne National Laboratory [239], but does not offer the convenience factor of comparing with arbitrary input data. For the analysis that follows, Bruker DIFFRAC.SUITE LEPTOS was used, attached to a Bruker D8 DISCOVER system. **Malvern** Panalytical (formerly Panalytical) X'Pert software and Jordan Valley Rocking Curve Analysis by Dynamical Simulations (RADS) were also used. In all cases, it is worth noting that the XRD may show unpredictable features should the strained epitaxy relax. Sophisticated software methods can compensate for mosaicity and interface roughness.

Calibration steps are important for the correct set-up and maintenance of an epitaxial growth reactor, such that maximum accuracy and precision are obtained. One such typical calibration would be to obtain the right flow and temperature conditions to obtain InP lattice-matched $In_{.532}Ga_{.468}As$. A typical sample grown in this case could involve a growth attempt of a few hundred nanometers of InGaAs on top of the substrate, or an additional InP buffer. This relatively simple sample may also be measured with ellipsometry techniques.

A pure substrate creates a *Sherrer* peak. When a thin-film of nearly lattice-matched material is grown, this will display Pendellösung fringes (whose width vary with material thickness), and create an additional peak next to the Bragg condition. This is illustrated in Fig. 4.3.3a. The amplitude of the secondary peak

gives an indication of the thickness of the layer, whilst the distance from the peak indicates the amount of compressive or tensile stress.

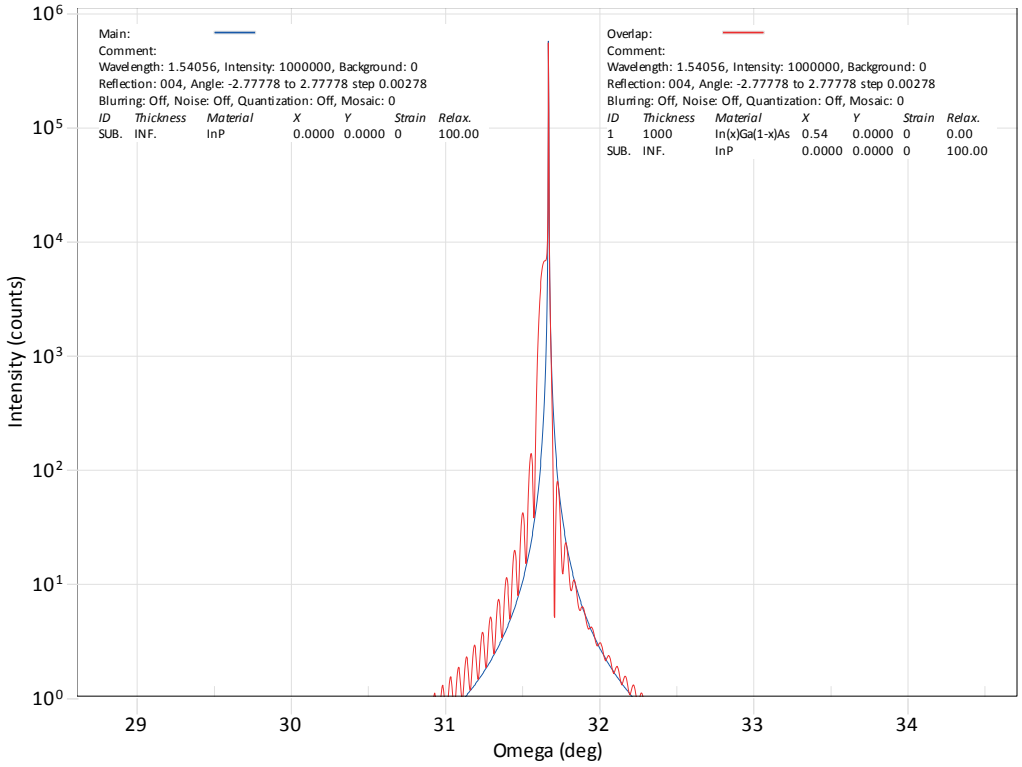


**Fig 4.3.3a Screen capture from Jordan Valley RADS software of simulating 100 nm of $In_{.54}Ga_{.36}As$ on InP**

This concept is then tested by modelling a variation, and linking, all LM-InGaAs mole fractions. Linking the thickness and mole fraction parameters has the expected physical sense of corresponding to epitaxial growth kinematics, i.e. growth rate and atom species migration. It is reasonable to assume that the specified calibration will be maintained for a layer of the same material with a differing thickness. Fig. 4.3.3b attempts a $\pm 5\%$ change in the mole fraction, showing the reference XRD curve in the middle. I would note that this is an exaggerated change for pictorial reasons. A secondary high-intensity peak appears, corresponding to the ~482 nm of InGaAs. In practice, the vast majority of samples were grown within a slightly compressive $-100arcs$ $(-0.027°)$, though sufficient to detect fractional changes with low-resolution (2 orders of magnitude) X-ray equipment. The distance from the peak in arcs is given by the mole fraction, whereas the amplitude of the peak is given by the layer thickness. The layer linking may be removed later to obtain a finer-grain fit.

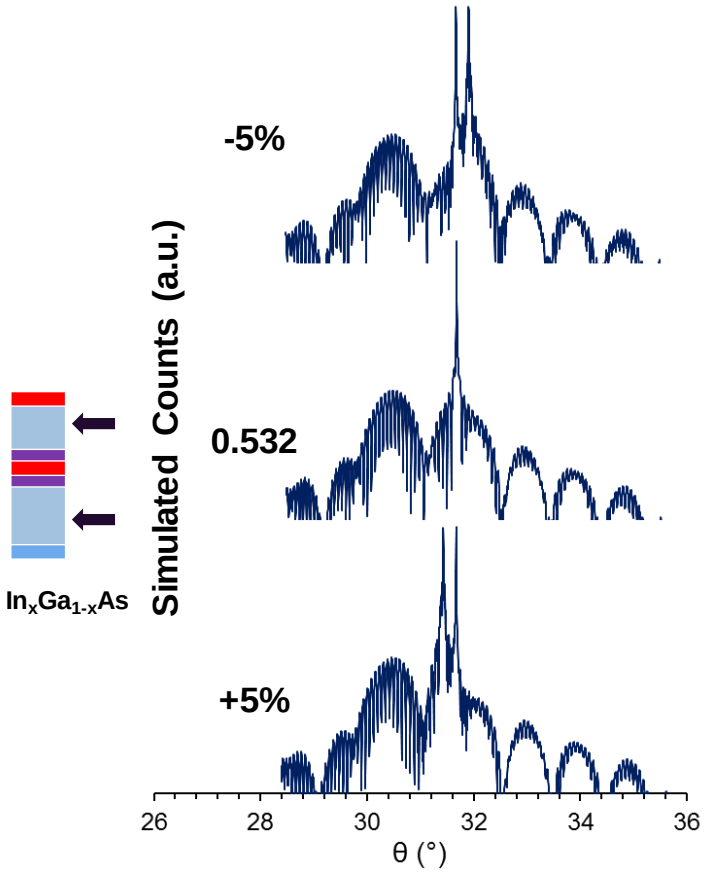


**Fig. 4.3.3b. Comparison of modelled $\omega - 2\theta$ rocking curves of layer-linked InGaAs mole fractions. With $In_xGa_{1-x}As$ x= 0.482 (top), reference lattice-matched (middle), x=0.582 (bottom). Inset modelled layer structure schematic of Fig. 4.3.2. as a guide to the changes.**

The other important concept used in this work is the superlattice. From the growth point of view, repeats of the layers of similar material will cause periodically occurring regions of higher particle counts per rocking angle known as “satellite peaks”. The basic RTD structure behaves as such with the QW and top cap, particularly when both share the InGaAs alloy concentration, and the two LM-InGaAs layers before and after the active regions, albeit their respective differing thickness can have a better analogy with a resonator.

In altering the layer thickness, the expectation is that the growth rate is broadly similar, especially for bulk material outside the limits of immediate channel (or effusion cell for MBE) switching times. Therefore, a sample alteration of $\pm 10\%$ of the growth rate can be expected to lead to a corresponding $\pm 10\%$ variation in layer thickness. This, is of course, assuming that the epitaxial growth operator does not intervene in the automated growth recipe, should the *in-situ* reflectivity plot or RHEED oscillogram suggest that the designed thickness has already been achieved. This is statistically more likely for thicker layers due to

the wider berth given to the operator reaction time, whereas the ML-thin AlAs barriers may well be at the mercy of the calibration, reactor condition, and quality of *ex-situ* characterisation.

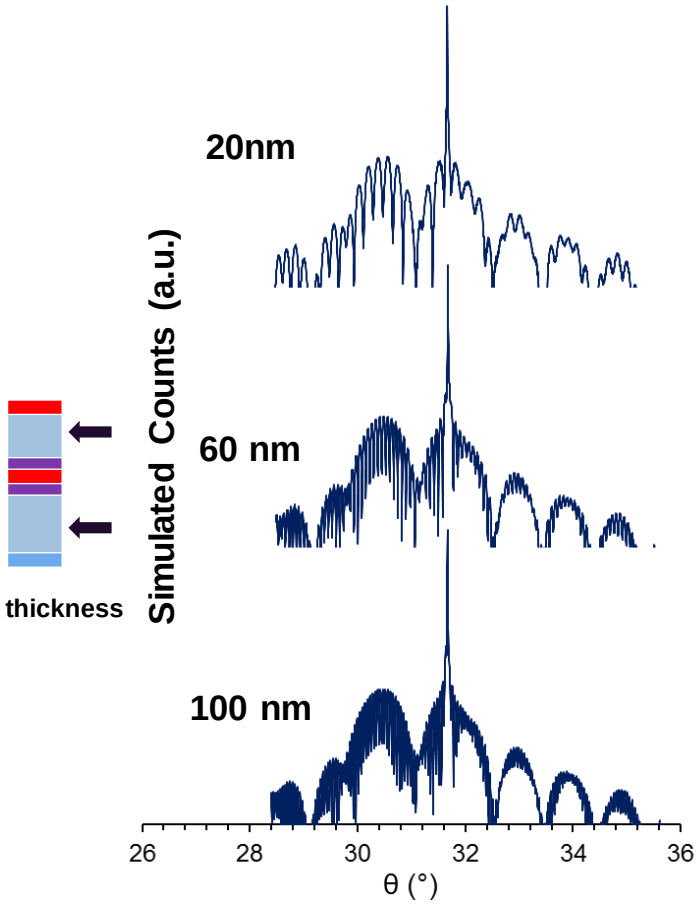


**Fig. 4.3.3c. Comparison of modelled $\omega - 2\theta$ rocking curves of layer-linked LM-InGaAs thickness. With top layer thickness 20nm (top), reference (middle), 100 nm (bottom), and proportional change corresponding to the bottom layer.**

Fig. 4.3.3c illustrates the change of varying the lattice-matched InGaAs layers. The bottom, thicker, layer can be deconvoluted from the top layer in lieu of the higher amplitude it generates. However, the top LM-layer changes the periodicity of the Pendellösung fringes. As the figure shows, this is not easily apparent with slight deviations from the target structure, and instead, is an effect of finesse. Characterising the double barrier single QW system has proven difficult using the PL emission linewidth alone, especially with respect to the difficulty of disassociating the thickness vs. the mole fraction. Fortunately, the entire XRD rocking curve appears to shift towards a more-compressive, or more-tensile region depending on the mole fraction. Fig. 4.3.3d shows this effect, noting the positions in the gaps between the satellite peaks. Due to quantisation noise, it is easier for both the eye, and fitting algorithms to fit to the gaps

rather than the satellite peaks themselves, therefore the highest resolution XRD system is helpful in this particular regard, but can be managed, with difficulty, with ~4 O.M. of usable signal (before quantisation noise). Should the top cap be of the same mole fraction as the QW, this can help boost the particle count, though this top layer is easier to characterise alone as more X-ray photons have a chance for diffraction.

On the other hand, the effect of changing the QW thickness is both subtle and different from the previous effects, working only on the satellite peaks. Fig 4.3.3e shows how the periodicity of the satellites is reduced with an increase in QW thickness, with an overall movement towards the lattice-matched condition. Should higher order of magnitude signals be available, additional satellite peaks may appear at higher rocking angles. This difference in both ends of the stress regime provides an adequate measure of the $In_{0.8}Ga_{0.2}As$ mole fraction.

The change of QW thickness of Fig 4.3.3e contrasts with the modelled adjustment of the AlAs barrier thickness. In Fig. 4.3.3f, comparatively subtle changes are seen in the compressive regimen (left of Bragg angle), whereas the distance and number of satellite peaks in the tensile region are clearly affected for changes as large as 2 ML. Nevertheless, paired with other effects, it is practically difficult to express averages of fractional monolayer changes, particularly as the AlAs diffraction is expected to be diffuse due to the interface roughness.

Therefore, HR-XRD can provide a coarse measurement of the average AlAs barrier. It is insufficient to deduce the thickness using HR-XRD alone, and even with the addition of PL this may be difficult where thicker (>4 ML) barriers are concerned. Therefore, additional dark-field HR-TEM is recommended for barrier characterisation beyond doubt, at least relegated to a periodic inspection of the growth quality. This contribution is experimentally verified in §4.3.5.

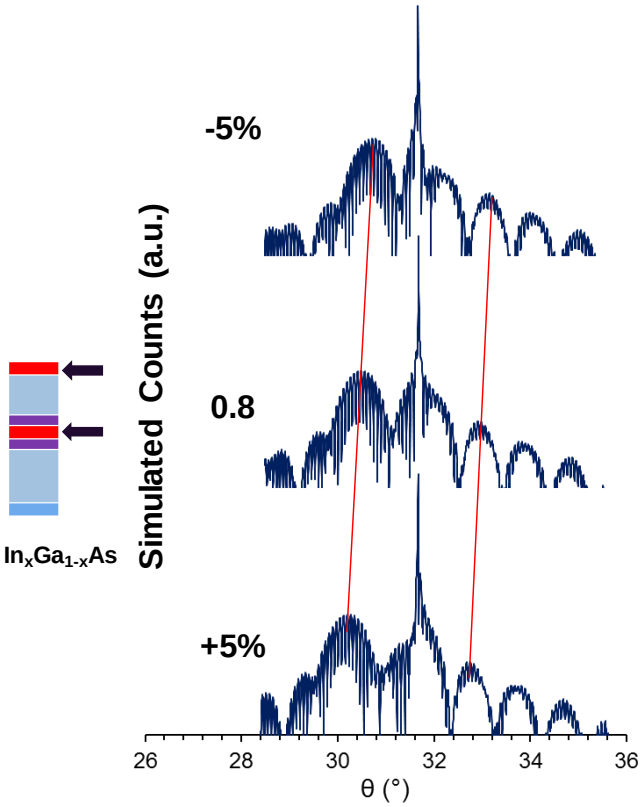


**Fig. 4.3.3d. Comparison of modelled $\omega - 2\theta$ rocking curves of layer-linked $In_{0.8}Ga_{0.2}As$ thickness. With x=0.75 (top), reference (middle), x=0.85 (bottom). Red lines as a guide for the eye.**

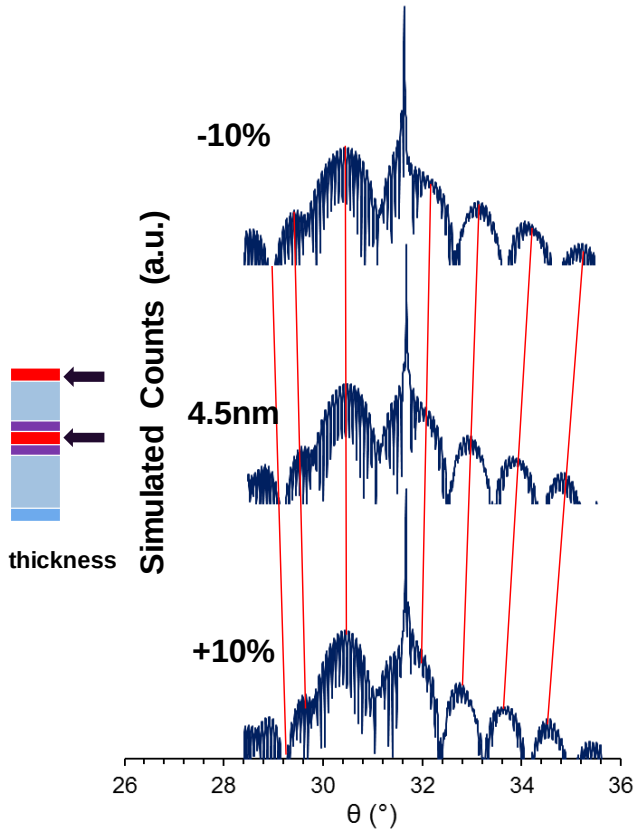


**Fig. 4.3.3e. Comparison of modelled $\omega - 2\theta$ rocking curves of layer-linked $In_{0.8}Ga_{0.2}As$ thickness. With QW thickness 4.05 nm (top), reference (middle), 4.95 nm (bottom), and proportional change corresponding to the top layer. Red lines as a guide for the eye.**

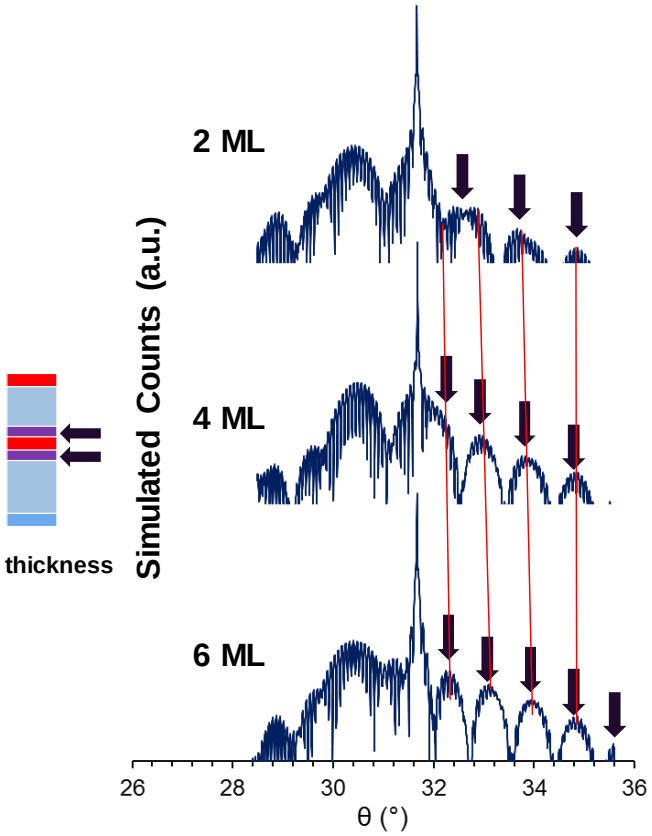


**Fig. 4.3.3f. Comparison of modelled $\omega - 2\theta$ rocking curves of layer-linked $AlAs$ thickness. With 2 monolayer (top), reference (middle), 6 ML (bottom). Red lines as a guide for the eye.**

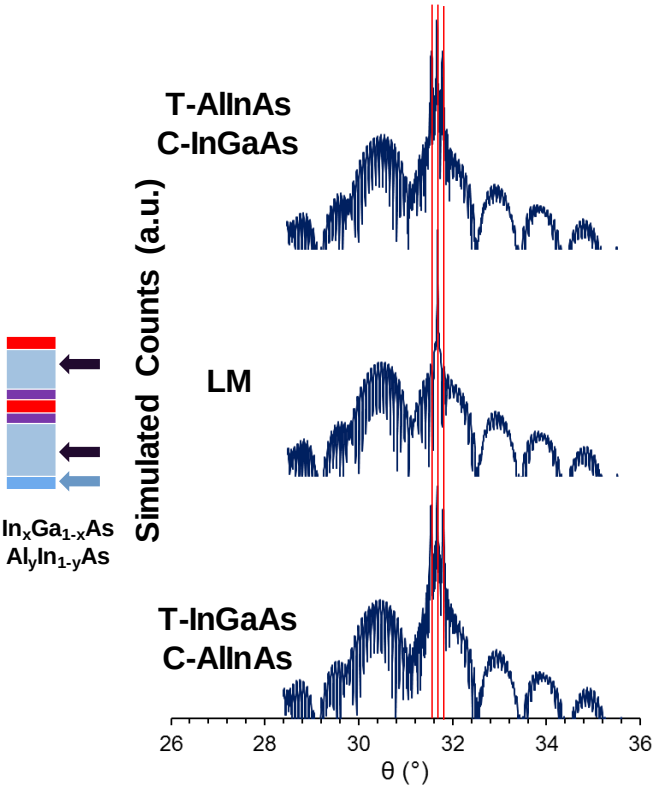


**Fig. 4.3.3g. Comparison of modelled $\omega - 2\theta$ rocking curves of layer-linked InGaAs contrasting with AlInAs thickness. With tensile $Al_{.53}In_{.47}As$ and with compressive $In_{.582}Ga_{.418}As$ (top), reference (middle), and $Al_{.43}In_{.57}As$ with $In_{.482}Ga_{.518}As$ (bottom).**

The AlInAs gettering layer was seen as a necessity in early growth attempts to prevent barrier thickness variation due to residual atomic oxygen incorporation with the highly chemically reactive Al atom species.

Unfortunately, in certain circumstances it is conceivably possible that the effect of the InGaAs vs. AlInAs may not be possible to be detected using HR-XRD alone. Fig. 4.3.3g illustrates such a case where the InGaAs and AlInAs layers have a changed $\pm 5\%$ and $\mp 5\%$ mole fraction, respectively. In practice, this was never observed and AlInAs could always be de-convoluted from InGaAs with ease, also confirmed by LT-PL. (see growth rate comment on Fig. 4.3.4b.)

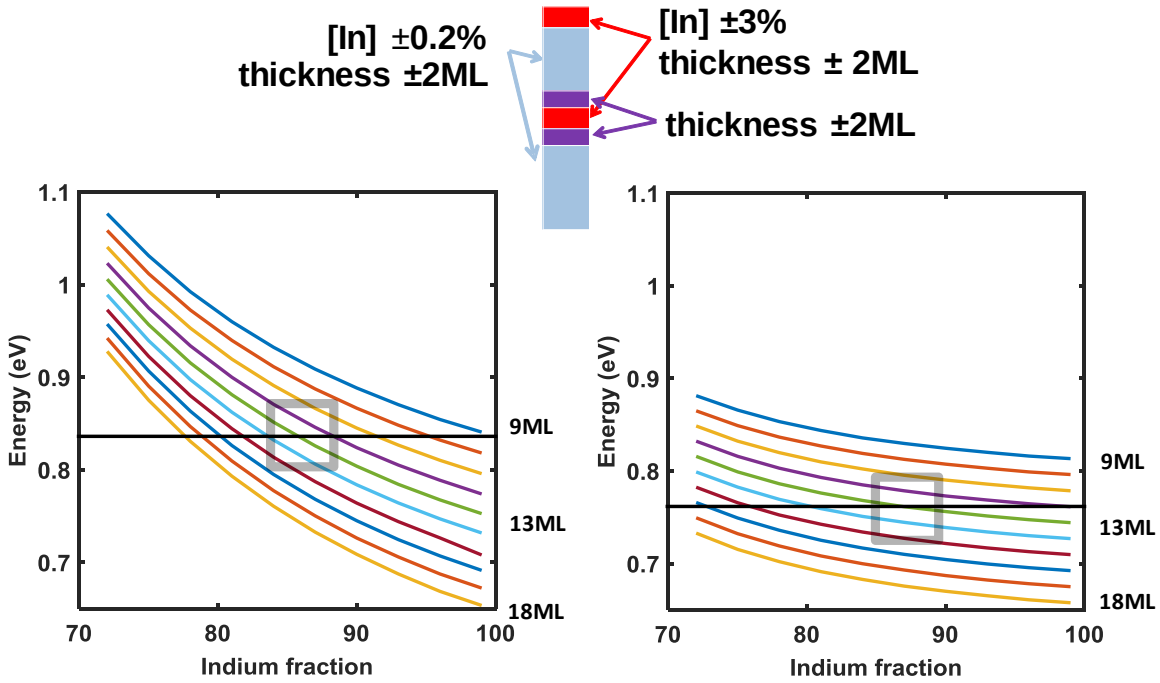


**Fig. 4.3.3h. Type-I (left) and Type-II (right) emission graphs with the PL linewidth marked by a horizontal line and possible structural values due to XRD analysis marked by grey box. The summary of a typical precision of a solitary XRD solution is shown above.**

To summarise thus far, XRD alone still does not provide a unique combination of QW thickness and mole fraction. The possible combinations, conservatively assuming 4 O.M. of signal are available, are highlighted in Fig. 4.3.3h, repeating the graphs of Fig. 4.2.3c, to highlight how the LT-PL linewidth greatly reduces the number of possibilities. It is important to note however, that this PL linewidth is broad due to the contribution of several emitters. Due to its large spot size compared to the wavelength, XRD provides an even larger averaged measure of the QW atomic interface. In the next sections it shown how a 5-O.M. of signal or higher helps extend that precision to ML fractions in ideal conditions.

### 4.3.4. Role of the buried well

Previously, a buried layer was introduced with the aim to improve PL emission qualities and better define the valence band alignment. An investigation is carried out on the impact it carries on the XRD rocking curve.

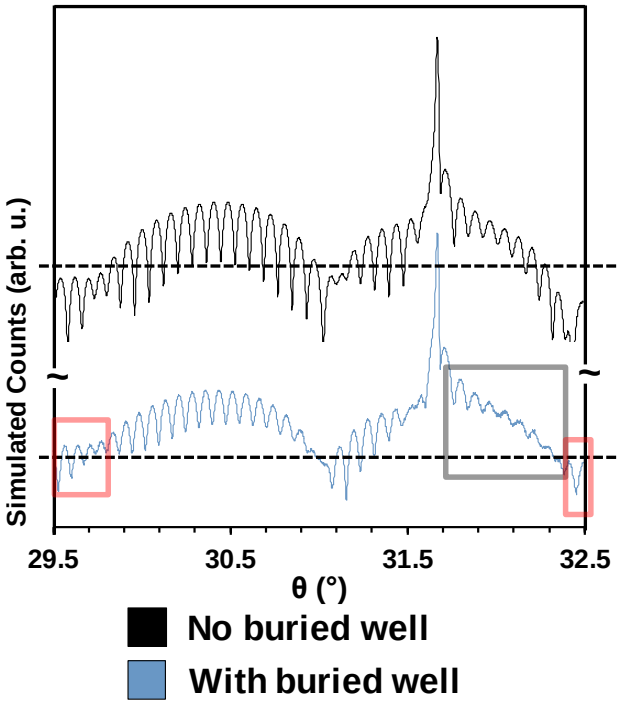


**Fig. 4.3.4a Modelled XRD rocking curve without (top) and with (bottom) the contribution of the buried well. Vertical axes in log scale, arbitrarily separated to facilitate comparison. A typical noise floor is represented with the dashed line. The rectangular boxes represent areas of concern (see text)**

Firstly, a comparative model is performed for the reference structure with and without the buried well, respectively. This result is shown in Fig. 4.3.4a, by setting the noise floor to an arbitrary ~4 O.M. from the peak count. I remind that this specific value depends on the intensity (and age) of the X-ray tube, the detector type, and beam conditioning.

To begin with, the general shape of the graphic is identical, which implies that the buried well does not significantly impact the strain regimen. The 522 nm of lattice matched InGaAs will prevent many crystal defects, except those caused under heavy strain. The disadvantage is that this large layer adds very fine Pendellösung fringes in the tensile (right-hand side of the substrate peak) region of the rocking curve. This behaviour is marked with a grey box, and may conceivably obscure satellite peaks in practice due to noise and quantisation.

It is important to note that for the same noise threshold, generally, the sample with the buried well is expected to detect diffracted photons over a larger rocking range, as highlighted by the red bounding boxes. In these regions, the sample with the buried well, diffracts on average 2x the amount of photons. This is welcoming aid in interpreting the data, particularly when it is close to the noise floor.

One disadvantage appears in the fringes often corresponding to the top ~60 nm InGaAs. The peak/valley magnitude is lowered, but in all cases studied, insufficiently so to be a cause of concern.

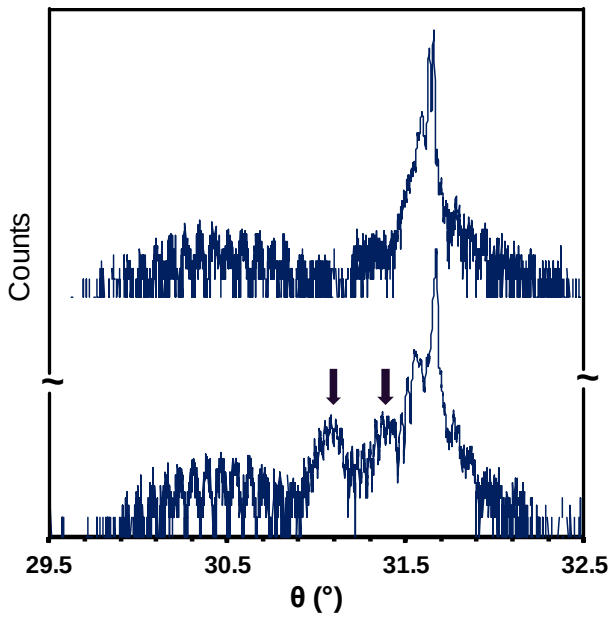


**Fig. 4.3.4b. Measured HR-XRD rocking curve of TS1904 4nm buried well (top) and TS1902 4.4 nm no buried well (bottom). The anomaly in TS 1902 is not seen in other wafer samples (see text).**

Fig. 4.3.4a predicted that the detected particle count is increased at the expense of an increase in Pendellösung fringes. Given an angular resolution (typically continuous, slow motor movement) and integration rate, it may be possible to confuse this as noise due to quantisation error. However, despite this complication, in lieu of the increased signal, this now allows the determination of the mole fraction of the InGaAs QW with better certainty, particularly as the features in the higher angle range can be seen more clearly.

Fig 4.3.4b compares two normally identical samples with (TS1904, top) and without (TS1902 bottom) the buried well, respectively. The thickness of the

active region layers is confirmed by averaging medium-resolution dark-field TEM images presented later in §4.4. In this comparison, an anomaly may be spotted in TS1902, XRD curve fitting has revealed that this may be caused by the sub-emitter regions (22 nm) $In_{.65}Ga_{.35}As$ (c.f. LM-InGaAs). This change is consistent with the growth sheet, where the growth rate for the contact layers is significantly slowed down (0.2392 nm/s vs. 0.0977 nm/s) to allow more Si diffusion. Since this region is intended as the collector, it will not adversely affect $E_1$ levels. The QW was fit to 4.4 nm, in line with growth rate predictions. No anomalous Trimethyl-In or Trimethyl-Ga channel flow rates were reported, and no reflectivity problems were reported. LT-PL could not confirm this presence ~950 eV (Fig. 4.2.2b), and TEM could not reliably reveal this information either, expected due to non-linear grey level/contrast dependency on Indium mole fractions [240].

## 4.3.5. HR-XRD and barrier thickness

Thus far, models predicted that the gross barrier thickness can be detected with HR-XRD, and the buried well increases the received signal by ~3dB. The same samples from §4.2.5 are used, designed nominally identical with symmetric 4, 3, and 2 ML AlAs barriers, respectively.

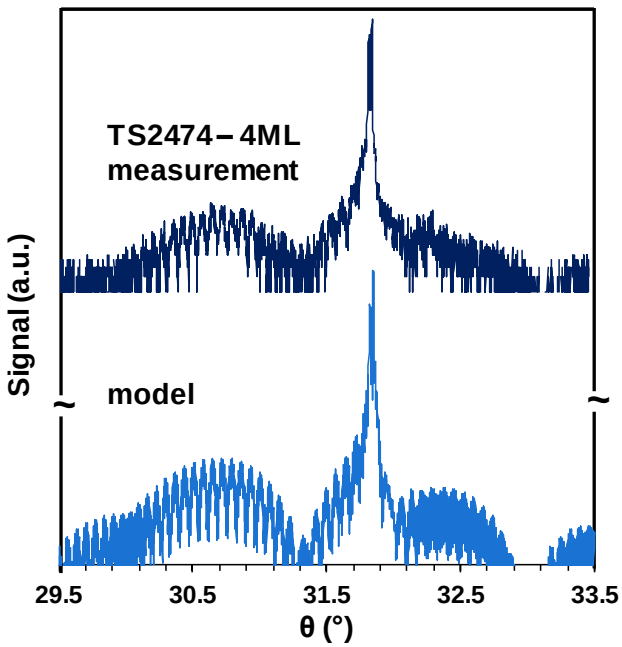


| | Design | | XRD fit | |
|---|---|---|---|---|
| | $In_{0.8}GaAs$ | 8nm | $In_{0.8}GaAs$ | 8 nm |
| | $In_{0.532}GaAs$ | 20nm | | |
| | $In_{0.532}GaAs$ | 25nm | $In_{0.532}GaAs$ | 65.4nm |
| | $In_{0.532}GaAs$ | 20nm | | |
| | AlAs | 4ML | AlAs | 1.2nm |
| | $In_{0.85}GaAs$ | 12ML | $In_{0.82}GaAs$ | 3.6nm |
| | AlAs | 4ML | AlAs | 1.0nm |
| | $In_{0.532}GaAs$ | 2nm | | |
| | $In_{0.532}GaAs$ | 20nm | $In_{0.537}GaAs$ | 525nm |
| | $In_{0.532}GaAs$ | 400nm | | |
| | $In_{0.532}GaAs$ | 100nm | | |
| | AlAs | 4ML | AlAs | 1.2nm |
| | $In_{0.85}GaAs$ | 13ML | $In_{0.82}GaAs$ | 3.6nm |
| | AlAs | 4ML | AlAs | 1.0nm |
| | $In_{0.532}GaAs$ | 100nm | $In_{0.532}GaAs$ | 100.6nm |
| | $In_{0.52}AlAs$ | 200nm | $In_{0.521}AlAs$ | 200nm |
| | $In_{0.532}GaAs$ | 25nm | $In_{0.532}GaAs$ | 25.2nm |
| | InP sub | | InP | |

**Fig. 4.3.5a. Measured & modelled HR-XRD $\omega - 2\theta$ rocking curves of TS2474 4ML AlAs. The results of the fit are presented in the table, and the colour coding is to suggest layer-linking.**

The same methodology was employed as before. Fig. 4.3.5a presents a partial fit of TS 2474. This structure provided a challenge to the fit process; despite the Nomarski surface morphology having a low defect count with no evidence of line or screw defects, as well as strong LT-PL emission, the stress & strain regimen is noticeably different from the other samples: the low-angle strained InGaAs fringes could not be reproduced with good fidelity, nor the high-tensile region gap at ~33°. The median fit of the LT-PL linewidth of at 840 meV suggests a QW combination of either 11 ML with x=0.88, 12 ML with x=0.86, or 13 ML with x=84. In the end, a nearest-neighbour fit algorithm offered a compromise solution of ~12.5 ML QW with x=0.82, but slightly asymmetric barriers to compensate the strain. Given that the LT-PL Type-I emission was broad, this is not scenario is not in disagreement with the data presented, and is likely to be a gross average.

Furthermore, wafers TS 2475 and TS 2476 had reported problems with fluctuations in disilane flow. If this problem began to manifest itself with TS 2474, it may be conceivable that the silicon atoms had an effect on overall stress, as evidenced by surface studies in Ref. [194].

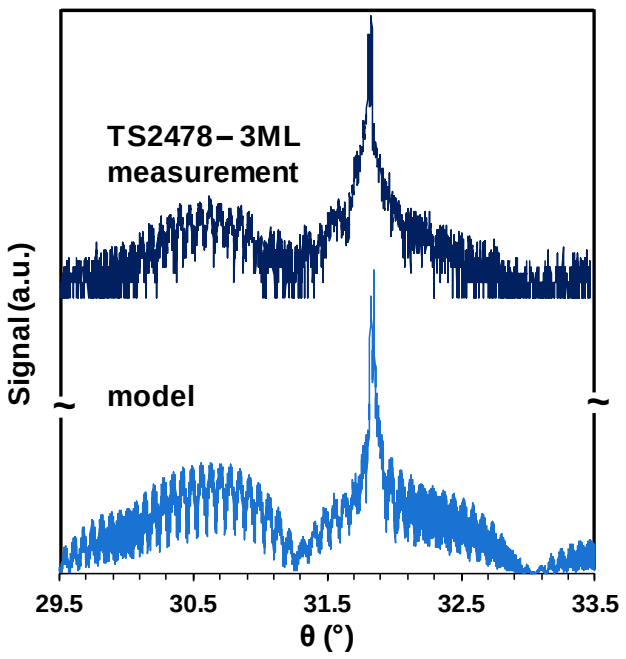


| | Design | | XRD fit | |
|---|---|---|---|---|
| | $In_{0.8}GaAs$ | 8nm | $In_{0.8}GaAs$ | 8 nm |
| | $In_{0.532}GaAs$ | 20nm | $In_{0.532}GaAs$ | 65nm |
| | $In_{0.532}GaAs$ | 25nm | | |
| | $In_{0.532}GaAs$ | 20nm | | |
| | AlAs | 3ML | AlAs | 1nm |
| | $In_{0.85}GaAs$ | 12ML | $In_{0.85}GaAs$ | 3.2nm |
| | AlAs | 3ML | AlAs | 1nm |
| | $In_{0.532}GaAs$ | 2nm | $In_{0.536}GaAs$ | 525nm |
| | $In_{0.532}GaAs$ | 20nm | | |
| | $In_{0.532}GaAs$ | 400nm | | |
| | $In_{0.532}GaAs$ | 100nm | | |
| | AlAs | 3ML | AlAs | 1nm |
| | $In_{0.85}GaAs$ | 12ML | $In_{0.85}GaAs$ | 3.2nm |
| | AlAs | 3ML | AlAs | 1nm |
| | $In_{0.532}GaAs$ | 100nm | $In_{0.532}GaAs$ | 100nm |
| | $In_{0.52}AlAs$ | 200nm | $In_{0.521}AlAs$ | 200nm |
| | $In_{0.532}GaAs$ | 25nm | $In_{0.536}GaAs$ | 25.4nm |
| | InP sub | | InP | |

**Fig. 4.3.5b. Measured & modelled HR-XRD $\omega - 2\theta$ rocking curves of TS2478 3ML AlAs. The results of the fit are presented in the table, and the colour coding is to suggest layer-linking.**

The wafer with 3 ML AlAs in Fig. 4.3.5b did not show the extent of stress problems compared to the 4 ML wafer. An apt fit was obtained with slightly thicker AlAs barriers but a thinner QW. This is consistent with HR-TEM

observations at the ternary/binary interface, where [In,Ga] atom species may not hold well-defined pattern in the lattice.

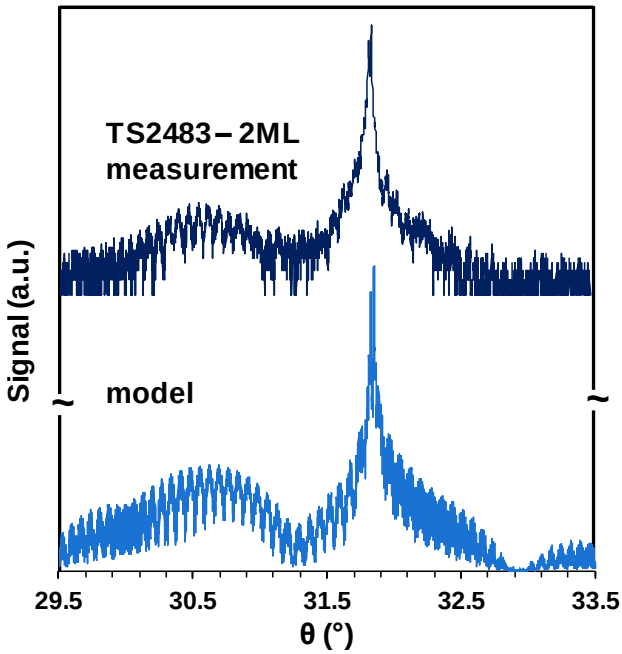


| | Design | | XRD fit | |
|---|---|---|---|---|
| | $In_{0.8}GaAs$ | 8nm | $In_{0.8}GaAs$ | 8 nm |
| | $In_{0.532}GaAs$ | 20nm | | |
| | $In_{0.532}GaAs$ | 25nm | $In_{0.532}GaAs$ | 65nm |
| | $In_{0.532}GaAs$ | 20nm | | |
| | AlAs | 2ML | AlAs | 0.7nm |
| | $In_{0.85}GaAs$ | 12ML | $In_{0.85}GaAs$ | 3.2nm |
| | AlAs | 2ML | AlAs | 0.7nm |
| | $In_{0.532}GaAs$ | 2nm | | |
| | $In_{0.532}GaAs$ | 20nm | $In_{0.536}GaAs$ | 525nm |
| | $In_{0.532}GaAs$ | 400nm | | |
| | $In_{0.532}GaAs$ | 100nm | | |
| | AlAs | 2ML | AlAs | 0.7nm |
| | $In_{0.85}GaAs$ | 12ML | $In_{0.85}GaAs$ | 3.2nm |
| | AlAs | 2ML | AlAs | 0.7nm |
| | $In_{0.532}GaAs$ | 100nm | $In_{0.532}GaAs$ | 100nm |
| | $In_{0.52}AlAs$ | 200nm | $In_{0.521}AlAs$ | 200nm |
| | $In_{0.532}GaAs$ | 25nm | $In_{0.536}GaAs$ | 25.4nm |
| | InP sub | | InP | |

**Fig. 4.3.5c. Measured & modelled HR-XRD $\omega - 2\theta$ rocking curves of TS2483 2ML AlAs. The results of the fit are presented in the table, and the colour coding is to suggest layer-linking.**

The same effect in ML halves was seen on the 2 ML structure of Fig. 4.3.5c. The only necessary adjustment performed is a subtraction of 1 ML from the AlAs thickness compared to the previous case. The Type-I PL emission was notably shifted compared to the 3, 4 ML case, however, this was expected. XRD confirms that the shift is not additionally due to the indium mole fraction or other compositional modulation factors.

## 4.4 CELFA-TEM

Interpretation of HR-XRD data can provide a remarkably accurate characterisation of the double barrier—QW system. The solution, even with the addition of LT-PL is not unique. PL linewidths tend to be broad, with estimated carrier lifetimes within 30-200 fs, and XRD itself providing limited information should the sample stray from the pseudomorphic condition.

Whilst secondary ion mass spectroscopy has the relative advantage of speed, it still cannot provides an average of measurements where the ion beam impacts the sample. For ultimate interface characterisation, TEM remains an

indispensable tool. Specifically, dark field TEM employs diffraction pattern apertures to block the direct beam. This allows only the sample-interacting diffracted beam to pass [216,217]. As with optical microscopy, the disadvantage is reduced image intensity and the potential contrast issue if long exposure times are not possible (due to oxidation or low activation energy samples, for instance).

The TEM sample preparation and imaging was performed by Integrity Scientific Ltd. To prepare a TEM specimen, cleaving the wafer, then a focused ion beam miller is employed to section off a required device. Since the specimen was a virgin wafer surface after growth, mainly thinning was required. The 2 inch InP substrate is 350um thick, requiring thinning at ~100 nm around the active region of the RTD for optimum transmission. Since InP is a particularly fragile material (MOHS hardness 3), there is a high failure rate associated with handling the thin film. A chemically-sensitive beam in the [002] is employed in the TEM itself, with suitable acceleration voltage and careful focusing. Any astigmatism in the image may result in shadows or attempting to interpret data which has otherwise no physical meaning, and due to the high magnification (100kX to 300kX), the alignment process is more laborious and crucial than common SEM usage might be. The resulting image is a 32-bit-per-pixel bitmap-like image, lending itself to processing in common microscopy & image processing software.

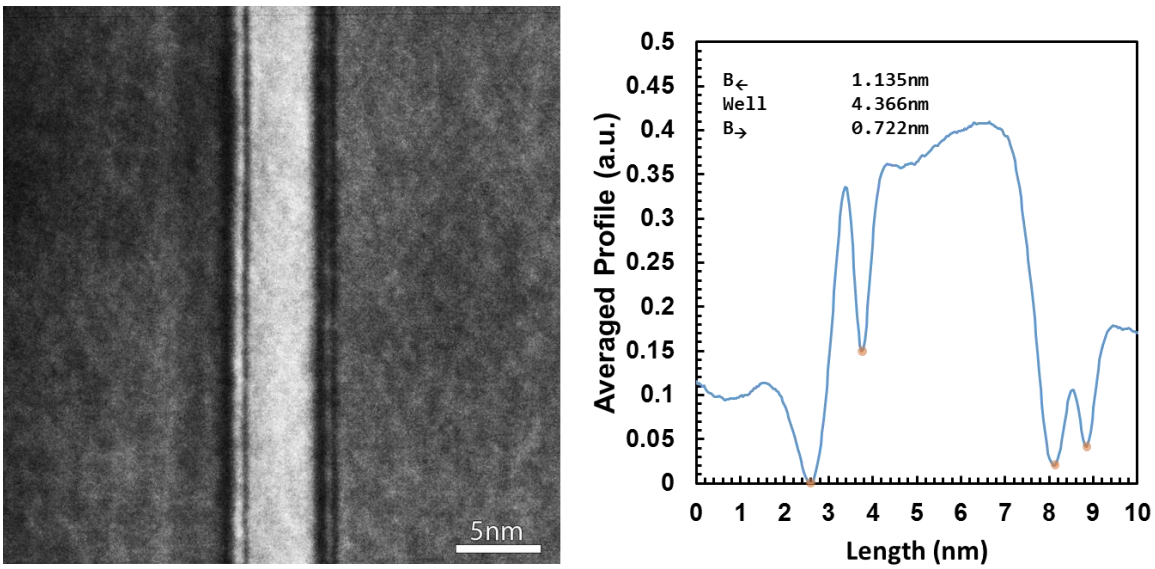


**Fig 4.4a [002] Dark field TEM image of TS1009 active region, ~200kX magnification, with artificially enhanced linear contrast for the eye (left). Unintentionally asymmetric AlAs barriers(dark) and strained QW(light) in centre. Plot of averages of horizontal slices of grey levels around the region of interest (right), where 0= black and 1= white, normalised to pixel depth. Shown with measurements of barriers and QW at the turning points.**

Fig. 4.4a shows a dark field image of TS 1009 wafer. The scale bar is an estimation based on the metafile data. Most native resolution TEM images at this had >29 bitmap pixels / 1 nm. The linear contrast and brightness of the image themselves are enhanced for display purposes, but the data processing is done on the raw image itself. Unkempt image alterations may result in gamut (saturation of pixel amplitude), therefore a clipping/quantisation distortion of the image. A rectangle is then dragged in ImageJ software, and the "Plot profile" is used. This function takes 1 pixel-wide horizontal slices and performs an average on the amplitude (grey level) of the bitmap information along the horizontal axis. This result is displayed in the figure. Contrast modulations correspond to new layers or variations in mole fractions. The image itself is an average of the diffraction pattern filtered by the TEM image, and thus not a truly atomistic representation.

This sample was intended to be nominally identical to the reference structure, with a 15 ML $In_{0.8}Ga_{0.2}As$ QW. A wafer from an identical run was used to generate 353 GHz [181]. However, a stark I-V characteristic asymmetry in forward and reverse bias was observed [177], perhaps beyond expectation given that both undoped spacer are relatively short. TEM analysis then reveals the reason for the high current peak exceeding 1.7 MAcm$^{-2}$: the barrier closer to the substrate, in this case the right hand side barrier, is 2 ML instead of the intended 4 ML. Moreover, significant compositional modulation (appearing as parallel bands) occurs after the 2$^{nd}$ AlAs barrier. This was attributed to the unique way the gas sources are diluted and switched in the MOVPE reactor at hand.

The real problem is measuring the layer thickness in these average DF images, and whether this measurement is cannot be misinterpreted. For this purpose, it is important to acknowledge that the image is the result of the interaction of diffracted electron-waves with a sample and the instrument's optics. For the latter, experimental error is always a consideration, particularly when the experimenter does not have prior knowledge of the material pair handled. Therefore, in such cases, the thin low-intensity shades marking a turning point in the profile which are used as a marker for an interface may, in some cases be misleading. Regardless, as flawed as it is, this method is an improvement in

accuracy over XRD, which may, at best, detect ½ ML instead of fractions of Angstrom with DF-TEM (quantisation error $\pm 0.04\ nm$).

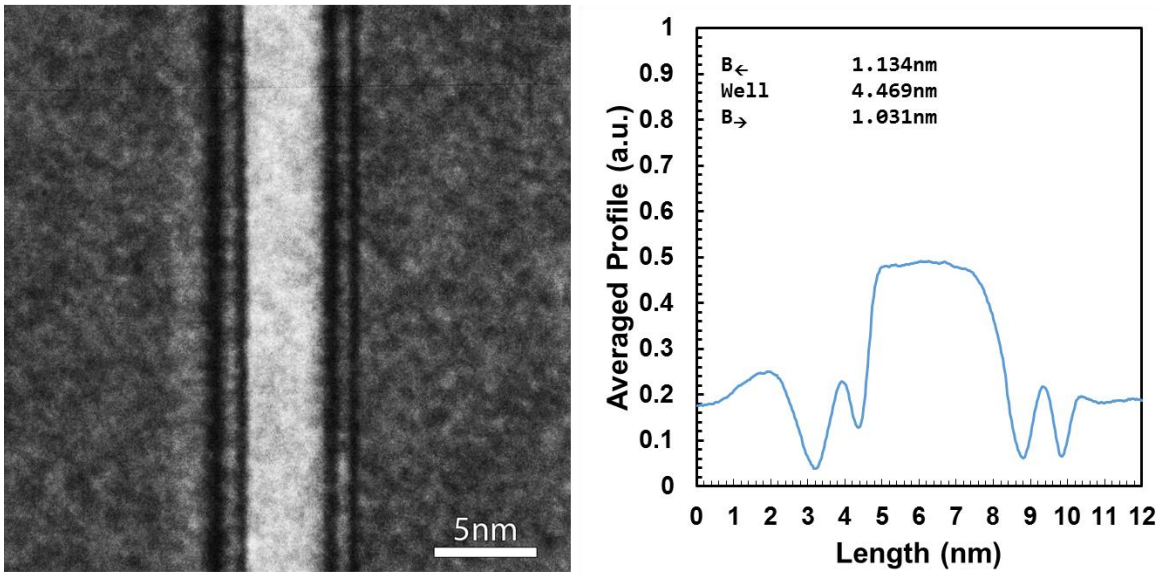


**Fig 4.4b [002] Dark field TEM image of TS1902 active region, ~200kX magnification, with artificially enhanced linear contrast for the eye (left). AlAs barriers and strained QW in centre. Plot of averages of horizontal slices of grey levels around the region of interest (right), where 0= black and 1= white, normalised to pixel depth.**

This method is repeated for the TS 1902 sample previously tested. A weak 9.08% barrier asymmetry is detected, but more importantly, the QW is as expected. Some of the compositional modulation remains, but this is comparatively thin compared to the 22-25 nm prediction of a $In_{.65}Ga_{.35}As$ region causing a strain-triggered diffraction pattern in the rocking curve. This highlights the difficulty in attributing specific grey values to a chemical composition.

The images presented however do not describe with good accuracy the material interface. An exceptionally high resolution technique, High-angle annular dark field imaging, employs a specialised ring-shaped detector around the backscattered beam, and, in this case extends to high angles to capture incoherently scattered electrons which have interacted with atomic nuclei. This technique produces superb images, but due to the extra attention required to prepare an ever-thinning specimen, it is not commonly used in production environments, being mainly reserved for one-off scientific, fault characterisation and/or intellectual property investigations.

An alternative suggestion is to employ Composition Evaluation by Lattice Fringe Analysis (CELFA) technique [241]. This involves obtaining an interference pattern

from the (000), (004), and (002) beams, with the result of showing contrast regions corresponding to each stacked plane.

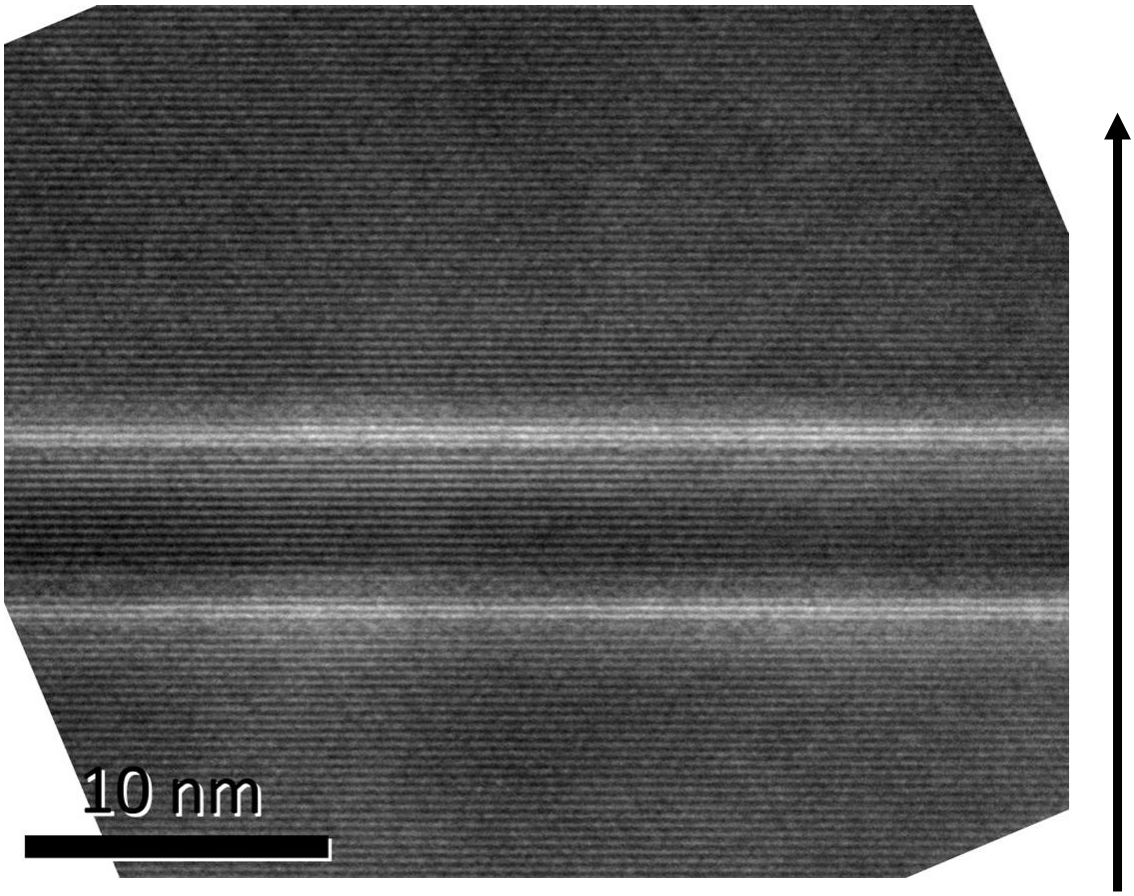


**Fig. 4.4c. TS 2390 bottom UD layer 15 ML InGaAs QW of test structure CELFA TEM (002) dark field image ~500kX magnification, digitally rotated and with artificial contrast enhancement for viewing. Arrow indicates growth direction.**

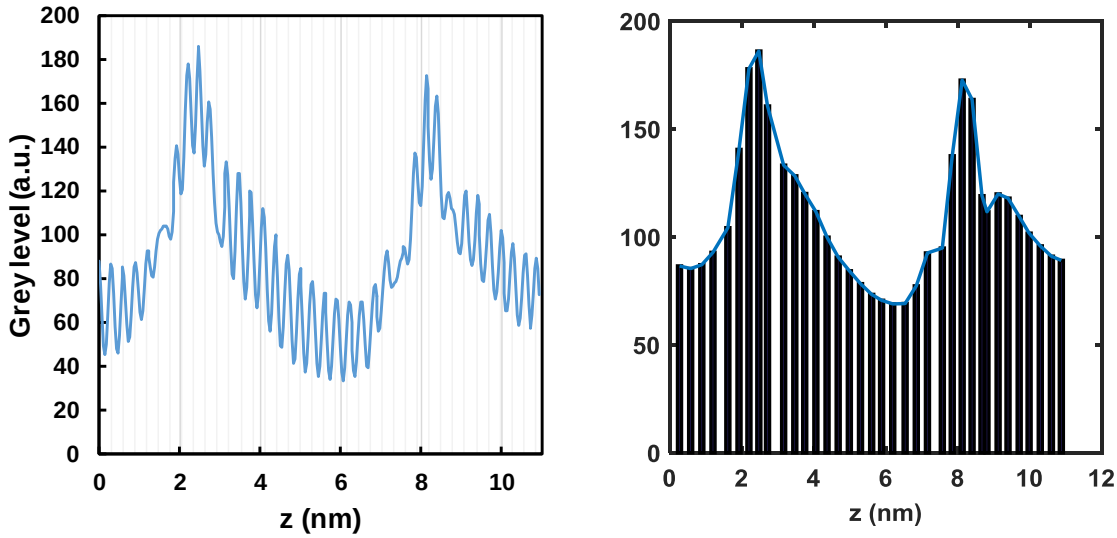


**Fig. 4.4d. Plot of averages of 15 ML QW horizontal slices of grey levels across the growth direction, with a 0.293nm grid as a guide for the eye (left). Fringe peaks plotted as bars of an arbitrary size (right).**

CELFA-mode images were obtained for test structure TS2390 consisting of a stack of 15 ML $In_{.8}Ga_{.2}As$ (Fig. 4.4c) and 12 ML $In_{.85}Ga_{.15}As$ (Fig 4.4e), in their

doped and undoped versions. Here, the UD versions closer to the substrate are presented. Each fringe is expected to correspond to the lattice peak. However, the raw TEM image are difficult to follow for the eye. Thus *Fig. 4.4d* shows the result of the same technique of slice gray level averaging. The fringes are visible as oscillations of the contour. In order to present the quality of the lattice ad-extension (pseudomorphic growth), the local maxima of each fringe is plotted in a bar chart, against its relative position on the position axis. In Fig 4.4c & d, a count of exactly 15 ML can be found between the 2 points where the AlAs barriers are expected to be found. The thickness of the AlAs barriers is harder to discern on this plot alone (4-5 ML) but the binary/ternary mismatch is apparent due to the irregular spacing at their interface.

The wafer miscut for these particular wafers is $0.13°$. The miscut is necessary to facilitate MOVPE nucleation. This can potentially result in a terracing effect of the growth. As $\cos 0.13° = 0.99999742$, for a 2000 nm radius device the plane length is 2000.0051 nm. The difference is within the lattice half-radius, therefore interface non-uniformity cannot be attributed to this effect alone.

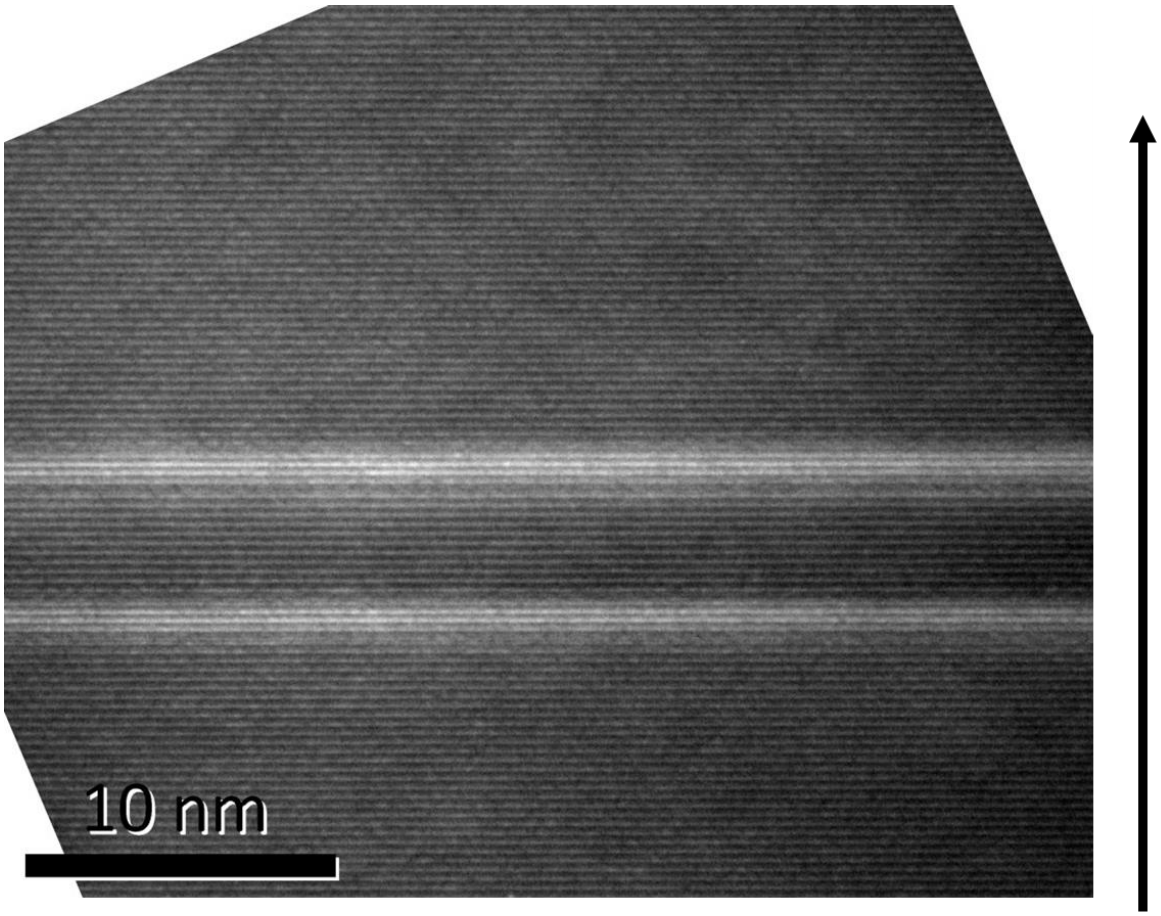

**Fig. 4.4e. TS 2390 2nd UD 12 ML InGaAs QW from bottom of test structure CELFA TEM (002) dark field image ~500kX magnification, digitally rotated and with artificial contrast enhancement for viewing. Arrow indicates growth direction.**

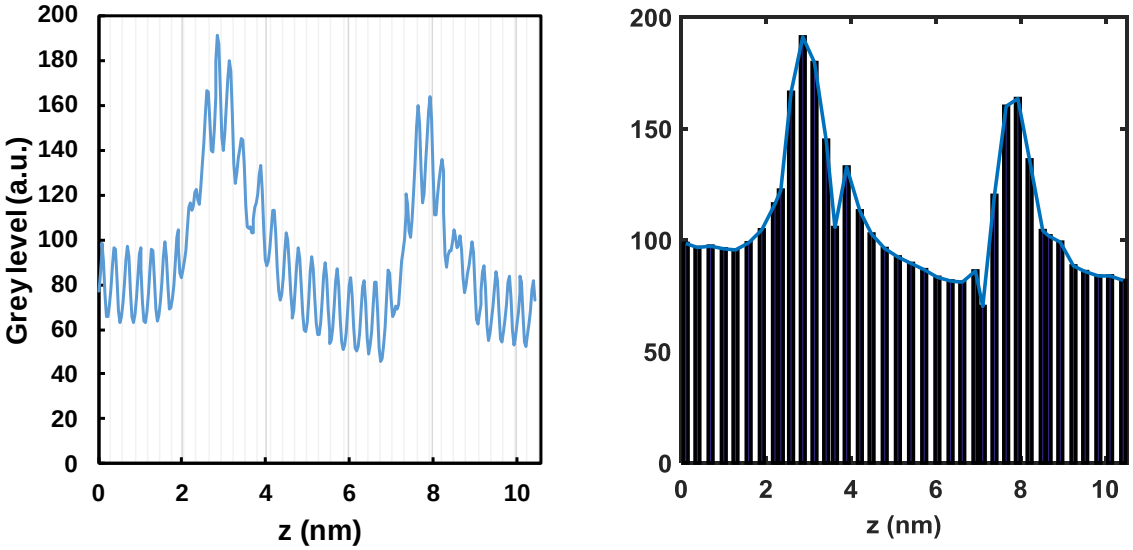


**Fig. 4.4f. Plot of averages of 12 ML QW horizontal slices of grey levels across the growth direction (left). Fringe peaks plotted as bars of an arbitrary size (right).**

In the case of the 12 ML QW (Fig 4.4e & f), the situation changes. 11 ML may be clearly attributed to the InGaAs alloy, whereas the low amplitude peaks at the interface could signify uncertainty of the migration of the In, Al atom species in their respective sites. One possible interpretation is to assign each such low-intensity fringe a 0.5 ML value. It is worth reminding that the accumulated stress is different in this case, due to the higher [In] mole fraction.

In order to visually highlight the interface roughness in a better human-readable form, the following procedure was applied to the images:

- Lossless images cut/crop to active region
- Apply unsharp mask transform with a 0.5 pixel (arbitrary value) radius and a standard deviation of 20 pixel, ensuring that the standard deviation causes <0.05% gamut (grey level saturation)
- Apply Sobel edge filter in the direction parallel to the fringes only (also known as “find edges”), 50% mix with original image to preserve contour shape. Further contrast adjustment, as needed.
- (optional) after unsharp mask, create another image with a grey-level pass at 85% of the grey threshold of AlAs peaks

These changes are presented in Fig. 4.4g for both TEM images. It is now possible to observe that all fringes follow a straight line pattern, except at the interface,

where the fringe line is thicker and discontinuous, where the filtered interference pattern suffered significant diffraction.

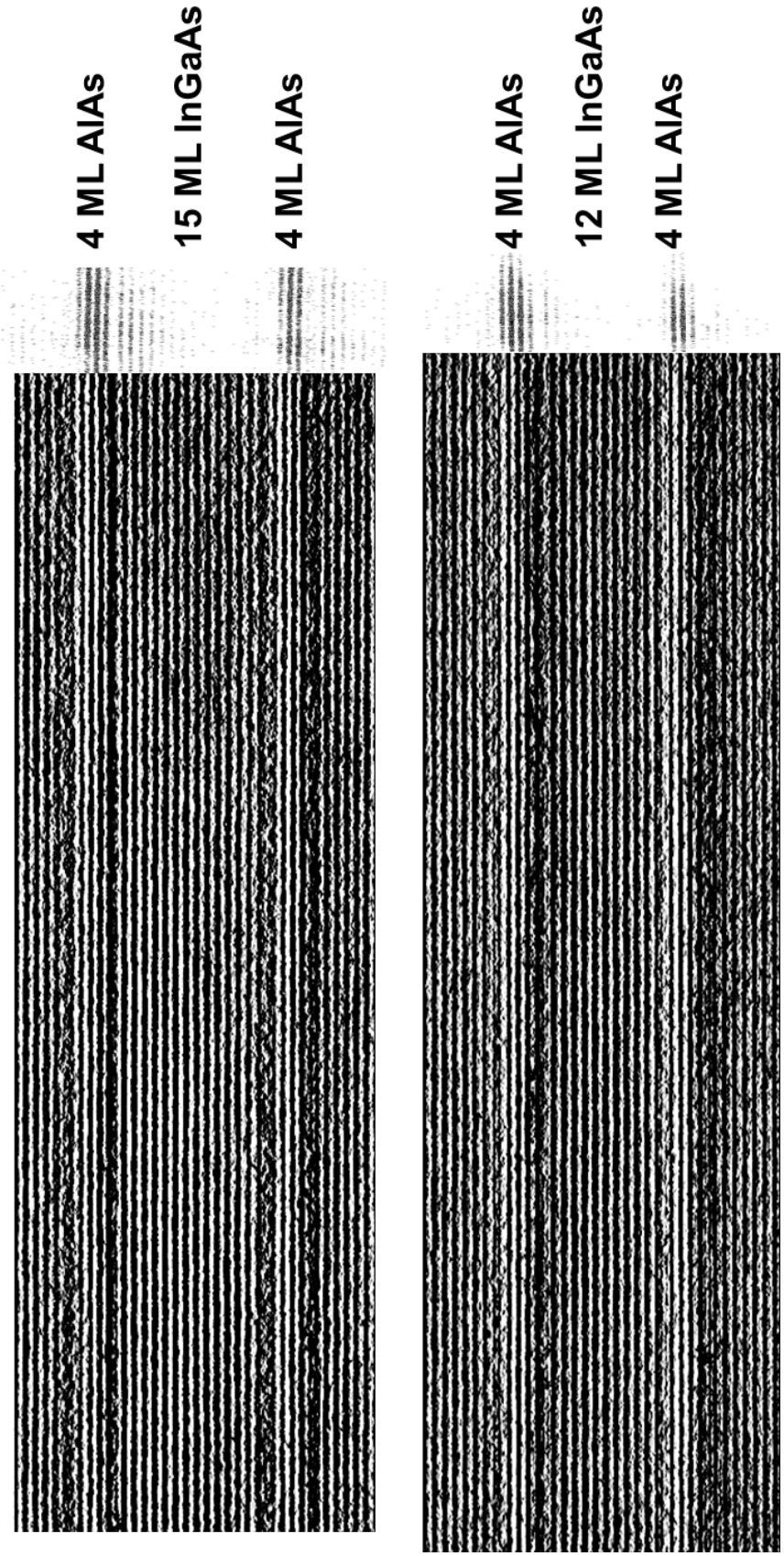


**Fig. 4.4g. Sobel-transformed images (direction parallel to fringes), after unsharp mask and non-linear contrast to enhance interface edges from Fig. 4.4c&e. Top figures are narrow-band grey level contours set at 80% of the AlAs maximum, resized for clarity.**

## 4.5. Summary and Further work

### 4.5.1. Towards automated characterisation equipment

LT-PL can be a very slow methodical process that requires significant user interaction. Currently, there are several user-unfriendly steps in place:

- Difficult sample mounting. Using cryostat-rated vacuum grease for guaranteed thermal bonding is not only expensive, but it is a laborious, time-consuming process with a failure rate associated with it. Highly strained wafers do not mount well to a flat cold finger.
- Pump down & cooling time. Temperature-dependent PL has shown adequate features can be seen below 100K, within the reach of nitrogen temperature. A wet nitrogen cryostat reaches equilibrium significantly quicker than the equivalent closed-cycle pump, but it does require access to liquid nitrogen, and the precautions that entails.
- Monochromator scan time. The system uses an opto-mechanical monochromator to obtain a linewidth, largely due to availability. An order of magnitude increase in speed may be achieved by replacing the 0D detector with a 1D InGaAs array, such that it can snapshot a wide spectral region directly from the diffraction grating. Tests were carried out for room temperature PL with a diffraction grating of 300 groves/mm and a Blaise $\lambda = 1250\ nm$, yielding a usable spectra of ~170 nm per snapshot. The entire InGaAs responsivity range can be covered by 6 data points. If the system can be designed to be micro-actuated, this can be achieved in fraction of a second.

Professional room-temperature PL spectroscopy equipment may achieve a peak-wafer scan in a matter of minutes by the use a spiral motion, using a rotational & actuating stage. In our case, only X-Y stages were available, further complicated by the presence of high-vacuum hoses. Designing a system with bespoke parts, where this problem is removed is in the realm of possibility.

The real impediment however, is software. Industrial users may be quick to point out that there very few pieces of software which have sufficient flexibility to account for all processing needs on a tool inside a fab or foundry. The problem is the programming paradigm: the designer created the tool with a few common processes in mind, and perhaps tested them on these specific limit-cases, but may not have thought broadly enough to include ways to extend the

functionality. Most often, such software may include a way to attach batch files or custom scripts, which in a mature company, may lead to a labyrinthine mine field of deprecated code, hidden functions and abandoned projects.

To give a trivial example, in the case of spectroscopy of a wafer, a particular point may not offer a clear spectral feature, or the spectra itself may not lie within the limits chosen by the user. Whilst this behaviour can be rectified with any linear programming language methodology, in a complex research & low-volume fab environment dozens of variables could change at any given time. The system must be defensively programmed to not only account for situations where auto-processing goes wrong, but it has to understand the physics empirically, such that the system may do empirical corrections a human operator would. An automated tool that could do all of this on a routine basis with minimal input may mean that the company could afford to continue the project, or sell a THz transceiver chip for a lower price.

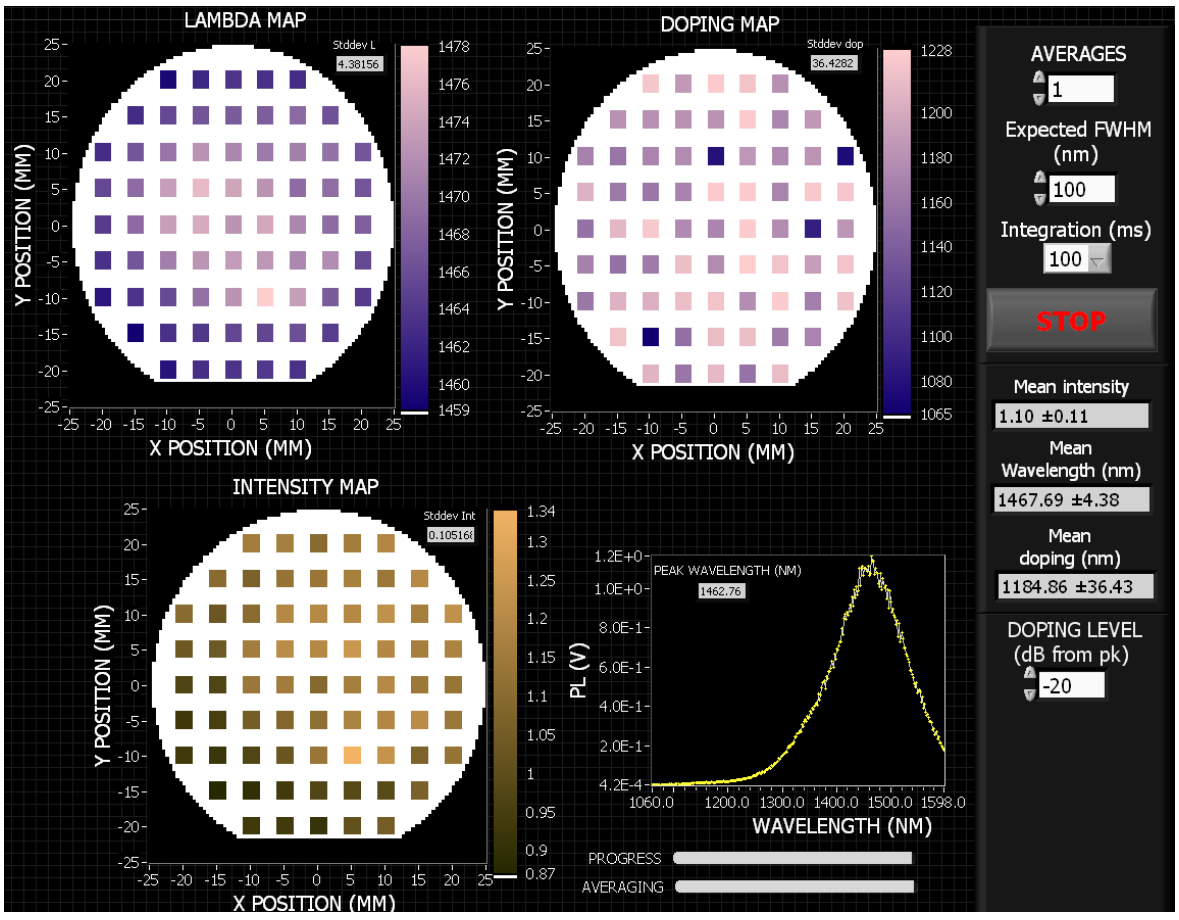


**Fig. 4.5.1. LabVIEW screen capture of the LT-PL spectroscopy interface, with a 69-wafer point scan in 3 hours. Data processed includes peak wavelength (top left), peak amplitude (bottom left), doping estimation (top right), and the last scanned spectra (bottom right). Means displayed with standard deviation on right pane. The integration time dictates the sample & hold time of the measurement.**

### 4.5.2. Characterisation of advanced RTDs

In Chapter III, several predictions were made on InAs sub-well RTDs, the most important being that there is a potential of achieving a better intrinsic resonance efficiency compared to the similarly-strained InGaAs QW RTD.

This assertion could not be fully tested, though early LT-PL tests confirm that the $E_1$ level predictions follow the modelled trends. Broadly speaking the LT-PL and XRD characterisation schema applies, but further consideration must be given to the TEM-CELFA mole fraction contrast results of Fig. 4.4d & f, where there appears to be a trend of fluctuation across the QW. As the RTD performance is largely dictated by the AlAs barrier thickness, significant local variations due to any causes of interface roughness may cause an exponential increase in current density, attracting excess heat and poor noise performance.

This characterisation schema also ignores the analysis of triple barrier structure, which remain an effective competitor to double barrier systems due to their implicitly engineered energy level bistability. Several extra optical transitions are expected from such a system, resulting in further broadened linewidths and complicated interpretation of the data.

Another class ignored by this characterisation schema is the Type-II RTD, or the interband RTD, realised especially with InAs/AlSb[242] barriers on a GaSb bulk system. Due to the different operating principle, the buried well cannot be used to create a Type-I/ Type-II transition differential. Furthermore, due to the inter-band process, very different scattering processes and fitting parameters apply.

### 4.5.3. Conclusions

Several characterisation methods were discussed, settling on the necessity of a reliable non-destructive technique for a production environment. However, this proves to be a complicated prospect: Both PL and XRD have associated failure rates when highly-strained wafers are in question: LT-PL may fail to adequately bind thermally to the cryostat, whereas XRD may produce no interpretable result should the epitaxial growth stray outside of the pseudomorphic growth condition.

However, with experimented care, it was shown that the non-unique XRD solutions offered may be further confirmed by a PL emission and fit to modelling. The PL emission itself is broadened by several average QW thicknesses being captured across the length of an exciton. This conclusion is then supported by an interface study using CELFA TEM, suggesting that the AlAs/InGaAs binary interface is markedly unstable compared to any other epitaxial layer on the structure.

# Chapter V : Further work

This chapter presents key necessary steps in order to improve general RTD performance.

Firstly, a system-level approach is discussed, where subsequent improvement of the RTD antenna element and impedance matching are required for a better extraction and radiation of THz oscillation.

In the short-term, direct improvements are discussed by optimising heat extraction from the active element, with minimal performance impairment and modification to the current fabrication scheme.

Ways to improve the statistical process control of the epitaxy are discussed, noting the need for further investigation upon the nature of carrier scattering in InGaAs/AlAs RTDs, and a brief presentation of a succession of RTD epitaxial growth attempts whose detailed investigation was incomplete at the time of writing are presented.

Three critical optical and electrical material parameters that limit the operation of RTDs are discussed, and based on these, some predictions on the course of future RTD research is made. A proposal to revisit the GaAs/AlAs system is made, and enhance it with a GaAs/InGaAs/AlAs towards the compressive strain limit acceptable.

The chapter ends with a discussion on the design merits of triple AlAs barrier RTDs in the InGaAs on InP system, and a summary modelling study based on the prior epitaxial experience.

# 5.1. Experimental verification & optimisation

## 5.1.1. RTD Technological roadmap

RTDs are an integral for the family of THz generating technologies. Whilst bench-top systems (either photonic or RF) are readily available for this purpose, and other competing technologies such as unitravelling carrier diodes[28–31,243] have been developed to a higher technology readiness level due to the momentum gained by the comparative ease of manufacturing. RTDs, however, remain a prime candidate for compact, solid-state, high efficiency THz transceivers due to their intrinsic resonant behaviour. However, in order to exploit this behaviour to maximum effect, not only high power and high conversion efficiency is needed, but also a small form factor.

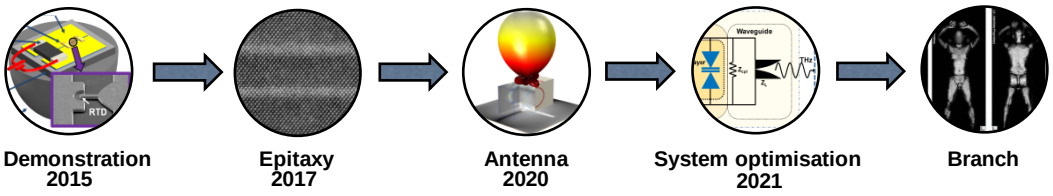


**Fig. 5.1.1. Progression of RTD towards technological readiness levels of 9. RTD schematic from** [181]**, SiO2 antenna image from** [244]**, THz security scanner image from** [79]**.**

In doing so, the current approach is bottom-up: first optimise the quality obtainable by mass-scalable MOVPE processes, with the help of a schema that has been discussed in detail in the previous section. As the epitaxial quality approaches expected key performance indicators (NDR value, $V_{peak}$, high-quality electrical contacts etc.) with finished electrical devices, a new process needs developing such that the antenna element is monolithically integrated with the RTD oscillator.

There are several candidates for this. Demonstrations of THz technologies often feature quasi-optical hyperhemispherical Si lenses or bulky THz waveguide components, which prevent widespread adoption through their added cost. In terms of single-chip engineering, of the conventional RF approaches, bowtie-shaped (metal) patch antennas have been frequently employed [245], with the signal being reflected back as the chip is bonded onto another metallic reflector. This raises concerns about the back-absorption of such radiation, as well as the fact that surface states in metals give raise to additional plasmonic

effects [246] which may interfere with the antenna. This effect, could be, in theory exploited however with careful antenna design, but if there is a mismatch, there is a return to this condition. Bonding is also non-ideal fabrication practice where high degree of precision levels (w.r.t. component alignments) are involved.

Terahertz photonic crystals and related techniques [247–249] can be employed, though it is an active research area with a lesser technological readiness level at the time of writing. Fabricating THz photonic crystals is an awkward subject, as the fraction of 1 mm feature sizes needed are just out-of-reach for conventional mechanical manufacturing methods, but may not be economically advantageous to realise very large arrays of these employing microfabrication techniques such as the reactive ion etching Bosch process on Si.

A more encouraging techniques that does not have the physical limitation of surface charged states formation, nor manufacturing issues is to create a cubic dielectric resonator antenna[250–252]. Standing waves are formed in a volumetric cavity of the antenna and are emitted through the electromagnetically transparent walls of the material. The antenna could be line-fed with a $\lambda/4$ stub transformer. For future perfection of this matching and addition of tenability options, the stub dimensions could be altered via a MEMS actuator or, less ideally, through piezoelectric materials. Alternatively, the electric field could be locally compensated with additional switching elements, such as buried MESFET or varactor elements[253]. The InP substrate itself could be used in this case to realise the antenna, in an “epitaxy-down” configuration, or overgrowth is also an option. A concentrated engineering effort and multi-physics simulations are required to ensure in the end that the system will behave as expected.

### 5.1.2. Heat sinking for reliability

In previous work[159], we have determined that only 30% of the valley current is thermally activated. Yet the optimum devices predicted in Chapter III have an increased peak current, which would undoubtedly result in heating effects. To prolong the usable life time of an RTD (and avoid early catastrophic failure), it is imperative to improve heat extraction efficiency.

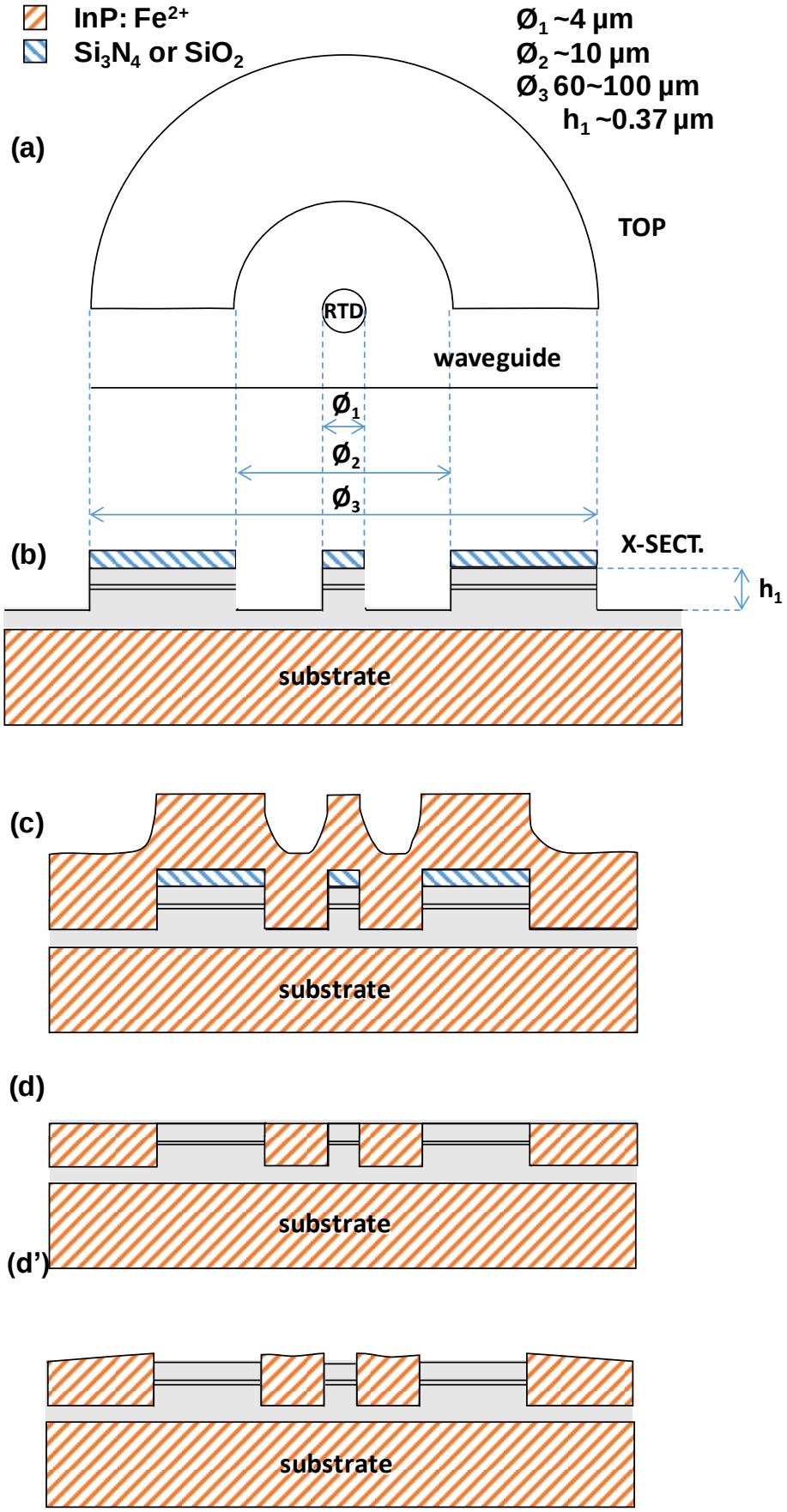


**Fig. 5.1.2. Schematic process flow of overgrowth of the RTD showing a (a) top view of the mesa with the air bridge removed (b) deposition of dielectric to protect metal (c) growth of heatsinking material. Followed by removal and re-exposure of the metallic contacts via (d) chemical-mechanical polishing or (d') 2 steps of selective wet etching**

Currently, the RTD is naturally cooled by air convection, a poor method of heat dissipation compared to conduction. If the RTD mesa is overgrown with a low process temperature material with suitably high semi-insulating properties, it is possible to better conduct excess heat through this layer.

Fig. 5.1.2. presents a schematic of 2 possible implementations. In the current I-line photolithography process, the RTD mesa has a semi-circular shape with an air bridge on top of a slot waveguide. The emitter electrode passes through a non-resonant RTD before reaching the active element [177]. As a first step (b), the electrical contacts are covered with a sacrificial dielectric, such as $Si_3N_4$ or $SiO_2$. The material is then over-grown (c); for this purpose iron-doped InP (the same material as the substrate) could be suggested due to its affinity to the system. Diamond is an excellent insulator and thermal conductor simultaneously, but requires noticeably high temperatures for deposition, which may disorder the AlAs barriers. Finally, the contacts can be exposed again through chemical-mechanical polishing (d) or through successive selective wet etch processes (d'). Both of these methods have the potential to damage and contaminate the wafer, albeit in different ways: polishing could delaminate the contacts, whereas the possible uneven surfaces due to wet etch could degrade the waveguide performance.

## 5.1.3. Quantifying scattering mechanisms

In §3.2.2, the importance of the semi-physical scattering parameter $\Gamma$ was shown, with its influence over the computed I-V characteristic of an RTD. Understanding the practical nature of the factors that contribute towards the broadening of the quasi-bound resonance linewidth is still very much an area ripe for research at the time of writing, with benefits that directly extend to other device classes, such as quantum cascade lasers [33,254–256].

In Chapter IV, an outline was set for microstructural analysis using non-destructive techniques. This is further aided by observation of the final electrical parameters (see Table 3.1.) such as the $\Delta V \Delta I$ of the NDR, resonance linewidth as observed in LT-PL spectroscopy, and the maximum $\delta I \backslash \delta V$ giving the bistable NDR value, setting the basis for transceiver performance. The final values must take into any process variations that may lead to different electrical

path lengths. Finally, perhaps the most important value of all from a practical perspective is the $V_{pk}$ where the differential conductance turns from the positive slope to a negative slope. Large variations in this value across similar RTDs on a wafer suggest a need for a better development of *statistical process control*. These $V_{pk}$ variations are largely attributed to alloy scattering and local lattice ad-extension under stress and strain[175], leading to a variation in current density.

Achieving this degree of statistical process control could only be done by successive epitaxial growth of similar RTDs with parameters such as the well width and depth inside a 2D matrix. Deviations from the simulated PL linewidth can be plotted and then compared. This would effectively create a high-value empirical process map, with the added advantage that then scattering effects can be decoupled from the expected band-edge effects, with relative PL intensity also providing a good indication[122].

The final goal may come in the form of creating an automated tool where the barrier fluctuation and resonance Q-factor can be gauged, for the purpose of 'binning' wafer zones before they are even processed.

### 5.1.4. Description of wafer campaign

A summary description of the rationale behind the sequential growth of RTD wafers follows. Not all wafers could be studied in sufficient detail by the time this document was completed.

The preliminary checks consisted of doping checks (Hall and LT-PL measurements), and calibration of the InGaAs QW. This was followed by two sample stacks of doped/ undoped QW, using the 2 reference structures in this work, with an active region of $12ML\ In_{.85}Ga_{.15}As$ and $15ML\ In_{.80}Ga_{.20}As$, where the difference was the presence of a LM-AlInAs gettering layer, in order to avoid this possible cause of AlAs barrier asymmetry. AlAs asymmetry could not be confirmed beyond any doubt between 3 repetitions of these samples, though, on average, average AlAs layer thickness appeared to be ~7% more consistent on average in the case with the AlInAs layer, therefore this was kept for future growth attempts.

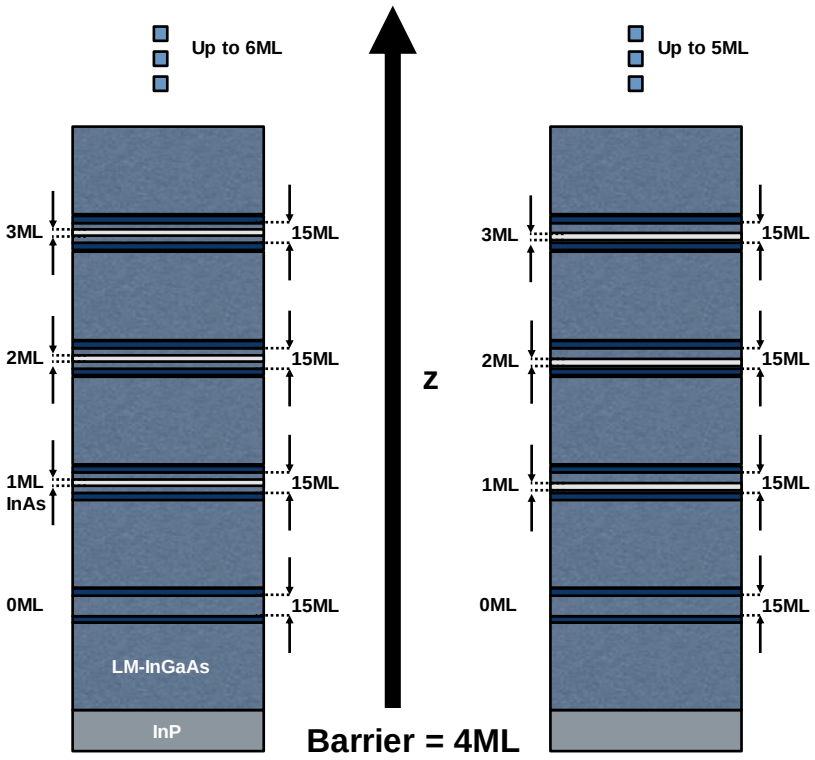


**Fig. 5.1.4a. Schematic structure of symmetric and asymmetric**

One of the targets of the campaign was to confirm how many strained layer of binary InAs crystalline alloy can be grown, and to this effect two epi-layer stacks were grown, reflecting the InGaAs/InAs/InGaAs and InGaAs/InAs layouts in Chapter III. In Fig. 5.1.4a, noting that the overall QW thickness is maintained constant, and 1 ML InAs is to be added at a time, with a separation of 167 nm LM-InGaAs between the active-region model structures. In one case, the InAs layer was placed as close to the centre as possible (the growth duration for both InGaAs layers similar), and in the other case, the InAs layer was attached to the AlAs barrier (i.e. trimethylgallium TMG $Ga(CH_3)_3$ channel closed). Such test wafers can be grown until the *in situ* reflectometer shows a drop in signal strength (attributed to relaxation), or until other monitoring conditions appear to deviate from ideality. It can be the case however, that under the chosen temperature, the wafer may grow adequately, only to relax when the stress conditions change with the cool-down period.

As the result of the InGaAs/InAs/InGaAs test structures were deemed satisfactory, wafers employing a 4 /4 /4 ML (to compare with 12 ML $In_{.85}Ga_{.15}As$, with mole-equivalent fraction of x=68.8%), 4/8 ML asymmetric (direct comparison with the previous), 5/ 5 /5 ML (to compare with 15 ML

$In_{.80}Ga_{.20}As$ with mole-equivalent fraction of x=68.8%). In some of these wafers there are notable low-temperature bonding issues due to bowing, likely caused by accumulated stress.

Further test structures were grown and analysed via TEM (Fig. 5.1.4c) and PL (Fig. 5.1.4 & d). Preliminary analysis shows that in the central InAs sub-well, good quality can be grown with 5 ML InAs, with a beginning of severe barrier asymmetry and occasional quantum dot formation at 6 ML InAs, as seen in (Fig. 5.1.4c). PL intensity of the 5 ML AlAs-side InAs was weaker than the central 5ML AlAs, but more careful analysis is required before a conclusion is reached. These results confirm the computed 5.04 ML InAs critical thickness from the Matthews-Blakeslee theory, and are in agreement with the trend observed by S-L. Weng [122].

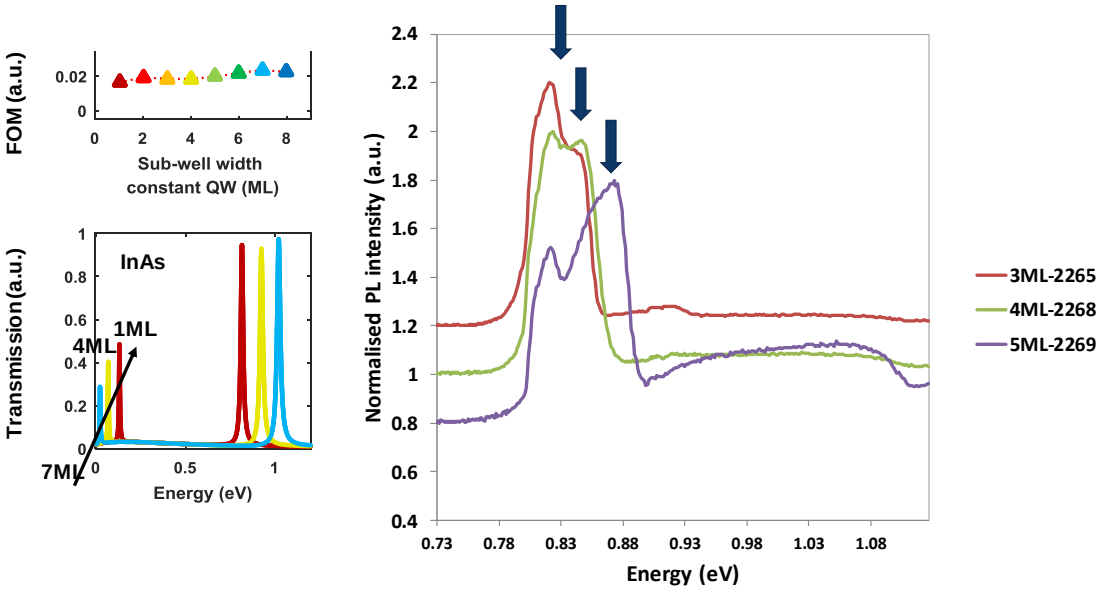


**Fig.5.1.4b LT-PL spectra comparison of wafer samples with 0.88 nm, 1.17 nm, and 1.465 nm of central InAs sub-well thickness, respectively. The modelled shift in quasi-bound energy and expected change in the efficiency figure of merit shown on the left.**

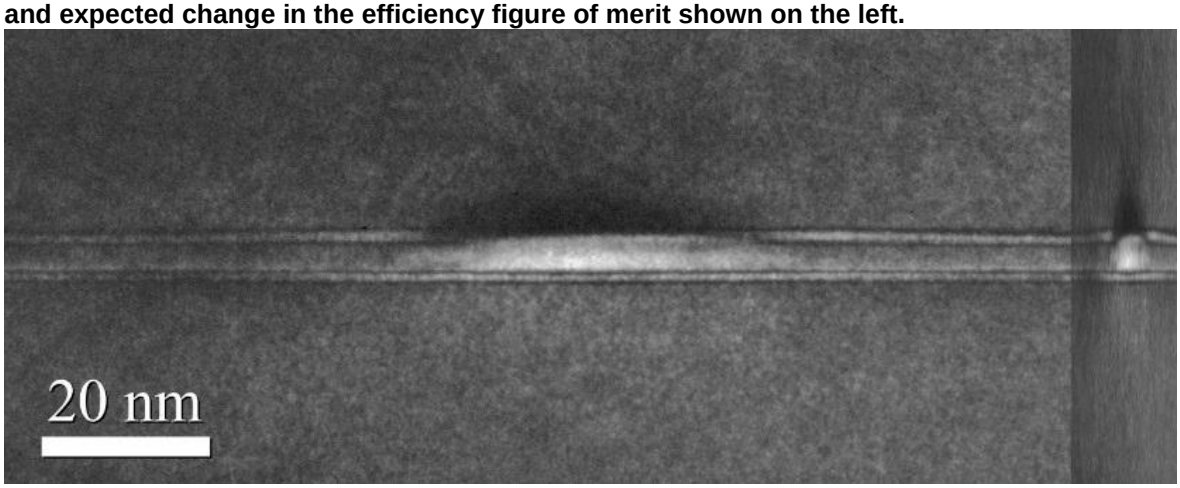


**Fig.5.1.4c. Dark Field TEM [002] image (Integrity Scientific Ltd.) showing a relaxation of an InAs-rich 3D growth zone ("quantum dot") in the 1.46nm asymmetric InAs device.**

Figures 5.1.4b shows the stark correlation between the data and modelling, with the warning that these samples did not include our buried well to obtain a Type-II transition, which would have made the determination of the bound energy possible. We note a slight inconsistency of the shape of the LM-InGaAs peaks, whose broadening and presence of multiple “shoulder” features (i.e. contributions of several Gaussian-Voigt spectral components) can only be attributed to the modification of the stress regimen.

Later, dark field-TEM [002] analysis confirmed this expectation, finding increasingly grainy contrast in the Indium-rich well, to the point where the 1.46 nm (5 ML) asymmetric InAs layer was observed to form occasional stress-relaxed formations similar to that of a quantum dot (Fig 5.1.4c).

The asymmetric InAs structures, show a lesser, but perhaps perceptible shift in Type –I transition energies, which concur with the trends in Chapter III. However, more attentive study of this structure is required before a definitive verdict on the epitaxial quality is reached.

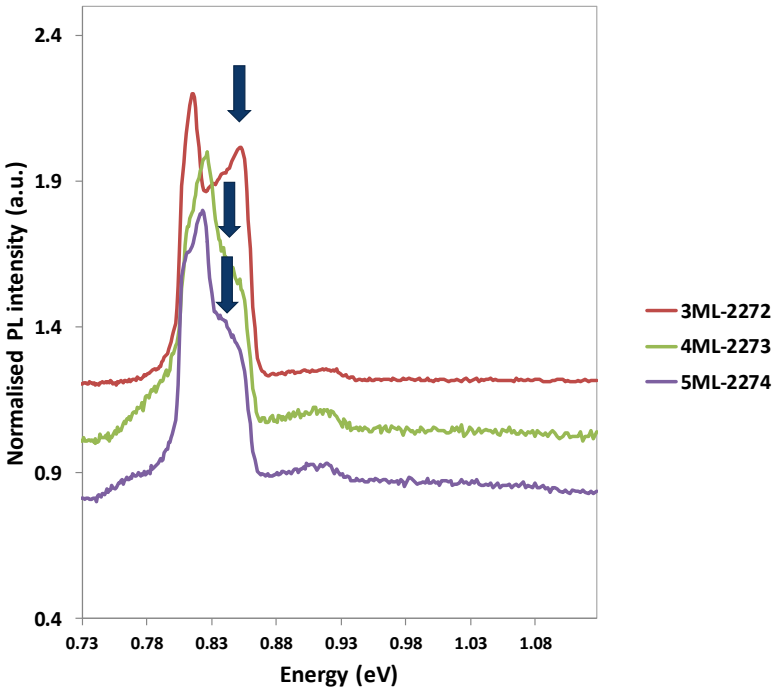


**Fig. 5.1.4d. LT-PL spectra comparison of wafer samples with 0.88 nm, 1.17 nm, and 1.46 nm of AlAs-sided InAs sub-well thickness, respectively.**

Then in short order, the two reference structures with an active regions of $12ML\ In_{.85}Ga_{.15}As$ and $15ML\ In_{.80}Ga_{.20}As$ were grown in short order, as full RTD structures, including our buried layer for the purpose of PL analysis.

One of the unanswered questions regarding the stability and perfection of the contacts was a concern where a minority number of carriers might spread/diffuse from the emitter n++ region towards the substrate. To provide a dis-incentive, an RTD TS2493 structure nominally identical to the reference was grown, adding a buried InGaAs p-layer under the n++ region. There are concerns that this approach may affect the epitaxial quality of the wafer.

As part of the growth campaign, one of the aims was to investigate possible performance improvements with thinning the symmetrical barriers from 4 ML to 3 ML and 2 ML. These small deviations from the 12ML $In_{.85}Ga_{.15}As$ reference wafer are investigated in §4.2.5.

An additional aim of this growth sequence was to investigate the growth of triple barrier devices. To maintain an optimum footprint based on known calibration, the QW was kept as the reference 12ML $In_{.85}Ga_{.15}As$, but with asymmetric 3/3/4 ML barriers. This was a compromise solution, as TS2478 – 3 ML AlAs sample was a known good sample. A 2nd "ideal" device followed, with 2/2/3 ML AlAs barriers, respectively. The design considerations are expanded in §5.4.

Wafers that were not grown in this series include a 1 THz+ optimised RTDs, with intentionally thinner emitter-sided AlAs barrier, thinner spacers, and graded mole fractions of InGaAs QW. Due to the multitude of changes, this plan was left for future trial of epitaxy limits.

## 5.2. RTDs in other material systems

### 5.2.1. Free-carrier absorption

One of the optical properties of materials problematic for THz emission is the free-carrier absorption. Scattering via different modes have power-dependency on $\lambda$, with the free carrier absorption $\alpha_c \propto \lambda^3$ for InAs [257]. However, as $\lambda < 1$,

the worst-case is assumed, a combined-absorption where the exponent ~2. Therefore, in the Drude-Zener model:

$$a_c = \frac{q_0^3}{4\pi^2 c^3 \epsilon_0} \cdot \frac{\lambda^2}{n^*} \cdot \left[ \frac{n}{m_n^2 \mu_n} + \frac{p}{m_p^2 \mu_p} \right]$$

Where n,p are the electron, hole densities, $m_n = m_0 * m_e, m_p$ are the carrier masses, and $\mu_n, \mu_p$ are the carrier mobilities and $n^*$ is the real part of the refractive index. The rest of the values are elementary constants, $q_0$ the electron charge, $\epsilon_0$ the vacuum permittivity, and c the speed of light.

Fig. 5.2.1a & b plot the free carrier absorption for the InP substrate material. At our target $\lambda \sim 1\, mm$, the absorption has a value of ~0.1 $cm^{-1}$. An insignificant value considering that for a semi-insulating (i.e. impurity concentration close to the intrinsic concentration of the material) substrate of 250 $\mu m$ thick, this means a figure of 0.025 lost to free carrier scattering, worst-case.

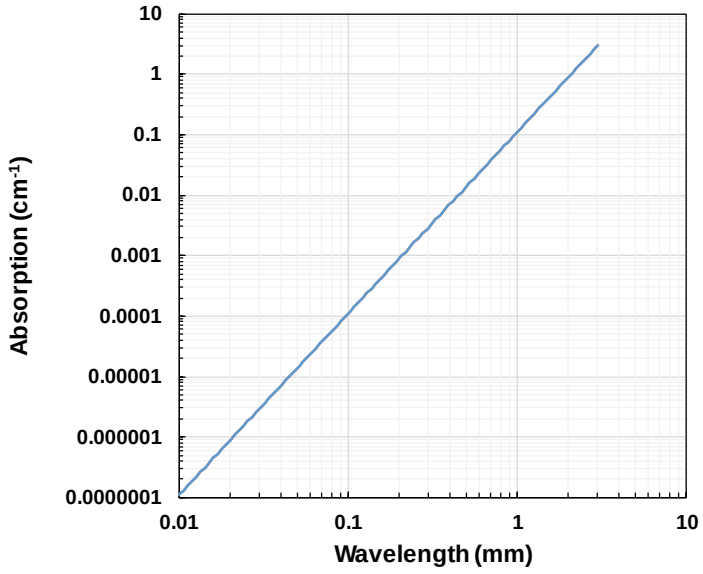


**Fig. 5.2.1a. Free Carrier absorption of semi-insulating InP vs. target wavelength, assuming $2.6 \cdot 10^9 carriers/cm^{-3}$ [258]. Refraction index assumed static, Re{n}=3.6**

For the case of 200 nm of $10^{19} carriers/cm^3$ doped contacts, these may effectively quench the transmission of THz radiation, therefore a shallow doping region is a balance against high power- high current density devices. The

recommendation here is to provide the THz oscillation a means of escape out-of-plane compared to the electrical contacts. In a pillar-and slot waveguide via air bridge configuration, this is achieved by default, but this is not necessarily the case in a epi-down design.

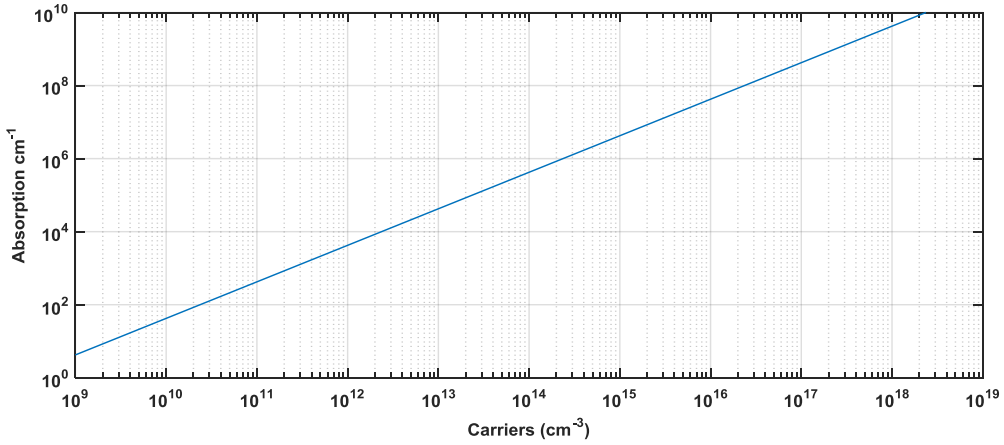


**Fig. 5.2.1b. Free carrier absorption of n-doped InP with varying carrier densities, assuming $\lambda = 1\ mm$**

These values correspond with the canon [114,258], though more advanced models for modelling free-carrier absorption exist [259].

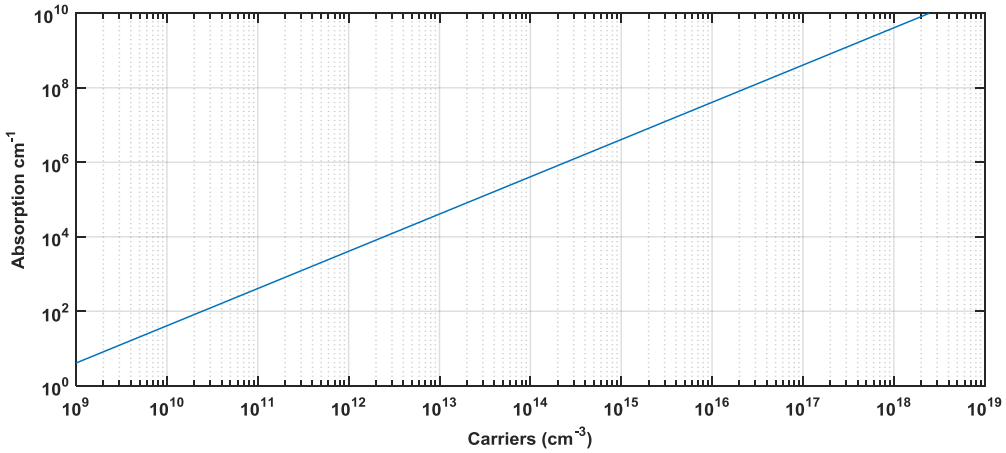


**Fig. 5.2.1c. Free carrier absorption of n-doped GaAs with varying carrier densities, assuming $\lambda = 1\ mm$**

Despite the different values of $\mu_n, m_e^*$, and $\mu_e$, GaAs overall achieves the same absorption performance as InP (Fig. 5.2.1c), as the substrates are also suitable for THz optics.

The situation is very different for GaN, whether hexagonal or cubic. The higher m* and lower mobility, and increased baseline of the intrinsic carrier

concentration means that the absorption is > 1 O.M. increased. This poor optical performance can be compensated by the affinity of GaN for Sapphire, Si or SiC substrates which do not have this problem.

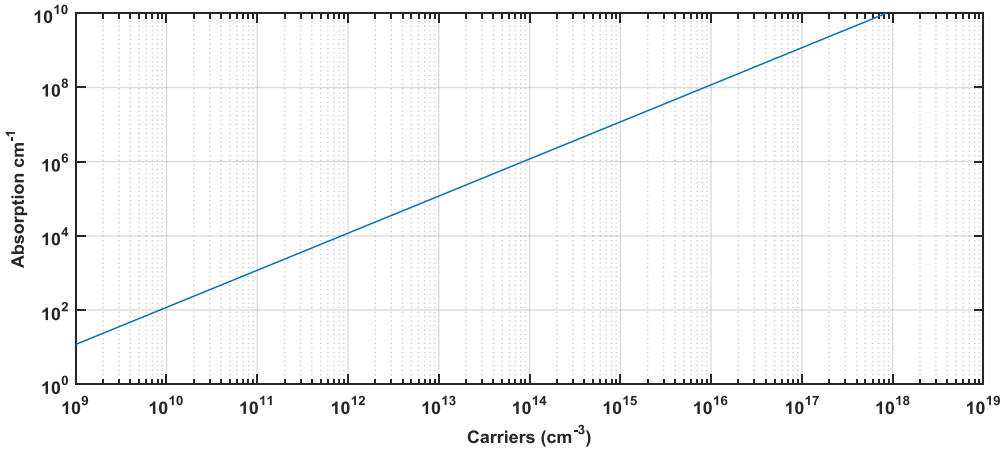


**Fig. 5.2.1d. Free carrier absorption of n-doped GaN with varying carrier densities, assuming $\lambda = 1\ mm$**

## 5.2.2. Thermal properties and Impact Ionisation

In order to adapt to the Joule heating due to the excessive current density, it does help if the semiconductor itself has a good thermal transfer properties. Furthermore, perhaps counterintuitively, as the crystal lattice is "rigid", a smaller cross section of the device may help by accommodating any lateral dimension expansion due to heat. On the other hand, as the proposal in §5.1.2. shows, if the device cross section is exposed to air, this is overall detrimental to thermal performance as convective air cooling is an inferior method for continuous heat transfer compared to conduction, in most cases.

| | *GaAs* | *InP* | *GaN(w)* | *$Al_2O_3$* | *Si* | *$SiO_2$* | *3C-SiC(zb)* | *GaSb* |
|---|---|---|---|---|---|---|---|---|
| ***CTE*** $10^{-6}K^{-1}$ | 5.7 | 4.6 | **3.2/5.6** | 5.6/6.6 | 2.6 | 0.55 | 3.8 | 7.75 |
| ***E bow*** $meV \cdot K^{-1}$ | 0.54 | 0.36 | 0.91 | / | 0.49 | / | **0.34** | 0.42 |
| ***Thermal κ*** $Wcm^{-1}K^{-1}$ | 0.55 | 0.68 | **1.3** | 0.18 | 1.3 | 0.13 | 3.6 | 0.32 |
| ***Thermal α*** $cm^2s^{-1}$ | 0.31 | 0.37 | 0.43 | 0.06 | **0.8** | 0.14 | 1.6 | 0.23 |

**Table 5.2.2a. Thermal parameters, including the coefficient of thermal expansion (CTE), the change of the band gap with temperature, thermal conductivity $\kappa$ and the related planar thermal diffusivity $\alpha$. GaN and alumina CTE shown in parallel and optical axes. Compiled from** [111,114,260,261]**.**

Table 5.2.2a presents a 3 thermal parameters: the coefficient of thermal expansion, a useful gauge of the thermal cycling-induced mechanical strain that will affect reliability of the packaging (lower is better), the thermal conductivity (analogous to electrical, higher is better), and the thermal diffusivity, a measure of the material that can act as a heat spreader (higher is better). Last, but not least, is the bowing of the band gap under temperature variations, which unfortunately does not offer information in terms of effective band alignment.

GaN appears to be a very suitable material in terms of its thermal properties, competing with group IV materials such as Si and SiC allotropes, being the best substrate material from the technology group, coming only second to Si in its heat spreading capability. Due to the high growth temperature, diamond was excluded from this chart. The Tetragonal sapphire was the historic substrate of choice for GaN, and is a suitable optical material for THz, but its very poor thermal performance otherwise disqualify its use. Fortunately, (111) Si substrates have been shown to be viable candidates for mass growth of GaN LEDs [262,263] and may yet gain commercial traction for RTDs due to the lower expenses compared to other GaN-target family substrates.

It is worth noting that GaAs and InP thermal properties are comparable, With GaAs being an overall better performer, but raising questions regarding the CTE. As an addition, GaAs is known to cope with ionisation damage due to cosmic high energy photons or other gamma radiation sources[264]. On the other hand, III-Sb materials tend to have lower expectations of thermal performance.

| | ***GaAs*** | ***InAs*** | ***InP*** | ***GaN(w)*** | ***Si*** |
|---|---|---|---|---|---|
| $\alpha_i\ (cm^{-1})\ at\ F = 4 \cdot 10^6\ Vcm^{-1}$ | 20000 | 700 | 7000 | **<10** | 3000 |
| ***Breakdown field*** $\cdot 10^5\ Vcm^{-1}$ | 4 | 0.4 | 5 | **50** | 3 |

**Table 5.2.2b. Impact ionisation parameter of electrons $\alpha_i$ and breakdown electric field from** [114].

It is not only the current that may provoke a catastrophic failure of the device, but the kinetic process (such as that caused by the presence of a strong electric field), can ionise the carriers. In table 5.2.2b, only the contribution of the electrons in shown. Assuming an operating device bias (extrinsic effects

excluded) of 0.15V, for a path length of ~300 nm, at a first order of approximation, the average field is $0.5\ MVcm^{-2}$, above the breakdown of both GaAs and InAs (therefore, likely any ternary alloy combination). It is possible that resonant tunnelling may coexist with the ionisation current, but this effect has not been investigated. Such effects may perhaps be confirmed using low-temperature photoluminescence excitation spectroscopy. In any case, it is unclear to what degree do these effects contribute towards the catastrophic failure of RTDs running at room temperature.

### 5.2.3. Recommendations

Given the above recommendation sets, it would be premature to dismiss GaAs as a valid candidate for THz RTDs. The Fermi level conduction band-edge alignment *w.r.t.* AlAs is inferior to the case given LM-InGaAs on InP. On the other hand, GaAs is a much more studied material system and GaAs/AlAs superlattices can be grown with minimal strain, meaning that any photolithographic process will be less likely to feature convergence errors due to wafer bow. I may suggest that even if a GaAs RTD oscillator will have a diminished intrinsic resonant efficiency figure, conventional fabrication techniques could push the extraction efficiency to compensate for this factor. Furthermore, an emitter may be comprised of an array, which may further present advantages for adding the possibility of micro-mechanical or electrical beam steering and fine frequency tuning, amongst the lower processing costs for larger wafers. Due to the impressive cut-off frequency of RTDs, they may also find use as modulators in optical systems as electro-optic and opto-electric converters, having demonstrated equivalent, if not better, performance to conventional InGaAs *p-i-n* diodes [265].

RTDs will likely keep being developed on the InP platform, as there is a wealth of materials that are nearly lattice-matched, as well as the InP optical performance in the THz range, providing that the limits of the epitaxy continue to be tried.

Antimonides are materials well-known to the mid-infrared community, and record oscillation of GaSb/InAs RTDs were recorded [196], before further improvement attempts were abandoned. Perhaps antimonide-containing RTDs

have not been exploited to their fullest potential, and may yet be candidates for 1 THz++ oscillation devices.

The GaN system has proven to be one of the odd-one-out in the III-V compound semiconductor world. Due to the material's high threshold for breakdown, transistors operating in excess of $600\ °C$ have been reported [266]. As it is ubiquitous in the LED world, the comparatively less-explored GaN RTD may one day be featured in 5G base stations or local terminals.

### 5.2.3. GaAs test structures

In order to investigate the epitaxial growth quality in the GaAs system, 2 GaAs-based wafer structures with different stacks of RTDs were grown.

The first wafer is meant to investigate slightly extensile (nearly lattice-matched) pure GaAs/AlAs RTDs. With this, a comparison with the canon can be made, but it a baseline for further epitaxial improvements can be set based on epitaxial quality. It remains to be seen whether the diminished barrier height, and the alignment of the indirect valley states lead to high rates of thermally-activated tunnelling current in these high-J, thin AlAs barrier structures.

Fig. 5.2.3a presents a matrix of 6 QWs to be grown. This proposal was preceded by modelling, but the 16 ML /4.5 nm case is also sufficiently similar to the previously-grown InP samples for a direct comparison. To minimise the amount of test material grown, the 6 QW-barrier systems were stacked with a separation of 180 nm of GaAs, sufficient to locally compensate for any strain-induced defects (if any). The disadvantage of this method is that the analysis of the structure through PL and X-ray is very limited; however, the intention is to perform microstructural analysis via CELFA-TEM. The top GaAs layer is degenerately doped for contact surface testing.

I note that the atomic sheet distance "monolayer unit" (ML) in the GaAs substrate is lower than that of InP (a/2 = 0.283 nm vs 0.293 nm).

*Schematic C.B. not to scale

| Barrier width ML (nm) | Well width ML (nm) | | |
|---|---|---|---|
| | **14** (4) | **16** (4.5) | **18** (5.1) |
| **3** (0.85) | | ✓ | ✓ |
| **4** (1.13) | ✓ | ✓ | ✓ |
| **5** (1.42) | | ✓ | |

180nm n++ GaAs

180nm GaAs

…

180nm GaAs

| | Stack 1 (ML) | |
|---|---|---|
| **QW** | **Barrier** | **WW** |
| **6** | 5 | 16 |
| **5** | 4 | 14 |
| **4** | 4 | 16 |
| **3** | 4 | 18 |
| **2** | 3 | 16 |
| **1** | 3 | 18 |
| **S.I. GaAs** | | |

**Fig. 5.2.3a Target structures to grow based on modelled GaAs/AlAs structures, shown with schematic conduction band. (top) Schematic layer structure of the first wafer (bottom)**

However, purely binary GaAs/AlAs growth has been achieved in the past[156,206,267], and by itself, is not a sufficiently novel subject of further attention as it offers very little improvement. GaAs/AlAs/$In_xGa_{1-x}As$-QW RTDs, have been attempted with mole fractions up to x=0.33 [267], noting that the authors suggested intervalley resonant tunnelling as one of the dominating effects. The question that comes is whether a similar GaAs/InAs schema inside the QW (as the LM-InGaAs-InAs sub-well schema tested in Chapter III) may help alleviate the lossy intervalley process. To this extent, it is known that on a GaAs substrate, ~1.8 ML of InAs can be grown [268] until uniform, 2D epitaxy, shifts to strain-relaxed 3D *Stranski-Krastanov* [269] growth modes.

Therefore, Fig. 5.2.3b suggests a conservative approach (x=0.14 mole-equivalent fraction) to this strain limitation, by placing individual InAs layers between GaAs growth interruptions. To better accommodate accumulated stress, these InAs layer are best placed towards the middle of the QW. As the net effect will be to

lower the quasi-bound energy state level, there is an expected increase in the IRE figure of merit.

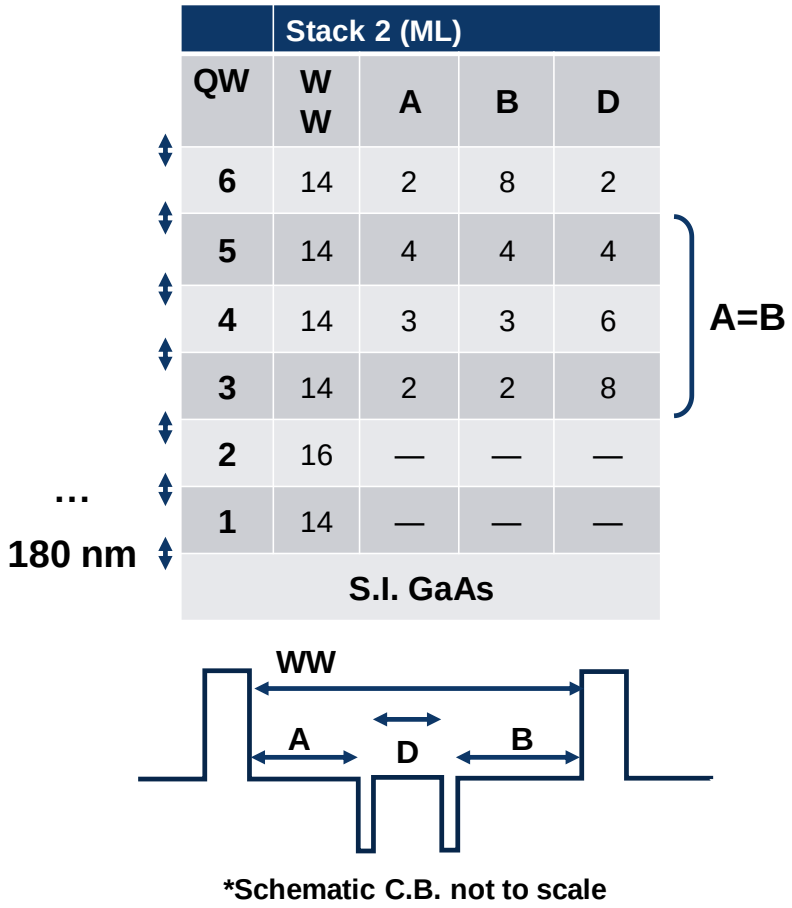


**Fig. 5.2.3b. Schematic layer structure of the 2nd QW & barrier test structure stack, separated by 180 nm of GaAs. This test structure incorporates GaAs/InAs altercations, with 1 ML of "layers" of InAs placed at strategic points, in-between layer 'D'. The lower diagram is a conduction band schematic of this effect. The top QW(6), contains asymmetric placement of InAs.**

A further improvement could be achieved by shifting the position of the InAs layers towards the emitter, creating an asymmetric graded-ternary QW equivalent, shown by the 6th QW in the stack. All of the QW in this stack have the same well width, for the purpose of direct comparison.

## 5.3. Triple barrier RTDs

The phenomenon of resonant tunnelling through a double well (triple barrier) [270–274], or even triple well[184] RTD was less studied throughout the years, despite being a referenced in theoretical work since Esaki's early attempts[137].

In this section the latest highly strained RTD structure from our wafer series was chosen as a base, with a 1st QW of 12 ML $In_{.85}Ga_{.15}As$. Following this template,

the choice of barrier thickness is investigated, as well as the width of the 2nd QW, with the mole-fraction proposed to be lattice-matched. In theory, this attempts to obtain the best of both worlds in terms of raw oscillator/emission power and efficiency figures, with a perhaps lesser critical sensitivity on barrier symmetry and structural perfection, as the next paragraph explains.

One of the less obvious advantages of triple-barrier RTDs is that they can include multiple stability regions, which may be advantageous for oscillator performance. This stability is a result of the splitting of the transmission level peaks, as a result of the presence of multiple quasi-bound levels. This, in turn, results in an increased $\Delta V$ NDR region, often cited [204] as desirable for improvement of emission power. Should this characteristic be undesirable in other applications, it is possible to engineer a structure such that the separation between the levels is very low, or overlap. Fig. 5.3.1a represents the transmission probability at different levels of carrier energies in the case of a triple barrier QW. A reminder that the non-unitary amplitude of the peaks is caused by the inclusion in the model of a generic elastic scattering process (physically representing a convolution of effects caused by *e.g.* phonons, impurities and interface disorder).

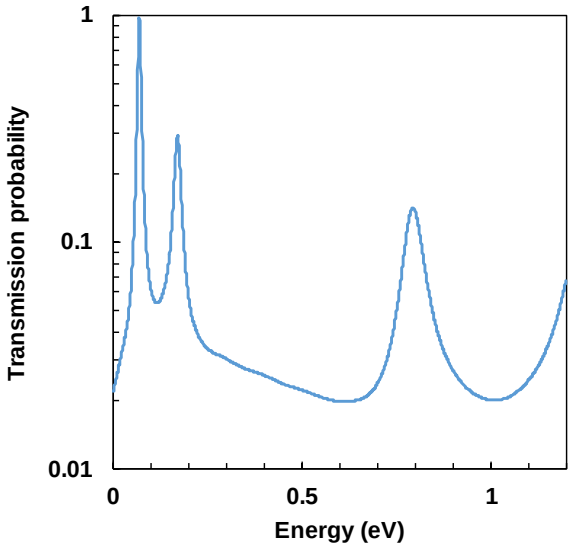


**Fig. 5.3.1a. Semilog plot of modelled transmission energy in a triple barrier 3/2/2 ML AlAs RTD with a 2nd QW of 15 ML. Energy scale bar stops close to the 1.16 eV of the AlAs conduction band offset at the Γ −point.**

The two peaks, of 69.6 and 170 meV (corresponding to the entry, and exit QWs, respectively), *w.r.t.* the injector Fermi level, are notable in that either may cause a standing wave function inside the triple barrier structure (i.e. *resonant*

*tunnelling*), and it is not a case where the two states re-align as bias is applied. Instead, I may suggest that scattering due to structural imperfections practically broaden the linewidths of these confined peaks. To the novice experimenter, this has the effect of electrical measurements appearing as a continuous NDR, (*i.e.* gentler slope apparently leading to poorer performance), in the case of the multi-barrier RTD compared to the equivalent double barrier RTD [184]. However, E.R. Brown *et al.* indicate that quasi-stable oscillation suppression highlights the contribution of each of these confined states in the measured I-V characteristic as multiple NDR regions.

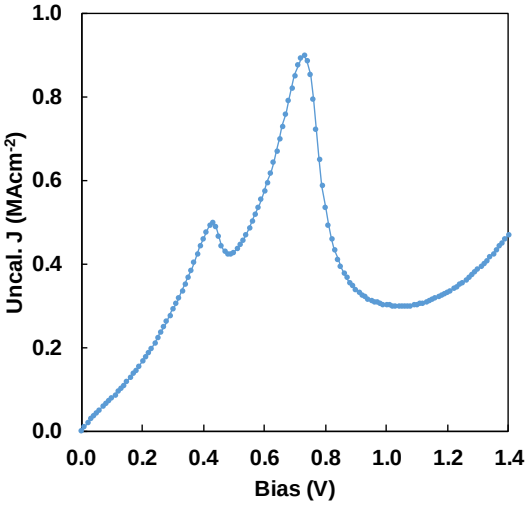


**Fig. 5.3.1b. Uncalibrated modelled I-V characteristic of a 3/2/2 ML AlAs RTD with a 2nd QW of 15 ML.**

The model I-V in Fig. 5.3.1b also predicts the behaviour shown by Brown *et al.*, noting that certain combinations of barriers and 2nd QW width can indeed merge these states. However, based on the structural characterisation in chapter IV, particularly for large area RTDs, it is distinctly possible that a realistic device may exhibit resonance through a continuum of broadened states due to localised barrier fluctuations.

In investigating the role of barrier thickness, based on the results of the modelling in §3.2.5, the role of the emitter-sided entry barrier, is to control the overall current density injected into the structure. When the RTDs were designed, it was uncertain whether either a 3ML or 2ML stable AlAs barrier would be possible to grow using MOVPE, therefore a decision was taken to attempt the growth of a 4/3/3 ML AlAs barrier structure, and a more optimised 3/2/2 ML AlAs structure as a secondary attempt. Fig. 5.3.1c compares the *IRE* between several

barrier schema, noting that the improvement from changing the entry barrier from 4 ML to 3 ML may be as much as +137%, whereas from 3 ML to 2 ML another +32%. The middle and exit barrier thickness may be used to fine-tune the operational input power, if needed, with simultaneous adjustments in both current peak and biasing points possible, in the limit of epitaxy calibration.

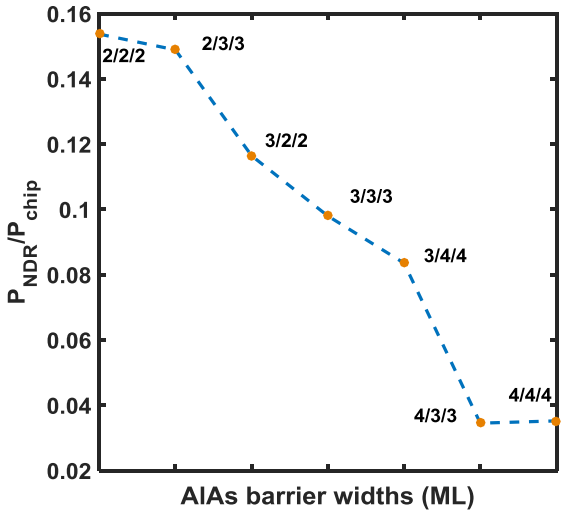


**Fig. 5.3.1.c. IRE figure from modelled quasi-static I-V characteristics of triple barrier RTDs with differing entry/middle/exit AlAs widths. Dashed line as a guide for the eye.**

The choice of the QW is less intuitive. Allford *et al.* in their design study[273] of a "traditional" $5.4\ nm\ Al_{0.33}Ga_{0.67}As/GaAs$ triple barrier RTD, have shown that an increased ratio of entry-QW:exit-QW favours performance by lowering the required activation energy (therefore lower bias requirement) and increasing peak current densities. In the situation presented in this work, the entry-QW was grown with the known partially strain-balanced reference structure to avoid unnecessary calibration & verification, leaving the exit-QW up for optimisation. In order to avoid additional stress, it was quickly decided that the 2nd QW would employ LM-InGaAs, therefore, the only parameter left to investigate was the we 2nd well width. The situation presented by Allford *et al.* translates to the entry-QW having a lower confined energy at zero bias vs. the exit-QW. In a recent work, Allford & Buckle [274] perform a modelling study of a very similar structure to that proposed in this work, it is stated that in order to optimise the $3D \rightarrow 2D$ resonant tunnelling condition, the magnitude of the transmission probabilities through each successive barrier must be in strictly descending order:

$$T_{entry} > \ T_{middle} > T_{exit}$$

This condition is fulfilled by default with the strained QW-lattice matched QW scheme, due to the differing $m_e^*$ at play. The largest PVCR is therefore expected to be obtained with the 2nd resonance, as there is potential for a larger charge storage/release difference in the QWs with increasing bias.

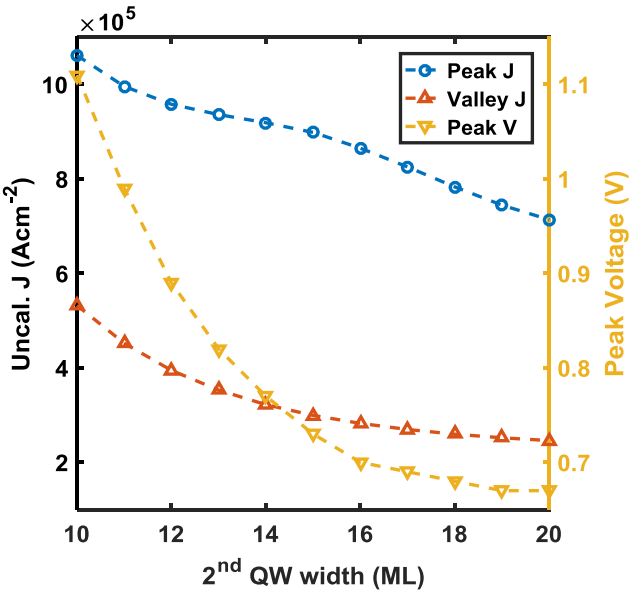


**Fig. 5.3.1d. Modelled I-V characteristics results with change in exit-QW width. Circles and triangles are the largest peak and valley current densities (left axis), and inverted triangles are the largest peak voltages (right axis).**

Several I-V characteristics were modelled using the same methodology and scattering parameter in Chapter III. Similar trade-offs between PVCR, J and operating bias are noted in Fig. 5.3.1d, as the trend already set by the double barrier structures analysed in Chapter III.

These trade-offs are summarised by a predicted IRE local optimum between 16-18 ML of exit-QW. A 15 ML QW was grown as a compromise, to better fit with previous growth variables.

Whether these thin-barrier structures will be able to deliver comparatively better performance to the double-barrier structure inside a packaged RTD emitter remains a subject for further investigation. However, it is important to note that these structures are considerably more difficult to characterise due to broad LT-PL emission linewidths, and reactor calibration may require additional

steps compared to the double-barrier structure if ultimate barrier thickness control is required.

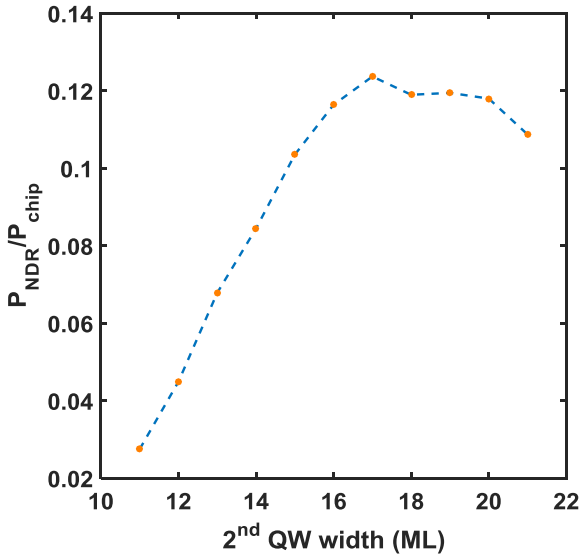


**Fig. 5.3.1e. IRE figure from modelled quasi-static I-V characteristics of triple barrier RTDs with a differing exit-QW width. Dashed line as a guide for the eye.**

Furthermore, for practical applications, the chip will need to be operated by an even more sophisticated power-point tracker which could discriminate between the optimum operating resonant condition as the device ages, and is thus subjected to the effects of electromigration, changing the extrinsic circuit conditions. Unfortunately, the failure modes related to the lifetime-aging of the active region of the mesoscopic structures are a subject of conjecture and further study.

## 5.4. Determining the RTD contact resistance

One of the challenges in specifying the $f_{max}$ of an optical RTD coupled to a waveguide is that the equipment necessary to perform this measurement is likely to be composed of piece-wise (due to spanning across different waveguide bands) vector network analyser Schottky multiplier-enabled “power heads”, which may be a costly affair for a university department. In previous work, K.J.P. Jacobs [181] has shown a method to perform THz frequency measurement using a coarse finesse interferometer from silicon wafers and a lithium tantalate ($LiTaO_3$) amplified far-IR detector. Though a frequency-amplitude plot could be extracted from successive measurements, the noise and losses in the system endanger the accuracy of the result. A more expensive option would be to

perform electro-optical scatter matrix $S_{11}$ (the coefficient of reflection at the input line) measurement.

Since calibration of such delicate RF instruments is an arduous process and measurements could be riddled with errors, it may help to have a theoretical "sanity check" available. §2.3.2. presented a simplified tank-circuit based equation to calculate $f_{max}$, though more complex measurements were employed by Asada *et al.*[204].

In either case, calculating this frequency starts with obtaining the small-signal quasi-stable (DC) negative conductance value, which is influenced by the electrical contact in practice. In order to remove this contribution, the classical approach is to compare fabricated test structures of circular[275–277] and rectangular [278,279] transmission line models with known dimensions.

However, as our previous mask used a dual-pass [177] approach, it was found that empirical measurements of successive wet etches may be offer a more representative contact resistance for a given mesa size:

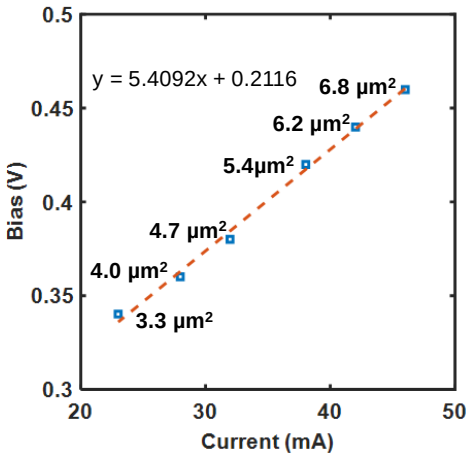


**Fig.5.4a. Device mesa-dependent resistance determined from successive wet etches, plotted with data from** [177].

In Fig. 5.4a, the mesa-dependent resistance is plotted. In the limit of an infinitesimal area, with a linear fit, peak voltage of 211.6 mV is determined. The slope on the equation 5.4092 Ω/mA represents the rate of change of the mesa resistance with current. However, certain components of the extrinsic resistance remain static, therefore a quadratic representation may be more appropriate.

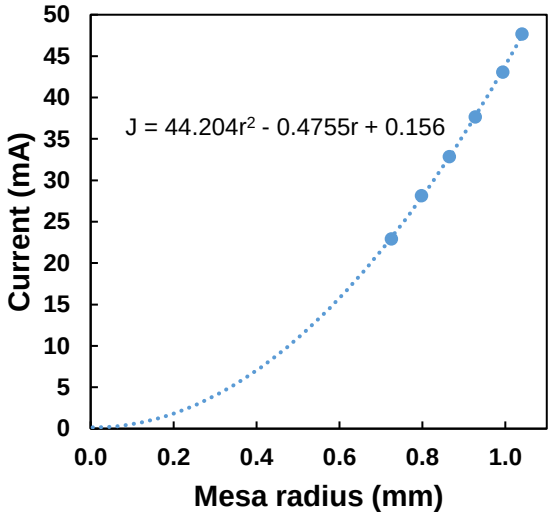


**Fig 5.4b Peak current against the radius of the approximately circular mesa extracted from the I-V characteristics as shown in Fig. 3.2.1b.**

In Fig. 5.4b this quadratic relationship is emphasised by plotting the peak current against the mesa radius. In previous work [159], it was shown that the valley current thus obtained exceeds the limit of the current limited by the device perimeter, therefore no leakage through device side walls is suspected in this wet etch process. This is a concern for micron-scale devices, as reactive-ion damaged regions may reach 100 nm depth in dry etch processes [193].

This value could then be used to scale the small signal conductance $g_n$ to an area-independent figure. With the dielectric resonant antenna, this approach becomes technically unnecessary, and is likely to be a case of an educated trial-and error fabrication process for the optimisation of the $\lambda/4$ stub.

In addition, Fig. 5.4c also provides predictions of the variation of $g_n$ with variations of InGaAs. It is seen that though slight InGaAs variation does not impact the quality of the resonance, it can in practice affect the oscillator emission power due to poorer coupling as a result. The range of values is in agreement with the measured conductance in [159]. To obtain the maximum cut-off frequency of the device, the dynamic capacitance must be taken into account, but this measurement could not be performed at the time of writing.

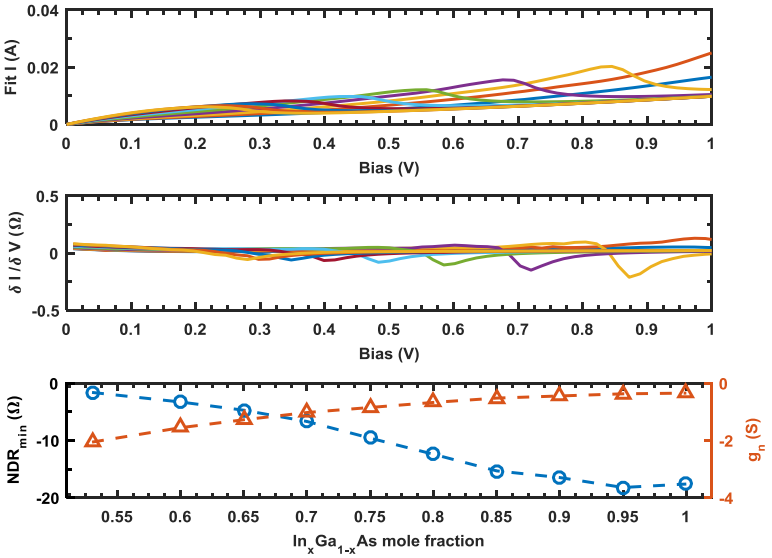


**Fig. 5.4c Graphic showing changes in QW InGaAs composition, altering: (top) Fit I-V characteristic (middle) differential resistance (bottom) small-signal conductance and the minimum value of the negative differential resistance.**

## 5.4. Summary

In this chapter, a template has been laid for further improvement of RTD emitter-oscillator performance.

First, a roadmap towards technological readiness levels in excess of 9 is presented, pointing out that the epitaxial characterisation is a very necessary first step towards improving precision of the statistical process manufacturing. However, this alone is insufficient to produce a solid business case for economical mass-manufacturing of RTD transceiver chips. Novel solutions for THz antennas are required, and here we present a schematic of a dielectric resonator antenna, briefly mentioning the roles of other conventional schemes such as patch antennas, with possible future investigation of THz photonic crystals. Though the thesis focuses on the realisation of emitters, more attention is needed to determine essential quasi-static characteristics (forming the base for THz heterodyning modelling) that will be necessary to realise an ideal receiver-RTD.

Concerns regarding heat extraction and premature device failure are highlighted, providing a direct alternatives via overgrowth to the current fabrication scheme. Another concern of early failure, the breakdown field limit of the material leading to impact ionisation is discussed, noting that as a first

order approximation, the electric field in these high-J structure is close to this value.

Addressing the optical losses via the main mechanism of free carrier absorption is discussed in 3 candidate RTD material systems. Together with the above points for reliability, some recommendations and predictions are made regarding the state-of-the-art, being hopeful that GaN RTDs may achieve a similar prestige to GaN LEDs in their scope of reaching portable, low-cost high-power THz emitters, whilst InGaAs/AlAs/InP RTDs will remain the proven platform of choice for single-emitter performance in the immediate future, whereas the maturity of the GaAs/AlAs material system may prove useful for scaling for large arrays to cope with the dr.

Finally, the practical role of an alternative triple-barrier structure is discussed, calling for further careful consideration of this benefits to extractable oscillation power this mesoscopic structure may offer.

# Conclusions

The exploitation of the THz spectrum is an incipient, but inevitable field which will impact several aspects of our daily lives. Though it may seem easy to see the instant availability of high-speed data in one's pocket as a fact of life, this is not universally true across the Globe, and especially in the cases of disaster and war zones where cable or fibre optic-based infrastructures collapse. Fulfilling the next-generation growth will require technologies that transcend the capacity of microwaves, whilst simultaneously offering a degree of robustness against conventional backhaul.

RTDs will remain technologically relevant as long as they remain on of the top candidates for at least one niche application, whether this will be found communications, computing, spectroscopy, imaging, or perhaps wearable technology that has not been invented yet. As a core technology, it is one of the keys to unlock several applications.

In order to bring this closer to reality, this thesis has discussed several performance issues exhibited by current generations of RTD oscillators, starting with an identification of the physical causes holding back progress. In this thesis, the reader is reminded about the effect structural imperfection has upon the electrical and optical properties of the RTD, starting from a theoretical interpretation of modelling data, towards examining physical evidence.

A distinction between the mesoscopic-scale transport is made, and how do the minute changes brought by scattering through epitaxial imperfection alter the observable, extrinsic circuit parameters of the oscillator system. After identifying a key figure of merit for the quasi-static performance of the RTD, the *intrinsic resonance efficiency,* a multi-parameter modelling space is investigated.

After detailing the conditions leading to the model setup, its boundary conditions and limitations, an alternative design strategy optimised for efficient power delivery is highlighted, using a shallower, but thicker quantum well with thinner barriers given the limitations of strained epitaxy.

The role of the strained epitaxy is verified with literature reports, and a preliminary investigation concludes that the Matthews and Blakeslee [119] model provides an adequate upper limit of the critical thickness for high quality epitaxy in these structures.

Models of sub-well devices employing lattice-matched InGaAs/InAs/InGaAs are also investigated with a level of detail not previously featured in the canon. The find is that these structures can perform, in the worst-case, as well as the high mole fraction InGaAs equivalent. However, the elimination of a growth reactor calibration step, as well as the expected improvement of the interface barrier quality may lead this type of device to be a long-term winner for commercialisation. Further improvement is suggested by also thinning the barrier, and placing the InAs sub-well asymmetrically, closer to the entry (intended emitter) barrier.

Investigate the structural perfection comes with improvements to conventional non-destructive optical characterisation techniques: low temperature photoluminescence spectroscopy (LT-PL), and high resolution X-ray diffractometry (HR-XRD). Both techniques are known in the semiconductor industry to be powerful indicators of conformity to a specified epitaxial structure.

Currently, the high-current density RTDs in this work use particularly thin single quantum wells (with active regions <10 nm), leaving a small window of opportunity for excitonic recombination, or for the incoming X-ray photons to be diffracted, respectively. Therefore, analysis is challenging in that either high-sensitivity detectors or signal recovery techniques may require employing, in addition to the development of a sophisticated optical transition model to realise the potential of optical spectroscopy.

Through a break-down of spectral components, PL shows crucial information about the average QW thickness and barrier thickness, as well as the high-intensity peaks relating to the bulk lattice-matched material. A similar path is followed with X-ray diffractometry, where the apparently high periodicity Pendellösung fringes introduce noise-like features on the XRD rocking curve. These components are explained with simulation and layer-linking of similarly

calibrated epitaxial layers, obtaining good information about the QW stress regimen, and therefore information about the compositional fraction of the $In_xGa_{1-x}As$ epitaxial alloy.

PL spectra from the QW could only be resolved by attributing a contribution of 3 different QW thicknesses, whereas HR-XRD can only offer an estimate of the average QW thickness. As this information appears to be inexact, further confirmation was obtained using a destructive, one-off analysis using high resolution transmission electron microscopy modes. Through this, a confirmation of atomic-level barrier non-uniformity is seen in detail for the first time in AlAs/InGaAs on InP RTDs.

Recommendations are made to improve and automate this process for industrial QC and yield improvement.

Finally, this works looks at further improvements of the RTD as an oscillator system: from current improvements to heat extraction and electrical insulation, towards laying ground work to consider a novel radiator, by the addition of a 3D dielectric resonator antenna. The THz properties of typical materials are reviewed, and taking the lessons learned from the experience gathered in this thesis, a set of recommendations for future development of RTDs in different material systems is made. In particular, the comparatively less explored GaN material system may be an excellent, affordable platform, as the compound semiconductor industry is already moving towards GaN LEDs on silicon (111) substrates.

Last, but not least, the design of a Type-I triple barrier AlAs/InGaAs RTD is investigated, with its merits and potential pitfalls discussed. It is found that despite the lesser peak current density (one of the conventional metrics), the devices are expected to be very efficient oscillators and emitters of THz radiation, conclusion which in principle agrees with data from the canon [184].

This renews the commitment to challenge epitaxial processes for next-generation devices.

# Bibliography

[1] M. Hangyo, Development and future prospects of terahertz technology, Jpn. J. Appl. Phys. 54 (2015) 120101. doi:10.7567/JJAP.54.120101.

[2] International Telecommunication Union, Radio Regulations, Edition of 2012, Geneva, 2012. http://www.itu.int/pub/R-REG-RR-2012.

[3] D.J. Fixsen, The Temperature of the Cosmic Microwave Background, Astrophys. J. 707 (2009) 916–920. doi:10.1088/0004-637X/707/2/916.

[4] B. Abel, Domaines du spectre électromagnétique.svg, Wikimedia Commons. (2018). https://en.wikipedia.org/wiki/File:Frequency_vs._wave_length.svg (accessed June 9, 2018).

[5] N.M. Ridler, R.A. Ginleyt, A review of the IEEE 1785 standards for rectangular waveguides above 110 GHz, in: 2017 89th ARFTG Microw. Meas. Conf., IEEE, 2017: pp. 1–4. doi:10.1109/ARFTG.2017.8000830.

[6] International Telecommunication Union, Attenuation by atmospheric gases Rec. ITU-R P.676-10, Geneva, Switzerland, 2013. https://www.itu.int/dms_pubrec/itu-r/rec/p/R-REC-P.676-10-201309-S!!PDF-E.pdf.

[7] R. Appleby, H.B. Wallace, Standoff Detection of Weapons and Contraband in the 100 GHz to 1 THz Region, IEEE Trans. Antennas Propag. 55 (2007) 2944–2956. doi:10.1109/TAP.2007.908543.

[8] Y. Yang, A. Shutler, D. Grischkowsky, Measurement of the transmission of the atmosphere from 0.2 to 2 THz, Opt. Express. 19 (2011) 8830–8838. doi:doi: 10.1364/oe.19.008830.

[9] P. Kilcullen, I.D. Hartley, E.T. Jensen, M. Reid, Terahertz Time Domain Gas-phase Spectroscopy of Carbon Monoxide, J. Infrared, Millimeter, Terahertz Waves. 36 (2015) 380–389. doi:10.1007/s10762-014-0139-z.

[10] D.M. Mittleman, R.H. Jacobsen, R. Neelamani, R.G. Baraniuk, M.C. Nuss, Gas sensing using terahertz time-domain spectroscopy, Appl. Phys. B-Lasers Opt. 67 (1998) 379–390. doi:10.1007/s003400050520.

[11] T. Uno, H. Tabata, In situ Measurement of Combustion Gas Using Terahertz Time Domain Spectroscopy Setup for Gas Phase Spectroscopy and Measurement of Solid Sample, Jpn. J. Appl. Phys. 49 (2010) 04DL17. doi:10.1143/JJAP.49.04DL17.

[12] D. Grischkowsky, S. Keiding, M. van Exter, C. Fattinger, Far-infrared time-domain spectroscopy with terahertz beams of dielectrics and semiconductors, J. Opt. Soc. Am. B. 7 (1990) 2006–2015. doi:10.1364/JOSAB.7.002006.

[13] R. Mendis, D.M. Mittleman, Comparison of the lowest-order transverse-electric (TE1) and transverse-magnetic (TEM) modes of the parallel-plate waveguide for terahertz pulse applications, Opt. Express. 17 (2009) 14839. doi:10.1364/OE.17.014839.

[14] M. Tonouchi, Cutting-edge terahertz technology, Nat. Photonics. 1 (2007) 97–105. doi:10.1038/nphoton.2007.3.

[15] L. Wang, Reliable design of tunnel diode and resonant tunneling diode based microwave sources, Glasgow University, 2011. http://theses.gla.ac.uk/id/eprint/3423.

[16] M. Ino, T. Ishibashi, M. Ohmori, C.W. oscillation with p+-p-n+ silicon IMPATT diodes in 200 GHz and 300 GHz bands, Electron. Lett. 12 (1976) 148. doi:doi: 10.1049/el:19760115.

[17] G. Ok, K. Park, M.-C. Lim, H.-J. Jang, S.-W. Choi, 140-GHz subwavelength transmission imaging for foreign body inspection in food products, J. Food Eng. 221 (2018) 124–131. doi:10.1016/j.jfoodeng.2017.10.011.

[18] H. Eisele, Second-harmonic power extraction from InP Gunn devices with more than 1 mW in 260-320 GHz frequency range, Electron. Lett. 34 (1998) 2412. doi:doi: 10.1049/el:19981659.

[19] J.P. Sun, G.I. Haddad, P. Mazumder, J.N. Schulman, Resonant tunneling diodes: models and properties, Proc. IEEE. 86 (1998) 641–660. doi:10.1109/5.663541.

[20] H. Eisele, A. Rydberg, G.I. Haddad, Recent advances in the performance of InP Gunn devices and GaAs TUNNETT diodes for the 100-300-GHz frequency range and above, Microw. Theory Tech. IEEE Trans. 48 (2000) 626–631. doi:10.1109/22.841952.

[21] N. Shimizu, T. Waho, T. Ishibashi, Capacitance Anomaly in the Negative Differential Resistance Region of Resonant Tunneling Diodes, Jpn. J. Appl. Phys. 36 (1997) L330–L333. doi:10.1143/JJAP.36.L330.

[22] M. Feiginov, R. Gonzalo, I. Maestrojuán, O. Cojocari, M. Hoefle, E. Limiti, THz Electronics, in: Semicond. Terahertz Technol., John Wiley & Sons, Ltd, 2015: pp. 254–303. doi:10.1002/9781118920411.ch6.

[23] V. Radisic, D. Sawdai, D. Scott, W.R. Deal, L. Dang, D. Li, J. Chen, A. Fung, L. Samoska, T. Gaier, R. Lai, Demonstration of a 311-GHz Fundamental Oscillator Using InP HBT Technology, Microw. Theory Tech. IEEE Trans. 55 (2007) 2329–2335. doi:10.1109/TMTT.2007.907722.

[24] V. Radisic, X.B. Mei, W.R. Deal, W. Yoshida, P.-H. Liu, J. Uyeda, M. Barsky, L. Samoska, A. Fung, T. Gaier, R. Lai, Demonstration of Sub-Millimeter Wave Fundamental Oscillators Using 35-nm InP HEMT Technology, Microw. Wirel. Components Lett. IEEE. 17 (2007) 223–225. doi:10.1109/LMWC.2006.890495.

[25] T. Watanabe, S.B. Tombet, Y. Tanimoto, Y. Wang, H. Minamide, H. Ito, D. Fateev, V. Popov, D. Coquillat, W. Knap, Y. Meziani, T. Otsuji, Ultrahigh sensitive plasmonic terahertz detector based on an asymmetric dual-grating gate HEMT structure, Solid. State. Electron. 78 (2012) 109–114. doi:http://dx.doi.org/10.1016/j.sse.2012.05.047.

[26] H. Ito, T. Furuta, S. Kodama, T. Ishibashi, InP/InGaAs uni-travelling-carrier photodiode with 310 GHz bandwidth, Electron. Lett. 36 (2000) 1809. doi:10.1049/el:20001274.

[27] M.N. Feiginov, Analysis of limitations of terahertz p-i-n uni-traveling-carrier photodiodes, J. Appl. Phys. 102 (2007). doi:10.1063/1.2801400.

[28] T. Kleine-Ostmann, T. Nagatsuma, A Review on Terahertz Communications Research, J. Infrared, Millimeter, Terahertz Waves. 32 (2011) 143–171. doi:10.1007/s10762-010-9758-1.

[29] H.-J. Song, K. Ajito, Y. Muramoto, A. Wakatsuki, T. Nagatsuma, N. Kukutsu, Uni-Travelling-Carrier Photodiode Module Generating 300 GHz Power Greater Than 1 mW, IEEE Microw. Wirel. Components Lett. 22 (2012) 363–365. doi:10.1109/LMWC.2012.2201460.

[30] N. Singh, C.K.F. Ho, G.X. Tina, M.K. Chandra Mohan, K.E.K. Lee, H. Wang, H.Q. Lam, MOCVD Growth and Fabrication of High Power MUTC Photodiodes Using InGaAs-InP System, J. Nanomater. 2015 (2015) 1–6. doi:10.1155/2015/436851.

[31] A.W. Mohammad, H. Shams, K. Balakier, C. Graham, M. Natrella, A.J. Seeds, C.C. Renaud, 5 Gbps wireless transmission link with an optically pumped uni-traveling carrier photodiode mixer at the receiver, Opt. Express. 26 (2018) 2884. doi:10.1364/OE.26.002884.

[32] Lianhe Li, Li Chen, Jingxuan Zhu, J. Freeman, P. Dean, A. Valavanis, A.G. Davies, E.H. Linfield, Terahertz quantum cascade lasers with >1 W output powers, Electron. Lett. 50 (2014) 309–311. doi:10.1049/el.2013.4035.

[33] J.M. Tavish, Z. Ikonić, D. Indjin, P. Harrison, Intervalley Scattering and the Role, of Indirect Band Gap AlAs Barriers: Application to GaAs/AlGaAs Quantum Cascade Lasers, Acta Phys. Pol. A. 113 (2008) 891–902.

[34] M.A. Belkin, F. Capasso, F. Xie, A. Belyanin, M. Fischer, A. Wittmann, J. Faist, Room temperature terahertz quantum cascade laser source based on intracavity difference-frequency generation, Appl. Phys. Lett. 92 (2008) 201101. doi:10.1063/1.2919051.

[35] M.A. Belkin, F. Capasso, A. Belyanin, D.L. Sivco, A.Y. Cho, D.C. Oakley, C.J. Vineis, G.W. Turner, Terahertz quantum-cascade-laser source based on intracavity difference-frequency generation, Nat Phot. 1 (2007) 288–292. http://dx.doi.org/10.1038/nphoton.2007.70.

[36] P.G. and F.C. and M.T. and K.S. and Ci-Ling Pan, Generation of Coherent cw-Terahertz Radiation Using a Tunable Dual-Wavelength External Cavity Laser Diode, Jpn. J. Appl. Phys. 38 (1999) L1246. http://stacks.iop.org/1347-4065/38/i=11A/a=L1246.

[37] M. Tacke, Lead–salt lasers, Philos. Trans. R. Soc. London A Math. Phys. Eng. Sci. 359 (2001) 547–566.

[38] E. Bründermann, H.P. Röser, A.V. Muravjov, S.G. Pavlov, V.N. Shastin, Mode fine structure of the p-Ge intervalenceband laser measured by heterodyne mixing spectroscopy with an optically pumped ring gas laser, Infrared Phys. Technol. 36 (1995) 59–69. doi:10.1016/1350-4495(94)00054-O.

[39] T. de Graauw, F.P. Helmich, T.G. Phillips, J. Stutzki, E. Caux, N.D. Whyborn, P. Dieleman, P.R. Roelfsema, E. Al., The Herschel-Heterodyne Instrument for the Far-Infrared (HIFI), A&A. 518 (2010) L6. doi:10.1051/0004-6361/201014698.

[40] D. Dragoman, M. Dragoman, Terahertz fields and applications, Prog. Quantum Electron. 28 (2004) 1–66. doi:10.1016/S0079-6727(03)00058-2.

[41] Y. Silberberg, D.A.B. Miller, A.C. Gossard, W. Wiegmann, P.W. Smith, D.J. Eilenberger, Passive mode locking of a semiconductor diode laser, Opt. Lett. 9 (1984) 507–509. doi:doi: 10.1364/ol.9.000507.

[42] A.N. Majeed, P. Ivanov, D.T.D. Childs, E. Clarke, R.A. Hogg, O. Kojima, Substrate removal and capillary bonding of a quantum beat sample, in: 2015 8th UK, Eur. China Millim. Waves THz Technol. Work., IEEE, 2015: pp. 1–3. doi:10.1109/UCMMT.2015.7460634.

[43] K.T. Nguyen, D. Pershing, E.L. Wright, J. Pasour, J. Calame, L. Ludeking, J. Rodgers, J. Petillo, Sheet-Beam 90 GHz and 220 GHz Extend-Interaction-Klystron Designs, in: Vac. Electron. Conf. 2007. IVEC '07. IEEE Int., 2007: pp. 1–2. doi:10.1109/IVELEC.2007.4283282.

[44] L. Hu, R. Song, G. Ma, Y. Jiang, W. Lei, F. Meng, H. Chen, Experimental Demonstration of a 0.34-THz Backward-Wave Oscillator With a Sinusoidally Corrugated Slow-Wave Structure, IEEE Trans. Electron Devices. 65 (2018) 2149–2155. doi:10.1109/TED.2018.2805699.

[45] D. Rosenheck, S. Chankova, G. Scriven, A. Selby-Boothroyd, J. Tozer, The world's refugee crisis: past and present, Econ. (2016). https://www.economist.com/graphic-detail/2016/05/27/the-worlds-refugee-crisis-past-and-present (accessed June 9, 2018).

[46] Special Report, Looking for a Home, Econ. (2016). https://www.economist.com/special-report/2016/05/28/looking-for-a-home (accessed June 9, 2018).

[47] Migrants with mobiles: phones are now indispensable for refugees, Econ. (2017). https://www.economist.com/international/2017/02/11/phones-are-now-indispensable-for-refugees (accessed June 9, 2018).

[48] GSM Association Disaster Response, The Importance of Mobile for Refugees: A Landscape of New Services and Approaches, London, UK, 2017. https://www.gsma.com/mobilefordevelopment/wp-content/uploads/2017/02/The-Importance-of-mobile-for-refugees_a-landscape-of-new-services-and-approaches.pdf.

[49] C. Locke, Refugees' Stories Told Through Their Smartphones, Wired Online. (2018). https://www.wired.com/2017/02/personal-stories-refugees-told-smartphones/ (accessed June 9, 2018).

[50] W. Worley, Syrian woman explains why refugees need smartphones, Indep. (2017). https://www.independent.co.uk/news/world/europe/why-do-refugees-have-smartphones-syrian-woman-explains-perfectly-refugee-crisis-a7025356.html (accessed June 9, 2018).

[51] Y.F. Chang, C.S. Chen, H. Zhou, Smart phone for mobile commerce, Comput. Stand. Interfaces. 31 (2009) 740–747. doi:10.1016/j.csi.2008.09.016.

[52] UN Refugee Association, Connecting Refugees: How Internet and Mobile Connectivity can Improve Refugee Well-Being and Transform Humanitarian Action, Geneva, Switzerland, 2016. http://www.unhcr.org/5770d43c4.

[53] E. Cresci, Chatbot that overturned 160,000 parking fines now helping refugees claim asylum, Guard. (2017). https://www.theguardian.com/technology/2017/mar/06/chatbot-donotpay-refugees-claim-asylum-legal-aid (accessed June 9, 2018).

[54] J. O'Shea, Contactless payment fraud soars to £7m, BBC News. (2017).

https://www.bbc.co.uk/news/uk-england-devon-39942246 (accessed June 9, 2018).

[55] C. Wood, Why Mobile Wallets are Safer than Physical Wallets, Capterra Retail Manag. Blog. (2015). https://blog.capterra.com/mobile-wallets-are-safer-than-physical-wallets/ (accessed June 9, 2018).

[56] Y. Jin, S. Wang, Y. Qu, Q. Guo, J. Li, Study on Security of Mobile Payment, in: 2018: pp. 123–127. doi:10.1007/978-3-319-65978-7_19.

[57] Cisco Inc., Cisco Visual Networking Index: Global Mobile Data Traffic Forecast Update, 2015–2020 White Paper, 2016.

[58] S. Cherry, Edholm's law of bandwidth: telecommunications data rates are as predictable as Moore's law, IEEE Spectr. 58 (2004). doi:http://dx.doi.org/10.1109/MSPEC.2004.1309810.

[59] S. Garg, Is millimeter wave technology future of wireless communications?, Microw. J. (2017). http://www.microwavejournal.com/blogs/25-5g/post/28775-is-millimeter-wave-technology-future-of-wireless-communications (accessed July 9, 2018).

[60] H. Wang, W.-D. Hu, R.-T. Liu, L.-M. Si, J.-Y. Yin, T. Dong, A design of 300 GHz waveguide bandpass filter with H-plane offset inductive window, in: 2016 IEEE 9th UK-Europe-China Work. Millimetre Waves Terahertz Technol., IEEE, 2016: pp. 189–191. doi:10.1109/UCMMT.2016.7874007.

[61] Society of Motion Picture and Television Engineers, OV 2082-0:2016 - SMPTE Overview Document - 12G-SDI Bit-Serial Interfaces — Overview for the SMPTE ST 2082 Document Suite, 32NF - Technol. Comm. Netw. Facil. Infrastruct. (2016). doi:10.5594/SMPTE.OV2082-0.2016.

[62] T. Shiode, T. Mukai, M. Kawamura, T. Nagatsuma, Giga-bit wireless communication at 300 GHz using resonant tunneling diode detector, in: Microw. Conf. Proc. (APMC), 2011 Asia-Pacific, 2011: pp. 1122–1125. http://ieeexplore.ieee.org/xpl/articleDetails.jsp?tp=&arnumber=6173953&queryText%3DShiode%2C+T.%3B+Mukai%2C+T.+%3B+Kawamura%2C+M.+%3B+Nagatsuma%2C+T.

[63] S. Diebold, K. Nishio, Y. Nishida, J.-Y. Kim, K. Tsuruda, T. Mukai, M. Fujita, T. Nagatsuma, High-speed error-free wireless data transmission using a terahertz resonant tunnelling diode transmitter and receiver, Electron. Lett. 52 (2016) 1999–2001. doi:10.1049/el.2016.2941.

[64] D.R. Vizard, M. Gashinova, E.G. Hoare, M. Cherniakov, Compact 300–670 GHz frequency extenders for portable automotive radar applications, in: 2015 8th UK, Eur. China Millim. Waves THz Technol. Work., IEEE, 2015: pp. 1–2. doi:10.1109/UCMMT.2015.7460616.

[65] D.R. Vizard, E.G. Hoare, M. Gashinova, M. Cherniakov, A hybrid VNA frequency extender for 670 GHz portable automotive radar applications, in: 2017 10th UK-Europe-China Work. Millimetre Waves Terahertz Technol., IEEE, 2017: pp. 1–2. doi:10.1109/UCMMT.2017.8068477.

[66] I. Duling, D. Zimdars, Revealing hidden defects, Nat. Photonics. 3 (2009) 630–632. doi:10.1038/nphoton.2009.206.

[67] A. Cosentino, Terahertz and Cultural Heritage Science: Examination of Art and Archaeology, Technologies. 4 (2016) 6. doi:10.3390/technologies4010006.

[68] S. Fan, T. Li, J. Zhou, X. Liu, X. Liu, H. Qi, Z. Mu, Terahertz non-destructive imaging of cracks and cracking in structures of cement-based materials, AIP Adv. 7 (2017) 115202. doi:10.1063/1.4996053.

[69] C.-C. Chen, D.-J. Lee, T. Pollock, J.F. Whitaker, Pulsed-terahertz reflectometry for health monitoring of ceramic thermal barrier coatings, Opt. Express. 18 (2010) 3477. doi:10.1364/OE.18.003477.

[70] D.K. Hsu, K.-S. Lee, J.-W. Park, Y.-D. Woo, K.-H. Im, NDE inspection of terahertz waves in wind turbine composites, Int. J. Precis. Eng. Manuf. 13 (2012) 1183–1189. doi:10.1007/s12541-012-0157-5.

[71] Y. Sun, A promising diagnostic method: Terahertz pulsed imaging and spectroscopy, World J. Radiol. 3 (2011) 55. doi:10.4329/wjr.v3.i3.55.

[72] S.A. Harmon, R.A. Cheville, Part-per-million gas detection from long-baseline THz spectroscopy, Appl. Phys. Lett. 85 (2004) 2128–2130. doi:10.1063/1.1788896.

[73] N. Shimizu, H.-J. Song, Y. Kado, T. Furuta, A. Wakatsuki, Y. Muramoto, Gas Detection Using Terahertz Waves, NTT Tech. Rev. 7 (2009) 1–6. https://www.ntt-review.jp/archive/ntttechnical.php?contents=ntr200903sf7.html.

[74] Y.-D. Hsieh, S. Nakamura, D.G. Abdelsalam, T. Minamikawa, Y. Mizutani, H. Yamamoto, T. Iwata, F. Hindle, T. Yasui, Dynamic terahertz spectroscopy of gas molecules mixed with unwanted aerosol under atmospheric pressure using fibre-based asynchronous-optical-sampling terahertz time-domain spectroscopy, Sci. Rep. 6 (2016) 28114. doi:10.1038/srep28114.

[75] T. Lim, B. Swinyard, M. Griffin, A. Aramburu, J.-P. Baluteau, J. Bock, M. Ferlet, T. Fulton, D. Griffin, S. Guest, P. Hargrave, K. King, S. Leeks, D. Naylor, E. Polehampton, D. Rizzo, E. Sawyer, B. Schulz, S. Sidher, L. Spencer, D. Smith, H.T. Nguyen, I. Valtchanov, T. Waskett, A. Woodcraft, Preliminary results from Herschel-SPIRE flight instrument testing, in: 2006: p. 62650F–62650F–10. http://dx.doi.org/10.1117/12.672752.

[76] R. Appleby, R.N. Anderton, Millimeter-Wave and Submillimeter-Wave Imaging for Security and Surveillance, Proc. IEEE. 95 (2007) 1683–1690. doi:10.1109/JPROC.2007.898832.

[77] E.F. Plinski, Terahertz spectroscopy of organic molecular crystalline forms, in: 2012 19th Int. Conf. Microwaves, Radar Wirel. Commun., IEEE, 2012: pp. 279–281. doi:10.1109/MIKON.2012.6233516.

[78] S. Kitagawa, M. Mizuno, S. Saito, K. Ogino, S. Suzuki, M. Asada, Frequency-tunable resonant-tunneling-diode terahertz oscillators applied to absorbance measurement, Jpn. J. Appl. Phys. 56 (2017) 058002. doi:10.7567/JJAP.56.058002.

[79] L-3 Technologies, SafeView™ Compact advanced imaging system, Secur. Def. Syst. (2012). http://safe-view.com/advancedimaging/safeview.htm (accessed June 1, 2018).

[80] M. Koch, Terahertz Communications: A 2020 vision, in: R. Miles, X.-C. Zhang, H. Eisele, A. Krotkus (Eds.), Terahertz Freq. Detect. Identif. Mater. Objects SE - 18, Springer Netherlands, Dordrecht, 2007: pp. 325–338. doi:10.1007/978-1-4020-6503-3_18.

[81] A. Luukanen, R. Appleby, M. Kemp, N. Salmon, Millimeter-Wave and Terahertz Imaging in Security Applications, in: 2012: pp. 491–520. doi:10.1007/978-3-642-29564-5_19.

[82] T. Nagatsuma, H. Nishii, T. Ikeo, Terahertz imaging based on optical coherence tomography [Invited], Photonics Res. 2 (2014) B64. doi:10.1364/PRJ.2.000B64.

[83] J. Roberts, Using Imperfect Semiconductor Systems for Unique Identification, Springer International Publishing, Cham, 2017. doi:10.1007/978-3-319-67891-7.

[84] K. Maezawa, T. Mizutani, New resonant tunneling logic gate employing monostable-bistable transition, Japanese J. Appl. Physics, Part 2 Lett. 32 (1993). doi:10.1143/JJAP.32.L42.

[85] K. Maezawa, M. Sakou, W. Matsubara, T. Mizutani, A novel resonant tunneling Delta-Sigma A/D converter having no feedback loop for ultrahigh-speed operation, in: Int. Conf. Indium Phosphide Relat. Mater. 2005., IEEE, n.d.: pp. 254–255. doi:10.1109/ICIPRM.2005.1517471.

[86] P. Mazumder, S. Kulkarni, M. Bhattacharya, Jian Ping Sun, G.I. Haddad, Digital circuit applications of resonant tunneling devices, Proc. IEEE. 86 (1998) 664–686. doi:10.1109/5.663544.

[87] J. Soderstrom, T.G. Andersson, A multiple-state memory cell based on the resonant tunneling diode, IEEE Electron Device Lett. 9 (1988) 200–202. doi:10.1109/55.689.

[88] J.P.A. van der Wagt, Tunneling-based SRAM, Proc. IEEE. 87 (1999) 571–595. doi:10.1109/5.752516.

[89] I. Sanyal, M. Das Sarkar, Parameter optimization of a single well nanoscale resonant tunneling diode for memory applications, in: 2015 IEEE Int. Conf. Electron Devices Solid-State Circuits, IEEE, 2015: pp. 439–442. doi:10.1109/EDSSC.2015.7285145.

[90] H.M. Manasevit, Single-crystal gallium arsenide on insulating substrates, Appl. Phys. Lett.

12 (1968) 156–159. doi:10.1063/1.1651934.

[91] J.J. Coleman, Metalorganic chemical vapor deposition for optoelectronic devices, Proc. IEEE. 85 (1997) 1715–1729. doi:10.1109/5.649647.

[92] P.R. Hageman, X. Tang, M.H.J.M. de Croon, L.J. Giling, Temperature dependence of silicon doping of GaAs by SiH4 and Si2H6 in atmospheric pressure metalorganic chemical vapour deposition, J. Cryst. Growth. 98 (1989) 249–254. doi:10.1016/0022-0248(89)90139-5.

[93] H. Sugiyama, A. Teranishi, S. Suzuki, M. Asada, Structural and electrical transport properties of MOVPE-grown pseudomorphic AlAs/InGaAs/InAs resonant tunneling diodes on InP substrates, Jpn. J. Appl. Phys. 53 (2014) 031202. doi:10.7567/JJAP.53.031202.

[94] R. Lückerath, P. Tommack, A. Hertling, H.J. Koss, P. Balk, K.F. Jensen, W. Richter, CARS in situ diagnostics in MOVPE: The thermal decomposition of AsH3 and PH3, J. Cryst. Growth. 93 (1988) 151–158. doi:10.1016/0022-0248(88)90520-9.

[95] LayTec AG, 3λ Reflectance, (2014). http://www.laytec.de/key-technologies/metrology-methods/3l-reflectance/ (accessed April 17, 2018).

[96] T. Sakamoto, Rheed Oscillations in MBE and Their Applications to Precisely Controlled Crystal Growth, in: P. Dhez, C. Weisbuch (Eds.), Physics, Fabr. Appl. Multilayered Struct., Springer US, Boston, MA, 1988: pp. 93–110. doi:10.1007/978-1-4757-0091-6.

[97] H.S. Sommers, Tunnel Diodes as High-Frequency Devices, Proc. IRE. 47 (1959). doi:10.1109/JRPROC.1959.287351.

[98] I. Poole, Tunnel Diode Theory & Operation, Radio Electron. (2013). http://www.radio-electronics.com/info/data/semicond/tunneldiode/theory-operation.php (accessed June 9, 2018).

[99] S. Luryi, Quantum capacitance devices, Appl. Phys. Lett. 52 (1988) 501–503. doi:10.1063/1.99649.

[100] P. Atkins, T. Overton, J. Rourke, M. Weller, F. Armstrong, Inorganic Chemistry, in: Inorg. Chem., 5th ed., Oxford University Press, New York, 2010: pp. 101–103.

[101] T. Tohyama, Recent Progress in Physics of High-Temperature Superconductors, Jpn. J. Appl. Phys. 51 (2012) 010004. doi:10.1143/JJAP.51.010004.

[102] C. Kittel, Wave Diffraction and the Reciprocal Lattice, in: S. Johnson (Ed.), Introd. to Solid State Phys., 8th ed., John Wiley & Sons, Ltd, Hoboken, NJ, 2005: pp. 33–43.

[103] Cambridge Dissemination of IT for the Promotion of Materials Science (DoITPoMS), Brillouin Zone construction, Teach. Learn. Packag. Libr. (2009). https://www.doitpoms.ac.uk/tlplib/brillouin_zones/zone_construction.php (accessed March 26, 2018).

[104] User:Inductiveload, Brilouin Zone (1st, FCC), Wikimedia Commons. (n.d.). https://commons.wikimedia.org/wiki/File:Brillouin_Zone_(1st,_FCC).svg.

[105] P. Vogl, H.P. Hjalmarson, J.D. Dow, A Semi-empirical tight-binding theory of the electronic structure of semiconductors†, J. Phys. Chem. Solids. 44 (1983) 365–378. doi:10.1016/0022-3697(83)90064-1.

[106] M.B. Steer, R.J. Trew, Microwave Devices, in: R.C. Dorf (Ed.), Electron. Power Electron. Optoelectron. Microwaves, Electromagn. Radar, CRC Taylor & Francis, Boca Raton, Florida, 2006: pp. 18–15.

[107] S.M. Sze, K. Ng, K., K.K. Ng, Physics of Semiconductor Devices, in: Phys. Semicond. Devices, 3rd ed., Wiley, Hoboken, New Jersey, 2007: pp. 416–475. http://eu.wiley.com/WileyCDA/WileyTitle/productCd-0471143235.html#.

[108] I. Vurgaftman, J.R. Meyer, L.R. Ram-Mohan, Band parameters for III-V compound semiconductors and their alloys, J. Appl. Phys. 89 (2001) 5815–5875. doi:10.1063/1.1368156.

[109] C.G. Van De Walle, Band lineups and deformation potentials in the model-solid theory,

Phys. Rev. B. 39 (1989) 1871–1883. doi:10.1103/PhysRevB.39.1871.

[110] G. Klimeck, R. Chris Bowen, T.B. Boykin, T.A. Cwik, sp3s*Tight-binding parameters for transport simulations in compound semiconductors, Superlattices Microstruct. 27 (2000) 519–524. doi:10.1006/spmi.2000.0862.

[111] K. Montgomery, Semiconductor Band Parameters, (n.d.). http://kmontgomery.net/slider/semiconductor-band-parameters/ (accessed March 13, 2018).

[112] S. Adachi, Properties of Semiconductor Alloys: Group-IV, III-V, and II-VI Semiconductors, Chichester, 2009.

[113] I. Vurgaftman, J.R. Meyer, Band parameters for nitrogen-containing semiconductors, J. Appl. Phys. 94 (2003) 3675–3696. doi:10.1063/1.1600519.

[114] Ioffe Physico-Technical Institute, Semiconductors on NSM, (2007). http://www.ioffe.ru/SVA/NSM/Semicond/.

[115] J. Singh, Properties of Semiconductors: Electronic States, in: Semicond. Optoelectron. Phys. Technol., McGraw-Hill, New York, 1995: p. 67.

[116] W.R. Wilcox, T.J. LaChapelle, Mechanism of Gold Diffusion into Silicon, J. Appl. Phys. 35 (1964) 240–246. doi:10.1063/1.1713077.

[117] C.G. Van de Walle, J. Neugebauer, Universal alignment of hydrogen levels in semiconductors, insulators and solutions, Nature. 423 (2003) 626–628. doi:10.1038/nature01665.

[118] S.C. Jain, M. Willander, H. Maes, Stresses and strains in epilayers, stripes and quantum structures of III - V compound semiconductors, Semicond. Sci. Technol. 11 (1999) 641–671. doi:10.1088/0268-1242/11/5/004.

[119] J.W. Matthews, A.E. Blakeslee, Defects in epitaxial multilayers, J. Cryst. Growth. 27 (1974) 118–125. doi:10.1016/S0022-0248(74)80055-2.

[120] R. People, J.C. Bean, Calculation of critical layer thickness versus lattice mismatch for GexSi1−x/Si strained-layer heterostructures, Appl. Phys. Lett. 47 (1985) 322. doi:10.1063/1.96206.

[121] R. People, J.C. Bean, Erratum: Calculation of critical layer thickness versus lattice mismatch for GexSi1−x/Si strained-layer heterostructures [Appl. Phys. Lett. 47, 322 (1985)], Appl. Phys. Lett. 49 (1986) 229. doi:10.1063/1.97637.

[122] S.-L. Weng, Experimental studies of misfit dependence of critical layer thickness in pseudomorphic InGaAs single-strained quantum-well structures, J. Appl. Phys. 66 (1989) 2217. doi:10.1063/1.344272.

[123] N.J. Ekins-Daukes, K.W.J. Barnham, J.P. Connolly, J.S. Roberts, J.C. Clark, G. Hill, M. Mazzer, Strain-balanced GaAsP/InGaAs quantum well solar cells, Appl. Phys. Lett. 75 (1999) 4195. doi:10.1063/1.125580.

[124] J. Tatebayashi, M. Ishida, N. Hatori, H. Ebe, H. Sudou, A. Kuramata, M. Sugawara, Y. Arakawa, Lasing at 1.28 /spl mu/m of InAs-GaAs quantum dots with AlGaAs cladding layer grown by metal-organic chemical vapor deposition, IEEE J. Sel. Top. Quantum Electron. 11 (2005) 1027–1034. doi:10.1109/JSTQE.2005.853788.

[125] F. Hetsch, N. Zhao, S. V. Kershaw, A.L. Rogach, Quantum dot field effect transistors, Mater. Today. 16 (2013) 312–325. doi:10.1016/j.mattod.2013.08.011.

[126] R. Beanland, A.M. Sánchez, D. Childs, K.M. Groom, H.Y. Liu, D.J. Mowbray, M. Hopkinson, Structural analysis of life tested 1.3 μm quantum dot lasers, J. Appl. Phys. 103 (2008) 014913. doi:10.1063/1.2827451.

[127] M. Sugawara, K. Mukai, Y. Nakata, H. Ishikawa, A. Sakamoto, Effect of homogeneous broadening of optical gain on lasing spectra in self-assembled InGaAs/GaAs quantum dot lasers, Phys. Rev. B. 61 (2000) 7595–7603. doi:10.1103/PhysRevB.61.7595.

[128] W. Lu, P. Xie, C.M. Lieber, Nanowire Transistor Performance Limits and Applications, IEEE Trans. Electron Devices. 55 (2008) 2859–2876. doi:10.1109/TED.2008.2005158.

[129] L. Esaki, R. Tsu, Superlattice and Negative Differential Conductivity in Semiconductors, IBM J. Res. Dev. 14 (1970) 61–65. doi:10.1147/rd.141.0061.

[130] B. Ricco, M.Y. Azbel, Physics of resonant tunneling. The one-dimensional double-barrier case, Phys. Rev. B. 29 (1984) 1970–1981. doi:10.1103/PhysRevB.29.1970.

[131] M.N. Feiginov, Does the quasibound-state lifetime restrict the high-frequency operation of resonant-tunnelling diodes?, Nanotechnology. 11 (2000) 359–364. doi:10.1088/0957-4484/11/4/333.

[132] M. Feiginov, H. Kanaya, S. Suzuki, M. Asada, 1.46 THz RTD oscillators with strong back injection from collector, in: Int. Conf. Infrared, Millimeter, Terahertz Waves, IRMMW-THz, 2014. doi:10.1109/IRMMW-THz.2014.6956452.

[133] R.E. Carnahan, K.P. Martin, R.J. Higgins, B.G. Park, E. Wolak, K.L. Lear, J.S.H. Jr, Gamma -X intervalley tunnelling in a GaAs/AlAs resonant tunnelling diode under uniaxial stress, Semicond. Sci. Technol. 9 (1994) 500. http://stacks.iop.org/0268-1242/9/i=5S/a=027.

[134] F. Chevoir, B. Vinter, Calculation of phonon-assisted tunneling and valley current in a double-barrier diode, Appl. Phys. Lett. 55 (1989) 1859. doi:10.1063/1.102188.

[135] P.A. Lebwohl, R. Tsu, Electrical Transport Properties in a Superlattice, J. Appl. Phys. 41 (1970) 2664–2667. doi:10.1063/1.1659279.

[136] W. Müller, D. Bertram, H.T. Grahn, K. von Klitzing, K. Ploog, Competition between thermally induced resonant tunneling and phonon-assisted tunneling in semiconductor superlattices, Phys. Rev. B. 50 (1994) 10998–11001. doi:10.1103/PhysRevB.50.10998.

[137] R. Tsu, L. Esaki, Tunneling in a finite superlattice, Appl. Phys. Lett. 22 (1973) 562–564. doi:10.1063/1.1654509.

[138] L. Chang, L. Esaki, R. Tsu, Resonant tunneling in semiconductor double barriers, Appl. Phys. Lett. (1974). http://scitation.aip.org/content/aip/journal/apl/24/12/10.1063/1.1655067 (accessed February 25, 2014).

[139] S. Datta, Electrical resistance: an atomistic view, Nanotechnology. 15 (2004) S433–S451. doi:10.1088/0957-4484/15/7/051.

[140] J.N. Schulman, H.J. De Los Santos, D.H. Chow, Physics-based RTD current-voltage equation, IEEE Electron Device Lett. 17 (1996) 220–222. doi:10.1109/55.491835.

[141] J.N. Schulman, Extension of Tsu-Esaki model for effective mass effects in resonant tunneling, Appl. Phys. Lett. 72 (1998) 2829–2831. doi:10.1063/1.121471.

[142] R. Landauer, Spatial variation of currents and fields due to localized scatterers in metallic conduction (1957 reprint and comment), J. Math. Phys. 37 (1996) 5259–5268. doi:10.1063/1.531590.

[143] M. Büttiker, Coherent and sequential tunneling in series barriers, IBM J. Res. Dev. 32 (1988) 63–75. doi:10.1147/rd.321.0063.

[144] G. Strinati, Application of the Green's functions method to the study of the optical properties of semiconductors, La Riv. Del Nuovo Cim. 11 (1988) 1–86. doi:10.1007/BF02725962.

[145] A. Jauho, Introduction to the Keldysh nonequilibrium Green function technique, Lect. Notes. (2006) 17. https://isis.ku.dk/kurser/blob.aspx?feltid=55674.

[146] Alexandre Reily Rocha, Theoretical and Computational Aspects of electronic transport at the Nanoscale, Trinity College Dublin, 2007. http://www.smeagol.tcd.ie/PAPER/AlexThesis.html.

[147] S. Birner, T. Kubis, Ballistic current in a resonant tunneling diode (RTD), (2014). http://www.nextnano.com/nextnano3/tutorial/1Dtutorial_RTD_green.htm (accessed October 7, 2014).

[148] R. Lake, G. Klimeck, R.C. Bowen, D. Jovanovic, Single and multiband modeling of quantum electron transport through layered semiconductor devices, J. Appl. Phys. 81 (1997) 7845–7869. doi:10.1063/1.365394.

[149] R. Lake, S. Datta, Nonequilibrium Green's-function method applied to double-barrier

resonant-tunneling diodes, Phys. Rev. B. 45 (1992) 6670–6685. doi:10.1103/PhysRevB.45.6670.

[150] T. Sandu, W.P. Kirk, Intrinsic bistability and emitter scattering in resonant tunneling diodes, in: Phys. E Low-Dimensional Syst. Nanostructures, 2003: pp. 83–88. doi:10.1016/S1386-9477(03)00295-9.

[151] D. Mamaluy, M. Sabathil, P. Vogl, Efficient method for the calculation of ballistic quantum transport, J. Appl. Phys. 93 (2003) 4628–4633. doi:10.1063/1.1560567.

[152] D.R. Hartree, The Wave Mechanics of an Atom with a Non-Coulomb Central Field. Part I. Theory and Methods, Math. Proc. Cambridge Philos. Soc. 24 (1928) 89. doi:10.1017/S0305004100011919.

[153] D.R. Hartree, The Wave Mechanics of an Atom with a Non-Coulomb Central Field. Part II. Some Results and Discussion, Math. Proc. Cambridge Philos. Soc. 24 (1928) 111. doi:10.1017/S0305004100011920.

[154] M. Scheffler, A. Tkatchenko, P. Rinke, Theoretical Material Science, Chapter 3, Fritz Haber Institute of the Max Planck Society, 2012. https://www.itp.tu-berlin.de/fileadmin/a3233/upload/SS12/TheoFest2012/Kapitel/Chapter_3.pdf.

[155] R.T. Syme, M.J. Kelly, R.S. Smith, A. Condie, I. Dale, Tunnel diode with asymmetric spacer layers for use as microwave detector, Electron. Lett. 27 (1991) 2192. doi:10.1049/el:19911356.

[156] T. Wei, S. Stapleton, O. Berolo, Capacitance and hysteresis study of AlAs/GaAs resonant tunneling diode with asymmetric spacer layers, J. Appl. Phys. 77 (1995) 4071–4076. doi:10.1063/1.359490.

[157] T.B. Boykin, R.E. Carnahan, K.P. Martin, Inadequacy of the one-dimensional approximation for resonant-tunneling-diode current-voltage calculations, Phys. Rev. B. 51 (1995) 2273–2281. doi:10.1103/PhysRevB.51.2273.

[158] H. Mizuta, T. Tanoue, The Physics and Applications of Resonant Tunnelling diodes, Cambridge, New York, 1995. www.cambridge.org/9780521432184.

[159] K.J.P.J.P. Jacobs, B.J.J. Stevens, R. Baba, O. Wada, T. Mukai, R.A.A. Hogg, Valley current characterization of high current density resonant tunnelling diodes for terahertz-wave applications, AIP Adv. 7 (2017) 105316. doi:10.1063/1.4997664.

[160] J. Chen, J.G. Chen, C.H. Yang, R.A. Wilson, The I - V characteristics of double-barrier resonant tunneling diodes: Observation and calculation on their temperature dependence and asymmetry, J. Appl. Phys. 70 (1991) 3131–3136. doi:10.1063/1.349292.

[161] A.K. Jonscher, The physics of the tunnel diode, Br. J. Appl. Phys. 12 (1961) 654. http://stacks.iop.org/0508-3443/12/i=12/a=304.

[162] W.A. Edson, Vacuum Tube Oscillators, 1st editio, John Wiley and Sons Inc., New Yorkpn, New York, 1953. http://www.tubebooks.org/Books/vto.pdf.

[163] T.J. Slight, B. Romeira, L. Wang, J.M.L. Figueiredo, E. Wasige, C.N. Ironside, A Liénard oscillator resonant tunnelling diode-laser diode hybrid integrated circuit: Model and experiment, IEEE J. Quantum Electron. 44 (2008) 1158–1163. doi:10.1109/JQE.2008.2000924.

[164] C.S. Kim, A. Brandli, High-Frequency High-Power Operation of Tunnel Diodes, Circuit Theory, IRE Trans. 8 (1961) 416–425. doi:10.1109/TCT.1961.1086849.

[165] M. Asada, S. Suzuki, N. Kishimoto, Resonant Tunneling Diodes for Sub-Terahertz and Terahertz Oscillators, Jpn. J. Appl. Phys. 47 (2008) 4375–4384. doi:10.1143/JJAP.47.4375.

[166] T.C.L.G. Sollner, W.D. Goodhue, P.E. Tannenwald, C.D. Parker, D.D. Peck, Resonant tunneling through quantum wells at frequencies up to 2.5 THz, Appl. Phys. Lett. 43 (1983) 588. doi:10.1063/1.94434.

[167] E.R. Brown, W.D. Goodhue, T.C.L.G. Sollner, Fundamental oscillations up to 200 GHz in resonant tunneling diodes and new estimates of their maximum oscillation frequency from stationary-state tunneling theory, J. Appl. Phys. 64 (1988) 1519–1529.

doi:10.1063/1.341827.

[168] C.A. Neugebauer, M.B. Webb, Electrical Conduction Mechanism in Ultrathin, Evaporated Metal Films, J. Appl. Phys. 33 (1962) 74–82. doi:10.1063/1.1728531.

[169] R.A. Matula, Electrical resistivity of copper, gold, palladium, and silver, J. Phys. Chem. Ref. Data. 8 (1979) 1147–1298. doi:10.1063/1.555614.

[170] Y. Namba, Resistivity and Temperature Coefficient of Thin Metal Films with Rough Surface, Jpn. J. Appl. Phys. 9 (1970) 1326–1329. doi:10.1143/JJAP.9.1326.

[171] H. Mera, M. Lannoo, C. Li, N. Cavassilas, M. Bescond, Inelastic scattering in nanoscale devices: One-shot current-conserving lowest-order approximation, Phys. Rev. B. 86 (2012) 161404. doi:10.1103/PhysRevB.86.161404.

[172] G. García-Calderón, Tunneling in Semiconductor Resonant Structures, in: P. Butcher, N.H. March, M.P. Tosi (Eds.), Phys. Low-Dimensional Semicond. Struct., Plenum Press, New York, 1993: pp. 267–297.

[173] N. Zainal, P. Walker, A.J. Kent, Modelling of cubic AlxGa1–xN/GaN resonant tunnel diode structures, Phys. Status Solidi. 7 (2010) 2262–2264. doi:10.1002/pssc.200983543.

[174] G.H. Rieke, Visible and Infrared Coherent receivers, in: Detect. Light from Ultrav. to Submilim., 2nd Ed., Cambridge University Press, Cambridge, United Kingdom, 2003: pp. 275–279.

[175] P. Roblin, R.C. Potter, A. Fathimulla, Interface roughness scattering in AlAs/InGaAs resonant tunneling diodes with an InAs subwell, J. Appl. Phys. 79 (1996) 2502. doi:10.1063/1.361104.

[176] R. Baba, B.J. Stevens, T. Mukai, R.A. Hogg, Epitaxial Designs for Maximizing Efficiency in Resonant Tunneling Diode Based Terahertz Emitters, IEEE J. Quantum Electron. 54 (2018) 1–11. doi:10.1109/JQE.2018.2797960.

[177] K.J.P. Jacobs, B.J. Stevens, O. Wada, T. Mukai, D. Ohnishi, R.A. Hogg, A Dual-Pass High Current Density Resonant Tunneling Diode for Terahertz Wave Applications, IEEE Electron Device Lett. 36 (2015) 1295–1298. doi:10.1109/LED.2015.2491339.

[178] Y. Miyamoto, H. Tobita, K. Oshima, K. Furuya, Barrier thickness dependence of peak current density in GaInAs/AlAs/InP resonant tunneling diodes by MOVPE, Solid. State. Electron. 43 (1999) 1395–1398. doi:10.1016/S0038-1101(99)00079-9.

[179] T. Maekawa, H. Kanaya, S. Suzuki, M. Asada, Oscillation up to 1.92 THz in resonant tunneling diode by reduced conduction loss, Appl. Phys. Express. 9 (2016) 24101. http://stacks.iop.org/1882-0786/9/i=2/a=024101.

[180] M. Kim, J. Lee, J. Lee, K. Yang, A 675 GHz Differential Oscillator Based on a Resonant Tunneling Diode, IEEE Trans. Terahertz Sci. Technol. 6 (2016) 510–512. doi:10.1109/TTHZ.2016.2554399.

[181] K.J.P. Jacobs, Development of Resonant Tunnelling Diode Terahertz Emitter, Ph.D. Dissertation, Dept. of Electronic & Electrical Engineering, The University of Sheffield, 2015. doi:uk.bl.ethos.655292.

[182] S. Suzuki, M. Shiraishi, H. Shibayama, M. Asada, High-Power Operation of Terahertz Oscillators With Resonant Tunneling Diodes Using Impedance-Matched Antennas and Array Configuration, Sel. Top. Quantum Electron. IEEE J. 19 (2013) 8500108. doi:10.1109/JSTQE.2012.2215017.

[183] P. Zhao, H.L. Cui, D. Woolard, K.L. Jensen, F.A. Buot, Simulation of resonant tunneling structures: Origin of the I–V hysteresis and plateau-like structure, J. Appl. Phys. 87 (2000) 1337. doi:10.1063/1.372019.

[184] E.R. Brown, C.D. Parker, A.R. Calawa, M.J. Manfra, Resonant tunneling through mixed quasibound states in a triple-well structure, Appl. Phys. Lett. 62 (1993) 3016–3018. doi:10.1063/1.109175.

[185] M. Reddy, R.Y.Y. Yu, H. Kroemer, M.J.W.J.W. Rodwell, S.C.C. Martin, R.E.E. Muller, R.P.P. Smith, Bias stabilization for resonant tunnel diode oscillators, IEEE Microw. Guid.

Wave Lett. 5 (1995) 219–221. doi:10.1109/75.392280.

[186] L. Wang, J.M.L. Figueiredo, C.N. Ironside, E. Wasige, DC characterization of tunnel diodes under stable non-oscillatory circuit conditions, IEEE Trans. Electron Devices. 58 (2011) 343–347. doi:10.1109/TED.2010.2091507.

[187] S.G. Muttlak, O.S. Abdulwahid, J. Sexton, M.J. Kelly, M. Missous, InGaAs/AlAs Resonant Tunneling Diodes for THz Applications: An Experimental Investigation, IEEE J. Electron Devices Soc. 6 (2018) 254–262. doi:10.1109/JEDS.2018.2797951.

[188] K.J.P. Jacobs, R. Baba, B.J. Stevens, T. Mukai, D. Ohnishi, R.A. Hogg, D. Ohnishi, R.A. Hogg, Characterisation of high current density resonant tunneling diodes for THz emission using photoluminescence spectroscopy, in: D.L. Huffaker, H. Eisele, K.A. Dick (Eds.), Proc. SPIE 9758, Quantum Dots Nanostructures Growth, Charact. Model. XIII, 97580L (March 15 2016), 2016: p. 97580L. doi:10.1117/12.2212669.

[189] T. Sandu, W.P. Kirk, The role of emitter quasi-bound state and scattering on intrinsic bistability in resonant tunneling diodes, Phys. E Low-Dimensional Syst. Nanostructures. 22 (2004) 815–824. doi:10.1016/j.physe.2003.09.038.

[190] M.A. Pate, Observation of intrinsic bistability in resonant tunnelling devices, Electron. Lett. 24 (1988) 1190–1191(1). http://digital-library.theiet.org/content/journals/10.1049/el_19880809.

[191] L. Eaves, G.A. Toombs, F.W. Sheard, C.A. Payling, M.L. Leadbeater, E.S. Alves, T.J. Foster, P.E. Simmonds, M. Henini, O.H. Hughes, J.C. Portal, G. Hill, M.A. Pate, Sequential tunneling due to intersubband scattering in double-barrier resonant tunneling devices, Appl. Phys. Lett. 52 (1988) 212–214. doi:10.1063/1.99522.

[192] P.D. Yoder, M. Grupen, R.K. Smith, Demonstration of Intrinsic Tristability in Double-Barrier Resonant Tunneling Diodes With the Wigner Transport Equation, IEEE Trans. Electron Devices. 57 (2010) 3265–3274. doi:10.1109/TED.2010.2081672.

[193] C.D.W. Wilkinson, L. Deng, M. Rahman, Issues in Etching Compound and Si-based Devices, Jpn. J. Appl. Phys. 41 (2002) 4261. http://stacks.iop.org/1347-4065/41/i=6S/a=4261.

[194] B. Ściana, M. Badura, W. Dawidowski, K. Bielak, D. Radziewicz, D. Pucicki, A. Szyszka, K. Żelazna, M. Tłaczała, LP-MOVPE growth and properties of high Si-doped InGaAs contact layer for quantum cascade laser applications, Opto-Electronics Rev. 24 (2016). doi:10.1515/oere-2016-0013.

[195] M. Asada, S. Suzuki, Terahertz oscillators using electron devices - an approach with Resonant tunneling diodes, IEICE Electron. Express. 8 (2011) 1110–1126. doi:10.1587/elex.8.1110.

[196] E.R. Brown, J.R. Söderström, C.D. Parker, L.J. Mahoney, K.M. Molvar, T.C. McGill, Oscillations up to 712 GHz in InAs/AlSb resonant-tunneling diodes, Appl. Phys. Lett. 58 (1991) 2291–2293. doi:10.1063/1.104902.

[197] N. Orihashi, S. Suzuki, M. Asada, Voltage-controlled sub-terahertz oscillation of resonant tunneling diode integrated with slot antenna, Electron Lett. 41 (2005). doi:10.1049/el:20051828.

[198] T.P.E. Broekaert, C.G. Fonstad, In0.53Ga0.47As/AlAs resonant tunneling diodes with peak current densities in excess of 450 kA/cm2, J. Appl. Phys. 68 (1990) 4310. doi:10.1063/1.346226.

[199] M.A. Md Zawawi, M. Missous, Dependencies of Peak Current Density on Barrier and Spacer Thickness in InGaAs/AlAs Resonant Tunneling Diode, in: Procedings UK Semicond. 2014, Sheffield, UK, Sheffield, 2014.

[200] F. Capasso, K. Mohammed, A. Cho, Resonant tunneling through double barriers, perpendicular quantum transport phenomena in superlattices, and their device applications, IEEE J. Quantum Electron. 22 (1986) 1853–1869. doi:10.1109/JQE.1986.1073171.

[201] R. Baba, B.J. Stevens, T. Mukai, R.A. Hogg, K.J.P. Jacobs, B.J. Stevens, R.A. Hogg, T. Mukai, D. Ohnishi, Optimization of the epitaxial design of high current density resonant

tunneling diodes for terahertz emitters, in: M. Razeghi (Ed.), Proc. SPIE 9755, Quantum Sens. Nano Electron. Photonics XIII, 97552W (13 Febr. 2016), 2016: p. 97552W. doi:10.1117/12.2212346.

[202] R. Baba, B.J. Stevens, T. Mukai, R.A. Hogg, Epitaxial design for maximising wall plug efficiency in resonant tunnelling diode terahertz emitters, in: 2016 41st Int. Conf. Infrared, Millimeter, Terahertz Waves, IEEE, 2016: pp. 1–2. doi:10.1109/IRMMW-THz.2016.7758959.

[203] M. Feiginov, C. Sydlo, O. Cojocari, P. Meissner, High-frequency nonlinear characteristics of resonant-tunnelling diodes, Appl. Phys. Lett. 99 (2011) 133501. doi:10.1063/1.3644491.

[204] M. Shiraishi, H. Shibayama, K. Ishigaki, S. Suzuki, M. Asada, H. Sugiyama, H. Yokoyama, High Output Power (~400 μW) Oscillators at around 550 GHz Using Resonant Tunneling Diodes with Graded Emitter and Thin Barriers, Appl. Phys. Express. 4 (2011) 064101. doi:10.1143/APEX.4.064101.

[205] M. Feiginov, C. Sydlo, O. Cojocari, P. Meissner, Resonant-tunnelling-diode oscillators operating at frequencies above 1.1 THz, Appl. Phys. Lett. 99 (2011) 233506. doi:10.1063/1.3667191.

[206] E.R. Brown, T.C.L.G. Sollner, C.D. Parker, W.D. Goodhue, C.L. Chen, Oscillations up to 420 GHz in GaAs/AlAs resonant tunneling diodes, Appl. Phys. Lett. 55 (1989) 1777–1779. doi:10.1063/1.102190.

[207] M.N. Feiginov, Displacement currents and the real part of high-frequency conductance of the resonant-tunneling diode, Appl. Phys. Lett. 78 (2001) 3301–3303. doi:10.1063/1.1372357.

[208] T. Maekawa, H. Kanaya, M. Asada, S. Suzuki, 1.92 THz Oscillator using Resonant Tunneling Diode Integrated with Slot Antenna with Reduced Conduction Loss, in: 3rd Int. Symp. Microwave/Terahertz Sci. Appl. (MTSA 2015), Okinawa, 2015.

[209] S. Suzuki, M. Asada, A. Teranishi, H. Sugiyama, H. Yokoyama, Fundamental oscillation of resonant tunneling diodes above 1 THz at room temperature, Appl. Phys. Lett. 97 (2010) 242102. doi:10.1063/1.3525834.

[210] S. Suzuki, K. Sawada, A. Teranishi, M. Asada, H. Sugiyama, H. Yokoyama, Fundamental oscillations at ~900 GHz with low bias voltages in RTDs with spike-doped structures, Electron. Lett. 46 (2010) 1006. doi:10.1049/el.2010.1102.

[211] R. Izumi, S. Suzuki, M. Asada, 1.98 THz resonant-tunneling-diode oscillator with reduced conduction loss by thick antenna electrode, in: 2017 42nd Int. Conf. Infrared, Millimeter, Terahertz Waves, IEEE, 2017: pp. 1–2. doi:10.1109/IRMMW-THz.2017.8066877.

[212] T. Koga, J. Nitta, H. Takayanagi, S. Datta, Spin-Filter Device Based on the Rashba Effect Using a Nonmagnetic Resonant Tunneling Diode, Phys. Rev. Lett. 88 (2002) 126601. doi:10.1103/PhysRevLett.88.126601.

[213] S. Sen, F. Capasso, A.C. Gossard, R.A. Spah, A.L. Hutchinson, S.N.G. Chu, Observation of resonant tunneling through a compositionally graded parabolic quantum well, Appl. Phys. Lett. 51 (1987) 1428–1430. doi:10.1063/1.98646.

[214] Y. Horikoshi, M. Kawashima, H. Yamaguchi, Migration-Enhanced Epitaxy of GaAs and AlGaAs, Jpn. J. Appl. Phys. 27 (1988) 169–179. doi:10.1143/JJAP.27.169.

[215] T. Bergunde, B. Henninger, M. Lünenbürger, M. Heuken, M. Weyers, J.-T. Zettler, Automated emissivity corrected wafer-temperature measurement in Aixtrons planetary reactors, J. Cryst. Growth. 248 (2003) 235–239. doi:10.1016/S0022-0248(02)01856-0.

[216] J. Cowley, J. Spence, P. Self, M.A. O'Keefe, P. Buseck, D. Veblen, L. Eyring, O.L. Krivanek, K. Yagi, A. Howie, High-Resolution Transmission Electron Microscopy: and Associated Techniques, 1989.

[217] J.M. Gibson, High Resolution Transmission Electron Microscopy, MRS Bull. 16 (1991) 27–33. doi:10.1557/S0883769400057377.

[218] P. Williams, Secondary Ion Mass Spectrometry, Annu. Rev. Mater. Sci. 15 (1985) 517–548. doi:10.1146/annurev.ms.15.080185.002505.

[219] R. Kinder, B. Paszkiewicz, B. Sciana, L. Huleny, The influence of the electrolyte-semiconductor interface on the doping profile measurement of a GaAs structure, ASDAM 2000. Conf. Proceedings. Third Int. EuroConference Adv. Semicond. Devices Microsystems (Cat. No.00EX386). (2000) 335–338. doi:10.1109/ASDAM.2000.889514.

[220] K.J.P. Jacobs, B.J. Stevens, T. Mukai, D. Ohnishi, R.A. Hogg, Non-destructive mapping of doping and structural composition of MOVPE-grown high current density resonant tunnelling diodes through photoluminescence spectroscopy, J. Cryst. Growth. 418 (2015) 102–110. doi:10.1016/j.jcrysgro.2015.02.017.

[221] V.I. Zubkov, M.A. Melnik, A. V. Solomonov, E.O. Tsvelev, F. Bugge, M. Weyers, G. Tränkle, Determination of band offsets in strained InGaAs⁄GaAs quantum wells by capacitance-voltage profiling and Schrödinger-Poisson self-consistent simulation, Phys. Rev. B. 70 (2004) 075312. doi:10.1103/PhysRevB.70.075312.

[222] D.L. Dorset, X-ray Diffraction: A Practical Approach, Microsc. Microanal. 4 (1998) 513–515. doi:10.1017/S143192769800049X.

[223] M. Adachi, X.Y. Chen, R. Chen, M. Cotlet, M. Darbandi, H. V. Demir, et al., UV-VIS and Photoluminescence Spectroscopy for Nanomaterials Characterization, Springer Berlin Heidelberg, Berlin, Heidelberg, 2013. doi:10.1007/978-3-642-27594-4.

[224] R.T. Collins, K. v. Klitzing, K. Ploog, Photocurrent spectroscopy of GaAs/ AlGaAs quantum wells in an electric field, Phys. Rev. B. 33 (1986) 4378–4381. doi:10.1103/PhysRevB.33.4378.

[225] M.S. Skolnick, P.R. Tapster, S.J. Bass, A.D. Pitt, N. Apsley, S.P. Aldred, Investigation of InGaAs-InP quantum wells by optical spectroscopy, Semicond. Sci. Technol. 1 (1986) 29–40. doi:10.1088/0268-1242/1/1/003.

[226] J. Finders, J. Geurts, A. Kohl, M. Weyers, B. Opitz, O. Kayser, P. Balk, Composition of selectively grown InxGa1−xAs structures from locally resolved Raman spectroscopy, J. Cryst. Growth. 107 (1991) 151–155. doi:10.1016/0022-0248(91)90448-E.

[227] M. Fox, Phonons, in: Opt. Prop. Solids, 2nd ed., Oxford University Press, New York, 2010: pp. 271–293.

[228] C.Y. Poon, B. Bhushan, Comparison of surface roughness measurements by stylus profiler, AFM and non-contact optical profiler, Wear. 190 (1995) 76–88. doi:10.1016/0043-1648(95)06697-7.

[229] J. Jahanmir, J.C. Wyant, Comparison of surface roughness measured with an optical profiler and a scanning probe microscope, in: J. Tsujiuchi (Ed.), Proc. Vol. 1720, Intl Symp Opt. Fabr. Testing, Surf. Eval., 1992: pp. 111–118. doi:10.1117/12.132117.

[230] V.A. Vilkotskii, D.S. Domanevskii, R.D. Kakanakov, V. V Krasovskii, V.D. Tkachev, Burstein-Moss effect and near-band-edge luminescence spectrum of highly doped indium arsenide, Phys. Status Solidi. 91 (1979) 71–81. doi:10.1002/pssb.2220910106.

[231] M. Muñoz, F. Pollak, M. Kahn, D. Ritter, L. Kronik, G. Cohen, Burstein-Moss shift of n-doped In0.53Ga0.47As/InP, Phys. Rev. B. 63 (2001) 233302. doi:10.1103/PhysRevB.63.233302.

[232] K.J.P. Jacobs, R. Baba, B.J. Stevens, T. Mukai, D. Ohnishi, R.A. Hogg, Characterisation of high current density resonant tunneling diodes for THz emission using photoluminescence spectroscopy, in: Proc. SPIE - Int. Soc. Opt. Eng., 2016. doi:10.1117/12.2212669.

[233] G. Duggan, A critical review of heterojunction band offsets, J. Vac. Sci. Technol. B Microelectron. Nanom. Struct. 3 (1985) 1224. doi:10.1116/1.583045.

[234] M.D. Dawson, G. Duggan, Exciton localization effects and heterojunction band offset in (Ga,In)P-(Al,Ga,In)P multiple quantum wells, Phys. Rev. B. 47 (1993) 12598–12604. doi:10.1103/PhysRevB.47.12598.

[235] D. Guimard, M. Ishida, D. Bordel, L. Li, M. Nishioka, Y. Tanaka, M. Ekawa, H. Sudo, T. Yamamoto, H. Kondo, M. Sugawara, Y. Arakawa, Ground state lasing at 1.30 microm from InAs/GaAs quantum dot lasers grown by metal-organic chemical vapor deposition., Nanotechnology. 21 (2010) 105604. doi:10.1088/0957-4484/21/10/105604.

[236] D. Bimberg, N. Kirstaedter, N.N. Ledentsov, Z.I. Alferov, P.S. Kop'ev, V.M. Ustinov, InGaAs-GaAs quantum-dot lasers, IEEE J. Sel. Top. Quantum Electron. 3 (1997) 196–205. doi:10.1109/2944.605656.

[237] U. Pietsch, V. Holý, T. Baumbach, High-Resolution X-Ray Scattering, Springer New York, New York, NY, NY, 2004. doi:10.1007/978-1-4757-4050-9.

[238] Y. Waseda, E. Matsubara, K. Shinoda, X-Ray Diffraction Crystallography, Springer Berlin Heidelberg, Berlin, Heidelberg, Heidelberg, 2011. doi:10.1007/978-3-642-16635-8.

[239] S.A. Stepanov, Dynamical X-Ray Diffraction From Multilayers, GID_sl Web. (2012). http://x-server.gmca.aps.anl.gov/cgi/www_form.exe?template=GID_sl_multilay_simplified.htm&method=post.

[240] G. Patriarche, L. Largeau, J.-C. Harmand, D. Gollub, Morphology and composition of highly strained InGaAs and InGaAsN layers grown on GaAs substrate, Appl. Phys. Lett. 84 (2004) 203–205. doi:10.1063/1.1639510.

[241] A. Rosenauer, U. Fischer, D. Gerthsen, A. Förster, Composition evaluation by lattice fringe analysis, Ultramicroscopy. 72 (1998) 121–133. doi:10.1016/S0304-3991(98)00002-3.

[242] J.R. Söderström, E.R. Brown, C.D. Parker, L.J. Mahoney, J.Y. Yao, T.G. Andersson, T.C. McGill, Growth and characterization of high current density, high-speed InAs/AlSb resonant tunneling diodes, Appl. Phys. Lett. 58 (1991) 275. doi:10.1063/1.104659.

[243] M. Achouche, M. Chtioui, Uni-travelling-carrier photodiode, US9214582B2, 2010. https://patents.google.com/patent/US9214582B2/en.

[244] COMSOL AB, Dielectric Resonator Antenna Application ID: 12042, (2016). https://www.comsol.fi/model/dielectric-resonator-antenna-12042 (accessed May 12, 2018).

[245] K.H. Alharbi, A. Khalid, A. Ofiare, J. Wang, E. Wasige, Broadband bow-tie slot antenna with tuning stub for resonant tunnelling diode oscillators with novel configuration for substrate effects suppression, in: 2016 46th Eur. Microw. Conf., IEEE, 2016: pp. 421–424. doi:10.1109/EuMC.2016.7824369.

[246] T. Otsuji, M. Shur, Terahertz Plasmonics: Good Results and Great Expectations, IEEE Microw. Mag. 15 (2014) 43–50. doi:10.1109/MMM.2014.2355712.

[247] H. Zhang, L.A. Dunbar, G. Scalari, R. Houdré, J. Faist, Terahertz photonic crystal quantum cascade lasers, Opt. Express. 15 (2007) 16818. doi:10.1364/OE.15.016818.

[248] W. Withayachumnankul, C. Fumeaux, Photonic crystal traps THz waves, Nat. Photonics. 8 (2014) 586–587. doi:10.1038/nphoton.2014.168.

[249] A. Sharma, G. Singh, Rectangular Microstrip Patch Antenna Design at THz Frequency for Short Distance Wireless Communication Systems, J. Infrared, Millimeter, Terahertz Waves. 30 (2009) 1–7. doi:10.1007/s10762-008-9416-z.

[250] A. Petosa, A. Ittipiboon, Dielectric Resonator Antennas: A Historical Review and the Current State of the Art, IEEE Antennas Propag. Mag. 52 (2010) 91–116. doi:10.1109/MAP.2010.5687510.

[251] R.S. Yaduvanshi, H. Parthasarathy, Rectangular Dielectric Resonator Antennas, Springer India, New Delhi, 2016. doi:10.1007/978-81-322-2500-3.

[252] S. Keyrouz, D. Caratelli, Dielectric Resonator Antennas: Basic Concepts, Design Guidelines, and Recent Developments at Millimeter-Wave Frequencies, Int. J. Antennas Propag. 2016 (2016) 1–20. doi:10.1155/2016/6075680.

[253] S. Kitagawa, K. Ogino, S. Suzuki, M. Asada, Wide frequency tuning in resonant-tunneling-diode terahertz oscillator using forward-biased varactor diode, Jpn. J. Appl. Phys. 56 (2017) 040301. doi:10.7567/JJAP.56.040301.

[254] R. Terazzi, J. Faist, A density matrix model of transport and radiation in quantum cascade lasers, New J. Phys. 12 (2010) 33045. http://stacks.iop.org/1367-2630/12/i=3/a=033045.

[255] T. Kubis, P. Vogl, Self-consistent quantum transport theory: Applications and assessment of approximate models, J. Comput. Electron. 6 (2007) 183–186. doi:10.1007/s10825-006-

0078-6.

[256] M. Franckié, D.O. Winge, J. Wolf, V. Liverini, E. Dupont, V. Trinité, J. Faist, A. Wacker, Impact of interface roughness distributions on the operation of quantum cascade lasers, Opt. Express. 23 (2015) 5201–5212. doi:10.1364/OE.23.005201.

[257] P.Y. Yu, M. Cardona, Fundamentals of Semiconductors, 4th ed., Springer Berlin Heidelberg, Berlin, Heidelberg, 2010. doi:10.1007/978-3-642-00710-1.

[258] O. Mizuno, H. Watanabe, Semi-insulating properties of Fe-doped InP, Electron. Lett. 11 (1975) 118. doi:10.1049/el:19750089.

[259] H.F. Tiedje, H.K. Haugen, J.S. Preston, Measurement of nonlinear absorption coefficients in GaAs, InP and Si by an optical pump THz probe technique, Opt. Commun. 274 (2007) 187–197. doi:10.1016/j.optcom.2007.01.049.

[260] R. Kucharski, Ł. Janicki, M. Zajac, M. Welna, M. Motyka, C. Skierbiszewski, R. Kudrawiec, Transparency of Semi-Insulating, n-Type, and p-Type Ammonothermal GaN Substrates in the Near-Infrared, Mid-Infrared, and THz Spectral Range, Crystals. 7 (2017) 187. doi:10.3390/cryst7070187.

[261] T.L. Bergman, A.S. Lavine, F.P. Incropera, D.P. DeWitt, Introduction to Heat Transfer, 6th ed., Wiley, Hoboken, NJ, 2011.

[262] A. Strittmatter, A. Krost, M. Straßburg, V. Türck, D. Bimberg, J. Bläsing, J. Christen, Low-pressure metal organic chemical vapor deposition of GaN on silicon(111) substrates using an AlAs nucleation layer, Appl. Phys. Lett. 74 (1999) 1242–1244. doi:10.1063/1.123512.

[263] C.A. Tran, A. Osinski, R.F. Karlicek, I. Berishev, Growth of InGaN/GaN multiple-quantum-well blue light-emitting diodes on silicon by metalorganic vapor phase epitaxy, Appl. Phys. Lett. 75 (1999) 1494–1496. doi:10.1063/1.124733.

[264] L. Adams, L. Adams, Space Radiation Effects in Electronic Components., Radiat. Eff. (2003). http://esamultimedia.esa.int/docs/industry/SME/2003/Space-Component/ESA-Training-Radiation-ESTEC_May03.pdf.

[265] B. Romeira, K. Seunarine, C.N. Ironside, A.E. Kelly, J.M.L. Figueiredo, A Self-Synchronized Optoelectronic Oscillator Based on an RTD Photodetector and a Laser Diode, IEEE Photonics Technol. Lett. 23 (2011) 1148–1150. doi:10.1109/LPT.2011.2154320.

[266] S. Wang, F. Xue, A.Q. Huang, S. Liu, Physics understanding of high temperature behavior of Gallium Nitride power transistor, in: 2016 IEEE 4th Work. Wide Bandgap Power Devices Appl., IEEE, 2016: pp. 324–327. doi:10.1109/WiPDA.2016.7799961.

[267] R.M. Kapre, A. Madhukar, S. Guha, Highly strained GaAs/InGaAs/AlAs resonant tunneling diodes with simultaneously high peak current densities and peak-to-valley ratios at room temperature, Appl. Phys. Lett. 58 (1991) 2255–2257. doi:10.1063/1.104943.

[268] T.S. Roberts, B.J. Stevens, E. Clarke, I. Tooley, J. Orchard, I. Farrer, D.T.D. Childs, N. Babazadeh, N. Ozaki, D. Mowbray, R.A. Hogg, Strain Balancing of Metal-Organic Vapour Phase Epitaxy InAs/GaAs Quantum Dot Lasers, IEEE J. Sel. Top. Quantum Electron. 23 (2017) 1–8. doi:10.1109/JSTQE.2017.2703666.

[269] I.N. Stranski, L. Krastanov, Abhandlungen der Mathematisch-Naturwissenschaftlichen Klasse IIb, Akad. Der Wissenschaften Wien. 146 (1938) 797–810.

[270] J. Leo, G.A. Toombs, Resonant tunneling through a symmetric triple-barrier structure, Phys. Rev. B. 43 (1991) 9944–9946. doi:10.1103/PhysRevB.43.9944.

[271] P.D. Buckle, P. Dawson, C.Y. Kuo, A.H. Roberts, W.S. Truscott, M. Lynch, M. Missous, Charge accumulation in GaAs/AlGaAs triple barrier resonant tunneling structures, J. Appl. Phys. 83 (1998) 882. doi:10.1063/1.366772.

[272] R. Sekiguchi, Y. Koyama, T. Ouchi, Subterahertz oscillations from triple-barrier resonant tunneling diodes with integrated patch antennas, Appl. Phys. Lett. 96 (2010) 062115. doi:10.1063/1.3315868.

[273] C.P. Allford, R.E. Legg, R.A. O'Donnell, P. Dawson, M. Missous, P.D. Buckle, Thermally activated resonant tunnelling in GaAs/AlGaAs triple barrier heterostructures, Semicond. Sci.

Technol. 30 (2015) 105035. doi:10.1088/0268-1242/30/10/105035.

[274] C.P. Allford, P.D. Buckle, Strain Compensated InGaAs/AlAs Triple Barrier Resonant Tunneling Structures for THz Applications, IEEE Trans. Terahertz Sci. Technol. 7 (2017) 772–779. doi:10.1109/TTHZ.2017.2758266.

[275] G.K. Reeves, Specific contact resistance using a circular transmission line model, Solid. State. Electron. 23 (1980) 487–490. doi:10.1016/0038-1101(80)90086-6.

[276] G.S. Marlow, M.B. Das, The effects of contact size and non-zero metal resistance on the determination of specific contact resistance, Solid. State. Electron. 25 (1982) 91–94. doi:10.1016/0038-1101(82)90036-3.

[277] J.H. Klootwijk, C.E. Timmering, Merits and limitations of circular TLM structures for contact resistance determination for novel III-V HBTs, in: Proc. 2004 Int. Conf. Microelectron. Test Struct. (IEEE Cat. No.04CH37516), IEEE, n.d.: pp. 247–252. doi:10.1109/ICMTS.2004.1309489.

[278] V.L. Rideout, A review of the theory and technology for ohmic contacts to group III–V compound semiconductors, Solid. State. Electron. 18 (1975) 541–550. doi:10.1016/0038-1101(75)90031-3.

[279] A.. Baca, F. Ren, J.. Zolper, R.. Briggs, S.. Pearton, A survey of ohmic contacts to III-V compound semiconductors, Thin Solid Films. 308–309 (1997) 599–606. doi:10.1016/S0040-6090(97)00439-2.